Observations and Measurements of $\mathrm{L} = 1$ Orbitally Excited B Mesons at the D0 Experiment

Mark Richard James Williams *MPhys*

Lancaster University

A thesis submitted for the degree of
Doctor of Philosophy

September 2008

“Three quarks for Muster Mark!”

— James Joyce (‘Finnegan’s Wake’, 1939)

“There is no excellent beauty that hath not some strangeness in the proportion.”

— Francis Bacon (‘On Beauty’, 1625)

OBSERVATIONS AND MEASUREMENTS OF L = 1 ORBITALLY EXCITED B MESONS AT THE D0 EXPERIMENT

Mark Richard James Williams *MPhys*

Lancaster University

A thesis submitted for the degree of Doctor of Philosophy

September 2008

Abstract

THIS THESIS describes investigations of the first set of orbitally excited ($L = 1$) states for both the B_d^0 and B_s^0 meson systems (B_d^{**} and B_s^{**}). The data sample corresponds to 1.35 fb^{-1} of integrated luminosity, collected in 2002-2006 by the D0 detector, during the Run IIa operation of the Tevatron $p\bar{p}$ colliding beam accelerator.

The B_d^{**} states are fully reconstructed in decays to $B^{(*)+}\pi^-$, with $B^{(*)+} \to (\gamma)J/\psi K^+$, $J/\psi \to \mu^+\mu^-$, yielding 662 ± 91 events, and providing the first strong evidence for the resolution of two narrow resonances, B_1 and B_2^*. The masses are extracted from a binned χ^2 fit to the invariant mass distribution, giving $M(B_1) = 5720.7 \pm 2.4$ (stat.)± 1.3 (syst.)$\pm$ 0.5 (PDG) MeV/c^2 and $M(B_2^*) = 5746.9 \pm 2.4$ (stat.) $\pm\, 1.0$ (syst.) $\pm\, 0.5$ (PDG) MeV/c^2. The production rate of narrow $B_d^{**} \to B\pi$ resonances relative to the B^+ meson is determined to be $[13.9 \pm 1.9$ (stat.) $\pm\, 3.2$ (syst.)] %.

The same B^+ sample is also used to reconstruct the analogous states in the B_s^0 system, in decays $B_s^{**} \to B^{(*)+}K^-$. A single resonance in the invariant mass distribution is found with a statistical significance of 5σ, interpreted as the B_{s2}^* state. The mass is determined to be $M(B_{s2}^*) = 5839.6 \pm 1.1$ (stat.) $\pm\, 0.4$ (syst.) $\pm\, 0.5$ (PDG) MeV/c^2, and the production rate of $B_{s2}^* \to BK$ resonances is measured to be a fraction $(2.14 \pm 0.43 \pm 0.24)$ % of the corresponding rate for B^+ mesons. Alternative fitting hypotheses give inconclusive evidence for the presence of the lighter B_{s1} meson.

Acknowledgments

THE four years of my PhD course have been a wonderful time in my life, and I feel very lucky to have made the transition from student to scientist, meeting some great people along the way. I have been consistently surprised by the selflessness of researchers in high energy physics, who will gladly give their time to help a colleague; and I've realised that the real collaborations are not limited to individual experiments, but to the entire field. I have neither the space nor the memory to thank everyone who helped me along the way, but there are a number of people who deserve special acknowledgment.

Firstly, my supervisor Peter Ratoff, who has been a calm, approachable, and insightful mentor, always available to discuss issues of all kinds, academic or personal. Peter has allowed me to apply my own approach to problems, and I'm very grateful for the independence and skills I have gained by this experience. At the same time, he has been a constant guiding presence, encouraging me and increasing my confidence as a researcher. I always felt better after our meetings, whatever the subject. Thank you Peter.

Guennadi Borissov played a major role in the physics analyses I worked on. His drive and dedication to improving experimental results was an inspiration to me. Aside from his detailed knowledge of B physics theory, experimental history and analysis methods, he was always quick to respond to any questions I asked, by phone, e-mail, or in person. I am excited to continue working alongside Guennadi over the next few years at D0: hopefully we can continue to produce world-leading results and keep the LHC experiments on their toes!

The close-knit nature of the Lancaster D0 group meant that I also worked closely with Iain Bertram, to my considerable benefit. Iain's expertise in Monte Carlo simulation was

invaluable, teaching me how to shape and generate my own samples of data for use in several different studies. In general, Iain was always willing to spend time to help me solve technical problems, with ROOT, MINUIT and several other packages. I also want to thank the Lancaster University HEP group collectively: for the excellent lectures provided in my first year, for the friendly open-door atmosphere, and for the support that I always discerned, even from the other side of the Atlantic.

While in Fermilab, there have been so many individuals who have played important parts in my early physics career. The conveners and members of the B group were always accessible and interested in my analyses: their comments and advice shaped the studies and elevated them to the quality required for publication. In particular, thanks to Brendan Casey, Rick Van Kooten and Dmitri Tsybychev. Also, I am indebted to all the members of Editorial Board 23, headed by Gene Fisk and Arthur Maciel, who were so helpful and efficient in closely examining and refining both B^{**} and B_s^{**} analyses. The D0 experiment is a fantastic collaboration of people, all the way up to the top —I have been humbled and impressed by the interest of the Spokespersons in my progress, and would like to thank Dmitri Denisov especially for taking the time to discuss my current and future plans, treating me as a valuable member of the collaboration: it won't be forgotten.

I have been tremendously lucky to be supported wholeheartedly by my wonderful parents, who have always given me support in any decision I've made. Without their positivity, love, and assistance, I am sure that this thesis would not have been possible. All my life they have encouraged me to foster an interest in the world, be it scientific, artistic, or social. Thank-you so much for everything!

My final words must be dedicated to Leena, my beautiful girlfriend, who constantly amazes me with her energy, kindness and balance. She has shared in all my experiences for the last two-and-a-half years, always showing interest in my work, and completely unselfish in her support. Leena, your intelligence is stimulating, your smile is calming, and when you're near it all seems easier, somehow. I couldn't dream of a better person to spend my life with. Thank-you.

Contents

List of Tables

List of Figures

Preface

THIS THESIS PRESENTS THE RESULTS of two studies which I undertook while a member of the D0 collaboration during 2004–2008, namely: "Observation and Properties of $L = 1$ B_1 and B_2^* Mesons", and "Observation and Properties of the Orbitally Excited B_{s2}^* Meson". For most of this time I was based at the experiment in Fermilab, near Chicago, USA. In addition to being the primary author for these analyses, I was involved in a number of service tasks aimed at improving and maintaining the quality of data collected by the experiment.

I completed a full six-week rotation of control room shifts at the data acquisition (DAQ) console, with the objective of minimising the interruption of data flow. I was also involved in a tracking task force, where my main responsibility was to determine the positions and orientations of various detector components. By looking for differences in these coordinates before and after the Run IIb detector upgrade, a new alignment file was produced, improving the performance of the tracking algorithms used to turn the raw data into useable particle-oriented information. As part of the B-physics group, I have taken a leading role in the organisation and arrangement of data: converting the collaboration-wide files into a suitable format for use with the group's specialist analysis framework; skimming these new files to produce 'event lists' for some common samples (such as dimuon events); and documenting this process online.

Both the physics analyses were brought to a conclusion, and passed through the various stages of peer review: B-group feedback, collaboration-wide review, and investigation by a dedicated editorial board. I took the leading role in replying to the comments and questions which arose in this period, making additional studies when required. As part of this process, I twice presented my results to the entire collaboration, and wrote an internal note for each analysis. On successfully satisfying the collaboration, and the

journal referees, the analyses were accepted by *Physical Review Letters* and published in December 2007 [3] and February 2008 [4]. In recognition of my research, I received a share of the Rutherglen Prize In July 2007, awarded annually to a research student in high energy physics from an institution associated with the Daresbury Laboratory.

Chapter 1

Introduction

THE ANCIENT GREEKS are often credited with having provided the foundations of the physical sciences, with their attempts to classify the structure of the universe in terms of a discrete, finite number of 'elements'. However, their deductive *a priori* approach is very far removed from the modern inductive methods with which we investigate the world. Since the scientific revolution of the sixteenth and seventeenth centuries, our understanding of the fundamental processes and substance of the universe has been advanced by a close partnership of theory and experiment. In particular, measurements made on complex systems have allowed theorists to penetrate to the underlying cause. For example, Johannes Kepler's laws of planetary motion (c. 1605) were extracted from observations of the solar system, a complex arrangement of interacting bodies. In turn, these rules helped Newton to construct his law of universal gravitation (1687). Similarly, the patterns observed in the periodic table of elements led to the belief that there must be some deeper truth than simply a collection of unrelated substances. We now know that every element is made up of the same three components, electrons, neutrons and protons, and that the different chemical properties of elements can be explained in terms of the interactions and combinations of these electrons.

In general, the observation of such patterns in a system is indicative of some underlying structure. The study of these systems allows the structure to be probed and promotes a more general understanding of the fundamental processes at work. An excellent example

is the investigation of the spectral lines of certain chemicals: the observed patterns first led to an empirical formula to explain their energy spacing (Rydberg, 1888), and later to a complete overhaul in the theoretical description of atomic structure (the Rutherford-Bohr model, 1913). This was in turn a major driving force in the development of a quantum mechanical theory of electromagnetism (QED), one of the most important achievements of the twentieth century.

Aside from gravity and electromagnetism, there is a third fundamental interaction which produces bound states, analogous to the solar system or the hydrogen atom, and responsible for binding protons and neutrons into atomic nuclei. In the 1950s, the proton and neutron were assumed to be fundamental particles, but experiments at this time had also identified an increasing number of other nucleon-like states (called baryons), in addition to similar 'meson' states, thought to be the force carrier through which these nucleons interacted. The proliferation of this particle 'zoo' motivated attempts to simplify the picture and repeat the successes of the atomic model, by postulating some 'more fundamental' objects out of which the mesons and baryons (collectively termed 'hadrons') were constructed. The resulting quark model of Gell-Mann [5] (with important contributions from Zweig and others) was an elegant and simple solution, which explained the properties of all known hadrons in terms of their quark composition. At the time, three types ('flavours') of quark were sufficient to explain the observed particle zoo, but we now believe that there are six. In fact, the nature of quarks means that they can only be investigated through the bound states which they form, so the study of patterns and symmetries in the baryons and mesons is of huge importance.

The force associated with binding these quarks together is called the strong or chromomagnetic interaction. In analogy with the development of QED following observations in the atomic spectra, there are firm reasons for believing that the corresponding quantum field theory of the strong force (QCD) can be refined by investigation of hadronic spectra. The different energy levels of atoms arise through interactions between electrons and the atomic nucleus, while quark interactions lead to a similar quantised energy structure in mesons and baryons. In atomic theory, measurements in the hydrogen system are particularly useful: the relative ease with which QED predictions can be made facilitates

comparison with experiment and allows various small effects to be isolated and studied separately. Certain hadrons offer a similar opportunity: so-called heavy-light mesons containing one massive quark and one relatively light quark. Since the b quark is the most massive which is observed in bound states, the energy spectra of mesons containing a b quark (B mesons) are considered a key area in which experimental results can be used to drive forward the theoretical understanding of QCD.

However, although the lowest energy states of several B mesons are well established experimentally, measurements of the higher energy levels are lacking. The information collected in the last seven years by the D0 and CDF experiments on the Tevatron $p\bar{p}$ collider offers an opportunity to improve on this situation, with powerful and well understood detectors collecting very large samples of B mesons for subsequent analysis. In this thesis certain 'orbitally excited' energy states in the B_d^0 and B_s^0 systems are investigated, and precise measurements are made of their properties. The results are compared with predictions of various theoretical approaches, giving additional experimental leverage with which to improve the calculations of QCD interactions.

This first chapter gives a general introduction to modern particle physics, providing the foundations required to understand the specific orbitally excited states under investigation. In Chapter 2, the theoretical details are described more thoroughly, with reference to the production, properties and decays of excited B mesons. The results of different groups of theorists are reviewed, which helps to motivate an appropriate experimental methodology. Chapter 3 describes the experimental apparatus, including the accelerator complex used to generate the particles of interest, and the detection components used to search for and measure them. This is followed in Chapter 4 by a detailed description of the particle reconstruction and selection algorithms. In order to extract maximum information from the data, computer simulations are required. Such studies are described in Chapter 5; they improve our understanding of the detector environment, allowing the experimental observations to be transformed into the 'true' particle properties. The extraction of these properties from the data involves fitting observations to a suitable parameterisation, which is the subject of Chapter 6. The final results are given in Chapter 7, and in Chapter 8 are

compared to the findings of previous studies, and the expectations of the various theoretical approaches.

1.1 Overview

The aim of this chapter is to introduce the concepts of meson spectroscopy, and describe the particular states of interest to this analysis. This involves the discussion of several general theoretical aspects, although the specific approaches to determining the excited B meson properties, and the resulting predictions, are reserved for Chapter 2.

The properties of quark-antiquark (meson) bound states are reviewed, with reference to certain important parameters defining the arrangement of the internal quark configuration. These ideas are used to explain how a set of distinct mass states emerges from a single quark composition, in analogy with hydrogen energy levels. The expected structure of energy levels in B mesons is then described, and the allowed decays of these states are determined. Finally, the previous experimental studies are summarised, leading to an identification of the primary objectives of this analysis.

However, before delving into the details of meson spectroscopy, it is useful to examine the broader picture of particle physics, forming the so-called standard model. This represents our current best understanding of the structure and dynamics of the universe; it consists of a list of fundamental particles, with their properties, and a set of theories governing their interactions with each other. The motivation for observing and investigating certain aspects of meson spectroscopy will then be seen in the context of the standard model and its limitations.

1.2 The Standard Model of Particle Physics

The following is a very brief summary of the standard model, with emphasis placed on describing the properties of the various particles and interactions, without explicit mathematical derivation. More details can be found in numerous excellent textbooks, for example, Ref. [6]– [7].

1.2.1 The Fundamental Particles and their Organisation

In the standard model, all matter in the universe is made up of a small number of different particle types, each with a particular fixed mass and defined by a set of parameters called quantum numbers. Examples of quantum numbers are the electric charge, spin, lepton number and baryon number, which are described below. Some quantum numbers are conserved in all types of interaction, while others may be conserved only in specific types of process. Their values determine the ways in which different particles interact (for example, only particles with a non-zero electric charge can interact via the electromagnetic force). For this reason, they form a basis for organising the different particles into distinct categories.

Bosons and Fermions

Particles are either denoted as fermions or bosons, depending on the value of their 'spin' quantum number (s). This represents an intrinsic angular momentum of the particle, and can be either integral (bosons), or half-integral (fermions) units of the reduced Planck constant $\hbar$. The two categories of particle behave differently: fermions obey Fermi-Dirac statistics, which prevents multiple particles from possessing the same quantum state (i.e. having all the same quantum numbers, including position and momentum); bosons obey Bose-Einstein statistics, which does not impose this restriction. Spin is treated in exactly the same way as quantised angular momentum: composite systems of particles have a spin (here denoted by an upper-case 'S') defined by the vector addition of their constituent spins. For example, a system of two fermions will produce a boson with spin $S = 0$ (for antiparallel fermion spin vectors) or $S = 1$ (for parallel fermion spin vectors).

The fundamental ('gauge') bosons observed in nature all have spin $s = 1$, and act as force carriers through which different particle interactions occur. Photons mediate the electromagnetic force, gluons the strong force, and the massive Z^0 and $W^{\pm}$ bosons mediate the weak force. The general form of these particle interactions is described later in this section. The standard model predicts an additional $s = 0$ particle, the Higgs boson, as a result of the spontaneous symmetry breaking of the unified electroweak interaction. The

Higgs mechanism is required to explain why many particles have mass, via interactions with the Higgs field which possesses a non-zero vacuum expectation value.

Fermions: Quarks and Leptons

The fundamental fermions are further divided into quarks (q), which participate in the strong force (see later) and leptons (l), which do not. The leptons comprise three charged particles (l^-): the electron (e^-), muon (μ^-) and tau (τ^-), each associated with a neutral, light (or massless) neutrino ($\nu_{e,\mu,\tau}$). The number of leptons is a constant in any interaction, quantified by assigning them a lepton number of $L = +1$, which is a conserved quantity once antiparticles are taken into account (see below). Furthermore, the lepton sector forms three generations, shown in Table 1.1, with almost all interactions preserving the lepton number *within each generation*. The exceptions are certain weak interactions, observed as neutrino mixing. The charged leptons can interact through both electromagnetic and weak interactions, with the neutrinos only experiencing the weak force.

Table 1.1: Properties of leptons in the standard model [8], showing the division into three generations. Here and elsewhere, s is the spin (in units of $\hbar$), L is the lepton number, Q is the electric charge and M is the particle mass.

Particle	Symbol	s	L	Q	M (MeV/c^2)	Generation
electron	e^-	$1/2$	1	-1	0.511	1
electron neutrino	ν_e			0	< 0.000002	
muon	μ^-	$1/2$	1	-1	105.7	2
muon neutrino	ν_μ			0	< 0.19	
tau	τ^-	$1/2$	1	-1	1777	3
tau neutrino	ν_τ			0	< 18.2	

At this stage it is convenient to introduce the concept of *antiparticles*. Each type of particle (both fermions and bosons) is associated with a 'mirror image' partner of the same mass, called an antiparticle, in which the signs of all quantum numbers (e.g. charge, lepton number and baryon number) are reversed; the sign reversal of spin is not defined, since it is a vector quantity. For example, the antiparticle partner of an electron is a positron

(e^+), with $L = -1$; hence the annihilation process $e^+ + e^- \rightarrow \gamma$ satisfies lepton number conservation. If all the quantum numbers are equal to zero, as is the case for the photon, a particle is indistinguishable from its antiparticle, and the concept becomes meaningless. Where there is ambiguity regarding notation, antiparticles are always indicated with a bar over them (such as $\bar{\nu}_e$).

The remainder of the fundamental fermions are quarks, which come in six 'flavours' (up, down, strange, charm, top, bottom) denoted by their initial letters. These can also be arranged into three generations, each containing an up-type quark with charge $Q = +2/3$, and a down-type quark with charge $Q = -1/3$. Table 1.2 summarises the quark properties, which show that the masses are not well measured. This is because quarks are never observed separately, only as part of a multi-quark bound state, called a *hadron*. The only bound states which have observed to date are (anti-) baryons, formed from three quarks, qqq ($\bar{q}\bar{q}\bar{q}$) and mesons formed from a quark-antiquark pair $q\bar{q}$, although other more complex bound states (such as pentaquarks) may exist. The number of quarks is a conserved quantity, under the usual scheme whereby antiquarks are assigned a negative quark number. Historically, this rule is quantified as conservation of baryons, via the baryon quantum number B. This is equal to $+\frac{1}{3}(-\frac{1}{3})$ for all quarks (antiquarks), and zero for other particles.

Table 1.2: Properties of quarks in the standard model [8], showing the division into three generations. B is the baryon number, with other quantities defined as usual. Throughout this thesis, the quark masses are denoted by m_f, where f is the flavour.

Particle	Symbol	s	B	Q	m_f (MeV/c^2)	Generation
up quark	u	$1/2$	$1/3$	$+2/3$	~ 3	1
down quark	d			$-1/3$	~ 5	
charm quark	c	$1/2$	$1/3$	$+2/3$	~ 1300	2
strange quark	s			$-1/3$	~ 100	
top quark	t	$1/2$	$1/3$	$+2/3$	$\sim 171,000$	3
bottom quark	b			$-1/3$	~ 4500	

The confinement of quarks into bound states arises from the particular form of the strong force, described by quantum chromodynamics. All quarks possess a 'colour charge', which is the strong force equivalent of the electric charge, except that it comes in three varieties: conventionally chosen to be red (R), green (G), and blue (B); the antiquarks possess the 'anticolours' ($\bar{R}$, $\bar{G}$, $\bar{B}$). All coloured objects are subject to the strong force, which is mediated by gluons, much like photons in the case of electromagnetism. However, unlike photons, which are uncharged and so cannot self-interact, the gluons do carry colour, leading to some very important differences between electromagnetic and strong interactions, of which quark confinement is one effect. The observed bound state structure of quarks can be reproduced by requiring that all directly observable objects be 'colourless', which is clearly not the case for separate quarks, but is true for suitable combinations of colour inside baryons ($q_R q_G q_B$), or mesons (e.g. $q_R \bar{q}_{\bar{R}}$).

1.2.2 Particle Interactions

Excluding the force of gravity, which is negligible in fundamental particle interactions, there are three forces which may act upon the particles listed above. These are the electromagnetic force, the strong force, and the weak force. In each case, the interaction between two particles takes the form of a boson exchange, with the nature of the force depending strongly on the properties of the boson, summarised in Table 1.3. The strong force controls the properties of B mesons, and the decays of $L = 1$ excited B mesons to the ground state, or to the singly excited B^*; the electromagnetic force is involved in the de-excitation of the B^* meson; and the weak force controls the subsequent decay of the ground state B meson. Hence all three interactions play a role in the analysis described by this thesis. In the following text, the three forces are reviewed and some relevant aspects are discussed qualitatively.

The Electromagnetic Force

The electromagnetic interaction is described by Quantum Electrodynamics (QED), which acts on all charged particles by the exchange of photons. The field has infinite range,

Table 1.3: The fundamental forces of nature (excluding gravity), and properties of the mediating bosons. The gluon mass has not been measured, so its theoretical value is given; the relative strengths are taken from [7], and express the magnitude of each force experienced by two protons in contact. J is the total angular momentum (equal to the spin for fundamental particles) and P is the parity, discussed in Section 1.3.

Force	Boson	J^P	M (GeV/c^2)	Strength
Strong	Gluon (g)	1^-	0	1
Electromagnetic	Photon (γ)	1^-	0	10^{-2}
Weak	$W^{\pm}$	1^-	80.398 ± 0.025	10^{-7}
	Z^0	1^+	91.1876 ± 0.0021	

with a magnitude decreasing as $1/r^2$, where r is the distance between the interacting charged particles. Formally, QED is derived by requiring $U(1)$ gauge symmetry (see, for instance, Ref. [9]), meaning that the Lagrangian must be unchanged when the charged particle wavefunction undergoes the transformation $\psi(x) \rightarrow e^{i\alpha(x)}\psi(x)$, where $\alpha(x)$ is a real constant with spatial dependence. This can only be achieved by introducing a photon field to the free particle Lagrangian. This method is extended to determine the Quantum Field Theory for the other interactions, by constructing appropriate Lagrangians which satisfy local gauge invariance.

Amongst the numerous consequences of QED is the combination of nuclei and electrons into bound states: atoms; all chemical reactions and properties are therefore described by this force. The energy levels of hydrogen provide a testing ground for the theoretical predictions of QED, and show excellent agreement with theory.

The Strong Force

The strong force has many similarities with electromagnetic interaction, acting on all colour-charged objects by the exchange of massless gluons, under a field theory called Quantum Chromodynamics (QCD). However, there is a very important difference with respect to QED: colour comes in three varieties. This changes the $U(1)$ gauge invariance to the $SU(3)$ phase transformation group, which in turn requires the introduction of eight

gluon fields. These gluons are bi-coloured to allow the conservation of the colour charge in QCD interactions. They are formed by superposition of the nine possible colour combinations $C\bar{C}$, with $C = \{R, G, B\}$. The ninth orthogonal combination forms a colour singlet of the form $(R\bar{R}+G\bar{G}+B\bar{B})$, which is colourless, and therefore cannot participate in QCD. The consequence is that gluons self-interact, limiting the range of the force to be very short, extending over nuclear scales ($\sim 10^{-15}$ m). In addition to the formation of hadrons, the strong force also results in stable baryons (protons and neutrons) combining to form nuclei.

Both the strong and electromagnetic forces conserve quark flavour: in any process mediated by photons or gluons, the quark content for each flavour will be unchanged. This can be quantified by defining new conserved quantum numbers, such as 'upness', 'downness', 'strangeness' and so on, which have unit magnitude for quarks of the appropriate type, with antiparticles having the opposite sign to particles. In practice, only 'strangeness' (S) is commonly used now; for historical reasons the s ($\bar{s}$) quark is defined with $S = -1(+1)$.

The Weak Force

The weak force is distinct from QED and QCD in several ways. It is mediated by the exchange of both charged ($W^{\pm}$) and neutral (Z^0) bosons, and acts on all quarks and leptons. As implied by the name, the observed interaction strength at experimental energies is much lower than the other two forces, leading to smaller probabilities of weak processes occurring. However, it allows many possible processes which are forbidden by QED and QCD, therefore its effects are clearly felt. The weak interaction is the only way in which neutrinos participate in particle reactions, by couplings such as $W^- \rightarrow l^-\bar{\nu}_l$. It is also the only interaction which allows flavour-changing processes, via couplings of the type $W^+ \rightarrow u_i\bar{d}_j$, where u_i (d_j) is any up-type (down-type) quark. The amplitude for a particular $u\bar{d}$ interaction is set by the elements of the 3×3 CKM matrix V_{ij}, which expresses the fact that the quark states observed by the weak interaction (q') are actually superpositions of the quark strong eigenstates, e.g. $d' = V_{ud}d + V_{us}s + V_{ub}b$. In terms of physical observables, the CKM matrix contains three 'quark mixing angles' and one

phase. Amongst other things, weak interactions play an important role in decays of B hadrons.

The 'charge' of the $W^{\pm}$ weak interaction is called weak isospin (T), and its component along the quantised axis, T_3. Left-handed[1] fermions have $T = 1/2$, forming doublets in the quark ($T_3(u_i) = +\frac{1}{2}$; $T_3(d_i) = -\frac{1}{2}$) and lepton ($T_3(\nu_l) = +\frac{1}{2}$; $T_3(l^-) = -\frac{1}{2}$) sectors; right-handed fermions all have $T = 0$. As with the electric and colour charge, weak isospin is conserved by the weak force. The appropriate representation of this interaction is $SU(2)_L$, where the subscript indicates that only left-handed fermions participate. Note that for antiparticles, the situation is reversed and only right-handed antifermions have a non-zero weak isospin. It is also important to realise that the handedness of a massive particle depends on the reference frame, since one can always boost to a frame in which the particle's direction (and hence handedness) appears to be reversed. For this reason, the nature of the $SU(2)_L$ interaction is observed as a suppression of the interaction for right-handed massive fermions. In contrast, for massless neutrinos, right-handed ν and left-handed $\bar{\nu}$ states are forbidden from interacting weakly, and are hence not observed.

The full solution of the weak interaction in Lagrangian formalism leads to some interesting effects. Firstly, the electromagnetic and weak fields are seen to be unified into a single electroweak interaction, in an $SU(2)_L \times U(1)_Y$ gauge symmetry. The $SU(2)_L$ group described above results in the observed $W^{\pm}$ bosons, as well as a neutral W^0. The $U(1)_Y$ group is associated with 'weak hypercharge' $Y = 2(Q - T_3)$, and results in a quantum field B^0, which mixes with W^0 to produce the observed Z^0 and γ bosons. The $U(1)_Y$ component means that right-handed fermions can participate in weak interactions mediated by the Z^0 boson, but only if they are charged.

Secondly, the theory as it stands is only well behaved provided that all the bosons are massless. In order to allow non-zero masses, additional fields must be introduced into the electroweak Lagrangian, which manifest as the Higgs boson and its associated mass-giving field.

[1]Handedness is defined by the projection of the fermion spin vector onto the momentum vector: a left- (right-) handed particle has the spin antiparallel (parallel) to the direction of travel.

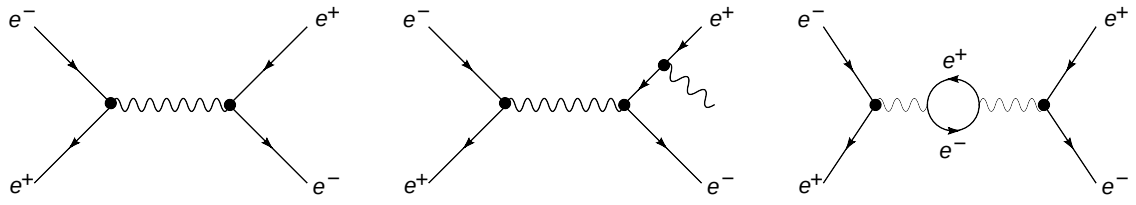

Figure 1.1: Examples of Feynman diagrams for the process $e^+e^- \rightarrow e^+e^-$. One leading order diagram is shown in (a), with higher order diagrams (3- and 4-vertex topologies respectively) shown in (b)–(c).

1.2.3 Feynman Diagrams

Once the Lagrangians have been constructed, the probability of any interaction can be determined by examining the appropriate *Feynman diagrams*, which are powerful and insightful visual tools, into which the full mathematical results of the Lagrangian approach are embedded. These diagrams show particle flow in terms of lines (solid for fermions, wavy for photons, curly for gluons, and dashed for $W^{\pm}$ and Z^0 bosons), connected by vertices. Figure 1.1 shows three examples of Feynman diagrams for the process $e^+e^- \rightarrow e^+e^-$. External (unbounded) lines represent free particles, which must have their true mass; internal lines represent 'virtual particles', in which the mass can differ from the nominal value, in order to conserve momentum in the system. This 'borrowing' of energy is allowed by the uncertainty principle, $\Delta t \Delta E \geq \hbar$, but only for very short lived particles. In this thesis, the left-to-right time axis convention is chosen to represent the evolution of interactions. One additional rule is that incoming antiparticles are equivalent to outgoing particles, and are drawn as such; hence antiparticles are interpreted as particles travelling backward in time (the Feynman-Stückelberg interpretation).

Each line and vertex is associated with a mathematical factor from the Lagrangian: the external lines with appropriate wavefunctions for the particle type, the internal lines with so-called 'propagators', and the vertices with vertex factors. An amplitude is calculated

for each diagram by multiplying the different factors, which is squared to produce an interaction probability. These amplitudes are in the form of matrices, since the wavefunctions of particles are not scalar, but elements of a vector space (e.g. an electron wavefunction has two components representing the possible spin orientations $s_z = \pm\frac{1}{2}$). The interaction probability is therefore given as the square of a matrix, $|\mathcal{M}|^2$. The details are outside the scope of this overview, but the general behaviour of the three types of interaction can be illuminated by examining some specific aspects of the Feynman diagrams.

One important consideration is that there are an infinite number of different internal topologies which connect the same initial and final states. The true interaction is in fact the sum of all these possibilities. Since these different processes can interfere with each other, a full solution requires that all the amplitudes be determined before squaring. This is not yet analytically possible, and so quantum field theory calculations use computerised numerical methods, or certain 'fixed-order resummation' techniques. The latter involve retaining a well-defined part of each term in the infinite series; the calculable sum of these contributions is then incorporated into the result. Luckily, in some cases there is a clear hierarchy in the size of each diagram's contribution to the probability, and so good precision can be obtained using only a few amplitude terms. This is possible because each vertex factor contains a dimensionless number quantifying the interaction strength: if this number is sufficiently small, then the contribution of processes decreases as their number of vertices increases.

Interaction Strengths in QED and QCD

In the electromagnetic force, each vertex is associated with a factor $\sqrt{\alpha}$, where $\alpha \approx \frac{1}{137}$. The lowest possible number of vertices in any interaction is two, so that the resulting probability is of order $\mathcal{O}(\alpha^2)$: diagrams with N additional vertices will be suppressed by $\mathcal{O}(\alpha^N)$. For any interaction topology, the diagrams containing fewest vertices are called the 'leading order' (LO) or 'tree level' processes; Next-to-leading-order (NLO) processes are those with minimal increase in the number of vertices compared to the LO diagrams. This allows calculations to be made using a perturbative approach, with interaction amplitudes dominated by the LO processes, and successive higher order terms

providing progressively finer corrections. This has allowed certain QED measurements to be made with extremely high precision, such as the famous gyromagnetic ratio of the electron which is now calculated using all Feynman diagrams up to eighth order [10]. In fact, α is not a constant, but scales with the interaction energy; the consequences of this type of behaviour are significant, and so this effect merits a short explanation.

In addition to summing over the various possible Feynman diagrams, there are some processes with internal degrees of freedom, which must also be taken into account. This turns out to be a very important effect in QED and QCD, as a result of loop diagrams such as that shown in Figure 1.1(c). In this process, a virtual e^+e^- pair is produced, followed by rapid annihilation to a photon. The equivalent process could happen with any $q_i\bar{q}_i$ pair instead, therefore the contribution from this diagram is the sum over all possible particle-antiparticle combinations in the loop. The probability of producing a particular pair of particles depends on the momentum carried by the photon: as this increases, so does the likelihood that a more massive loop is generated, for example a $c\bar{c}$ quark pair.

Significantly, the momenta of the particles in the loop are not constrained by external particle lines; as long as the e^+ and e^- momenta combine to give the photon momentum, they can take individual values up to infinity. This is a problem, since the sum over all possible states here becomes an integration over momentum, with infinite limits. Calculating the matrix element for the diagram gives an infinite probability, which is not physically meaningful. Fortunately this type of problem can be fixed, by redefining the basic tree level diagram to also be infinite, but in a controlled way, such that the combination of all infinities in the sum of Feynman diagrams gives a finite answer. Doing this is equivalent to redefining the vertex factor to be an infinite parameter in the theory: this 'bare' interaction strength is not seen in real physical processes, since the contributions from all other possible higher order diagrams cancel the infinities to give an observed interaction strength α. This process of absorbing infinities by changing the fundamental parameters of the theory is called renormalisation.

Since the loop contributions depend on the momentum of the propagating particle (i.e. the photon, in the above example), so does the final result once the infinities have been

cancelled; this leads to a dependence of α on the momentum transfer of the process (denoted by its square, Q^2). The scaling of $\alpha(Q^2)$ is a very important aspect of quantum field theories, since the size of this parameter controls the contribution of higher order diagrams. For QED, the notion of α as a small constant is very nearly correct at the typical momenta involved experimentally, allowing perturbation methods to be used; however, it diverges logarithmically as Q^2 increases. This can be considered in terms of the screening effect of the virtual e^+e^- pairs: at low energies interactions will be shielded by virtual e^+e^- pairs generated by the bare charge; but at higher energies the interaction time-frame will be shorter and the effective shielding is reduced. Fortunately, α remains reasonably small for all energies currently observed. However, at very high energies the perturbative approach described above will become invalid, and there is a hypothetical pole (the Landau Pole) at which it will reach infinity: this is a major motivation for attempts to develop a new theory of particle interactions at very large energies.

Similarly, in the strong force, each vertex is associated with a factor $\sqrt{\alpha_s}$. For QCD, however, the additional loop contributions from gluon-gluon interactions lead to a very different scaling of the equivalent interaction strength $\alpha_s(Q^2)$. This is small for large Q^2, leading to 'asymptotic freedom' where quarks act almost as free particles, but diverges at low values of momentum transfer resulting in confinement. The typical energy at which the theory becomes non-perturbative is quantified by the QCD confinement scale $\Lambda_{QCD} \approx 400$ MeV, such that $\alpha_s(\Lambda^2_{QCD}) \sim 1$. In terms of screening, the shielding effect of QED is actually reversed: the bare colour of a quark is anti-shielded by gluons which amplify the original quark colour, so that at low energies the interaction strength α_s diverges to very high values, preventing a perturbative approach from being used. On the other hand, at high energies the gluon shield is penetrated, and the true quark colour-charge is seen, leading to an apparent reduction in the interaction strength (and hence in α_s). Perturbative methods can therefore be used relatively successfully at energies above Λ_{QCD}, although for bound state interactions α_s is still larger than unity, and NLO processes are important.

Propagators and the Weak Interaction

Although the weak force will not be discussed in detail, it is worth noting that the equivalent interaction strength (the 'α' of the weak force) is in fact comparable to the electromagnetic α. However, experimental results show that weak interactions are heavily suppressed relative to the other forces: particles decaying through weak interactions typically have lifetimes of 10^{-6}–10^{-12} s, while electromagnetic and strong decays have timeframes of around 10^{-16} s and 10^{-23} s respectively. This is explained by the form of the propagators associated with internal particles in Feynman diagrams.

The general boson propagator contains a numerical factor $1/(p^2 - M^2)$, where p and M are respectively the four-momentum and the mass of the boson. Since the photon and gluon are massless, this reduces to $1/p^2$ for these cases. However, the W and Z bosons have large masses of almost 100 GeV/c^2. As a result, the propagator contributes an additional suppression factor to the interaction probability, relative to EM processes, of the order $p^4/(p^2 - M_{W,Z}^2)^2$, which comes to a factor of several thousand even at energies as high as 10 GeV. At energies above the boson masses, the weak and electromagnetic forces have similar strengths; this is expected as a result of the electroweak unification at large energy scales. In terms of the Heisenberg uncertainty principle, the weakness of the force is expected, since for low energy interactions the energy uncertainty ΔE required to produce the massive mediating boson will be very large, therefore the associated lifetime Δt will be small, leading to a very short spatial range and correspondingly small probabilities of interaction.

This completes the overview of the standard model. In the next section, the bound meson states formed by $q\bar{q}$ pairs are described in more detail, setting the scene for many of the ideas which arise in later chapters, including meson spectroscopy and allowed decay channels of particles.

1.3 Mesons: The Zoo of Bound $q\bar{q}$ States

This thesis is concerned with the way that quarks are arranged inside bound states, specifically in mesons containing a bottom quark. While the particular quark content is very important, the full meson state is only uniquely specified once the quantum numbers are known. In turn, this depends on the quark interactions inside the meson, for example the spins may be aligned parallel or antiparallel, to give a total meson spin S of 1 or 0 respectively. The masses, lifetimes and allowed decay channels of mesons depend on the quantum numbers of the system, meaning that mesons with the same quark content can be observed as distinct particle states. The *ground state* for a given $q\bar{q}$ combination corresponds to the lowest energy configuration of allowed quantum numbers. *Excited states* are those with different quark configurations, which have higher masses and shorter lifetimes. A full understanding of meson behaviour necessitates the introduction of some new symmetry principles.

1.3.1 Symmetries and Composite Particles

The decays of mesons are controlled by a number of conservation laws, some of which have already been discussed. The electric charge must be conserved, as must lepton and baryon number, and flavour-changing processes can only occur via the weak interaction. Conservation of energy and momentum is also imposed, which means that for decays of free mesons, the combined mass of the decay products cannot exceed the mass of the parent particle. One very important conserved quantity in particle physics is the total quantised angular momentum, J. In mesons this quantity is formed by the vector addition of the total spin S and the orbital angular momentum of the system, L. Additional conserved quantities, and the associated symmetries, are described below.

Parity

One important conserved quantity is the parity quantum number, P. The parity transformation changes the sign of all spatial coordinates of a state wavefunction, $(x, y, z) \rightarrow (-x, -y, -z)$. Since two successive parity transformations take the state back to its initial

form, the only allowable effects of a single transformation are to introduce a multiplicative factor of ± 1 to the wavefunction: this is the parity quantum number of that state. Often, the '1' is dropped and the parity denoted as either '$+$' (even) or '$-$' (odd). Fundamental particles possess an intrinsic parity, with fermions and antifermions having opposite values. For composite objects, the parities of the constituent particles are combined by multiplication, with an additional contribution arising from the interaction of the particles. In the case of mesons, the parity is given by:

$$P = (-1)^{L+1} \, . \tag{1.1}$$

This infers that all ground state mesons have odd parity. As with all conserved quantities in physics, parity is associated with a symmetry: physics processes should be invariant under a parity transformation. This is found to be true for all strong and electromagnetic interactions, but violated by the weak interaction. The parity transformation reverses the handedness of a particle: the absence of right-handed neutrino interactions is clear evidence for parity non-conservation.

Charge Conjugation

Charge conjugation is another parity-like (discrete) symmetry. In this case, the transformation is a replacement of all particles by their corresponding antiparticles, and vice versa: hence all internal quantum numbers change signs, but kinematic variables (mass, spin, energy etc) are unchanged. Again, the resulting quantum number C giving the change in the wavefunction can only take values ± 1. C-symmetry states that physics processes should be invariant under this transformation, which is true for the strong and EM forces. However, since charge conjugation transforms left-handed (LH) neutrinos into LH antineutrinos, the weak force violates C-symmetry. For mesons, C is given by:

$$C = (-1)^{L+S} \, . \tag{1.2}$$

Isospin

An additional symmetry, called isospin, reflects the fact that the up and down quark masses are almost identical. Isospin was initially introduced in an attempt to express protons and neutrons as two states of a single particle (the nucleon) differing in their projection of an additional spin-like quantity. The nucleon was assigned isospin $I = \frac{1}{2}$, with the projections along an axis, I_3, being $+\frac{1}{2}$ for protons and $-\frac{1}{2}$ for neutrons. The system was extended to include the lightest meson states (pions) which form an isospin triplet:

$$\begin{aligned} \pi^+ &= \quad u\bar{d} \qquad\quad (I = 1, I_3 = 1); \\ \pi^0 &= \tfrac{1}{\sqrt{2}}(u\bar{u} - d\bar{d}) \qquad (I = 1, I_3 = 0); \\ \pi^- &= \quad d\bar{u} \qquad\quad (I = 1, I_3 = -1); \end{aligned}$$

and the isospin singlet $\frac{1}{\sqrt{2}}(u\bar{u}+d\bar{d})$ has I=0. Strong decays preferentially conserve isospin, where the deviation from true symmetry arises from the non-zero mass difference $m_d - m_u$. As a result, decays in which I_3 cannot be conserved are suppressed. When combining with the other four quarks, this conservation is maintained by assigning each meson an effective isospin of $I = 1/2$ if it contains an up or down quark.

1.3.2 The Mesons of Interest

Of the six types of quark, all except the top form bound states; the top has such a short lifetime that it decays prior to hadron formation. This gives twenty-five possible $q\bar{q}$ combinations, all of which have now been observed as mesons. The similarity of the u and d quarks expressed by isospin symmetry means that the $u\bar{u}$ and $d\bar{d}$ combinations interfere to produce superpositions, as shown above for the pions. For other combinations, the quark masses are much larger, and so quantum interference is heavily suppressed: the states have a well defined quark content. The ground state mesons applicable to this thesis are shown in Table 1.4, with their quark content, mass and isospin. For consistency with the numbers used in the analysis publications [3, 4], the masses shown are from the PDG summary tables of 2006 [11]; there have been no significant changes since this time.

Table 1.4: Ground state properties of mesons used in this thesis, ordered by mass. For the B mesons, the isospin, angular momentum and parity have yet to be experimentally confirmed, so theoretical values are used.

Meson	Quark content	I	J^P	M (MeV/c^2)
π^0	$\frac{1}{\sqrt{2}}(u\bar{u} - d\bar{d})$	1	0^-	139.57018 ± 0.00035
$\pi^\pm$	$u\bar{d}$, $d\bar{u}$	1	0^-	134.9766 ± 0.0006
$K^\pm$	$u\bar{s}$, $s\bar{u}$	$1/2$	0^-	493.677 ± 0.016
$K^0, \bar{K}^0$	$d\bar{s}$, $s\bar{d}$	$1/2$	0^-	497.648 ± 0.022
J/ψ [a]	$c\bar{c}$	0	1^-	3096.916 ± 0.011
$B^\pm$	$u\bar{b}$, $b\bar{u}$	$1/2$	0^-	5279.0 ± 0.5
$B^0, \bar{B}^0$	$d\bar{b}$, $b\bar{d}$	$1/2$	0^-	5279.4 ± 0.5
$B_s^0, \bar{B}_s^0$	$s\bar{b}$, $b\bar{s}$	0	0^-	5367.5 ± 1.8

[a]The J/ψ meson is not technically a ground state particle, having spin $S = 1$. However, it is an important particle in searches for B mesons, so is included here.

The stage is now almost set for a discussion of hadron spectroscopy. It remains only to introduce a few additional concepts in particle decay, defining some new terms in the process.

1.4 Useful Concepts and Definitions

1.4.1 Phase-space

The notion of interaction probability has already been introduced, in terms of the square of the summed amplitudes determined from Feynman diagrams. For an individual interaction, with well defined initial and final states, the probability of interaction is in fact given exactly by $|\mathcal{M}|^2$. In real experiments, however, even if the initial state is known there will be a range of possible final states which must be summed over to produce the full interaction rate. As well as summing over the possible combinations of quantum numbers (such as the two possible spin orientations of fermions), the different allowed quantised momentum states must also be considered. This latter summation contributes

a *phase-space* factor to the interaction rate, which depends on the topology (number of initial and final particles) and the kinematics (range of allowed momenta which preserve conservation of energy) of the interaction. For example, in two-body decay $X \rightarrow ab$, the decay rate will be smaller when the mass difference $M(X) - M(a) - M(b)$ is smaller, because the number of allowed momentum states of particles a and b is reduced.

For now, it is sufficient to understand the concept of such phase-space suppression. Where an explicit calculation needs to be done, the appropriate relation is quoted, with a suitable reference, in the text.

1.4.2 Particle Decay, Lifetime and Width

All observed mesons are unstable, and will eventually decay by a strong, weak, or electromagnetic process; the allowed decays are limited by conservation of energy and the appropriate quantum numbers. Ground state B mesons decay via the weak force, usually in processes involving the heavy and short lived bottom quark, $b \rightarrow W^- c$, with the final state products depending on the decay of the virtual W^- boson; semileptonic decays such as $W^- \rightarrow e^- \bar{\nu}_e$ or hadronic decays such as $W^- \rightarrow s\bar{c}$. Since strong and electromagnetic decays are forbidden for these B mesons, they have a lifetime τ of around 1.6 ps, which corresponds to a characteristic decay length of several centimetres (at energies above 10 GeV$/c^2$). These distance scales are resolvable in particle physics experiments, making the lifetime determination possible. The lifetimes for all B mesons and baryons observed to-date are comparable, which is evidence that the non-b quark has low participation in the decay process, and is termed a 'spectator' quark.

As a result of the uncertainty principle, in its time-energy form, the finite lifetime of a particle leads to an uncertainty in its energy, and hence its mass. Because of this, the mass of a given particle can take a range of values, following a distribution of the form:

$$f(M) \sim \frac{M_0 \Gamma}{(M^2 - M_0^2)^2 + M_0^2 \Gamma^2} \, , \tag{1.3}$$

called the relativistic Breit-Wigner distribution. Here $f(M)$ is the probability of observing the particle with a mass M, when it has a mode mass of M_0; Γ is the *width*, related to the

lifetime by $\Gamma = \hbar/\tau$.

In some cases, phase-space factors can give a mass dependence to the width. For the decay of a particle of mass M into a number of daughter particles of masses m_i, this will be the case if the width is non-negligible compared to the decay mass difference $M - \Sigma_i m_i$. These *threshold effects* arise because phase-space suppression of decays at lower mass will distort the Breit-Wigner distribution, and the width must be parameterised as a function $\Gamma(M)$ according to the particular decay type. This is the case for the $L = 1$ excited B mesons, as detailed in Section 6.1.

Since a particle can in general decay into multiple final states, a partial width can be defined for each one, corresponding to the time-frame of that particular decay. Since the partial width gives the relative contribution of an individual channel to the full decay rate, it is also known as the *branching ratio*. Experimental determinations of mass, width, lifetime and the numerous branching ratios provide crucial tests of the various theories of particle interactions.

1.5 B Meson Spectroscopy

In the above discussion of mesons, the notion of excited states was explained in terms of quark-quark interactions leading to quantised energy levels above the ground state. In general, the QCD interaction inside mesons is outside the region of asymptotic freedom, and so perturbative calculation methods cannot be used. Predicting the masses and other properties of the excited states is therefore non-trivial, requiring the use of various approximations, such as Lattice QCD, $1/N$ expansions, or effective theories. These are briefly reviewed in Section 2.2. For B mesons, one particular effective theory approach is especially useful, as described below. In this introductory chapter, the emphasis is placed on describing the states of interest, with the specific theoretical predictions detailed in Chapter 2.

1.5.1 Orbital Excitations

In B mesons containing a light quark, the large mass difference $M(b) \gg M(u,d,s)$ allows the use of Heavy Quark Effective Theories (HQET), in which solutions are first determined under the approximation $M(b) \to \infty$, and then corrected by higher order terms in powers of $1/m_b$. This approach is equivalent to fixing the b quark as a static source of electromagnetic and colour fields, in which the light quark moves, and is described in more detail in Section 2.2.1. In fact, the more important inequality in this effective theory is $\Lambda_{QCD}/M(b) \ll 1$, without which the expansion could not be made. Under the heavy quark approximation, the spin interaction between the two quarks is suppressed, and the orbital excitations of the system can be characterised by three numbers: the orbital angular momentum L, the angular momentum of the light quark $j_q = L \pm \frac{1}{2}$, and the total angular momentum $J = j_q \pm \frac{1}{2}$. The HQET expansion predicts small mass differences for states with the same orbital angular momentum, and larger separations between these L multiplets. The $L = 0$ mesons form a doublet, the ground state (with $J = S = 0$) and the singly excited state $B^*_{(s)}$ with $J = S = 1$. In this thesis, the states of interest have $L = 1$, which corresponds to four different possible (J, j_q) combinations. These are collectively termed the *doubly excited* states, and labelled as B^{**} or B_J, with a flavour subscript where necessary.

In addition to these orbital excitations, there are energy levels corresponding to different solutions of the radial meson wavefunction. The radial excitations correspond to larger $q\bar{q}$ separations, and are pushed to higher energies by QCD confinement: the first set of radially excited states are therefore predicted to have larger masses than the corresponding $L = 1$ orbitally excited states. The radial and orbital states do not interfere, nor do their decay topologies look alike, therefore the radial states are disregarded from this point. The full spectroscopic notation of a meson state under the heavy quark limit has the form: $nL_J(j_q)$. Here n is the principal quantum number, expressing the degree of radial excitation (unity for all states discussed in this analysis); L is the orbital angular momentum denoted by a specific capital letter (S, P, D for $L = 1, 2, 3$ respectively); and J and j_q are the usual total angular momentum for the meson and the light quark respectively.

1.5.2 The B_d^0 System

As a result of isospin symmetry, the excited states of $B^{\pm}$ and B^0 are expected to have very similar masses, and are not listed separately by the Particle Data Group. Some previous experiments used inclusive selections, which did not distinguish between B_d^{**0} and $B_u^{**\pm}$. However, the exclusive reconstruction used in this analysis selects only the neutral $L = 1$ mesons, corresponding to a quark content $\bar{b}d$ and the antiparticle partner. Hereafter, all references to B^{**} refer to these neutral excited states. The charged states are denoted B_u^{**}, and combinations of both systems are denoted $B_{u,d}^{**}$. If there is any chance of ambiguity, the spectator quark flavour is explicitly included as a subscript.

Figure 1.2 shows the the energy levels for the $L = 1$ quartet of orbital excitations, relative to the $L = 0$ doublet. Also shown are the allowed transitions between the states, as justified in the next subsection. The shaded areas around the $L = 1, J_q = \frac{1}{2}$ doublet indicates that these states are expected to produce resonances with broad mass distributions, $\Gamma \sim \mathcal{O}(100)$ MeV/c^2. In contrast, the corresponding $j_q = \frac{3}{2}$ states are predicted to produce narrow mass resonances, $\Gamma \sim \mathcal{O}(10)$ MeV$/c^2$. This is a consequence of the angular momentum transfer involved in the decay, which is fixed according to conservation laws (see below). The result is that the B_0^* and B_1' mesons cannot be distinguished, in invariant mass distributions, from the combinatorial background. As such, the aim of this analysis is to observe only the narrow states B_1 and B_2^*, with the broad states considered as an irreducible source of background events.

The naming convention for the B_1' is not clear. In some cases both the narrow and broad $J^P = 1^+$ states are denoted B_1, since in principal they can interfere to produce superpositions of $j_q = \frac{1}{2}$ and $j_q = \frac{3}{2}$ components. However, the HQET decoupling of spins strongly suppresses this behaviour, causing each state to take on a well defined total spin, and resulting in the two orthogonal particles in Fig. 1.2. For this reason it is desirable that the notation distinguishes the broad and narrow B_1 excitations. Occasionally the notation B_1^* is used for the $j_q = \frac{1}{2}$ state, but this goes against the PDG convention, which reserves the asterisk superscript for 'natural' spin-parity combinations: $0^+, 1^-, 2^+$ and so on. As such, the primed notation is used throughout this thesis.

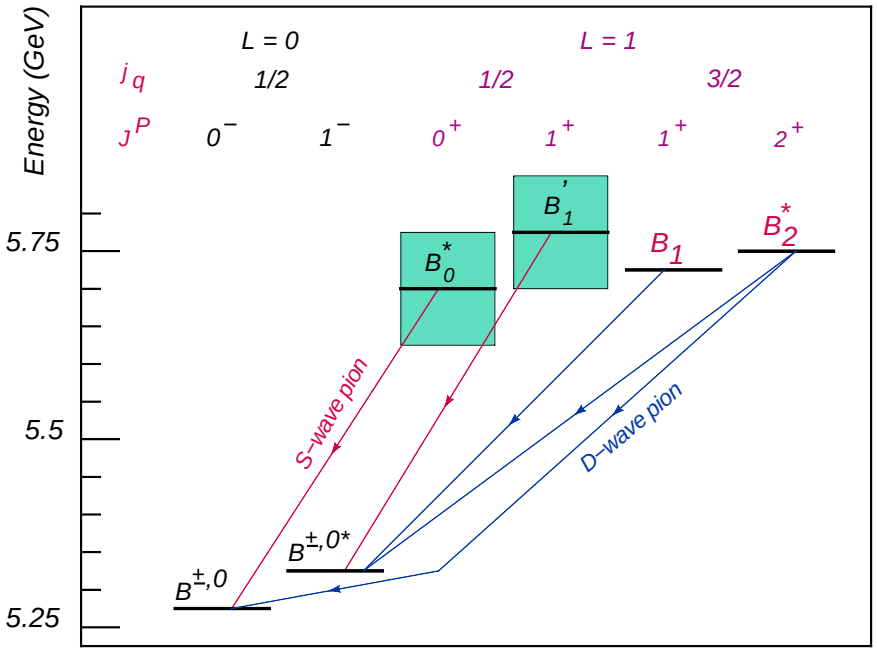

Figure 1.2: Energy level diagram for the $B_{u,d}$ system, showing the $L = 0$ doublet and $L = 1$ quartet of states. Also shown are the approximate energies, the quantum numbers under the heavy quark approach, and the allowed transitions to the $L = 0$ states.

Spin counting

In much the same way as isospin symmetry predicts that the three pions (π^+, π^0, π^-) are produced in equal amounts, the spin combinations of the B mesons provide a prediction for the relative production rates, by a spin-counting method. The $L = 0$ states $B_{(s)}$ and $B^*_{(s)}$ form respectively a singlet and a triplet in $SU(3)$ space, corresponding to the different possible angular momentum projections J_3:

$$B_{(s)}(J_3 = 0) = \frac{1}{\sqrt{2}}(\uparrow_Q\downarrow_q - \downarrow_Q\uparrow_q)\,, \qquad (S = 0 \text{ singlet}) \tag{1.4}$$

$$\begin{aligned} B^*_{(s)}(J_3 = +1) &= (\uparrow_Q\uparrow_q) \\ B^*_{(s)}(J_3 = 0) &= \frac{1}{\sqrt{2}}(\uparrow_Q\downarrow_q + \downarrow_Q\uparrow_q) \qquad (S = 1 \text{ triplet}) \\ B^*_{(s)}(J_3 = -1) &= (\downarrow_Q\downarrow_q)\,, \end{aligned} \tag{1.5}$$

where the arrows indicate the s_3 projections of the heavy and light quarks. By counting the number of spin combinations, and assuming that each is produced in equal quantities, the composition of the $L = 0$ mesons should satisfy $N(B^*)/N(B^{(*)}) = 3/4$. This is in agreement with the current PDG average for the Z^0 decay branching ratio $\Gamma(Z^0 \to B^*)/\Gamma(Z^0 \to B^{(*)}) = 0.75 \pm 0.04$ [8].

Similarly, the $L = 1$ mesons form multiplets corresponding to rotations in J-space, with the orbital angular momentum also contributing to the possible combinations. The $B^*_{(s)0}$ forms a $J_3 = 0$ singlet, both $B'_{(s)1}$ and $B_{(s)1}$ form triplets ($J_3 : -1, 0, +1$), while the $B^*_{(s)2}$ forms a quintet ($J_3 : -2, -1, 0, +1, +2$). Under this scheme, the relative production rates of the narrow $L = 1$ mesons should be $R(B_{(s)1})/R(B^*_{(s)2}) = 3/5$. The spin-counting method is also used to weight mass averages over L multiplets, for example in the calculations of Section 2.3.1.

Decays of B^{**} Mesons

As described in the following chapter, the predicted mass difference $M(B^{**}) - M(B^{(*)})$ is around 400–500 MeV. Therefore the only kinematically allowed strong decays of the doubly excited states occur through $B^{(*)}\pi$ channels. Decays to two pions are also allowed, but are not selected in this analysis. Experimentally, charged pions are much easier to detect and study than their neutral counterparts, which decay electromagnetically into two photons. Therefore the doubly excited mesons are studied only in decays to $B^{(*)+}\pi^-$, and the charge conjugate process. The quark flow diagrams for these decays are shown in Fig. 1.3. These diagrams represent in a simplified form the net flow of coloured objects: the true interaction picture will be more complicated, containing multiple gluon exchanges between quarks.

The three pions form an isospin triplet. Since the strong force satisfies isospin symmetry, decays to neutral $B^0\pi^0$ final states should comprise $1/3$ of the total $B\pi$ decay width. Hence the effect of these unobserved neutral states can be inferred by scaling the observed number of events by a factor $3/2$.

For each B^{**} state, the allowed single pion decay channels are determined by conservation of parity and angular momentum, as shown in Table 1.5. The approach here is to

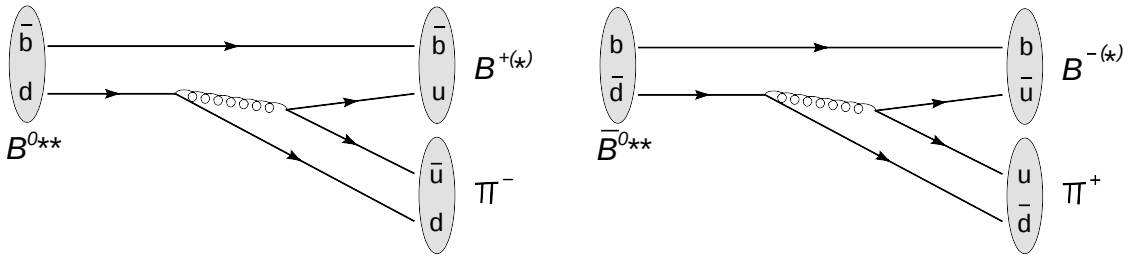

Figure 1.3: Quark flow diagrams for $B^{**} \to B^{(*)+}\pi^-$ decay (a) and the charge conjugated process (b). The corresponding decays to neutral $B^0\pi^0$ are not selected in this analysis.

first list all the possible final state values of orbital angular momentum $L_{B\pi}$ which conserve the total angular momentum by vector addition: $J = J_B + J_\pi + L_{B\pi}$. The resulting parity is then calculated by the usual combination relation $P_B \cdot P_\pi \cdot (-1)^L = (-1)^L$, since both final mesons have odd intrinsic parity. Finally, the conservation of the b quark spin implied by HQET further constrains the allowed $B_1^{(\prime)}$ decays.

Table 1.5 shows that except for the B_2^*, each of the B^{**} mesons has only one possible two-body decay route, and all decay channels are associated with a unique, fixed angular momentum in the final $B\pi$ state. All the broad state decays are through the $L = 0$ transition, called the s-wave decay in spectroscopic notation, while the narrow states always decay through $L = 2$ (d-wave) transitions. This explains the difference in widths of the two doublets, since s-wave decays have a shorter lifetime, and hence a larger mass uncertainty. The predicted values of relative production and decay branching ratios for the B^{**} states are discussed in the next chapter.

The singly excited B meson decays electromagnetically to the ground state, $B^*_{u,d} \to B_{u,d}\gamma$, almost 100% of the time. The photon energy is measured to be 45.78 ± 0.35 MeV, corresponding to the mass difference $M(B^*) - M(B)$ [8].

Table 1.5: Allowed decays of the B^{**} mesons into $B^{(*)}\pi$ channels, taking into account conservation of good quantum numbers. The column labelled $L_{B\pi}$ shows all allowed values for the orbital angular momentum in the final $B\pi$ system; these possibilities are then further tested by examining the corresponding final state parity, followed by the spin projection of the b quark. The crosses indicate the point at which a decay is found to be forbidden.

B^{**} State	J^P	B State	J^P	$J^P(\pi)$	$L_{B\pi}$	P_{B_π}	s_b
B_0^*	0^+	$B_{u,d}$	0^-	0^-	0	$(-1)^0 = +1$	✔
		$B_{u,d}^*$	1^-	0^-	1	$(-1)^1 = -1$ ✘	
B_1'	1^+	$B_{u,d}$	0^-	0^-	1	$(-1)^1 = -1$ ✘	
		$B_{u,d}^*$	1^-	0^-	0	$(-1)^0 = +1$	✔
					1	$(-1)^1 = -1$ ✘	
					2	$(-1)^2 = +1$	✘
B_1	1^+	$B_{u,d}$	0^-	0^-	1	$(-1)^1 = -1$ ✘	
		$B_{u,d}^*$	1^-	0^-	0	$(-1)^0 = +1$	✘
					1	$(-1)^1 = -1$ ✘	
					2	$(-1)^2 = +1$	✔
B_2^*	2^+	$B_{u,d}$	0^-	0^-	2	$(-1)^2 = +1$	✔
		$B_{u,d}^*$	1^-	0^-	1	$(-1)^1 = -1$ ✘	
					2	$(-1)^2 = +1$	✔

1.5.3 The B_s^0 System

Provided that the mass difference $M(B_s^{**}) - M(B)$ is large enough, the dominant decay channel for these doubly excited strange mesons will be $B_s^{**} \to B^{(*)}K$. This is because the $B_s\pi$ channel is forbidden by isospin conservation, since the final state isospins ($I_{B_s^0} = 0, I_\pi = 1$) cannot combine vectorially to match the initial state ($I_{B_s^{**}} = 0$). The $B^{(*)}K$ channel does satisfy this requirement, as seen from Table 1.4. In addition, this channel satisfies conservation of strangeness, which is enforced for strong interactions. Alternative decay channels to excited kaon states are expected to violate energy conservation, since the final state masses exceed the anticipated mass difference

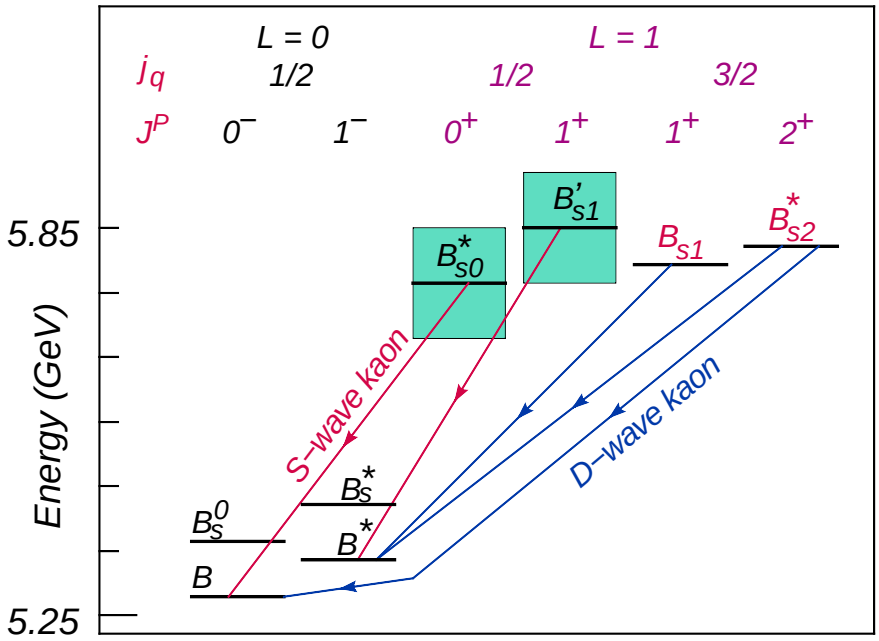

Figure 1.4: Energy level diagram for the B_s^0 system, showing the $L = 0$ doublet and $L = 1$ quartet of states. Also shown are the approximate energies, the quantum numbers under the heavy quark approach, and the allowed transitions to the $L = 0$ states of the $B_{u,d}$ mesons.

$M(B_s^{**}) - M(B) \lesssim 600$ MeV$/c^2$. This same argument should prevent decays to more than two products; this is not the case for the B^{**} states, which may have contributions from di-pion channels.

Since the strange quark is still light compared to the b quark, the same HQET arguments hold, and the energy level structure is expected to have the same form as the B^{**} system, as shown in Fig. 1.4. Since the relevant quantum numbers of all particles are unchanged from those given in Table 1.5, the structure of allowed transitions is also the same. The main differences between the two systems are:

- The production rate of B_s^{**} is expected to be lower (by a factor $\sim$4) than the corresponding B_d^{**} rate, as a result of the reduced probability that a b quark fragments into a B_s^0-type meson. This is described in more detail in Section 2.1.3.

- The different masses of the initial and final state particles may lead to kinematic

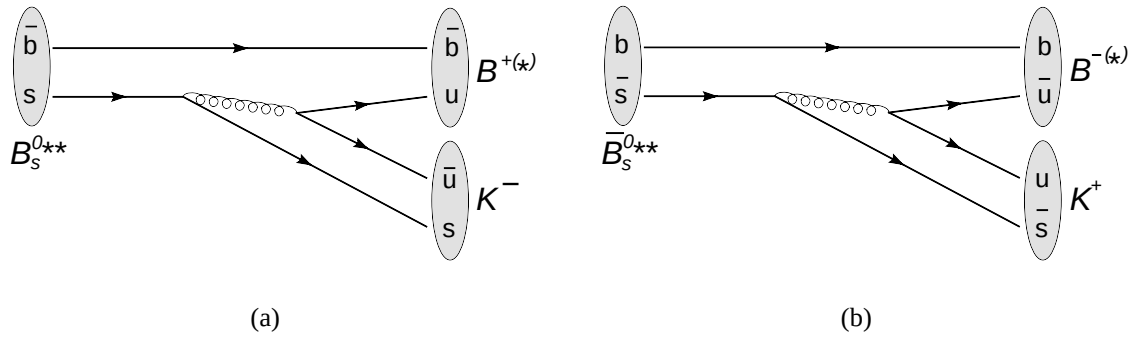

Figure 1.5: Quark flow diagrams for $B_s^{**} \to B^{(*)+}K^-$ decay (a) and the charge conjugated process (b). The corresponding decays to neutral B^0K^0 are not selected in this analysis.

(phase-space) effects being important in the B_s^{**} system, since the expected 'Q-value' $= M(B_s^{**}) - M(B^{(*)}) - M(K)$ is closer to the production threshold at zero. If one of the B_s^{**} transitions has a negative Q-value, it will be kinematically forbidden. More likely is that the different phase-space factors will result in suppression of some decays.

As a result of the similarities of the excited $b\bar{d}$ and $b\bar{s}$ systems, this thesis will contain many statements which apply to both cases. The convention is to use the symbol $B_{(s)}^{**}$ (or $B_{(s)J}$) to refer to the two systems in parallel.

Figure 1.5 shows the quark flow diagrams for the $B_s^{**} \to B^+K^-$ decay, and the corresponding charge conjugated reaction. This completes the qualitative description of B meson spectroscopy, and the states of interest for this analysis. In the remainder of this chapter, the previous experimental results in $B_{(s)}^{**}$ are reviewed, followed by a statement of the analysis objectives.

1.6 Previous Results

1.6.1 Inclusive Studies

The first results in B meson spectroscopy came in the mid 1990s, from colliding beam experiments on the Large Electron Positron (LEP) accelerating ring in CERN. This facility initiated symmetric beam e^+e^- collisions at four detectors around the ring (ALEPH, DELPHI, L3 and OPAL) at centre-of-mass energies corresponding to the central mass of the Z^0 boson. The detectors, although differing in design specifics, are comparable to the D0 facility described in Chapter 3, with concentric layers of various detection elements arranged around the collision region; typically comprising tracking and vertexing systems, calorimeters and muon detectors. The production of B mesons starts with an $e^+ + e^- \rightarrow Z^0$ resonance, which frequently decays to a $b\bar{b}$ quark-antiquark pair; subsequent fragmentation and hadronisation yields the final B mesons, which are collected for analysis.

In these early studies of excited B mesons, the states are reconstructed from suitable $B\pi$ (for $B^{**}_{u,d}$) or BK (for B^{**}_{s}) combinations, with appropriate selection to enhance the signal to background ratio. The B meson data samples are formed inclusively, without full reconstruction of the decay products. Instead, generic B meson events are inferred from a number of tagging algorithms, which build likelihood variables based on characteristic signatures, such as relatively long lifetimes, and high transverse momenta and topology of decay products. This reconstruction technique yields large samples of B mesons, but particular states are difficult to isolate, hence the $B\pi$ combinations in some studies yield both B^{**0}_{d} and $B^{**\pm}_{u}$ states. In addition, the procedures for determining the particle energy, by summing over the decay products, introduces additional uncertainties and relies on several assumptions: for example, the mass of the B candidate must be manually entered into the algorithm, and the centre-of-mass energy is fixed to be twice the beam energy. The use of inclusive event selection therefore limits the mass resolution for all measurements using this sample, preventing discrimination between separate $B^{**}_{(s)}$ states.

Evidence of excess events is observed in $B\pi$ mass distributions by all four experiments, corresponding to invariant mass resonances close to the theoretical expectations of $B^{**}_{u,d}$ masses. The study by OPAL also observes an excess in BK mass distributions interpreted as due to B^{**}_s production. The excess is defined relative to the expectations of data normalised computer simulations which exclude resonant production. In each case it is observed as a bump in the $B\pi$ (BK) invariant mass distribution, which is then fitted according to an appropriate interpretation of the signal composition.

First Evidence of Resonant Behaviour

Initial publications by ALEPH [12], DELPHI [13] and OPAL [14] made no attempt to resolve the structure of the $B^{**}_{u,d}$ resonance, simply returning the best-fit mass and width of the invariant mass peak. The $B^{**}_{u,d}$ production rate relative to the B meson sample was also determined, using the observed number of events combined with detection efficiencies calculated by computer simulations:

$$R^{**}_{u,d} = \frac{Br(Z^0 \to \bar{b} \to B^{**}_{u,d})}{Br(Z^0 \to \bar{b} \to B_{u,d})} \, . \tag{1.6}$$

For ALEPH and DELPHI this rate is extracted from the total number of $B^{**}_{u,d}$ and $B_{u,d}$ events; for the study by OPAL, which restricted event selection to $B^+\pi^-$ combinations, it is extracted from $N(B^{**}_d)$ and $N(B^+)$. Since B meson behaviour is not greatly influenced by the flavour of the spectator quark, these rates should be equivalent. The final values determined are:

$$\begin{aligned} \text{ALEPH [12]}: \quad M(B^{**}_{u,d}) &= [5703 \pm 4 \pm 10] \text{ MeV}/c^2 \, , \\ \sigma(B^{**}_{u,d}) &= [53 \pm 4 \pm 10] \text{ MeV}/c^2 \, , \\ R^{**}_{u,d} &= [27.9 \pm 1.6 \pm 5.9 \, ^{+3.9}_{-5.6}]\% \, ; \end{aligned} \tag{1.7}$$

$$\begin{aligned} \text{DELPHI [13]}: \quad M(B^{**}_{u,d}) &= [5732 \pm 5 \pm 20] \text{ MeV}/c^2 \, , \\ \sigma(B^{**}_{u,d}) &= [79 \pm 5 \pm 8] \text{ MeV}/c^2 \, , \\ R^{**}_{u,d} &= [35 \pm 2 \pm 8]\% \, ; \end{aligned} \tag{1.8}$$

$$\begin{aligned} \text{OPAL [14]}: \quad M(B_d^{**}) &= [5681 \pm 11]\ \text{MeV}/c^2\ , \\ \sigma(B_d^{**}) &= [120 \pm 24]\ \text{MeV}/c^2\ , \\ R_d^{**} &= [27.0 \pm 5.6]\%\ ; \end{aligned} \tag{1.9}$$

where the first quoted uncertainty is statistical, the second is systematic, and the third is related to modelling assumptions used in the calculation. In each of these analyses, the total width of the system σ is considerably higher than the typical mass resolutions of $\sim$30 MeV/c^2, suggesting that the signal cannot be assigned to a single narrow state, but is likely to originate from a combination of broad and narrow resonances as predicted by the theoretical models. The equivalent measurements in the B_s^{**} system are:

$$\begin{aligned} \text{OPAL [14]}: \quad M(B_s^{**}) &= [5853 \pm 15]\ \text{MeV}/c^2\ , \\ \sigma(B_s^{**}) &= [47 \pm 22]\%\ , \\ R_s^{**} &= [17.5 \pm 5.2]\%\ ; \end{aligned} \tag{1.10}$$

where R_s^{**} is defined by by replacing (u, d) with s in Eq. (1.6).

Model-Specific Resolution of B^{**} States

Subsequent publications by OPAL [15] and L3 [16] attempt to resolve structure in the $B_{u,d}^{**}$ mass peaks, by fitting to a combination of transitions from the four $L = 1$ states to $B^{(*)}$ shown in Fig. 1.2. The photons from $B^* \to B\gamma$ decays are not reconstructed, so this corresponds to five peaks (three narrow and two broad). In order to achieve stable fit convergence and reasonable uncertainties, a number of model-specific constraints must be applied to reduce the number of free parameters in the system; the inability to resolve the masses of the separate excited states increases the number of theoretical constraints which must be applied. As such, the conclusions of these studies are ambiguous and dependent on particular HQET predictions.

Both OPAL and L3 fix the relative contributions of the five peaks, according to some theoretical prescription (though the ratios used in the two studies are different). The mass splittings within each j_q doublet are also manually set to 12 MeV/c^2 (except $M(B_1') -$

$M(B_0^*) = 20$ MeV/c^2 in the OPAL fit), and the states within narrow and broad doublets are constrained to have equal widths (except $\Gamma(B_1') = 1.25 \cdot \Gamma(B_0^*)$ in the OPAL fit). The final results for the narrow state masses and widths are:

$$\begin{aligned} \text{OPAL [15]}: \quad M(B_1) &= [5738\ ^{+5}_{-6} \pm 7]\ \text{MeV}/c^2\ , \qquad (1.11) \\ \Gamma(B_1) &= [18\ ^{+15}_{-13}\ ^{+29}_{-23}]\ \text{MeV}/c^2\ ; \\ \text{L3 [16]}: \quad M(B_1) &= [5756 \pm 5 \pm 6]\ \text{MeV}/c^2\ , \qquad (1.12) \\ \Gamma(B_1) &= [24 \pm 19 \pm 24]\ \text{MeV}/c^2\ . \end{aligned}$$

These parameters are consistent between experiments, and the masses are measured with good precision, although the relative uncertainties on the width measurements reflect the poor ability to resolve such narrow resonances. The results for the broad states are not so consistent, with L3 finding $M(j_q = 1/2) < M(j_q = 3/2)$, as predicted by some theories, and OPAL finding an inverted mass relation, consistent with theoretical spin-orbit inversion models:

$$\begin{aligned} \text{OPAL [15]}: \quad M(B_0^*) &= [5839\ ^{+13}_{-14}\ ^{+34}_{-42}]\ \text{MeV}/c^2\ , \qquad (1.13) \\ \Gamma(B_0^*) &= [129\ ^{+27}_{-23} \pm 63]\ \text{MeV}/c^2\ ; \\ \text{L3 [16]}: \quad M(B_0^*) &= [5658 \pm 10 \pm 13]\ \text{MeV}/c^2\ , \qquad (1.14) \\ \Gamma(B_0^*) &= [70 \pm 21 \pm 25]\ \text{MeV}/c^2\ . \end{aligned}$$

However, the OPAL result explicitly warns against the robustness of the fit results for the broad states:

> "Systematic uncertainties in the reconstruction efficiency and the combinatorial background at low $B\pi$ masses together with the lack of knowledge of the exact functional form of the broad B_J states at $B\pi$ threshold do not allow an unambiguous determination of the widths and mass of B_0^* (or B_1')." [15]

Considering the similarity of the two studies, this statement encourages care to be taken in interpretations of either set of $j_q = 1/2$ results.

In addition to these measurements, the OPAL study makes two independent determinations of the decay branching fraction of $B^{**}_{u,d}$ states into the singly excited state B^*. The first method includes the fraction $Br(B^{**}_{u,d} \rightarrow B^*\pi)$ as a free parameter in the invariant mass fit, which will affect the relative contributions of peaks from the two direct and three indirect transitions:

$$\text{OPAL [15]} : Br(B^{**}_{u,d} \rightarrow B^*\pi) = [\ 74\ ^{+12}_{-10}\ ^{+21}_{-15}\ ]\ \% \ . \tag{1.15}$$

The second method assigns a weight to each B jet, representing the probability that the B meson arose from B^* decay, using information from the calorimeter and the tracking detector. The fraction of all $B^{**}_{u,d}$ particles which decay to B^* is then extracted:

$$\text{OPAL [15]} : Br(B^{**}_{u,d} \rightarrow B^*\pi(X)) = [\ 85\ ^{+26}_{-27} \pm 12\ ]\ \% \ , \tag{1.16}$$

where the (X) signifies that no constraints are placed on the additional decay products of the $B^{**}_{u,d}$ states.

1.6.2 Exclusive Studies

Of the LEP experiments, only ALEPH has attempted to search for orbitally excited B states in fully exclusive decays to $B\pi$ [17]. The B mesons were selected in a variety of fully reconstructed hadronic channels, with additional partly reconstructed B^+ channels missing only a single low energy γ or π^0. The precision is further improved by constraining the B mass to its world average value, leading to a $B\pi$ invariant mass resolution of $\sim$4 MeV/c^2. The disadvantage of this method is the large reduction in sample size: fewer than 500 B mesons are reconstructed in total. This limits the opportunity to resolve detail within the $B^{**}_{u,d}$ system without theoretical constraints.

The $B\pi$ sample is split into 'right-sign' ($B^+\pi^-$, $B^0\pi^+$) and 'wrong-sign' ($B^+\pi^+$, $B^0\pi^-$) components, respectively characterising the allowed and forbidden decay products from $B^{**}_{u,d}$ de-excitations. An excess of 45 ± 13 events is observed in the $B\pi$ mass distribution for the right-sign sample. This is fitted to the expected five-peak structure, but with all parameters except the B^*_2 mass and the total normalisation fixed according

to HQET predictions. The normalisation is then used to extract the usual production rate quantity, giving the final measurements:

$$\begin{aligned} \text{ALEPH [17]}: \quad M(B_2^*) &= 5739\,^{+8}_{-11}\,^{+6}_{-4}\ \text{MeV}/c^2\ , \\ R^{**}_{u,d} &= [\ 31 \pm 9\,^{+6}_{-5}\ ]\ \%\ , \end{aligned} \tag{1.17}$$

which are both consistent with the values determined from inclusive studies.

The first results from a hadronic collider were presented by CDF using around 10,000 $B^{0,\pm}$ partially reconstructed in semileptonic decays $B \rightarrow l^+\nu D^{(*)}$, with the $D^{(*)}$ fully reconstructed in a number of hadronic channels [18]. This selection allows the charge, flavour and production and decay vertices of the B mesons to be determined. The effect of the missing neutrino is taken into account by correcting the B momentum on an event-by-event basis, but the mass resolution of the reconstruction process is still limited by the missing energy inherent in this selection method. Charged pions originating at the same point as the B are used to form $B\pi$ combinations, with a resulting invariant mass resolution of around 50 MeV/c^2. As in the ALEPH study, the use of exclusively selected events allows the resulting $B\pi$ sample to be divided into right-sign and wrong-sign events, and an excess of events is observed in the former. Several possible sources of background events are investigated and their effects are suitably parameterised to extract the signal contribution to the invariant mass distribution. This is then fitted to a model-dependent four-state hypothesis, with all mass splittings and relative peak sizes fixed from theory. The production rate (via the total number of $B^{**}_{u,d}$ events) and the B_1 mass are determined to be:

$$\begin{aligned} \text{CDF [18]}: \quad M(B_1) &= 5710 \pm 20\ (\text{stat.} \oplus \text{syst.})\ \text{MeV}/c^2\ , \\ R^{**}_{u,d} &= [\ 28 \pm 6 \pm 3\ ]\ \%\ , \end{aligned} \tag{1.18}$$

showing consistency with all previous inclusive and exclusive measurements. This study shows that is is possible to isolate and examine B^{**} events in hadronic collisions, motivating further study using an enlarged data sample and improved reconstruction and selection algorithms.

1.7 Analysis Objectives

1.7.1 Resolving the Structure of B_d^{**} Transitions

The previous section showed that there is significant evidence, from multiple experiments, for resonant behaviour in the $B\pi$ system. The observed masses and production rates are consistent with theoretical expectations for the $L = 1$ orbitally excited $B_{u,d}^{**}$ mesons. However, the ability to resolve the structure of the invariant mass distribution has been hindered by mass resolutions exceeding 30 MeV/c^2, arising from inclusive event selection. Searches using fully reconstructed final states have been statistically limited, leading to ambiguous interpretation. There is strong motivation to pursue these investigations using data from hadron colliders, to confirm the source of the resonance, and extract additional measurements for comparison with the several theoretical predictions.

This thesis presents a search for B_d^{**} states produced in $p\bar{p}$ collisions at the D0 detector on the Tevatron accelerator. These states are fully reconstructed in decays to $B^{(*)+}\pi^-$, with $B^+ \to J/\psi K^+$ and $J/\psi \to \mu\mu$; the photons from $B^{*+} \to B^+\gamma$ are not detected. The primary objective is to resolve the invariant mass distribution sufficiently to confirm or deny the presence of narrow peaks, according to some quantifiable statistical approach. This evidence can aid in identifying the source of the repeatedly observed resonance as a B^{**} signal, or otherwise. If more than one peak is observed, the splittings and relative contributions from each will be extracted by fitting to an appropriate parameterisation, with the theoretical input minimised to reduce model dependency.

Regardless of the mass difference of the two $j_q = 3/2$ states, the detector resolution should allow the transitions $B_2^* \to B^{*+}\pi^-$ and $B_2^* \to B^+\pi^-$ to be distinguished, since the central value of the invariant mass peak will be reduced for the $B^{*+}\pi^-$ decay as a result of the missing photon: leading to a mass splitting of ~ 45.8 MeV/c^2. Hence, if both of these transitions occur at a sufficient rate, the observation of such a two-peak structure will be a signature of the B^{**} system. In addition, provided that $M(B_2^*) - M(B_1)$ is not too small, and the B_1 production rate is large enough, a third peak should be visible corresponding to $B_1 \to B^{*+}\pi^-$. If this is the case, the aim is to independently measure

the masses of the two narrow states for the first time, determining the splitting which has been fixed from theory in all previous studies. In addition, the number of events in each peak will be used to measure relative branching ratios for the three transitions, also for the first time. Finally, the total number of events in the narrow peaks will be used to measure the production rate relative to the B^+ meson, which can be compared to the previous results (for both narrow and wide states) in Equations (1.7)–(1.9), (1.17) and (1.18).

No attempt will be made to distinguish the broad $j_q = 1/2$ states from the combinatoric background: such isolation requires precise modelling of background contributions from computer simulations, which is not available in the important region close to the $B\pi$ production threshold.

1.7.2 Further Investigating the B_s^{**} System

Evidence for B_s^{**} states, via resonances in the BK invariant mass, has been less convincing, with only one experiment (OPAL) releasing a result. As such, it is important to make an independent search, and if an excess of events is observed, to provide a statistical significance for the signal. The $B^+ \to J/\psi K^+$ sample used for the B_d^{**} analysis will therefore also be used to reconstruct suitable B^+K^- candidates, and the resulting invariant mass spectrum will be investigated and interpreted in terms of the possible B_s^{**} transitions. If one or more significant narrow peaks are observed, their masses and production rates will be measured.

Searching in both systems with the same sample of B^+ mesons facilitates several aspects of the analysis. The relative production rates for each spectator quark can be safely compared, with only the respective pion or kaon efficiencies introducing any systematic effects. In addition, the effects of reflections between analyses (i.e. a pion from true B^{**} decay being incorrectly identified as a kaon and used to reconstruct a B_s^{**} candidate, or vice versa) can be well modelled, since the ratio of event types in the data sample will be known.

Chapter 2

Theoretical Predictions

MANY GENERAL THEORETICAL IDEAS have already been introduced in the previous chapter, including the expected energy level structure of the $B^{**}_{(s)}$ states, and the allowed transitions to the ground state. In this chapter, some specific theoretical applications are discussed, starting with an overview of B meson production at D0. A number of general approaches to solving QCD problems are then described, and in particular those most relevant to calculating the masses of B mesons. Finally, the different predictions for the $B^{**}_{(s)}$ masses and widths are listed, with a review of the methods used in reaching these predictions. These expected masses will later be compared to the findings of this thesis, giving improved experimental evidence for use in refining the theoretical models.

2.1 B Meson Production at the Tevatron

The Tevatron accelerator provides an excellent source of B hadrons, with a total effective $b\bar{b}$ production cross-section of order 10 μb [19], yielding around 7×10^{10} $b\bar{b}$ pairs in the 1.3 fb^{-1} of data used for the analyses presented here. This can be compared to the equivalent cross-section in e^+e^- collisions, which is typically less than 10 nb [8]. Hence there is significant scope to improve on the results of the previous generation of detectors at LEP, by utilising the large samples of B hadrons collected by the D0 and CDF detectors on the Tevatron accelerator. The main difficulty arises from the large background samples:

$b\bar{b}$ pairs account for around 1% of the total inelastic cross-section (see 2.1.1), increasing the reliance on appropriate detector triggers (Section 3.3) and event selection algorithms (Chapter 4).

This section gives an overview of the mechanisms by which B hadrons are produced from $p\bar{p}$ collisions at the Tevatron. This can be divided into two distinct parts: the production of the initial $b\bar{b}$ pair; and the subsequent hadronisation to form observable, colourless final states. This division is artificial, since the fundamental QCD interactions do not change. What does change is the way that the behaviour is modelled: the perturbative approach used to describe the initial interaction becomes increasingly unsuitable as the energy per QCD object reduces during particle showering. For a more in-depth description, see Ref. [20] (Section 2, and the works cited therein).

2.1.1 The Parton Model of Hadrons

The production of B mesons at D0 and CDF is initiated by colliding proton (p) and antiproton $(\bar{p})$ beams at a centre-of-mass energy of around 2 TeV. As a result of gluon radiation by the valence quarks inside hadrons, and the subsequent gluon decay into quark-antiquark pairs (the so-called "sea quarks"), the static picture of baryons as three valence quarks bound together by the strong force is insufficient to describe $p\bar{p}$ interactions. Instead, a parton model is used, whereby the energy and momentum of any hadron a is distributed among the three different types of constituent particle (valence and sea quarks, and gluons); a parton distribution function $f_i^a(x, Q^2)$ expresses the probability that a parton i carries a fraction x of the total hadron momentum, when probed at a momentum transfer of Q^2.

Since the $p\bar{p}$ collision energy exceeds the QCD confinement energy $\Lambda_{QCD} \approx 400$ MeV, the partons behave as free particles within the proton volume; this is because the collision of protons at this energy is characterised by an interaction timescale (related to the intersection time of the $p\bar{p}$ volumes) which is much shorter than the corresponding scale for internal parton-parton interactions. Equivalently, this interaction realm is

associated with a small strong-coupling constant $\alpha_s < 1$, meaning that interaction processes are dominated by the leading order Feynman diagrams, with higher order diagrams decreasing in importance as the number of QCD vertices increases. The result is that perturbative QCD can be used to determine interaction cross-sections, with relatively good precision, for a number of different processes. Collisions where the proton or antiproton (or both) are broken up by parton interactions are called inelastic, in contrast to elastic collisions (typically occurring at lower energies) where the colliding baryons behave as single, structureless objects.

The majority of $p\bar{p}$ collisions recorded at D0 correspond to a single parton from the proton interacting with a single parton from the antiproton, with a centre-of-mass energy corresponding to some fraction of the available 1.96 TeV possessed by the two baryons. The remaining fragments of proton and antiproton, which are not associated with the parton-parton interaction, carry away the balance of the energy. These remnants, and the hadrons resulting from their conversion to colourless final states, are referred to as the 'underlying event'.

2.1.2 $b\bar{b}$ Pair Production

Initial results from the Tevatron showed $b\bar{b}$ production cross-sections to be significantly larger (up to a factor of four) than would be expected from the leading order processes alone [19]. Attempts to include NLO processes have significantly reduced this discrepancy, leading to a production model comprising three different topologies: flavour creation, flavour excitation, and parton showering.

In the flavour creation process, a $b\bar{b}$ pair is produced from 2-to-2 parton interactions as shown in Figures 2.1(a)– 2.1(d); this includes both quark-antiquark annihilation, and gluon-gluon fusion. All leading order processes are of this type, with additional contributions from NLO terms, for example those shown in Figures 2.1(e)–2.1(f), where a final state parton radiates a gluon. Studies using Monte Carlo simulations show that flavour creation accounts for $\lesssim 35\%$ of total $b\bar{b}$ production at the Tevatron [19]. In the LO processes, the two b quarks are produced back-to-back in the centre-of-mass frame, giving

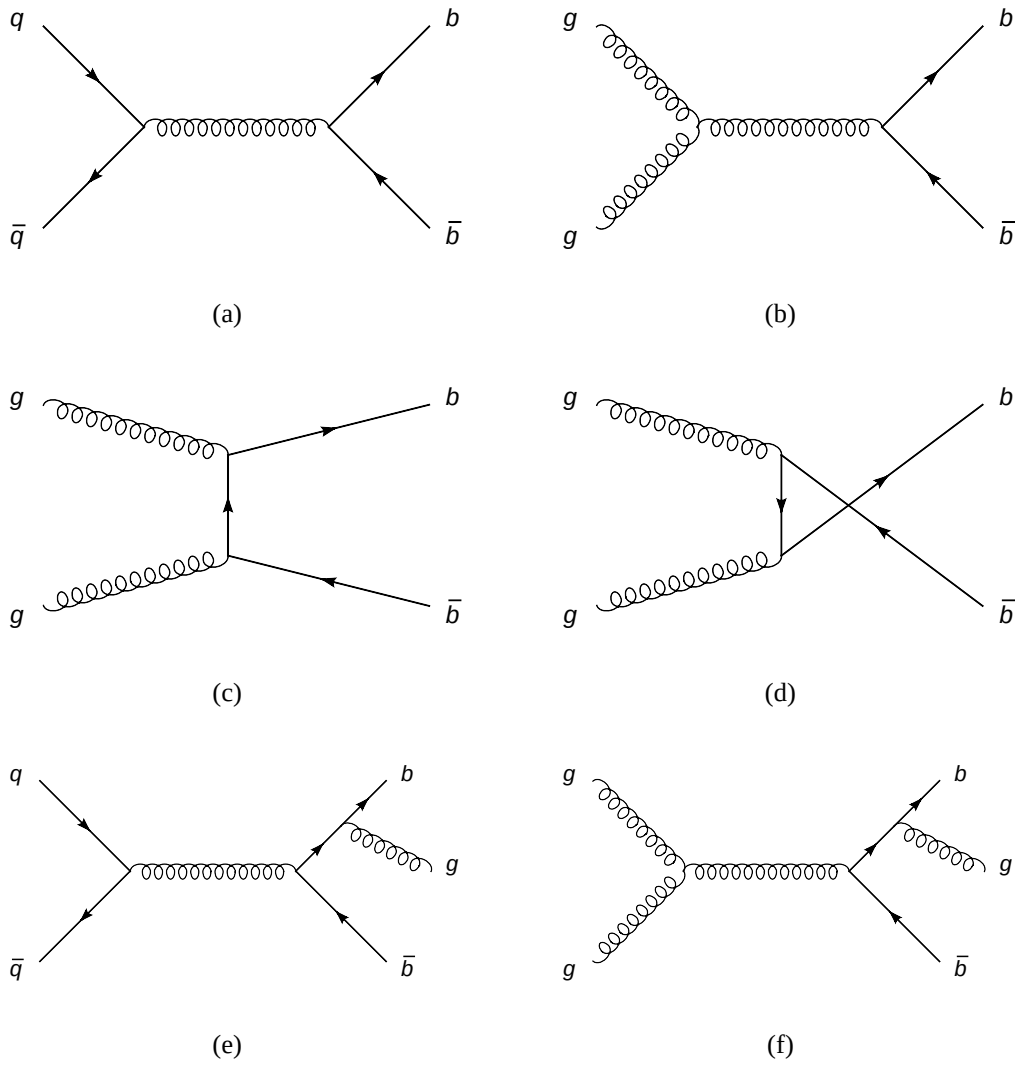

Figure 2.1: Production of $b\bar{b}$ pairs by flavour creation processes. Shown are leading order processes for quark-antiquark annihilation (a) and gluon-gluon annihilation (b)–(d). Two possible NLO processes are shown in (e)–(f).

equal transverse momenta in the lab frame.

The NLO processes contain an extra QCD vertex, and therefore have amplitudes proportional to α_s^3. In this small α_s phase-space, the naïve expectation is that these processes should be suppressed as a result of the additional vertex. However, the calculations show that NLO processes such as $g + g \rightarrow g + g$, with $g \rightarrow b + \bar{b}$ give larger contributions to $b\bar{b}$

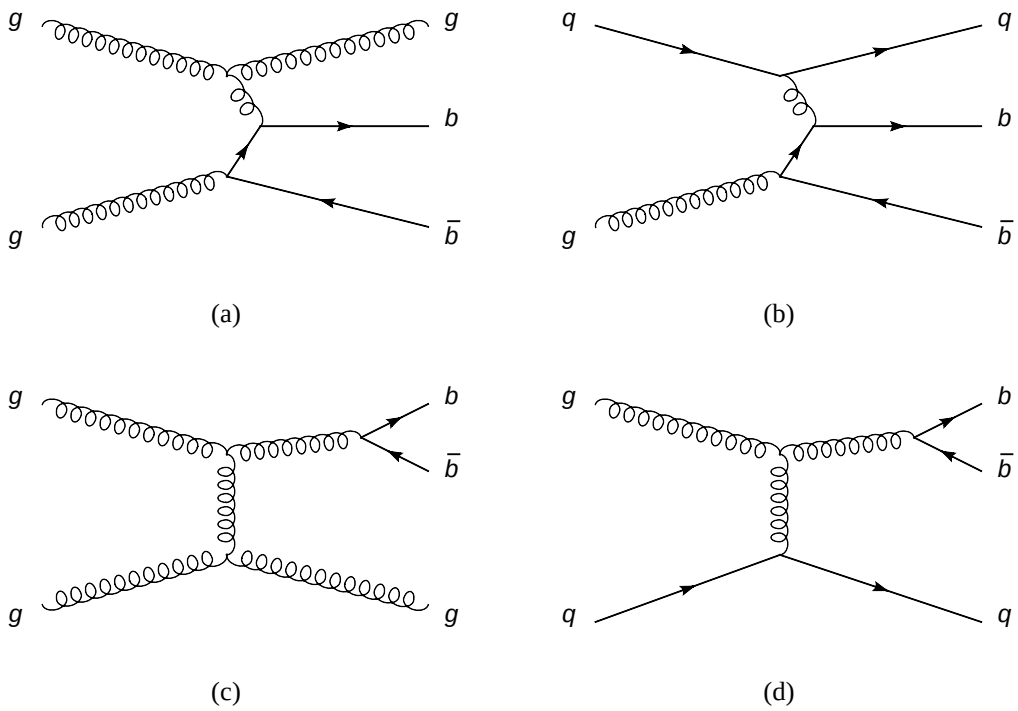

Figure 2.2: Production of $b\bar{b}$ pairs by flavour excitation and parton showering. The top two diagrams are examples of flavour excitation, where a b quark from the sea is scattered on mass shell by a gluon (a) or light quark (b) from the other baryon. Processes (c)–(d) show $b\bar{b}$ production from final state gluon splitting.

production than the leading order terms.

Figure 2.2 shows some possible NLO processes, other than the flavour creation modes described above. Flavour excitation occurs when b (or $\bar{b}$) sea quarks in the proton are scattered into the final state by interaction with a gluon or light quark from the other baryon, $q(g) + b \rightarrow q(g) + b$. The partner $\bar{b}$ (or b) quark forms part of the baryon remnant, and the kinematic properties of the two b quarks are therefore rather uncorrelated; for example, only one of the two is generally produced with high p_T. While the contribution of such excitations is difficult to calculate, relying on a precise understanding of the parton distribution functions, it is estimated that these processes give a production cross-section comparable to that from flavour creation.

The final production mechanism is parton showering, where a $b\bar{b}$ pair is generated by final state gluon splitting. In this case, the process favours the production of b and $\bar{b}$ quarks which are close in phase space: in practice, this means that the two quarks have similar momenta and a small angular separation. Again, the results of various simulations indicate that this source of $b\bar{b}$ pairs is comparable in magnitude to the flavour creation (and hence also flavour excitation) processes.

2.1.3 Hadronisation

As highlighted in Chapter 1, the strong force acts to confine all coloured objects into colourless bound states. This resulting reorganisation of quarks and gluons is called hadronisation (or fragmentation), and at Tevatron energies it is dominated by the production of additional $q\bar{q}$ pairs from gluon splitting. As the number of particles increases from radiative and splitting processes, the particle energies reduce below Λ_{QCD}, and perturbative methods are no longer valid. Instead, hadronisation is described by phenomenological models, tuned to describe the data. One successful description is the string model (see, for example, Ref. [21]), which is briefly described here.

Figure 2.3 illustrates the principle of the string model for an initial $b\bar{b}$ pair. As the quarks diverge from their production point, they experience a linear QCD field as a result of the self-interacting gluons. This field is called a string, and results in a field potential which increases in proportion to the quark separation (in analogy with a stretched elastic string in classical mechanics). The quarks are decelerated, losing energy to the string potential, until there is sufficient energy to produce a $q\bar{q}$ pair. At this stage, the string splits in two, with the ends bounded by the newly produced quarks. In this way the colour charge remains confined, since the original quark (antiquark) is paired with the new antiquark (quark) of opposite colour: ($R \leftrightarrow \bar{R}, B \leftrightarrow \bar{B}, G \leftrightarrow \bar{G}$). In turn, these new strings will stretch and divide into new colourless $q\bar{q}$ combinations, with the process continuing until the string energies are insufficient to generate new quarks. At this stage, the quark-antiquark pairs have formed into bound mesons. Similar, albeit more complex processes in the model describe baryon production, by terminating broken strings with

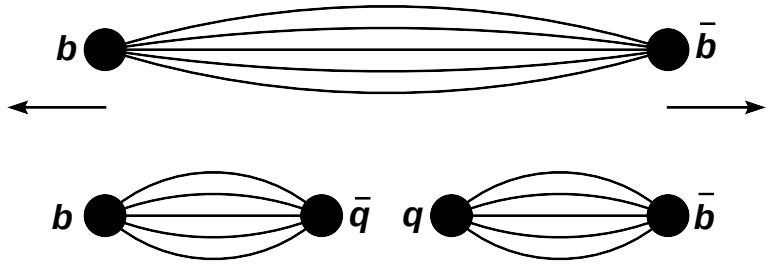

Figure 2.3: Schematic illustration of the string hadronisation model for a $b\bar{b}$ pair, as described in the text. The lines represent the strong-force field (the "string"), linearly connecting quark-antiquark pairs of opposite colour. As the quarks move apart they stretch the field lines (above), increasing the potential energy until it is sufficient to produce a $q\bar{q}$ pair (below), terminating the field lines into two colourless objects.

diquark-antidiquark pairs.

Hadronisation occurs on a timescale much shorter than the b quark lifetime, so that in most cases each $b\bar{b}$ pair from the perturbative phase survives fragmentation to become two B hadrons. The type of B hadron produced depends on the flavour of the $q\bar{q}$ pair generated at the final string break. This is quantified by a set of parameters $f_{u,d,s,c,baryon}$ giving the probability that a b quark hadronises to produce the appropriate $q\bar{q}$ pair (or any diquark-antidiquark pair, in the case of f_{baryon}), and form respectively a $B^0_{(d)}$, $B^+_{(u)}$, B^0_s or B^+_c meson, or a B baryon. The current Particle Data Group (PDG) values of the measured fractions are summarised in Table 2.1, with early results from the Tevatron suggesting that f_c is around 0.2% [8].

These fractions only give the probability that the final state hadron has a particular quark composition, without differentiating between the ground state and all possible excited states. Theoretical input on production fractions of excited B mesons is lacking: it is hoped that the experimental determination of such production fractions, as described in this thesis, will motivate and aid the development of appropriate theoretical models. This is in addition to the obvious value of understanding the B hadron composition at the Tevatron (in particular for B mixing studies).

Table 2.1: Relative production fractions of different B hadrons states, as described in the text. Shown are the values extracted from a fit to $e^+e^- \to Z^0 \to b\bar{b}$ decays, and a combined fit including results from the Tevatron. The numbers are constrained to sum to unity (before rounding).

Source	$Z^0 \to bb$ (%)	$Z^0 \to bb$ and $p\bar{p}$ (%)
$f_d = f_u$ [a]	40.2 ± 0.9	39.9 ± 1.1
f_s	10.5 ± 0.9	11.1 ± 1.2
f_{baryon}	9.1 ± 1.5	9.2 ± 1.9

[a] In all studies, the fraction f_u/f_d is found to be close to one, with the current combined result given as 1.065 ± 0.026 by the PDG [8].

Having described how B mesons are produced at the Tevatron, the next step is to introduce the methods used to predict their properties, such as masses, widths and branching ratios. This is the subject of the next section.

2.2 Symmetries and Approximations in QCD Calculations

The energy scales associated with interactions within hadrons are below the $\gtrsim 1$ GeV perturbative realm of QCD. As such, alternative approaches have to be used to calculate hadron properties. There are several different simplifications which can be successfully applied to yield results, depending on the circumstance; there are also certain approximate symmetries which aid in comparing different meson systems.

The most general simplification of strong interaction processes is represented by Lattice QCD, whereby the space-time structure of the universe is represented by a grid with finite spacing. This removes the infinities from the theory altogether, allowing calculations to be made numerically, for example the prediction of $B^{**}_{(s)}$ masses, described in Section 2.3.5.

Alternative approaches reformulate the calculations by expanding in terms of powers of some scale parameter, which is taken to be small enough that higher order terms can be neglected. One example is the $1/N$ expansion, where N is the number of colours in QCD, and is assumed to be infinite. Although we are very confident that there are only three

colours, this assumption significantly simplifies calculations, which can then be corrected to account for the true finite number of colours by including corrections of order $1/N$ or higher.

Another example, called the chiral formulation, first assumes that all quark masses are negligible compared to the confinement scale, and then applies corrections of order m_q/Λ_{QCD}. Calculations of this kind are therefore successful in predicting light meson properties, such as masses of pions and kaons. The complementary theory, whereby quark masses are assumed to be very large compared to Λ_{QCD}, is called Heavy Quark Effective Theory (HQET), which is of particular importance in describing heavy-light meson properties. This makes it a useful tool for predicting the masses of excited B mesons, as described below.

2.2.1 Heavy Quark Effective Theories

The principles of HQET have already been outlined in the previous chapter. Here the subject is treated a little more thoroughly, and some additional concepts of the approach are introduced. This description follows that given in Ref. [22], which offers an illuminating picture of the heavy quark approximation; a more mathematical approach can be found in the additional material cited in the above reference.

In the $m_Q \to \infty$ limit of a heavy-light $Q\bar{q}$ meson, the typical momenta exchanged inside mesons are comparable to Λ_{QCD}, which in this approximation are much smaller than m_Q. The recoil of the heavy quark can be neglected, leading to its treatment as a static object radiating colour (and electric) fields. Since the colour field does not depend on the mass, the light quarks have no way of distinguishing the mass (or flavour) of the heavy quark.

As a result, a new symmetry is introduced for heavy-light mesons in this limit: invariance under the flavour transformation $b \to c$. Such an operation cannot change the interactions within the meson state, provided that both quarks satisfy $m_{b,c} \gg \Lambda_{QCD}$. This is called Heavy Flavour Symmetry (HFS), and is tested by examining differences in the charm and bottom hadron sectors. Note that the requirement $m_c \approx m_b$ is not necessary,

only that both masses are large compared to the confinement scale.

Also associated with the heavy quark limit is a vanishing chromomagnetic moment:

$$\mu_Q = \frac{g}{2m_Q} \,, \tag{2.1}$$

which arises as a result of the spin $s_Q = \frac{1}{2}$ of the heavy quark, and is analogous to the magnetic moment of the hydrogen nucleus. This relation adds a further symmetry to HQET, called Heavy Spin Symmetry (HSS); it corresponds to the invariance of meson states under rotations in s_Q space, and predicts that the two states in each j_q doublet should be degenerate in energy.

Clearly, the initial assumption does not hold in actuality, since the masses of the c quark (≈ 1300 MeV/c^2) and b quark (≈ 4500 MeV/c^2) are relatively close to the QCD confinement energy $\Lambda_{QCD} \sim 400$ MeV, therefore corrections to this initial approach can be important. However, the power of the theory lies in the hierarchical arrangement of contributions, such that order n corrections scale as $(1/m_Q)^n$. For example, Eq. (2.1) is non-zero in the finite mass limit, which gives an s_Q contribution to meson energies; the degeneracies of the $m_Q \to \infty$ case are lifted, splitting the j_q doublets into two distinct mass states. Under HQET, the first order mass splitting is proportional to $1/m_Q$, so should be slightly different in the charm (D) and bottom mesons:

$$\begin{aligned} M(D^*) - M(D) &\sim 1/m_c \\ M(B^*) - M(B) &\sim 1/m_b \end{aligned} \tag{2.2}$$

This method gives good agreement (within around 20%) with the observed experimental values of these mass splittings, for example the prediction $B^* - B = 52$ MeV/c^2 is very close to the observed 46 MeV/c^2 mass difference. These relations can be derived independently from other approximate QCD methods (such as the constituent quark model); however, the benefit of HQET is that its approximations are controlled: the uncertainties can be estimated by examining the scale of the next corrective term. In the following section, a number of different theoretical approaches to the excited B meson sector are reviewed, and their predictions tabulated.

2.3 Predictions for Orbitally Excited B Mesons

There have been many attempts to calculate the masses of the $L = 1$ B mesons, particularly from the mid-1990s onward, when the LEP experiments started to make progress in measurements of D and B properties. There are a number of possible approaches, each depending on some QCD approximation, and all applying principles of heavy quark symmetry. In this section, the different methods are very briefly outlined, with reference to specific theoretical groups and their predictions.

2.3.1 Leading Order Corrections to HQET

The paper by Falk and Mehen [1] examines the leading order ($1/m_b$) corrections to HQET, applying heavy flavour symmetry to predict the properties of the narrow ($j_q = \frac{3}{2}$) $B^{**}_{(s)}$ mesons, based on observations in the charm sector. To first order, the masses are determined under the assumption that the average mass splitting between L multiplets is the same in D and B mesons. Here the average in each multiplet is weighted by spin, as described in Section 1.5.2:

$$\begin{aligned} \bar{M}_{B_{(s)}} &= \frac{3}{4}M_{B^*_{(s)}} + \frac{1}{4}M_{B_{(s)}} \ , \\ \bar{M}_{B^{**}_{(s)}} &= \frac{5}{8}M_{B^*_{(s)2}} + \frac{3}{8}M_{B_{(s)1}} \ , \\ \Delta M_{B^{**}_{(s)}} &= M_{B^*_{(s)2}} - M_{B_{(s)1}} \ , \end{aligned} \tag{2.3}$$

where the subscript notation is used to label particle masses, for improved clarity. By comparing with the corresponding splitting in the charm mesons, the following relations are found:

$$\begin{aligned} \bar{M}_{B^{**}_{(s)}} - \bar{M}_{B_{(s)}} &= \bar{M}_{D^{**}_{(s)}} - \bar{M}_{D_{(s)}} \ , \\ \Delta M_{B^{**}_{(s)}} &= \frac{m_c}{m_b}\Delta M_{D^{**}_{(s)}} \ , \end{aligned} \tag{2.4}$$

where m_c and m_b are respectively the charm and bottom quark masses. These equations can be solved by inputing the experimentally determined D masses, and taking the ratio

$m_c/m_b = 1/3$, giving the results shown in Table 2.2. The uncertainties are estimated by examining the size δ of leading order corrections to these masses, which are related by the QCD confinement energy $\Lambda_{QCD} \approx 400$ MeV, and the masses of charm (m_c) and bottom (m_b) quarks:

$$\delta \sim \Lambda_{QCD}^2 \left(\frac{1}{2m_c} - \frac{1}{2m_b} \right) \sim 40 \text{ MeV}/c^2 \, . \tag{2.5}$$

The width is calculated similarly, assuming that the single pion decay channel is dominant, and taking into account the phase-space effects. The widths of B_2^* and D_2^* mesons are related by:

$$\frac{\Gamma(B_2^*)}{\Gamma(D_2^*)} \;=\; \frac{M_{D_2^*}}{M_{B_2^*}} \cdot \left\{ \frac{0.4(p_B)^5 M_B + 0.6(p_{B^*})^5 M_{B^{*+}}}{0.4(p_D)^5 M_{\bar{D}} + 0.6(p_{D^*})^5 M_{\bar{D}^{*0}}} \right\} \, . \tag{2.6}$$

Here p_B (p_{B^*}) is the momentum of the pion in the centre-of-mass frame for the decay $B_2^* \rightarrow B\pi(B^*\pi)$, and p_D (p_{D^*}) is the same parameter for $D_2^* \rightarrow D\pi(D^*\pi)$ decays. These momenta are calculated using the standard expressions for relativistic two-body decay. The result is extracted by using the mass of the B_{s2}^* determined later in this thesis [Eq. (7.5)], and the PDG masses for all other particles [8].

The result of this calculation is given in Table 2.2, and it differs from the prediction quoted in the paper (16 ± 6 MeV/c^2); The latter uses earlier measurements for particle properties, of which the observed D_2^* width has increased significantly. The relative widths of B_1 and B_2^* mesons are calculated under the assumption that the B_1 decays only through the s-wave; the effect of possible mixing between the two $J^P = 1^+$ states (discussed in Section 1.5.2), is investigated by repeating the calculation for a pure d-wave B_1 decay, leading to the two extreme cases:

$$\begin{aligned} \Gamma(B_1)/\Gamma(B_2^*) &= 0.9 \qquad\qquad \text{pure } d\text{-wave} \, , \\ \Gamma(B_1)/\Gamma(B_2^*) &= 1.4 \qquad\qquad \text{pure } s\text{-wave} \, . \end{aligned} \tag{2.7}$$

These calculations are repeated for the B_s^{**} mesons, which are compared to the appropriate D_s^{**} states, to give the values tabulated below. It should be noted that the measured D_{s2}^*

width listed by the PDG has changed from 15–20 MeV/c^2 between the 2006 edition [11] and the most recent one [8], which translates into a 50% increase in the prediction of $\Gamma(B^*_{s2})$. Such fluctuations in predictions motivate and justify the allocation of suitable systematic uncertainties to any measurement which relies on theoretical input. The corresponding relation between B_{s1} and B^*_{s2} widths is $\Gamma(B_{s1})/\Gamma(B^*_{s2}) = 0.4$.

Table 2.2: Predictions of $B^{**}_{(s)}$ masses and widths, using the heavy quark symmetry model of Falk and Mehen [1], combined with observations in the charm sector. The uncertainties are approximate, as described in the text.

Particle	Mass (MeV/c^2)	Width (MeV/c^2)
B_1	$5780 \pm \mathcal{O}(40)$	23–36
B^*_2	$5794 \pm \mathcal{O}(40)$	26 ± 4
B_{s1}	$5886 \pm \mathcal{O}(40)$	0.7 ± 0.2
B^*_{s2}	$5899 \pm \mathcal{O}(40)$	1.8 ± 0.4

2.3.2 HQET with Quark-Potential Models

Implicit in the heavy quark approach is the expression of meson masses as the sum of several parts: the ground state mass, a light quark excitation energy (E), and corrections (C) of the order $1/m_Q$, with higher level terms neglected:

$$M[nL_J(j_q)] = M(1S) + E[nL(j_q)] + \frac{C[nL_J(j_q)]}{m_Q} \,, \tag{2.8}$$

where the usual spectroscopic notation is used, and the ground state mass $M(1S)$ refers to the spin-weighted average of the $S = 0$ and $S = 1$ masses. The work of Eichten, Hill and Quigg [23, 2] calculates the set of parameters E and C for a specific set of quantum numbers (n, L, J, j_q), using a non-relativistic potential well model to parameterise the excitation energy. The potential is first fitted to the experimentally measured masses of excited strange (K) and charm (D) mesons, in order to extract the free parameters of the model. The resulting values of E and C are then used to predict the corresponding mass

in the B meson sector. This is done for the narrow $j_q = \frac{3}{2}$ states, but not for the broad $j_q = \frac{1}{2}$ doublet, because the experimental data for the $1P(\frac{1}{2})$ D mesons was insufficient at the time of publication. The resulting predictions for masses of interest are listed in Table 2.3; these are the numbers given in the more recent of the two publications [2]. Disagreement with current measurements in the charm meson masses suggests a level of precision of around 20 MeV/c^2.

The approach is extended to calculate expected partial widths of a number of different decay channels. For B^{**} mesons, a small contribution ($\sim$ 15–20 %) from di-pion decays is expected, via the ρ resonance. The widths for each possible $B^{**} \to B^{(*)}\pi$ and $B_s^{**} \to B^{(*)}K$ decay are given in Table 2.3. The identical partial widths for both B_2^* decays is equivalent to a statement that this state should have equal branching ratios into these two channels, i.e.

$$R_2 = \frac{Br(B_2^* \to B^*\pi)}{Br(B_2^* \to B^{(*)}\pi)} \sim \frac{11}{11+11} \sim 0.5 \tag{2.9}$$

Table 2.3: Predictions of $B_{(s)}^{**}$ masses and widths, using the model of Eichten, Hill and Quigg [2], as described in the text. All widths are approximate, with no uncertainties quoted by the paper.

Particle	Mass (MeV/c^2)	Width (MeV/c^2)
B_1	$5759 \pm \mathcal{O}(20)$	17
B_2^*	$5771 \pm \mathcal{O}(20)$	11 $(\to B^*\pi)$ 11 $(\to B\pi)$
B_{s1}	$5849 \pm \mathcal{O}(20)$	$\sim$ 1
B_{s2}^*	$5861 \pm \mathcal{O}(20)$	$\sim$ 1 $(\to B^*K)$ 2.6 $(\to BK)$

2.3.3 Non-Relativistic Quark Model Predictions

Constituent quark models of mesons attempt to solve the wavefunction equation for the two-body interaction. The simplest such case arises when both quarks are massive enough that they can be described non-relativistically. Here the evolution of the system is described by the Schrödinger equation, with an appropriately chosen potential consisting of the sum of central, spin-spin, and spin-orbit terms, much like the description of the hydrogen atom. This method is used by Isgur [24], and gives interesting predictions, namely that in the $L = 1$ system, the $j_q = 3/2$ doublet (narrow) states are around 150 MeV/c^2 less massive than the $j_q = 1/2$ (broad) doublet. This result is called spin-orbit inversion.

The three potential components are formulated in a double heavy quark expansion, neglecting terms beyond $\mathcal{O}(1/m_Q^2)$; the resulting Schrödinger equation is solved to extract the expectation values of the different interaction potentials, which combine to give the predicted masses for the various excited states. The extension to cover mesons containing light quarks is made by reference to experimental observations, which appear to preserve the low m_Q-dependence of various mass splittings. The paper interprets such patterns as an indication that the breaking of heavy quark symmetry is a smooth function of m_Q, as it scales from $\infty \rightarrow \Lambda_{QCD}$. Extrapolation into the realm of real quark masses leads to the following predictions for masses in the B^{**} system:

$$\begin{aligned} M(B_0^*) &= 5870 \text{ MeV}/c^2 , \\ M(B_1') &= 5875 \text{ MeV}/c^2 , \\ M(B_1) &= 5700 \text{ MeV}/c^2 , \\ M(B_2^*) &= 5715 \text{ MeV}/c^2 . \end{aligned} \tag{2.10}$$

The equivalent masses in the B_s^{**} system are not predicted, nor are the widths.

2.3.4 Relativistic Quark Models

The natural extension to the above method is to model the light quark relativistically, while keeping the HQET expansion for the heavy quark. Such calculations have been performed

by Godfrey and Kokoski [25], by Van Orden, Roberts and Zeng [26], and by Ebert, Galkin and Faustov [27], with a more recent publication by Di Pierro and Eichten [28]; there are also several earlier works not cited here. The motivation for treating the light quark relativistically is clear, since the velocities are expected to exceed $0.85c$.

Aside from the use of relativistic operators on the light quark, the general approach follows the method described above: the Hamiltonian is constructed under some appropriate parameterisation of the potential, with the first approximation taking $m_Q \rightarrow \infty$. Selected higher order corrections to $(1/m_Q)$ are allowed to contribute, which lead to spin-orbit interactions, removing the j_q doublet degeneracy, and allowing mixing within these doublets. The main theoretical freedom in this calculation is the choice of potential, which generally leads to different predictions from group to group. For example, Ref. [28] splits the potential into two parts: a spin-independent term $V_s \propto r$ representing the long distance interaction, and giving rise to confinement effects; and a spin-dependent term $V_v \propto 1/r$, taking the form of a modified coulomb-like potential, with the heavy quark delocalised to avoid divergences.

The models are constructed with several free parameters, including quark masses and effective interaction strength and distance scales, which are extracted by fitting to the known spectrum of $D_{(s)}$ and $B_{(s)}$ excitations. The resulting functions are used to predict the masses for states of interest, by inserting their quantum numbers and quark compositions into the theory, as shown in Table 2.4 for the four papers cited above. There is considerable variation between the predictions listed here, which is partly a result of the improvement in experimental results over the ten year publication span of these works, and partly due to increased sophistication of the models. As such, only the two most recent will be included in the summary table at the end of this chapter. Of the four sets of predictions, the first two preserve the 'usual' spectrum hierarchy, with the broad states having smaller masses than the narrow ones, while both later results agree with the spin-orbit inversion found by Isgur [24], albeit with much reduced magnitude.

The paper by Eichten and Di Pierro also determines the expected partial widths of the

various $B^{**}_{(s)}$ states; these are predicted to be:

$$\begin{aligned}
\Gamma(B_2^* \to B\pi) &= 10.6 \text{ MeV}/c^2 \,, \\
\Gamma(B_2^* \to B^*\pi) &= 9.5 \text{ MeV}/c^2 \,, \\
\Gamma(B_1 \to B^*\pi) &= 13.1 \text{ MeV}/c^2 \,,
\end{aligned} \tag{2.11}$$

where there is also a small contribution ($\Gamma \sim 0.5$ MeV/c^2) allowed for $B_1 \to B\pi$ decays, due to a $1/m_b$ term allowing mixing between states. The similarity of the two B_2^* partial widths agrees with the relative branching ratio prediction given in Eq. (2.9). The broad states are both predicted to have widths of around 180 MeV/c^2. For the B_s^{**} system, the equivalent calculations give very small widths $\Gamma \sim \mathcal{O}(10^{-2})$ MeV/c^2 for the narrow states, which are expected to sit close to the kinematic threshold for decays to $B^{(*)}K$.

Table 2.4: Predictions of $B^{**}_{(s)}$ masses from four relativistic constituent quark models, as described in the text.

State	Mass (MeV/c^2)			
	[25] [a] (1991)	[26] [b] (1995)	[27] [c] (1997)	[28] [d] (2001)
B_0^*	5760	5650	5738	5706
B_1'	5780	5690	5757	5742
B_1	5780	5690	5719	5700
B_2^*	5800	5710	5733	5714
B_{s0}^*	5830	5750	5841	5804
B_{s1}'	5860	5790	5859	5842
B_{s1}	5860	5800	5831	5805
B_{s2}^*	5880	5820	5844	5820

[a] Godfrey and Kokoski
[b] Van Orden, Roberts and Zeng
[c] Ebert, Galkin and Faustov
[d] Di Pierro and Eichten

2.3.5 Lattice QCD Calculations

In lattice QCD, the strong interactions of quarks and gluons are discretised by placement on a grid in space-time, with characteristic spacing a. The quarks can only be located on the grid intersection points, and the gluons must travel between these points along the grid lines. Such a simplification of the continuous nature of the universe introduces a momentum cut-off of order $1/a$, which controls the QCD divergences, allowing numerical methods to be used to solve problems with a finite number of terms. As the lattice spacing is reduced, it is hoped that the predictions of lattice models will converge on the experimentally observed particle properties. As a result of the massive computational workload, calculations of this type for excited meson states have only recently been made with reasonable precision. The paper by Ali Khan *et al.* [29] uses lattice QCD to predict heavy-light meson masses, with the heavy quark modelled non-relativistically, and a lattice spacing corresponding to $1/a = 1.92$ GeV/$\hbar c$, or $a \approx 10^{-16}$ m. The resulting mass predictions for $B^{**}_{(s)}$ states are:

$$\begin{aligned} M(B_0^*) &= 5670 \pm 37\ ^{+16}_{-24}\ \text{MeV}/c^2\ , \\ M(\bar{B}_1^{(\prime)}) &= 5770 \pm 31\ ^{+24}_{-35}\ \text{MeV}/c^2\ , \\ M(B_2^*) &= 5822 \pm 45\ ^{+27}_{-35}\ \text{MeV}/c^2\ ; \end{aligned} \tag{2.12}$$

$$\begin{aligned} M(B_{s0}^*) &= 5742 \pm 27\ ^{+14}_{-20}\ ^{+15}_{-0}\ \text{MeV}/c^2\ , \\ M(\bar{B}_{s1}^{(\prime)}) &= 5836 \pm 25\ ^{+20}_{-28}\ ^{+14}_{-0}\ \text{MeV}/c^2\ , \\ M(B_{s2}^*) &= 5878 \pm 26\ ^{+23}_{-33}\ ^{+11}_{-0}\ \text{MeV}/c^2\ . \end{aligned} \tag{2.13}$$

Here the first uncertainty is statistical, the second is the systematic effect of varying the lattice spacing ($1.8 < a^{-1} < 2.0$) GeV/$\hbar c$, and the third relates to the uncertainty in the strange quark mass. The ability to quantify the precision of predictions in this way is one of the great benefits of lattice QCD. This approach leads to much larger predictions for the extent of mass splitting in j_q doublets, with the other models all yielding small values of less than 20 MeV/c^2.

2.4 Summary

As the preceding section illustrated, there have been a number of attempts to predict excited B meson masses, utilising several different techniques. The resulting calculations yield masses over a relatively wide range, as shown in Tables 2.5 and 2.6. In general, there is agreement that the splitting between $B_{(s)1}$ and $B^*_{(s)2}$ states should be around 10–20 MeV/c^2, with the lattice approach being the only exception. The total widths of both B^{**} mesons are predicted to be close, and a little wider than the mass difference; the corresponding B^{**}_s widths are expected to be very small, with maximum theoretical predictions of around 4 MeV/c^2.

The partial widths of B^*_2 into the two possible single pion channels $B\pi$ and $B^*\pi$ are determined to be very close (see Eq. (2.11) and Table 2.3), which implies that:

$$R_2 = \frac{Br(B^*_2 \to B^*\pi)}{Br(B^*_2 \to B^{(*)}\pi)} \sim 0.5\ . \tag{2.14}$$

This completes the survey of theoretical approaches to the excited B meson spectrum. In the following chapter the experimental groundwork is laid, with a description of the Tevatron accelerator and the D0 detector. The analysis itself is then detailed in Chapters 4–7, before returning to the theoretical predictions in Chapter 8, where they are compared to the analysis results.

Table 2.5: Summary of theoretical mass and width predictions for narrow B^{**} states. Uncertainties are only given if specifically quoted in the papers, and represent the combination of all sources.

Source	Mass (MeV/c^2)		Splittings (MeV/c^2)		Widths (MeV/c^2)	
	$M(B_1)$	$M(B_2^*)$	Δ_1 [a]	Δ_{21} [b]	$\Gamma(B_1)$	$\Gamma(B_2^*)$
F+M [1]	5780	5794	501	14	23–36	23 ± 4
E,H,Q [2]	5759	5771	480	12	17	22
I [24]	5700	5715	421	15	—	—
E,G,F [27]	5719	5733	434	14	—	—
DP+E [28]	5700	5714	421	14	14	20
K [29]	$5770\ ^{+39}_{-47}$	$5822\ ^{+52}_{-57}$	474	52	—	—

[a] $\Delta_{(s)1} = M(B_{(s)1}) - M(B^+)$
[b] $\Delta_{(s)21} = M(B^*_{(s)2}) - M(B_{(s)1})$

Table 2.6: Summary of theoretical mass and width predictions for narrow B_s^{**} states. The mass splittings are defined as in Table 2.5. Uncertainties are only given if specifically quoted in the papers, and represent the combination of all sources.

Source	Mass (MeV/c^2)		Splittings (MeV/c^2)		Widths (MeV/c^2)	
	$M(B_{s1})$	$M(B_{s2}^*)$	Δ_{s1}	Δ_{s21}	$\Gamma(B_{s1})$	$\Gamma(B_{s2}^*)$
F+M [1]	5886	5899	607	13	0.7 ± 0.2	1.8 ± 0.4
E,H,Q [2]	5849	5861	570	12	1	3.6
E,G,F [27]	5831	5844	546	13	—	—
DP+E [28]	5805	5820	526	15	< 1	< 1
K [29]	$5836\ ^{+35}_{-38}$	$5878\ ^{+36}_{-42}$	540	42	—	—

Chapter 3

Experimental Apparatus

THE DATA USED IN THIS ANALYSIS was collected by the D0 ("Đ-Zero") $\bar{p}p$ colliding beam detector on the Tevatron accelerator ring, part of a complex of accelerators in Fermilab (Fermi National Accelerator Laboratory, or FNAL). This occupies a site of approximately ten square miles near the Fox river in northern Illinois, in the United States of America.

Fermilab (originally just the 'National Accelerator Laboratory') was commissioned in 1967 under the directorship of Robert R. Wilson [30], who established not only the rigorous scientific aims of the project, but also aesthetic and environmental ideals, and a policy of equality for employees. The first major project was the construction of the 'main-ring' synchrotron, which in March 1972 successfully reached its design goal by accelerating a proton beam to 200 GeV, the highest energies ever achieved by humankind at the time [30]. At this stage, the technology required for beam-on-beam collisions was not in place, with experiments based on fixed-target detectors. The main-ring era of the complex was crowned in 1977 with the discovery of the bottom quark [30, 31], the first direct evidence of a third generation in the quark sector.

Renamed in honour of Enrico Fermi in 1974, the facility has been at the forefront of accelerator science since its construction, with numerous major upgrades and additions allowing different areas of high energy physics to be probed with increasing power and precision. Most significant in the context of this thesis is the construction, in 1983, of the

'Tevatron': a series of accelerating components designed to collide proton and antiproton beams, at a centre-of-mass energy $\sqrt{s} = 1.8$ TeV, inside the main-ring tunnel. Following the first collisions in 1985 a successful period of running from 1992–1996, termed Tevatron Run I, culminated in yet another ground breaking discovery: this time the first observation of the top quark in 1995 [32, 33, 34]. Since it reached its target beam energy over twenty years ago, the Tevatron has remained the highest energy (man made) particle accelerator in the world.

The progression to a colliding beam setup saw the introduction of the two detectors located at the beam crossings on the Tevatron ring; namely CDF ('Collider Detector at Fermilab') in 1985, and D0 (named after its location on the Tevatron ring) in 1992. These are multi-purpose systems comprising a number of sub-detectors, allowing different types of interesting events to be collected simultaneously. Both the accelerator and the detectors underwent large scale upgrades following the conclusion of Run I; including an increase in collision energy to $\sqrt{s} = 1.96$ TeV, an increase in collision rate, and several improvements in the detector components.

In March 2001 the Tevatron Run II collider program began. Following a year of detector commissioning, the upgraded D0 detector started to record collisions in April 2002. This period of data collection quickly surpassed the total integrated luminosity delivered by the Run I program, breaking records in instantaneous luminosity consistently throughout operation (see Section 3.1.2 for luminosity definitions and plots). In February 2006, the accelerator was turned off for an extended shutdown, during which time additional upgrades were made to D0 and CDF, in part to mitigate the effect of radiation damage to the inner layers of the silicon tracking detectors. As a result of these major changes, the Run II program of the Tevatron is divided into two detector eras: Run IIa, up to the 2006 shutdown; and Run IIb, for all data collected after this transition.

This thesis uses only Run IIa data, comprising approximately 1.35 fb^{-1} of integrated luminosity. In this chapter, both the accelerator and detector apparatus are summarised. For the purposes of this analysis, the details of how the beam is delivered and controlled, while extremely interesting, are less relevant than the properties of the final delivered beam. Therefore the discussion of the accelerator takes the form of a brief overview.

The D0 Run IIa detector has been well documented elsewhere [35], so the emphasis is on describing the particular components of interest, and introducing the basic ideas and terminology which will be used in later chapters.

3.1 The Tevatron Accelerator

The process of delivering collimated high energy proton and antiproton beams to the site of the D0 and CDF detectors is a technological feat encompassing numerous distinct stages, and relying on cutting-edge apparatus. This section outlines each stage of the acceleration process, starting with a cannister of hydrogen gas, and ending with the highest energy $p\bar{p}$ collisions ever achieved artificially. In addition, some properties of the beams and collision volume will be described for completeness. The beams division at Fermilab has produced detailed reports covering all aspects of the accelerator, which are referenced throughout the following summary.

3.1.1 The Accelerator Complex

Figure 3.1 shows a schematic, top-down view of Fermilab's accelerator complex, annotated with the proton and antiproton beam directions. Clearly visible are the two largest components in the acceleration chain: the Main Injector (and Recycler), and the Tevatron synchrotron. Additional significant parts of the complex are also shown, all of which are described in this section.

The Preaccelerator

The preaccelerator takes hydrogen gas (H_2) as an input, and produces a beam of negatively charged hydrogen ions at an energy of 750 keV. It consists of three major components: an H^- source; an accelerating electrostatic column, charged by a Cockcroft-Walton generator; and a transport line containing a number of beam control devices [36]. The beam is then injected into the Linac, described later. For redundancy, there are two complete preaccelerator systems, either of which can be used alone to generate beam at a given

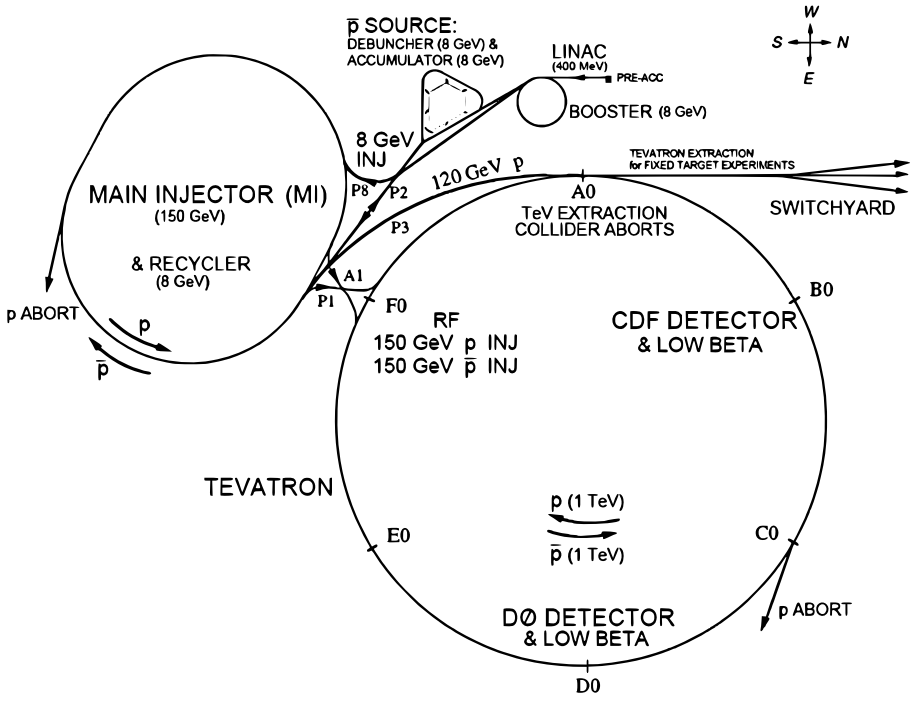

Figure 3.1: Schematic overview of the Fermilab accelerator complex. Shown are the major components, as described in the text, used in producing high energy proton and antiproton beams for collision at points D0 and B0.

time.

The first stage in producing the proton beam takes place in a magnetron surface plasma source [37, 38], which transforms hydrogen gas into a dense plasma of H^- ions. The gas is injected, at low pressures of a few thousand pascals, into the gap (of width $\sim$1 mm) between an oval cathode and the surrounding anode, as illustrated in Figure 3.2. The plasma is created under static electric and magnetic fields, with the electrons confined to helical paths within the magnetron gap. Negative hydrogen ions are discharged from the cathode by a number of scattering and reflection processes, and are extracted and accelerated through the anode aperture and a positively charged extractor plate. Adding caesium vapour to the system increases the efficiency of the source by thinly coating the cathode surface and reducing its work function, increasing the probability of the required electron capture by hydrogen atoms (or H^+ ions). A single bottle of hydrogen gas provides

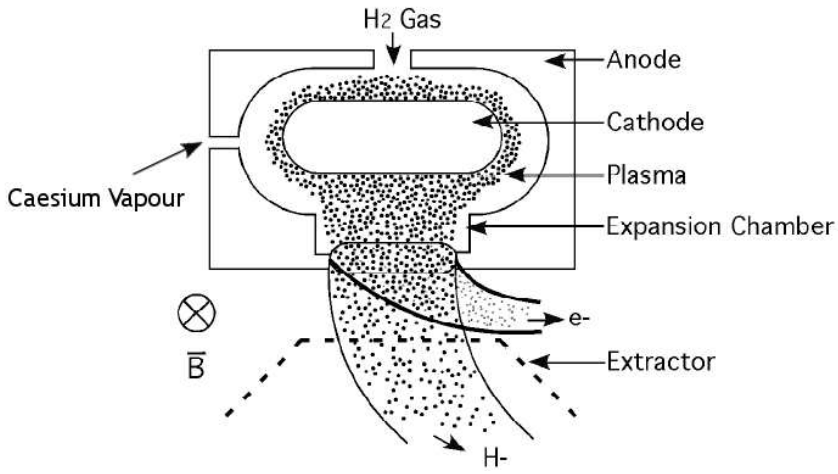

Figure 3.2: Magnetron negative hydrogen ion source, showing the principal components used in producing H^- ions from hydrogen gas.

sufficient material for six months of beam.

In order to aid the subsequent acceleration processes, it is convenient to produce a pulsed beam of H^- ions from the source. To this end, the H_2 input rate and the magnetron and extraction plate voltages are pulsed with a 15 Hz frequency, yielding pulse durations of approximately 80 μs. When active, the extractor plate voltage accelerates the H^- ions to energies of 18 keV. Stray electrons and other ions accompanying the desired particles are removed by magnetically bending the trajectories through a right angle.

The hydrogen ions are then passed into the electrostatic accelerating column. The magnetron source and all related operating systems (including the extractor plate) are maintained at a voltage of -750 keV, by enclosing them inside a metal dome charged by the Cockcroft-Walton generator [37]. As such, the H^- ions experience a large accelerating gradient as they pass through the column towards the electrically grounded transport line.

The transport line controls the beam shape and timing, to ensure a smooth transition into the Linac. The beam is steered and focused without acceleration, and unwanted sections of the pulsed beam are removed by an electrostatic 'chopper'. In addition, a single radio frequency (RF) cavity is used to raise the pulse rate to 201.25 MHz, matching the Linac operating frequency. This latter transformation doubles the transition efficiency

to the linear collider.

The Linac

The Linac ('LINear ACcelerator') takes the 750 keV beam of H^- ions from the preaccelerator, and provides additional acceleration in two stages, raising the beam energy to 400 MeV before sending it to the booster [39, 40, 41, 42, 43].

The first stage is a 79 m sequence of five Alvarez drift-tube tanks, each undergoing pulsed RF resonance at 201.25 Hz. These are high conductivity metal cylindrical tanks, in which an oscillating pulsed magnetic field is induced tangentially to the cylinder (i.e. the field lines form circles about the tank axis). The resulting electric field is directed along the cylinder (and hence beam) axis, with alternating polarity. While the net field over the whole system time-averages to zero, it can be harnessed as an accelerating device by the use of drift-tubes within the cylinder. These tubes shield particles passing through them from the electric field: by suitable arrangement the pulsed beam is exposed to the RF fields during the accelerating phase, but shielded by the drift tubes from decelerating forces when the polarity is reversed.

On leaving the fifth Alvarez tank, the beam has an energy of 116.5 MeV. It is then passed into the second stage: a side-coupled linear accelerator, comprising seven cavities over a 67 m section. This stage, and all subsequent acceleration, uses RF resonant cavities, with appropriate timing ensuring that the beam is exposed to the required accelerating field as it passes through the cavity. In this particular case, the RF frequency is 801 MHz, four times the Alvarez frequency, such that only one in four RF cycles contains beam. Power for these 12 MW cavities is provided by custom designed klystrons. Following this second linear accelerator, the beam has energy 400 MeV, with a pulse length of 40 μs. It is then passed into the booster, described below.

Throughout the Linac, alternating focusing and defocusing magnets ensure that the transverse beam size remains within the acceptable cavity aperture (around 3 cm), compensating for certain RF effects which can broaden the beam profile. Additional monitoring and beam steering is also utilised, leading to efficient, reliable operations.

The Booster

The booster is the first synchrotron in the accelerator chain, with a diameter of 151 m [39]. It takes the 400 MeV pulsed H^- ion beam from the Linac, strips the electrons off using a carbon foil filter, and accelerates the resulting proton beam to 8 GeV energy before passing it to the Main Injector (MI). Acceleration is provided by 18 RF cavities distributed around the booster ring, leading to 84 stable phase-space regions (or 'buckets') in which particles can be captured and accelerated. Focusing and bending is provided by 96 combined purpose magnets, arranged in twenty-four identical periods.

The booster operates under three distinct phases: injection, acceleration, and extraction. The full cycle of phases takes place over $\sim$35 μs, and is repeated as often as is required to fill the Main Injector. In the first phase, the RF phases are set to give zero net acceleration, and the H^- ions from the Linac are injected through the carbon foil. The 400 MeV proton beam makes one full revolution of the booster in around 2.22 μs, and to fill all 84 RF buckets the injection must continue though 5–6 revolutions. The momentum spread of particles from the Linac is undesirable in a synchrotron, where it translates into a spread in the radius of curvature through the bending magnets. As such, a 'debuncher' is used prior to injection, which focuses the ions in momentum space. The injection is controlled by a electrostatic deflector following the Linac; when beam is not wanted by the booster, it is dumped.

Once injection is complete, and the beam has been 'bunched' into the RF buckets, the acceleration can proceed. Each RF cavity undergoes sinusoidal field oscillation. The phase difference between adjacent cavities is varied according to the current beam energy, ensuring that a stable accelerating electric field is seen by each bunch as it passes through the cavities. In addition, bunch timing is arranged so as to ensure phase stability. The total acceleration process takes around 29 μs, after which the beam has reached 8 GeV energy, and is ready to be transfered to the Main Injector.

Extraction takes place over the course of just one booster revolution, yielding one booster 'batch'. This is performed by four pulsed 'kicker' magnets which deflect each bunch out of the synchrotron path and towards the P8 transfer line (see Figure 3.1). During

this process, one bunch is lost due to the turn-on time of the magnets. Depending on the running mode, some or all of the 83 booster bunches may be sent to the MI. Transfer is facilitated by phase locking the booster RF frequency to match the Main Injector: the bucket structure is then maintained with little loss during the transition.

The Main Injector

The Main Injector is a larger synchrotron accelerator, which fulfills several roles within the collider complex [39]. It has a circumference of 3320 m, and contains 18 RF cavities for acceleration, with 344 dipole and 208 quadrupole magnets providing focusing and beam steering around the ring. In total, there are 588 RF buckets in the MI, of which only a small number are used at any one time. The three running modes of interest for the collider program are as follows:

1. Antiproton production mode: The MI is injected with a single batch of 8 GeV protons from the booster, comprising $\sim 5 \times 10^{12}$ protons [1] over all 83 bunches. These are accelerated to 120 GeV and sent to the antiproton source through transfer lines P1 and P2 (see next section). Each complete cycle of $\bar{p}$ production takes around 2.4 s: this is then repeated tens of thousands of times to produce as many antiprotons as possible, in a process called 'stacking'.

2. Proton injection to the Tevatron: The MI is injected with twelve smaller batches of 8 GeV protons from the booster, each typically containing 5–13 bunches. Each batch ($\sim 4 \times 10^{11}$ protons) is coalesced to remove the internal bunch structure, and accelerated to 150 GeV for injection into the Tevatron (via the P1 transfer line) over a single turn. Three such cycles are required to fill the Tevatron with the required 36 coalesced proton bunches.

3. Antiproton injection to the Tevatron: The MI is injected with a single batch of 8 GeV antiprotons from the Accumulator, each containing four groups of eleven

[1] The number of protons and antiprotons present at each stage is increasing by year as the accelerator performance improves. Here, and in later descriptions, the number is approximate and reflects the beam conditions during Run IIa.

bunches. Again, each group ($\sim 3 \times 10^{10}$ antiprotons) is coalesced to remove the bunch structure, and accelerated to 150 GeV before fast extraction (via the A1 transfer line) to the Tevatron. Nine such cycles are required to obtain 36 coalesced antiproton bunches in the Tevatron. Alternatively, antiprotons can be transfered to the MI from the Recycler (see later).

In addition to these Tevatron oriented uses, the Main Injector also delivers 120 GeV protons to the switch-yard, for use in fixed target experiments. This can be performed concurrently with antiproton production.

As a result of the long timescale required to generate the required number of antiprotons (see next section), the Main Injector operation is dominated by the first of these three modes. Once sufficient $\bar{p}$ numbers are available from the antiproton source, the process of injection to the Tevatron is very quick. The duration of a single Tevatron 'store', during which collisions are occurring at the two beam crossings, is generally twelve hours or more; in this time, antiprotons are accumulated in readiness for the next Tevatron cycle.

The Antiproton Source

The Fermilab antiproton source [37, 44, 45] consists of a target on which 120 GeV protons are directed to produce antiprotons; a debuncher, which captures and stablises the resulting 8 GeV $\bar{p}$ beam; and an accumulator, which stores the antiprotons until enough have been collected to send to the Main Injector. An additional antiproton storage device is the Recycler, described later.

As described in the previous section, the MI delivers a single batch of $\sim 5 \times 10^{12}$ protons to the antiproton source. The beam is focused by quadrupole magnets to a cross-sectional radius of $\sim$0.15 mm, and impinged on a nickel target, producing a spray of secondary particles which are then focused by a lithium lens. Negative particles of approximately 8.9 GeV/c momentum are selected by magnetic bending, and the resulting antiprotons (around 5×10^7) are transfered to the debuncher. At this point, the bunch structure of the original proton beam remains, and the particles exhibit a broad range of momenta.

The debuncher is a rounded triangular synchrotron, of around 90 m radius, containing 90 RF buckets. Its purpose is not to accelerate, but rather to manipulate and control the antiprotons received from the target. These particles, while possessing a wide momentum distribution, are arranged in spatially compact bunches along the beam axis. By adiabatic debunching, the beam is rotated in phase space to achieve a small momentum spread. This is necessary in order to achieve stable orbits over the long periods of time the bunches will spend in the Accumulator. At the same time, the spatial distribution of the beam is transformed from the bunch structure into a fairly continuous finite ribbon of antiprotons.

To further aid particle transfer and storage, a process of 'betatron stochastic cooling' is undertaken, which reduces the beam phase space by a complex feedback procedure, utilising beam monitoring and corrective kicks. This technique was invented in the 1970s by Simon van der Meer, for use in antiproton cooling at the SPS experiment in CERN [46]. The term 'cooling' is used by analogy with temperature, since a smaller phase space is equivalent to a reduction in the random motion of the beam. The full Debuncher cycle, including cooling, takes around 2.4 s, after which the beam is transfered to the Accumulator, in time to receive the next batch arriving at the target from the Main Injector.

The Accumulator synchrotron is situated in the same tunnel as the Debuncher, with a slightly smaller radius ($\sim$75 m). A batch of antiprotons from the Debuncher are injected to the Accumulator, and navigate a closed orbit at the outer edge (largest radius of curvature) of the Accumulator aperture. Over the next hour this batch is gradually merged with the 'core' of the existing $\bar{p}$ stack at a smaller radius, by a gentle ($\sim$60 MeV) deceleration followed by additional stochastic cooling. Once in the core, the antiprotons are subject to momentum cooling, as well as a reduction in the horizontal and vertical spatial distributions. Collecting the required 10^{12} antiprotons takes around 12 hours of continuous running.

The Accumulator contains 84 RF buckets, which hold the beam in bunches during stacking. At the time of transfer to the Main Injector, a portion of the beam is accelerated to an orbit of larger radius in readiness for extraction. The RF frequency is phase locked to match the MI, and the beam portion is rearranged into eleven appropriately sized bunches. This is repeated four times, before the 4×11 bunches are delivered to the Main Injector

for additional acceleration as described in the previous section.

The Tevatron

The Tevatron is the final stage in the acceleration process, taking protons and antiprotons from the Main Injector at 150 GeV, and simultaneously accelerating them in opposite directions around a synchrotron of radius 1 km, to achieve the final collision energies of 980 GeV [39, 47]. Once the final collision energy has been reached, the beams are focused and outlying particles (the beam 'halo') removed by collimators. The particles then continue to circulate around the synchrotron for several hours (a so-called 'store'), with $p\bar{p}$ collisions initiated by crossing the beams at D0 and CDF, at an average rate of 1.7 MHz.

At each beam crossing a small fraction of particles are lost from the proton and antiproton beams; there are also additional losses, for example due to beam interaction with accelerator material. As a result, the beam intensity tends to fall over time. At some point, usually when the antiproton stack is large enough to initiate a new store, the Tevatron beam is dumped, and the whole cycle is repeated. In this way, the total luminosity (see Section 3.1.2) delivered by the accelerator is maximised. The transition time between terminating one store and starting collisions with the next is approximately one hour.

At the high particle energies reached by the Tevatron, the magnets used for bending (774 dipoles), focusing (216 quadrupoles), and correcting the beam use superconducting technology to reach fields in excess of 4 T, which necessitates liquid helium cooling to around 4.6 K. Acceleration is achieved by 8 RF cavities in a straight section at F0 (see Fig. 3.1), four each for protons and antiprotons. As described previously, for both protons and antiprotons, the beam is composed of 36 distinct bunches, each locked into one of 1113 RF buckets. In fact, these bunches are further grouped into three equal superbunches, or 'trains'; in which one in every 21 RF buckets is filled, and collisions occur every 396 ns. Each train therefore stretches over 232 buckets, and is separated from the other two by gaps of 139 buckets. These gaps are required to allow safe termination of running should any failure occur.

The implications of this Tevatron running scheme are that the D0 and CDF detectors

must be able to activate, trigger, read out and reset their systems within a few microseconds, in order to minimise the number of potentially interesting interaction events lost to detector dead time. This performance must be maintained for stretches of up to 30 hours to cover one store, and repeated for many consecutive stores. There are usually multiple $p\bar{p}$ interactions per crossing (around 2–3 on average during Run IIa), which can further complicate matters. The effect of such timing constrictions is described in Section 3.3.

The Recycler

The Recycler [39] is located in the same tunnel as the Main Injector. Its purpose is to siphon off antiprotons from the Accumulator for storage and additional cooling. This helps to prevent the instabilities which can occur when large $\bar{p}$ populations are present in the proton source. The addition of the recycler to the collider complex has led to an approximate doubling in instantaneous luminosity delivered by the Tevatron [47]. During storage, stochastic and electron cooling are performed to reduce the longitudinal and transverse phase-space of the beam.

Like the Main Injector, the Recycler uses a FODO lattice of focusing and defocusing quadrupole magnets, separated by dipoles, to control the beam orbit. A stream of antiprotons from the Accumulator is transfered to the Recycler, via the Main Injector; the four-cavity RF system in the Recycler then captures this continuous beam into discrete buckets, giving improved stability. No acceleration occurs: the beam is maintained at its injection energy of 120 GeV.

Cooling of the valuable antiprotons is particularly important, since it will reduce losses from beam scattering and stray particles. As in the Debuncher and Accumulator, stochastic cooling is performed by using beam monitoring information in conjunction with a downstream beam kicker to correct for deviations from the ideal orbit. In addition, electron cooling is performed [48]. This method uses a beam of 'cold' monochromatic electrons with momentum 4.8 GeV/c, travelling parallel to the antiproton beam over a 20 m straight section of the Recycler. By coulomb interaction, in analogy with the first rule of thermodynamics, the $\bar{p}$ beam is cooled to a smaller phase space, while the electron beam is heated. Electron cooling dominates when large numbers of antiprotons are present,

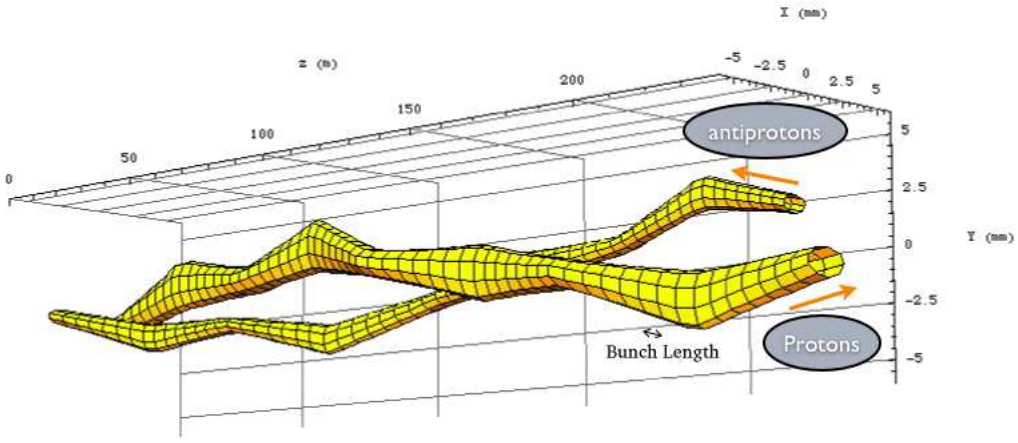

Figure 3.3: Beam envelopes for proton and antiprotons away from the collision points. Shown are the helical trajectories maintained by electrostatic fields, in order to prevent $p\bar{p}$ interactions as bunches pass in the beampipe.

since stochastic techniques become ineffective for denser beams.

When a new store is ready to commence, and the 36 proton bunches are safely in the Tevatron, the antiprotons from the Recycler are transfered to the Main Injector for acceleration to 150 GeV and injection to the Tevatron.

3.1.2 Collision Dynamics

The Interaction Region

Since the proton and antiproton bunches circulate the Tevatron in the same beampipe, travelling in opposite directions, they will regularly pass each other away from the desired collision points. To prevent unwanted interactions, the beam trajectories are separated by electrostatic fields; the resulting helical paths are shown in Fig. 3.3. Collisions are then initiated at D0 and B0 by additional field manipulation; this directs both beams straight down the centre of the beampipe, over a distance of several metres inside the collider detectors. In this way the crossing angle of $p\bar{p}$ bunches is fixed to be zero.

The bunch length for both particle types is around 37 cm [47], so that the beam overlap volume inside the collider detectors is extended by this distance along the beam axis

(the z-axis in the detector coordinate system). In practice, the longitudinal distribution of particles within a bunch means that the effective interaction region is approximately Gaussian in z, with mean $\mu_z = 0$ and standard deviation $\sigma_z \approx 25$ cm [35].

In contrast, the transverse size of the interaction volume is small, generally around 30 μm across. To quantify the transverse extent of the beam, it is convenient to introduce a new variable, the normalised transverse beam emittance, ϵ_N. This is defined to be the volume in (x, p_x) phase-space which contains 95% of all particles in the beam. It is a conserved quantity under adiabatic operations (such as acceleration), and therefore should remain constant as the particles orbit the Tevatron. For the proton beam, $\epsilon_N \approx 20\pi$ mm $\cdot$ mrad; for antiprotons, $\epsilon_N \approx 15\pi$ mm $\cdot$ mrad [47].

There are many processes at work which are not adiabatic, such as particle diffusion. The emittance will therefore tend to grow slowly over time. This will lead to some particle loss over the course of a store, as outlying particles leave the stable region and interact with accelerator material.

Luminosity

The rate at which protons and antiprotons interact in the Tevatron collision regions can be expressed as:

$$\mathcal{R} = \mathcal{L} \cdot \sigma_{int}, \tag{3.1}$$

where σ_{int} is the interaction cross-section, and $\mathcal{L}$ is the instantaneous luminosity. The former is a measure of the probability of an interaction for a single pass of two particles, expressed in units of area (an extension of the collision theory of classical mechanics, whereby interaction probability is proportional to the total transverse area of two projectiles). The luminosity is the constant of proportionality in this relation, giving a measure of the rate at which interaction *opportunities* occur, per unit area.

At the Tevatron, the luminosity is a function of many different parameters, including the number of protons (N_p) and antiprotons ($N_{\bar{p}}$) in each bunch, the revolution frequency

(f), the number of bunches (B) and the transverse ($\sigma_{p,\bar{p}}$) and longitudinal (σ_l) bunch size:

$$\mathcal{L} = \frac{fBN_pN_{\bar{p}}}{2\pi(\sigma_p^2 + \sigma_{\bar{p}}^2)} \cdot F(\sigma_l, \beta^*) \text{ [47]}. \tag{3.2}$$

Here F is a form factor which is a function of β^*, the value of the 'beta function' at the interaction point. This function describes the beam location and direction as a function of its evolution around the Tevatron, caused by the repeating FODO lattice of focusing and defocusing magnets described in Section 3.1.1. For Run IIa, the beta function at interaction was typically $\beta^* \approx 35$ cm [47].

As the number of particles in each bunch diminishes over the course of a single store, the luminosity will also reduce. Final luminosities generally fall to less than 10% of the initial peak value after an average store of 20 hours length. This has operational consequences for the two collider detectors. Since the rate of data collection by D0 and CDF is limited, the total number of events collected is maximised by dividing the store up into a number of smaller 'runs'. During each run, a different trigger scheme is used to select interesting events, based on the instantaneous luminosity at the time. As the store progresses, additional triggers are introduced, and existing ones expanded, to maintain a high rate of data acquisition. Triggers are discussed in more detail in Section 3.3.

Since real time determination of the beam parameters is not possible, the luminosity delivered by the Tevatron is determined by rearranging Eq. 3.1 to give $\mathcal{L}$ in terms of the rate of observed interactions and the known cross-section for a particular well understood reference process: the determination of luminosity at D0 is described in Section 3.2.6. Over the four years of the Run IIa program, peak instantaneous luminosities have consistently increased, from usual values of 2×10^{31} cm^{-2}s^{-1} in 2002, to in excess of 2×10^{32} cm^{-2}s^{-1} by 2006, as shown in Fig. 3.4.

The total number of interactions collected over time is given by the time integral of Eq. 3.1. The interaction cross-section is independent of time, so that the total number of events produced in collisions is proportional to the integrated luminosity $\int \mathcal{L}(t)dt$. This

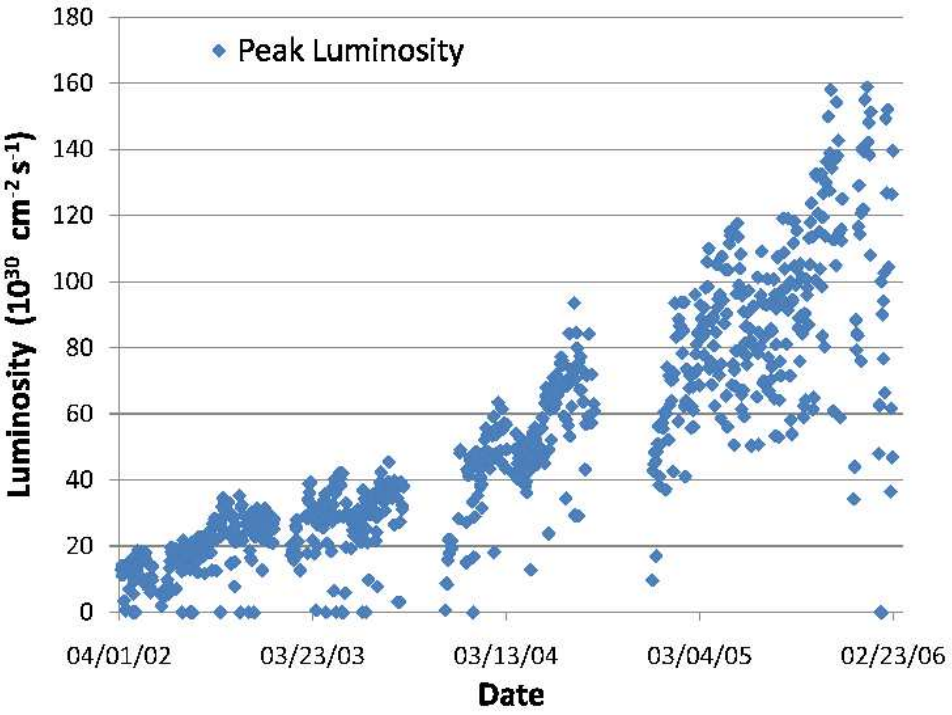

Figure 3.4: Store-by-store peak instantaneous luminosities delivered to the D0 detector during Run IIa.

figure is maximised by reducing accelerator and detector downtime, pushing peak luminosities to higher levels, and shortening the time taken between stores. Integrated luminosity is usually measured in terms of inverse picobarns (pb^{-1}), where 1 pb$= 10^{-36}$ cm^2 is a very small unit of area. In Run IIa, D0 collected a total integrated luminosity of around 1.35 fb$^{-1} = 1350$ pb^{-1}, as shown in Fig. 3.5.

The number of proton-antiproton interactions per bunch crossing follows a Poisson distribution, with a mean of around 2.3 for Run IIa data [47]. The possibility of multiple events in a single bunch crossing provides an additional challenge for data acquisition by CDF and D0.

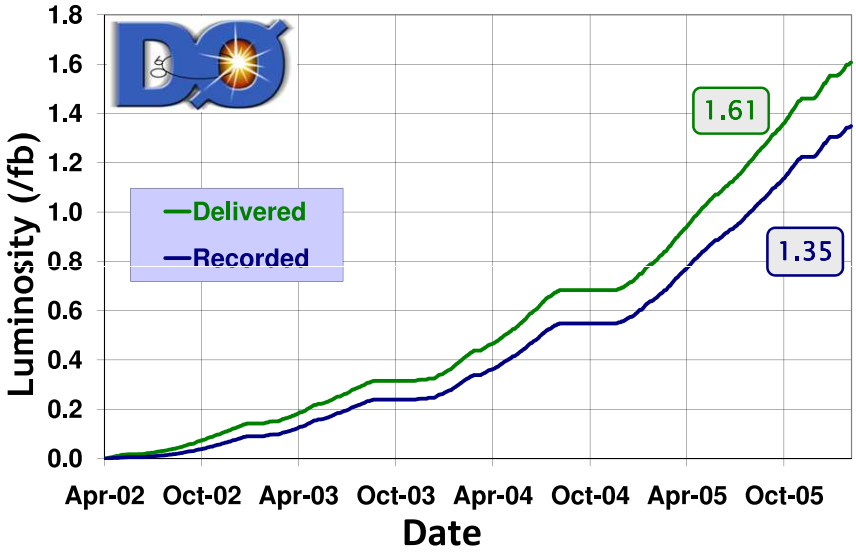

Figure 3.5: Cumulative integrated luminosity recorded by D0 during Run IIa. The difference between delivered and recorded luminosity arises from data acquisition inefficiencies, including hardware and software effects.

3.2 The D0 Detector

D0 is a general purpose colliding-beam detector, built with the object of capturing and recording many different types of particle physics 'events', for use in a wide range of studies. In this context, an event corresponds to the complete sequence of particle production, motion, interaction, and decay arising from a single $p\bar{p}$ collision at a bunch crossing. In practice, this definition is limited to those occurrences within the detector volume, since these are the only ones we can detect and study. The accelerator provides a very high rate of interactions, of order 5 GHz, of which the vast majority will be of low interest in the context of cutting edge research. A major challenge for D0 is to find the useful events from this sample, since the final data storage rate is limited to around 100 Hz. This is achieved by triggering the data collection on the basis of characteristic signals, indicative of 'interesting' events. More details on triggering and data acquisition can be found in Section 3.3.

Following the Run I era of the Tevatron, the D0 detector was upgraded significantly.

Improvements and additions were also made prior to commencing Run IIb. This section gives a description of the detector during Run IIa, corresponding to the years 2002–2006, when the data for this analysis was collected. Detailed descriptions of all aspects of the detector are available in the official write-up [35], which is the source of all information provided in this section, unless otherwise stated. What follows is a summary of the most relevant detector components and concepts required for the analysis of B meson spectroscopy.

3.2.1 Introduction

The general structure of a colliding beam experiment, such as D0, is a series of different sub-detectors arranged in layers around the interaction region. Each one can extract particular information about particles passing through it, such as momentum, energy, or particle type. Combining the data from all sub-detectors, a more complete picture can be developed than would be possible without this specialisation. Furthermore, each sub-detector is divided into many separate individual parts, called elements; a single element will only detect particles passing through a narrow solid-angle. Appropriate arrangement and orientation of the individual elements allows the total solid-angle coverage of the system to be maximised, so that as few events as possible are lost to detector 'dead areas'.

Figure 3.6 shows an overview of the D0 detector, within the 'collision hall', as viewed side-on from inside the Tevatron ring. The layered structure is clearly visible. Inside the detector, the beam is enclosed within a beryllium beampipe, 2.37 m long, 38.1 mm in outer diameter, and with an average thickness of 0.508 mm [35]. A tracking detector occupies the central region closest to the beampipe, contained within a 2 T magnetic field. This provides information on the trajectories and momenta of charged particles. The tracking detector is surrounded by a combined electromagnetic/hadronic calorimeter, which measures the energy of particles which have survived long enough to reach it. Furthest from the beampipe is the muon system, comprising three layers of tracking detectors and one layer of 1.8 T toroid magnets, for measuring muon trajectories and momenta. These components are described more fully in Sections 3.2.2–3.2.5. The forward

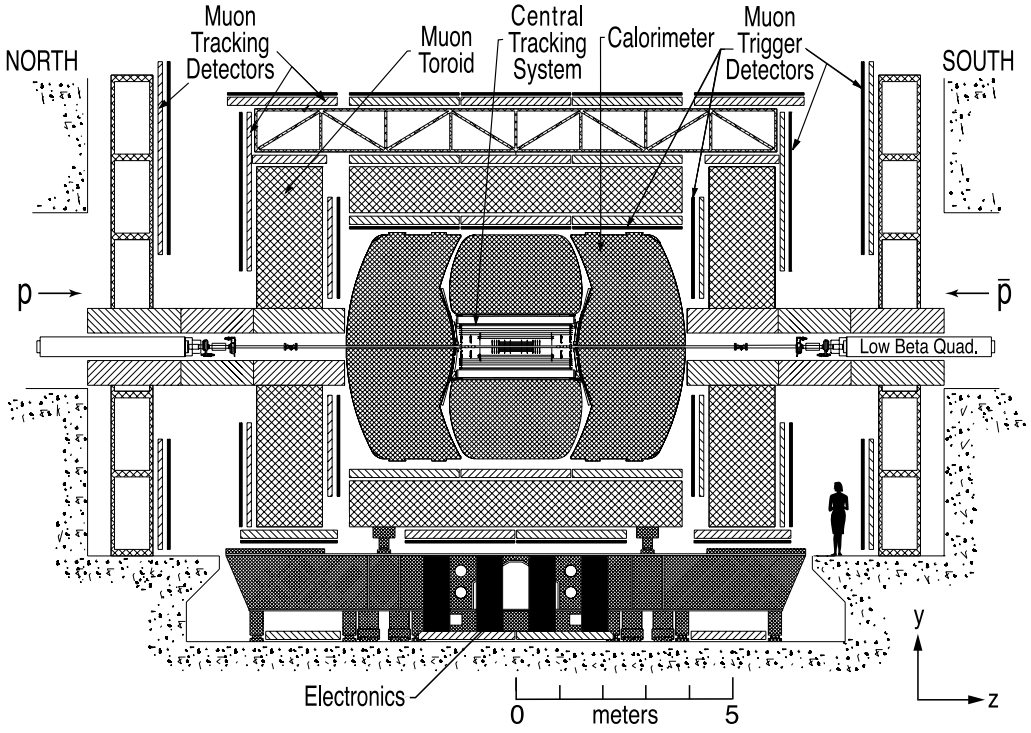

Figure 3.6: The D0 detector, viewed from inside the Tevatron ring. Protons from the north and antiprotons from the south enter the detector beampipe and collide; the resulting interactions produce secondary particles, which are detected and measured collectively by the various sub-systems shown in the diagram.

proton detector (FPD), located outside of the collision hall, is not used in this data analysis and so is excluded in the following detector description.

The Detector Coordinate System

As described in the previous section, the interaction region at bunch crossings is elongated along the beam axis by $\sim$25 cm, and typically 25 μm in transverse extent. The D0 detector exhibits cylindrical symmetry about the beampipe. For the purposes of detector alignment, and for data analysis, several coordinate systems are used, depending on the circumstance. In describing the detector, the origin is always located at the centre of the beampipe; while for analysis the origin can shift for convenience (for example, to the point-of-production of a certain particle).

The right-handed Cartesian system has the z-axis pointing along the proton direction, and the y-axis upwards, as shown in Fig. 3.6. A cylindrical coordinate system has the radial and azimuthal coordinates defined as usual, with $r = \sqrt{x^2 + y^2}$; and ϕ measuring the angular displacement from the positive x-axis, projected onto the (x, y) plane. In addition, the polar angle θ is commonly used, and measures the angle from the positive z-axis.

Another useful angular quantity is the pseudorapidity η which approaches the true rapidity in the relativistic limit. In this way, the complex kinematic quantity is approximated by a simple angular one:

$$\eta \equiv -\ln[\tan(\theta/2)] = \lim_{mc^2/E \to 0} \left\{ \frac{1}{2} \cdot \ln \left[\frac{(E + p_z c)}{(E - p_z c)} \right] \right\}, \tag{3.3}$$

where E, p_z and m are respectively the particle energy, momentum component along the z-axis, and mass. The pseudorapidity is useful in describing the structure of the detector sub-systems, which are comprised of 'central' sections at low $|\eta|$, and 'forward' sections at higher $|\eta|$. As a result of the beampipe, and the shielding which surrounds it outside of the central region, particles above a certain pseudorapidity cannot be detected. For the central tracking detector and the calorimeter, coverage extends up to $|\eta| \approx 4$; while the muon system is effective up to $|\eta| \approx 2$.

It is also convenient to introduce the transverse momentum p_T of a particle. This is the component of momentum in the $(x, y) \equiv (r, \phi)$ plane, perpendicular to the beam, and is used frequently in later chapters. Finally, the term 'upstream' ('downstream') is used in detector descriptions to refer to the section of a particle trajectory which occurred earlier (later) than the reference time. Since particles from $p\bar{p}$ interactions originate at bunch crossings in the centre of the detector, this effectively means that downstream is synonymous with "further from the detector centre", in r and/or in z. These terms should not be confused with similar concepts used in track selection, which are defined differently (see Section 4.3.1).

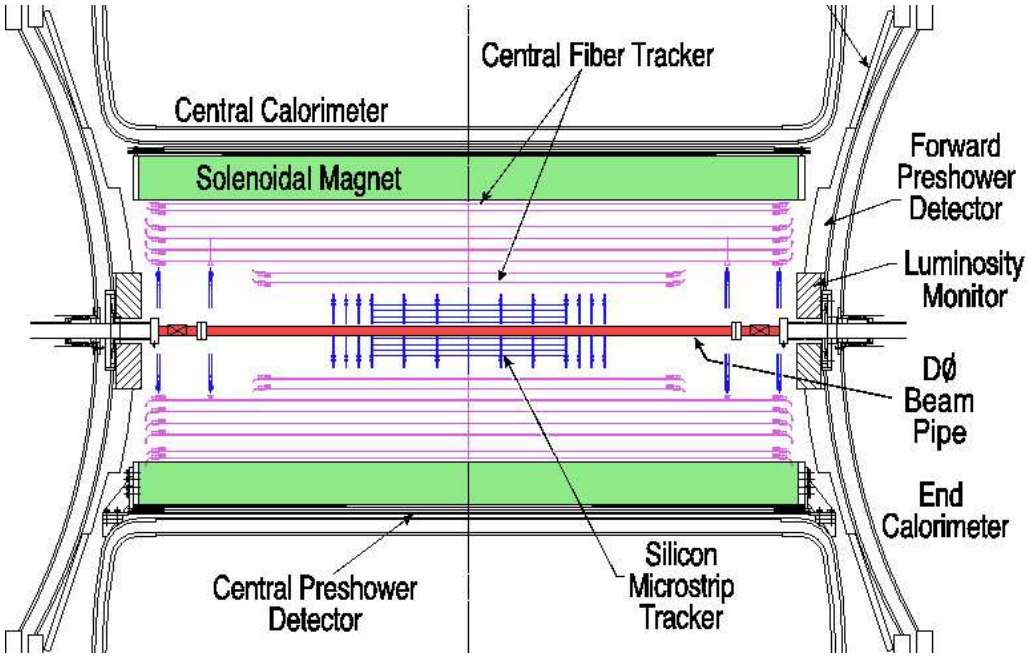

Figure 3.7: Top-down view of the central tracking detector at D0. Highlighted in colour are the beampipe, the SMT and CFT components, and the surrounding solenoid magnet, as described in the text.

3.2.2 The Central Tracking Detector

The tracking detector comprises two distinct systems: a silicon microstrip tracker (SMT) closest to the beampipe; and a central fiber tracker (CFT) surrounding it; the entire detector is enclosed within a solenoid electromagnet providing a 2 T field along the z-axis. Figure 3.7 shows the major components of the tracking detector, enclosed by the calorimeter. The tracking detector, and the associated software tools, are used extensively in the analysis presented in later chapters, so are described in some detail.

Introduction

The purpose of the tracking detector is to measure the instantaneous coordinates of charged particles, at one or more times, as they travel outward from the interaction point. This information is then used by subsequent software to reconstruct the three dimensional trajectories of these particles. The charge, momentum, and where relevant the production

and/or decay vertices of particles, can then be extracted. Any deflection, absorption or energy depletion caused by the tracking detector will result in lost or corrupted particle information. Emphasis is therefore placed on minimising the amount of detector material present.

Both the SMT and the CFT are formed from a number of individual sensor elements. As a charged particle passes through a sensor, it produces a signal which allows its position to be measured. The specific mechanisms by which this takes place depend on the sensor type, and are described later. A single charged particle will usually pass through several elements, and therefore produce a number of coordinate snapshots, called 'hits'. The series of hits traces the particle path through the entire tracking chamber, and can be extrapolated into the calorimeter and muon systems beyond: the hypothetical trajectory thus inferred is called a 'track'.

The task of combining several hits to form a track is complicated in practice by the high multiplicity of charged particles: several hundred can result from a single $p\bar{p}$ interaction, each producing a number of hits in the tracking system. For the purposes of data analysis, tracking software is used to associate the hits in the detector with tracks, as outlined in Section 4.1.1. The track fitting algorithms take a long time, and so this process is performed offline after the data is written to tape. However, track information is also a strong determinant of interesting events: for example, particles produced far from the initial $p\bar{p}$ interaction strongly suggest the presence of a B meson. Therefore, dedicated systems for both SMT and CFT sub-systems are in place to provide fast tracking capabilities for use by the trigger framework, as described in Section 3.3.

Each reconstructed track is associated with an uncertainty, arising from the limited spatial resolution of the tracker, and from limits to precise knowledge of the system alignment. In addition, mis-associated hits and detector noise can result in tracks being reconstructed which do not correspond to any real particle path: so called 'fake' tracks. The impact of these effects on an analysis can be reduced by selecting tracks which satisfy certain 'quality' constraints, such as having at least n hits from the SMT or CFT sectors.

Once the tracks have been constructed, the Primary Vertex (PV) can be found. This is the point in the beampipe where the initial $p\bar{p}$ interaction took place. The details of

how this is determined are related in Section 4.3.2; the location can be measured to within 35 μm along the z-axis, and is constrained to lie within 25 μm in the (x, y) plane by the accelerator dynamics. In the search for excited B mesons this is a crucial measurement, since signal events are discriminated from background by the proximity or distance of particle production vertices with respect to the PV (see Chapter 4 for more details).

The presence of the magnetic field allows the charge and momentum of particles to be measured from their track curvature, according to the usual relation for charged particle motion. The solenoid magnet was designed to fit into the space within the calorimeter cavity, with length 2.73 m and an outer diameter of 1.42 m. The field strength of 2 T aids in track recognition and provides the required momentum resolution, as described in Section 4.1.1. The arrangement and hardware components of the SMT and CFT are described in the following sections. The geometrical alignment of the combined SMT and CFT tracking detector, an essential input for determining hit coordinates, is known to within 10 μm [35].

The Silicon Microstrip Tracker

The SMT is an array of 912 individual semiconductor sensors, arranged into 'barrel' and 'disk' modules so as to give good tracking performance over a wide range of polar angles (particles can be detected up to $\eta \approx 4$). The arrangement of modules is shown in Fig. 3.8; the system exhibits cylindrical symmetry about the beam axis, and linear symmetry about the $z = 0$ plane. The combination of barrel elements perpendicular to the beam, and disk elements parallel to the beam, ensures that most particles will pass through several sensors with a large angle of incidence: a requirement for precise determination of position.

There are six barrels, each 12 cm long and with an inner (outer) radius of 2.7 cm (10.5 cm) [35]. A single barrel comprises four concentric cylindrical layers of silicon sensors called ladders, with each ladder forming a plane tangential to the cylinder. The central two layers have twelve ladders each, the outermost two layers have 24 ladders, giving 72 sensors per barrel, and 432 ladders in total.

There are three different types of ladder sensor used, depending on the barrel and layer, but all comprised of silicon semiconducting wafers. As a charged particle passes through

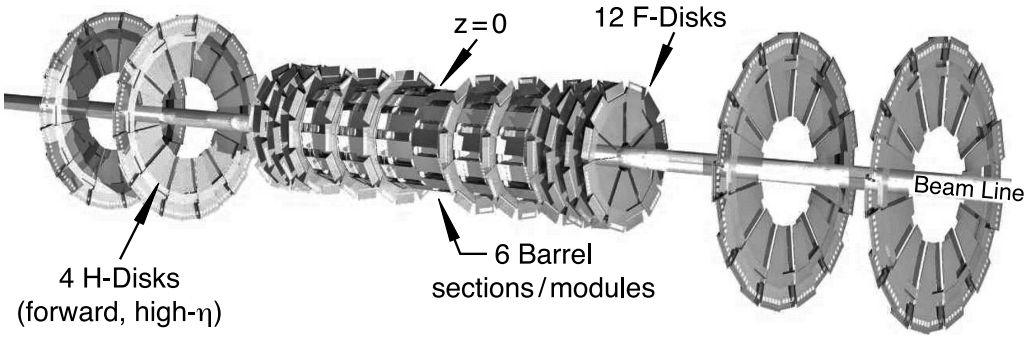

Figure 3.8: Three dimensional view of the SMT system in the D0 detector, showing the six barrel modules, twelve F-disks and four H-disks, as described in the text.

the sensor, it will ionise the silicon to produce free electrons and 'holes' (i.e. unoccupied states in the valence band). By applying a voltage across the wafer, the electrons and holes will drift with the electric field, producing a signal current indicating the presence of the charged particle. Semiconductors are identified as n-type or p-type, respectively denoting the principal charge carriers in the material as electrons or holes, although a single semiconductor can be manipulated to have both n- and p-regions.

The spatial resolution in one direction is improved by dividing each sensor into a number of independent microstrips perpendicular to that direction; the width, or 'pitch' of the strips then gives the precision of that coordinate measurement, while the resolution parallel to the strip direction corresponds to the strip length. The electrical output from each strip is called a channel, and is read out from an interface on the high-z side of the ladder, necessitating a gap of around 8 mm between barrels, in which particles cannot be detected. Further improvement of resolution is achieved by using double-sided sensors, where the strip orientation on one surface is rotated with respect to the other. At the passage of a charged particle, the electrical signals from both sides are combined to give an effective resolution corresponding to the overlap region of the strips. In analogy with depth perception in vision or hearing, the relative rotation of strips in double-sided sensors is called the 'stereo angle'.

The three sensors used in ladders are as follows:

- Single-sided (SS) sensors, used in the first and third layers of the outermost two barrels. These have a single detection surface (p-type), with microstrips of pitch 50 μm aligned along the z-axis. Each ladder is formed by the end-to-end bonding of two (6 cm long) sensors.

- Double-sided (DS) sensors, used in the second and fourth layers of all six barrels. These have two independent wafer surfaces, a p-type (with orientation and pitch the same as for SS sensors) and an n-type (pitch $= 62.5$ μm) with a stereo angle of 2°. In this way, the z position of the particle is measured more precisely. Again, each DS ladder is formed by bonding together two 6 cm sensors.

- Double-sided double-metal (DSDM) sensors, used in the first and third layers of the innermost four barrels. These also use two sensor surfaces, with the same p-surface configuration as SS and DS. Here, the stereo angle is 90° and the n-surface has a pitch of 153.5 μm. The use of perpendicular microstrips allows the full three dimensional coordinate of the particle to be obtained with high precision. The ladders are formed from single sensor units of 12 cm length.

Since only 144 of the 432 ladders use the DSDM sensors, and even these have a z resolution three times worse than for ϕ, the barrel modules primarily measure particle positions in terms of $r - \phi$ coordinates. More information on z position comes from the disk modules, in addition to the CFT system.

Each barrel is adjoined on its outer edge to an 'F-disk' module. In addition, three consecutive F-disks are located at each end of the barrel assembly, as illustrated in Fig. 3.8. The F-disks are 7.9 cm thick, with an inner (outer) radius of 2.6 cm (10.0 cm); each one is constructed from twelve double-sided 'wedge' silicon multi-strip devices, which use the same technology as the ladder sensors. The p-type surface strips (pitch $= 50$ μm) are oriented along one of the non-parallel edges of the trapezium shaped wafer, with the other edge used to align strips on the n-type surface (pitch $= 62.5$ μm). The stereo angle thus formed between the microstrips is 30°, improving the precision of the radial coordinate measurement. Another result of this orientation scheme is that not all strips have the same length. In total, there are 144 wedges in F-disk modules.

Finally, at high $|z|$, the SMT system is capped by two 'H-disks' at each end. These have an inner (outer) radius of 9.5 cm (26 cm) and are 7.9 cm thick. A H-disk is composed of twenty-four composite ('full') wedges, each formed by bonding two single-sided ('half') wedges together. The strip orientations follow the same scheme as used in the F-disk wedges, to give an effective stereo angle of 15°. Here the strip pitch is 40 μm, but each read-out channel connects to a pair of adjacent strips, resulting in an effective pitch of 80 μm. The four H-disks contain 96 wedges in total. For all disks, the channels are read out at the high-r (i.e. broad) end of the wedge.

The snapshots of particle coordinates (hits) are extracted from the signals received through 792,576 channels corresponding to the full array of ladder and wedge elements, of which around 90% were functional during Run IIa. This stream of data is mapped into three dimensional detector space by interfacing the tracking software with the measured detector alignment. As the integrated luminosity increased during this era, the silicon experienced radiation damage, which reduced the electrical signals produced by charged particles. Some sensors become unuseable as a result of excessive radiation, and although this was not a serious issue in Run IIa, it was a contributing factor in the addition for Run IIb of the so-called 'layer zero' detector between layer one and the beampipe.

The Central Fiber Tracker

The CFT consists of 76,800 scintillating fibres, arranged in doublet-layers which form sixteen concentric cylinders about the beampipe, in the range 20 cm $< r < 52$ cm. The innermost four doublets cover only the central 1.66 m along the z-axis, due to the presence of the SMT H-disks at larger z. The outer twelve doublets are 2.52 m long, giving coverage up to around $\eta \approx 1.7$. For convenience, the doublet layers are hereafter numbered from L1–L16, starting from the innermost.

Each doublet comprises two singlet layers of closely spaced fibres, with the fibres of the top layer running over the inter-fibre spaces of the lower layer. The fibres are 835 μm in diameter, and are uniformly distributed in ϕ, with centre-to-centre separations of 926–990 μm, depending on the radial location. In this way, near complete ϕ coverage is achieved in every doublet. The fibres in odd numbered ('axial') doublets are oriented

parallel to the z-axis. Fibres in even numbered ('stereo') doublets are rotated in ϕ by $+3^\circ$ ('u' stereo layer) for layers 2,6,10 and 14; and by -3° ('v' stereo layer) for layers 4,8,12 and 16. This rotation can be visualised as a small twist of one end of the cylinder with respect to the other.

The sixteen concentric layers are further arranged into eight pairs of axial-stereo doublets, separated in r by 1.8–2.0 mm. The radial distance between pairs is much larger, usually around 50 mm. Within a pair, the doublets contain the same number of fibres, which increases with cylinder radius, ranging from from 1280×2 for doublets in pair one (L1 and L2), to 3520×2 for doublets in pair eight (L15 and L16). The use of closely spaced axial-stereo doublet pairs results in improved spatial resolution of about 100 μm per doublet, in a similar manner as used for double-sided SMT sensors.

To aid in alignment, fibres are bonded into the precisely machined grooves of a flexible plastic 'ribbon', containing a total of 256 fibres corresponding to two layers of 128. These ribbons are then mounted onto the curved support structure at either end of the CFT assembly. Testing shows that the position of the fibres is known to within $\sim$25 μm.

The scintillating fibres are composed of a core of polystyrene doped with around 1% flourescent dye. As a charged particle passes through the material, it causes multiple excitations in the polystyrene, which then transfer via non-radiative dipole-dipole interactions to the dye. This de-excites with the emission of 340 nm photons, which are then converted to 530 nm by a wavelength shifting (WLS) dye, 3-hydroxyflavone, present in low concentrations. The polystyrene is transparent to light of this latter wavelength, which is therefore transmitted rapidly down the fibre by total internal reflection, aided by two layers of cladding around the fibre core. The yield for a single charged particle is estimated to be approximately 10 photons for each fibre it passes through [49]. Much more information regarding scintillating fibres is available in Ref. [50].

At one end of the scintillating fibres, the ends are mirrored by aluminium, providing around 90% reflectivity. Photons at the other end are collected by clear polystyrene waveguides, of length $\sim$8–12 m, which differ from the scintillating fibres only by the absence of flourescent or wavelength shifting dye. The waveguides channel photons from each fibre to visible light photon counters (VLPCs) [51, 52], which convert light from

the charged particles into an electrical signal, which is then written to tape if the event passes the required triggers. The entire process of excitation, light emission and conversion by VLPCs is completed well within the 396 ns between bunch collisions in the beampipe, making the CFT signal a suitable input for fast triggering ('Level One' - see Section 3.3.1). Since each fibre corresponds to a single read-out channel, there are 76,800 total channels from the CFT system, each providing hit information for subsequent track reconstruction.

3.2.3 Preshower Detectors

The pre-shower (PS) system is situated in the narrow gap between the solenoid magnet and the calorimeter; and comprises three separate units: a Central Pre-Shower (CPS) detector cylindrically wrapping around the solenoid, and two mirror-image Forward Pre-Shower (FPS) detectors forming the circular end-caps of the system. The layout in relation to the central tracking system can be seen in Fig. 3.7.

Like the central fiber tracker, both the FPS and CPS detectors utilise scintillating material to produce photons as charged particles pass through. In fact, the waveguides, VLPCs and read-out electronics are common for CFT and pre-shower detectors, and the signals from all scintillators are combined for use in the CTT trigger (see Section 3.3). However, unlike the CFT, information from the PS system is not used in track reconstruction. Its main use in offline data processing is to work in conjunction with the calorimeter in several ways: it aids in electron identification, and in general with the spatial identification of tracks to calorimeter signals; it also provides a method for correcting calorimeter energy deposits, to compensate for particle losses in the inner detector material (such as the solenoid magnet, cables and structural components). In this analysis, the calorimeter and PS system are used only minimally, for supplemental muon identification as described in Section 4.1.3. Therefore, these two detector components will be only briefly described. The interested reader is encouraged to consult Ref. [35] for further details.

Detection Material

The building blocks for both CPS and FPS detectors are extended triangular prisms of doped polystyrene scintillating material, covered with aluminised mylar to contain the signal photons. Each prism is a rounded equilateral triangle, of approximately 6 mm thickness along each edge, with a central core of WLS fibre, used to transport photons to the clear waveguides for read-out. These individual strips are built up into interleaved layers, as illustrated in Fig 3.9, with the nesting geometry different for CPS and FPS detectors. The precise arrangement and spacing of strips depends on the geometry of the layer, and can vary by up to 20% from the specifications in Fig. 3.9.

Lead radiators are used in the PS system to encourage particle showering, which is a process of particle multiplication (i.e. converting individual particles into cascades of lower energy ones), through processes such as electron-positron pair production (by photons), bremsstrahlung (by electrons) and decays (by hadrons). This provides a distinctive signature through which different particle types can be distinguished. Unlike the central tracking detector, which was designed for minimal particle interference, the pre-shower detectors and calorimeter must completely 'stop' a particle in order to determine its energy. In practice, this process involves converting as many of the shower products as possible into photons or low energy drift electrons, which are then captured and turned into an electrical signal. The pre-shower provides the first step in this process.

At this point, it is convenient to introduce the radiation length X_0. This is a characteristic length scale for electromagnetic interactions in matter, expressing the typical distances traversed by an EM object before significant interactions cause it to shower [11].

Central Pre-Shower Detector

The CPS is formed from three layers, forming concentric cylinders about the solenoid. Each layer has 1280 strips, which are silvered at $z = 0$ and read out independently from each end of the detector for a total of 7680 channels. As with the CFT, the layers are arranged with a stereo angle, to improve spatial resolution. The innermost layer is axial, i.e. the strips are aligned with the z-axis. The next layer has strips arranged at approximately

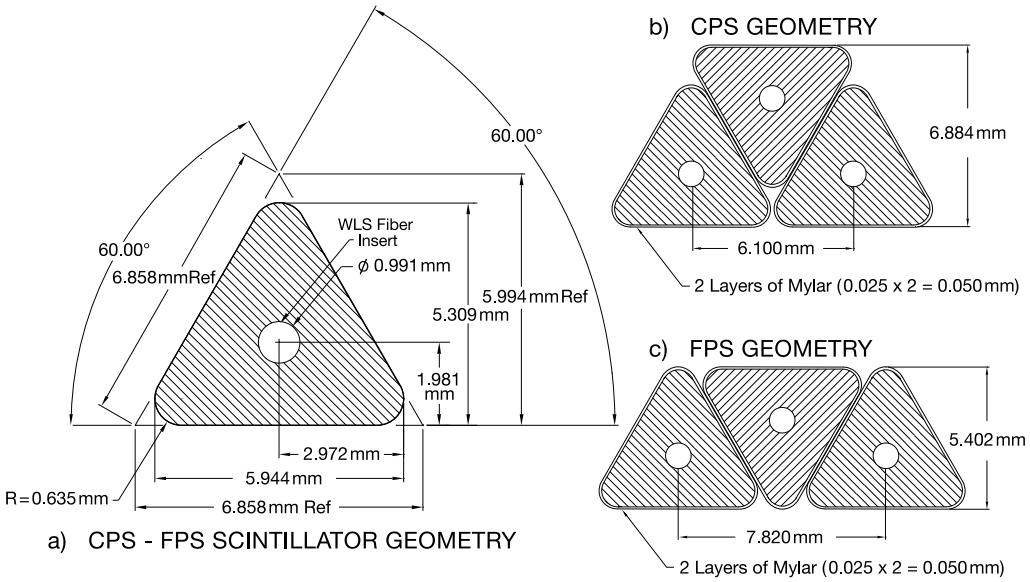

Figure 3.9: Cross-section of scintillating elements used in the pre-shower detectors. Both CPS and FPS are composed of rounded triangular prisms (left), but different nesting schemes are used to construct the interleaved layers (right).

$+23.8°$ to the axial, by a rotation of one end of the cylinder with respect to the other. The outermost layer has the strips rotated by around $-24.0°$ from the axial alignment.

The layers are formed from octant modules, comprising 160 strips sandwiched between 0.8 mm thick stainless steel skins. The gap between solenoid and central calorimeter is just 5 cm, which encloses the three layers of steel-skinned strips, as well as a lead radiator of thickness 5.6 mm between the CPS and the magnet. Collectively, the lead, steel and solenoid have a thickness of around $2X_0$, so that showering is likely to occur before electromagnetic particles reach the CPS.

Forward Pre-Shower Detectors

The FPS detectors are situated at either side of the central tracking chamber. Each one comprises two curved disk shaped sub-systems: a minimum ionizing particle (MIP) module, and a shower module, separated in z by a lead and stainless-steel absorber. In total, each FPS detector has 7442 read-out channels.

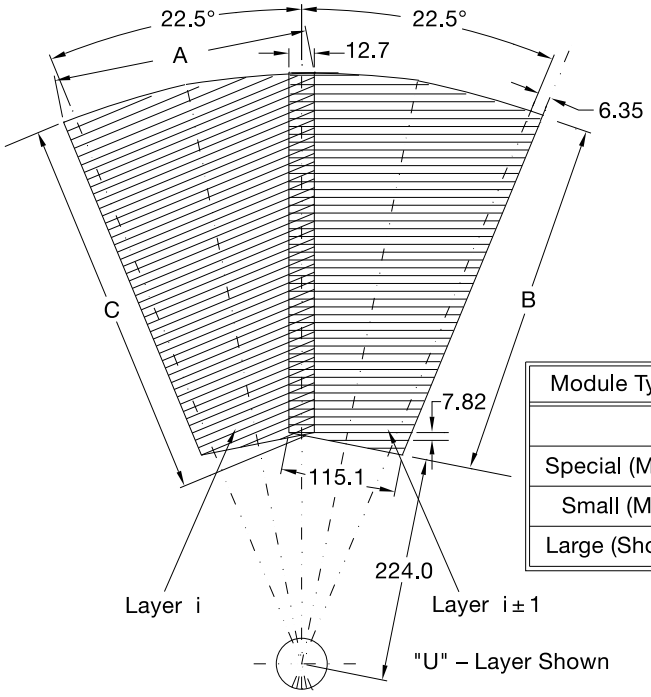

Module Type (Layer)	Dimension (in mm)		
	A	B	C
Special (MIP, Shower)	214.9	250.9	278.3
Small (MIP Layer)	255.3	352.3	381.7
Large (Shower Layer)	312.6	496.6	528.7

Figure 3.10: Arrangement of scintillating wedges in the FPS detector, showing how a single plane (here a u plane) is formed by interleaving sixteen wedges to give full ϕ coverage. The overlap region of 12.7 mm width is shown. Also shown are the dimensions of wedges for each module type.

Each MIP or shower module is constructed from two layers of scintillating material, denoted u and v, with a relative orientation of 22.5° between the layers. An individual module has full ϕ coverage, achieved by interleaving two 'half-ϕ' sub-layers. The sub-layers comprise eight 22.5° wedges of active material, uniformly distributed in ϕ about the full disk. This eight-bladed propeller shape is then combined with the partner sub-layer, which is rotated by 22.5° about the z-axis, to give full ϕ coverage over 16 scintillating wedges. The active material actually covers slightly more than half of each layer, resulting in overlapping regions of scintillators, as shown in Fig. 3.10. Inactive material provides structural support between the scintillating wedges.

Each full MIP u-v wedge contains 206 scintillating strips and provides coverage from $1.65 < |\eta| < 2.5$, as does the inter-module absorber. The shower module covers $1.5 < |\eta| < 2.5$, with 288 strips per wedge. In addition, there are four smaller wedges (two each

in the MIP and shower modules) with 142 strips, covering $1.8 < |\eta| < 2.5$. The latter are required to allow cryogenic service pipes to access the solenoid.

The absorber is divided into forty-eight wedges, each comprising a 3.5 mm stainless-steel plate sandwiched between two lead sheets, giving a thickness of around $2X_0$. This component accounts for the different particle behaviour (and hence the naming scheme) in the two FPS modules. The absence of any significant absorbing material upstream of the MIP results in particles interacting just as they would in the CFT: the MIP therefore measures the (η, r, z) coordinates of charged particles as they pass through. For heavy charged particles, the absorber is generally too short to cause showering, and so the shower module also sees a single-particle interaction. Electrons will almost all interact in the absorber, yielding a cascade of secondary particles which are seen in the shower module as a broad energy deposit, typically three strips in width, which is associated with the hit in the MIP module. Photons will also form electromagnetic cascades in the absorber, to be detected with a similar energy signature in the shower module, but without any MIP signal. In this way, photons, electrons and heavy charged (hadronic) objects are distinguished. From $1.5 < |\eta| < 1.65$, no absorber is required, since the solenoid coil lies between the $p\bar{p}$ interaction region and the shower module, providing a radiation length of $3X_0$.

3.2.4 The Calorimeter

The D0 calorimeter system surrounds the central tracking and pre-shower detectors, and is designed to measure the energy of electrons, photons and hadronic particle jets, in addition to helping with particle identification via the characteristic distribution of energy deposits. This latter ability is used in this analysis to collect a small sub-set of muons, as described in Section 4.1.3. However, the detailed structure of the calorimeter, and the associated reconstruction algorithms, are not of significance to the analysis. As in the previous section, the description will be brief, and the reader is encouraged to pursue the several excellent reviews [35, 53, 54] for further details.

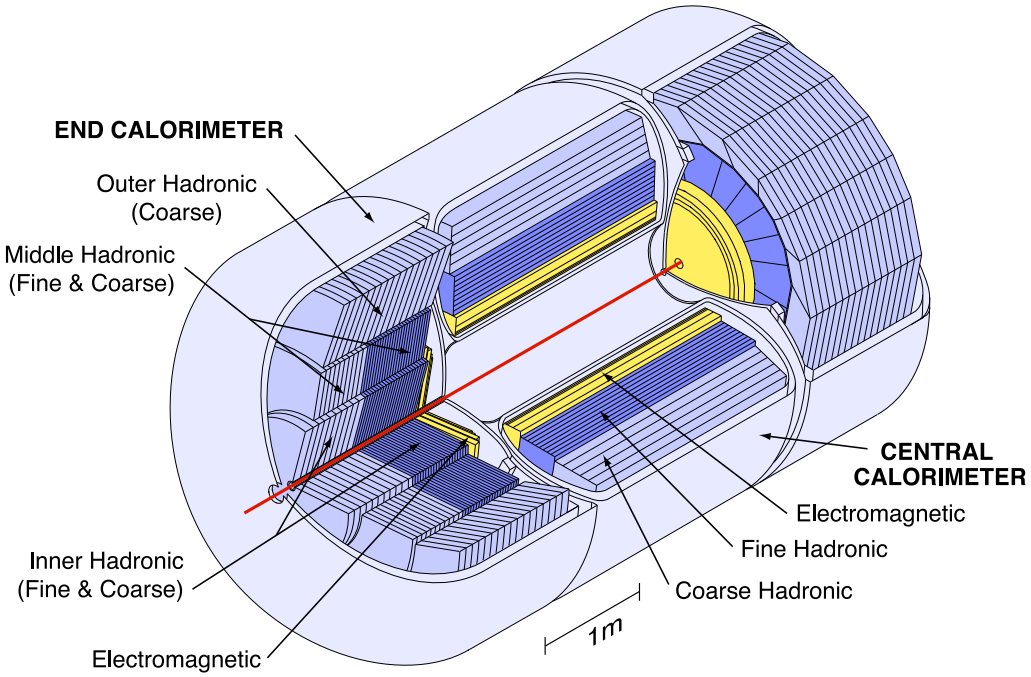

Figure 3.11: Cut-out view of the D0 calorimeter system, showing the three distinct units (central calorimeter, and two end calorimeters) and the arrangement of electromagnetic and hadronic modules.

The calorimeter is arranged in three units: a central calorimeter (CC) and end calorimeters to the north (ECN) and south (ECS), as shown in Fig. 3.11. Each one is is enclosed in a sealed cryostat, cooled by liquid nitrogen to 90K. This temperature is necessitated by the detection mechanism, which uses liquid argon as an active medium, as described later. The whole system offers hermetic coverage to high-η: The CC covers $|\eta| \leq 1.2$, with the EC units extending the coverage up to $|\eta| \approx 4$. The use of three distinct cryostats is required to allow access to internal parts of the detector: the SMT, CFT, pre-shower detectors, solenoid, and associated components.

Each unit houses three different types of calorimeter module, to provide suitable performance over a range of different particle types and energies. Closest to the detector are electromagnetic (EM) modules, followed by fine-hadronic (FH) and coarse hadronic (CH) modules, as shown in Fig. 3.11. The particular arrangement depends on the unit, and, for the EC units, on the detector pseudorapidity. All three module types work on the

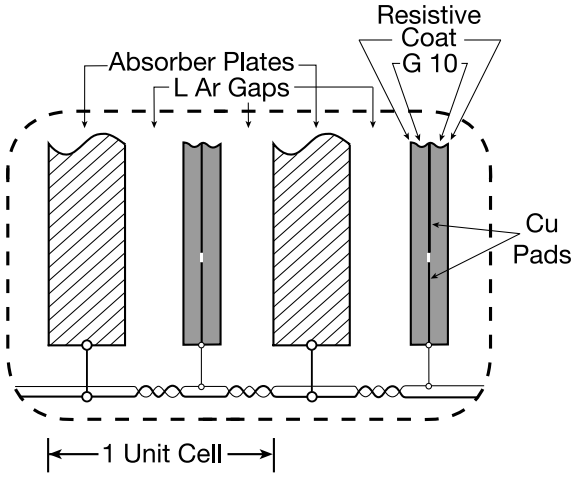

Figure 3.12: Schematic side view of a single calorimeter detection unit, showing the absorber and signal plates, surrounded by liquid argon.

same principle, outlined below.

Detector Material

Each module is composed of a series of absorber plates (of uranium, copper, or steel) interleaved with parallel signal boards, within the liquid argon medium, as illustrated in Fig. 3.12. Particles passing through the absorber plates initiate showers of secondary particles, which in turn cause ionisation of the active material. The signal plates are maintained at a high voltage of 2kV, with the absorber plates grounded; electrons therefore drift across the 2.3 mm gap between absorber and signal plate, yielding a signal which is amplified and read out for trigger use and storage. The characteristic detection time of the calorimeter is therefore limited by the 450 ns electron drift time. By stacking several cells, and using suitable absorber material, the showers from almost all particles can be completely contained within the detector volume, allowing the energy to be determined by appropriate summation. The major exception are muons, which will generally pass through the calorimeter without showering, leaving only minimum ionisation. This motivates the use of an outlying muon detector system, which is described in the next section.

In almost all modules, the signal plates are formed by bonding two G-10 (glass-reinforced epoxy laminate) substrate boards together, and coating the outer surfaces with highly resistive carbon epoxy. One of the inner surfaces is clad in copper, which collects the drift electrons as a signal voltage. The spatial resolution (in the plane of the board) is improved by etching the copper into isolated pads, which can be read out independently. For the innermost modules in the EC, the dead areas introduced by this etching are undesirable, since even a small transverse gap can correspond to a significant angular region. In these cases, multi-layer printed circuit boards (PCBs) are used instead of simple copper cladding.

For both the CC and EC units, the copper pads are etched so as to provide semi-projective 'towers' of constant (ϕ, η) relative to the interaction region, as illustrated in Fig. 3.13. Each tower subtends a solid angle corresponding to 0.1×0.1 in $\Delta\phi \times \Delta\eta$, and is composed of 8–12 longitudinal layers over all three module types. The term semi-projective indicates that while the towers are aligned with rays from the detector centre, the plates and signal boards are not perpendicular to this direction, as is clear from Fig 3.13. For the third layer (out of four) of the EM modules, the etching is arranged to give a resolution of 0.05×0.05 in $\Delta\phi \times \Delta\eta$, for improved determination of electromagnetic shower profiles. Each longitudinal layer is formed by 'ganging' signals from several adjacent boards into a single read-out: this simplifies subsequent electronics and triggering, with the minor drawback being an acceptable loss in longitudinal resolution.

Central Calorimeter

The central calorimeter comprises three concentric cylinders of modules, in the form of ϕ segments extending for the full length in z. Closest to the solenoid are 32 EM modules, forming four read-out layers, with the outermost signal board corresponding to a thickness of around $20X_0$. This provides sufficient thickness to ensure that almost all EM objects are completely captured by the calorimeter. In this case, the absorber material is formed from 3 mm thick uranium plates.

The thickness of the EM CC for hadronic objects is only $0.76\lambda_A$ (where λ_A is the attenuation length for hadronic showering, analogous to X_0 for EM showers), therefore

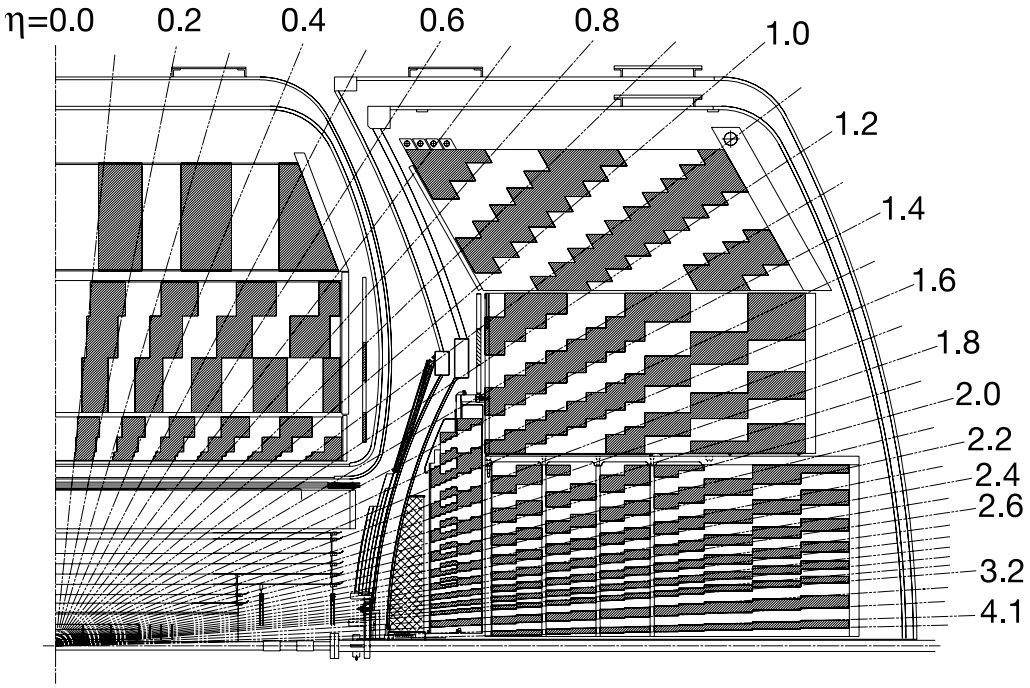

Figure 3.13: Side profile of the D0 calorimeter, showing transverse and longitudinal segmentation, with respect to rays originating at the geometric centre of the detector.

most hadronic showering occurs downstream. There are 16 fine-hadronic modules, each comprising three longitudinal readout layers with 6 mm thick uranium-niobium (2%) alloy absorbers, to give a total thickness of around $3\lambda_A$. The outer layer of the CC comprises 16 coarse-hadronic modules, each with a single read-out layer of $3.2\lambda_A$ thickness constructed with 46.5 mm copper plates as absorbers.

All modules in the CC are built by stacking the absorber and signal plates inside stainless steel boxes, with spacers used to arrange the plate separation. Modules in successive cylinders are rotated about ϕ, so that any single particle can pass through a maximum of one inter-module gap. In total, the CC unit weighs around 330 tons, and produces $\sim$15,000 signal channels.

End Calorimeters

Each EC contains four module types, best described in conjunction with Fig. 3.11. The innermost cylinder comprises two inner-hadronic (IH) modules, one fine and one coarse. Each one gives full ϕ coverage by wrapping completely around the beampipe, with the two modules adjacent in z. This layout eliminates particle loss to inter-module gaps. The fine hadronic module consists of four longitudinal ($1.1\lambda_A$) read-out layers, each containing 6 mm thick uranium plates arranged into eight circular absorbers. The coarse hadronic module has a single ($4.1\lambda_A$) read-out layer of 13 steel absorbers, each 46.5 mm thick.

The IH is adjoined at low z to the end-cap EM calorimeter. This is a single module, with four read-out layers covering a total thickness of around $20X_0$, and using 4 mm uranium plates as absorbers.

Surrounding the IH cylinder are 16 middle-hadronic (MH) modules, each comprising four fine-hadronic ($0.9\lambda_A$) and one coarse-hadronic ($4.4\lambda_A$) read-out layers. The outer-hadronic cylinder has steel absorbers and signal plates inclined with respect to the z-axis by 60° (see Fig. 3.13); this means that the calorimeter system offers relatively perpendicular surfaces for incident particles over a wide range of pseudorapidity.

Modules are built similarly to those in the CC, and enclosed by stainless steel skins. The total weight of each EC unit is around 250 tons, and the EC and hadronic modules collectively provide approximately 15,000 read-out channels per end calorimeter.

Inter-Cryostat Detectors

One result of the three-cryostat structure of the calorimeter is the presence of relatively large regions containing no detection elements, but with sufficient material for showering to occur (see Fig. 3.13, in the pseudorapidity range $0.8 < |\eta| < 1.4$). To improve energy resolution for particles passing though this region, additional scintillating detectors are attached to the external wall of the end-cap cryostats: this is the inter-cryostat detector (ICD).

The ICD on each end-cap is composed of an annulus of scintillating tiles, 12 mm thick, which are optically isolated in aluminium boxes. There are 16 trapezium boxes

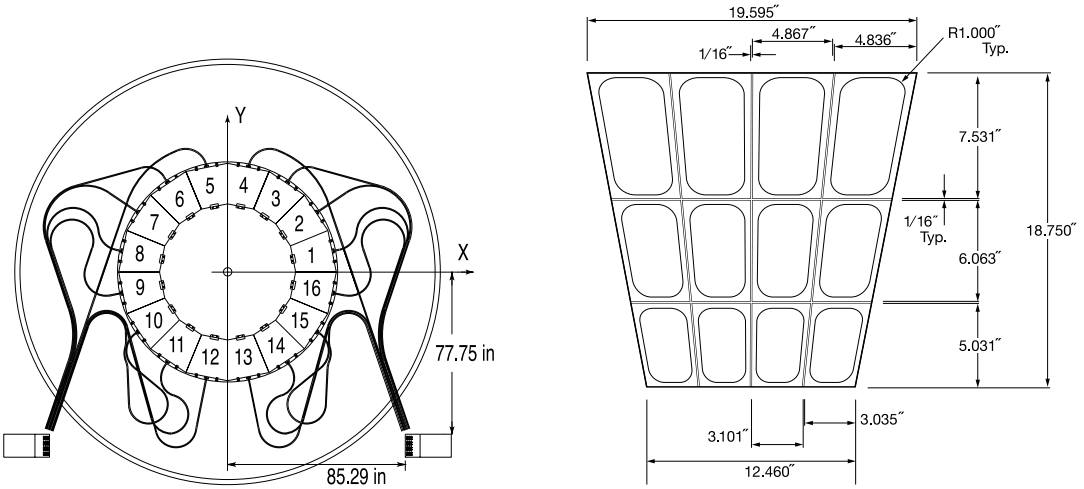

Figure 3.14: The D0 inter-cryostat detector. The diagram on the left shows the annulus of sixteen aluminium boxes and their optical connections to the PMTs; the layout of scintillating tiles within each trapezium box is shown on the right.

mounted in the ring, corresponding to $1.1 < |\eta| < 1.4$, which surround the forward preshower detector. A single box holds twelve trapezium tiles, each subtending 0.1×0.1 in $\Delta\phi \times \Delta\eta$, to match up with the calorimeter tower scheme. The arrangement of boxes, and the tiles within each box, is shown in Fig. 3.14. The photon yield from each tile is read out by WLS fibres, and passed to photo multiplier tubes (PMTs) which produce an electronic signal proportional to the energy deposited in the tile. In total, there are 384 scintillator tiles in the ICD, which are used in conjunction with the liquid argon calorimeter in triggers and data analysis.

3.2.5 The Muon System

The importance of muons in many different types of analysis motivates the presence of a dedicated muon detection system at D0 [35, 54, 55]. This forms the outermost layer of detector material, and comprises a scintillation counter detector and a tracking system. Both components are constructed in multiple planes enclosing much of the detector volume, arranged in layers to improve the efficiency and precision of detection. Toroidal

magnets between the detection layers allow the muon momentum to be measured, and give additional background excluding power. Instead of cylindrical symmetry, the magnets and detection elements form a cuboid surrounding the calorimeter: the general layout of muon components and magnets can be seen in Fig. 3.6.

The dual form of the muon system reflects the two important uses of muons in a collider environment. Firstly, a muon signal is a distinctive indication that the corresponding event may be worth capturing on tape, therefore it is important to be able to pass muon information to the trigger framework. The scintillation counters provide a fast and distinctive muon signal, enabling muon information to be used in all three trigger levels.

Secondly, more detailed muon information, particularly coordinate and momentum measurements, are of high value for data analysis. The muon tracking system, comprising proportional drift tubes in the central region, and mini drift tubes in the forward region, provides a confirmation of the scintillator signal, complemented by the required coordinate measurements from which momentum can be determined. In turn, this enables muons to be associated with tracks from the SMT and CFT system, giving a much more precise elucidation of momentum, as well as the ability to locate muon production vertices. In the analysis presented in the following chapters, muons from $J/\psi \rightarrow \mu\mu$ decays form the first part of event selection: collecting a large, pure sample of muons, with well known momenta and trajectories, is essential in reconstructing excited B mesons. As such, the muon system is here described in some depth.

The vast majority of charged particles from the $p\bar{p}$ interaction which reach the muon system will be muons: other electromagnetic and hadronic particles will be captured within the calorimeter volume. Backgrounds corresponding to particles which do not originate in the interaction region are suppressed by shielding and timing information from the scintillation counters, as described below. In consequence, the purity of the muon sample is very high: for example, the output from level two triggers using the scintillation counters alone is around 80% pure [55].

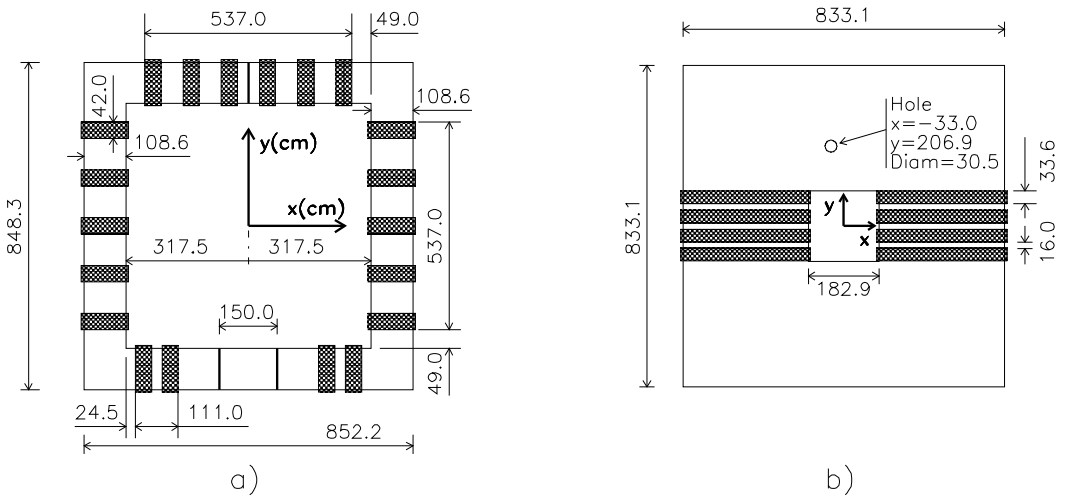

Figure 3.15: End view of the central (left) and end (right) toroid magnets in the muon system, showing (x, y) dimensions and coil windings. The CF extends over $|z| <\sim 379$ cm, with the EF magnets at $454 < |z| < 610$ cm.

Magnets and Shielding

The magnetic field in the muon system is provided by a central toroid (CF), surrounding the calorimeter by four planes parallel to the beam; and two end toroids (EFs), each forming a single (x, y) plane. The positions relative to the other detector components can be seen in Fig. 3.6, with the magnets shown in detail in Fig. 3.15. All toroids use steel yokes, which collectively make up 65% of the total 5500 ton mass of the detector. The CF is wound with twenty coils of ten turns, and each EF with eight coils of eight turns: all coils are connected in series with an operating current of 1500 A, to induce internal fields of around 1.9 T. The magnetic field within the torroid enclosure is complicated by the external fields from the superconducting solenoid; computer simulation is combined with measurements to construct a field map, for use by muon reconstruction and tracking software. There is a small aperture in each of the end torroids, thorugh which the old Main Ring beam (which shared the Tevatron tunnel) used to pass in Run I: the addition of the Main Injector for Run II allowed the Main Ring synchrotron to be removed.

The fields for both toroid and solenoid magnets is regularly reversed, to collect approximately equal amounts of data in each of the four possible polarity configurations. This process significantly reduces any systematic effects from magnet polarity; in addition, it allows certain charge asymmetry measurements to be made, which specifically require this facility (for a recent example, see Ref. [56]).

The experience of the Run I detector era showed significant backgrounds in the muon system, which were not associated with production at the $p\bar{p}$ interaction. These were identified as arising from two main sources: stray particles from the proton and antiproton beams, deflected into the D0 collision hall following interaction with accelerator material; and remnants from the $p\bar{p}$ collision deflecting off the beampipe and forward calorimeters. Background from the first source was significantly reduced by adding 2 m thick concrete walls to the ends of the collision hall, and by improving the halo removal scraper in the accelerator. Background from forward calorimeter deflection was reduced by encasing the forward regions of the beampipe in thick shielding. This is formed from square tubes extending from the ends of the calorimeter to the wall of the collision hall. The tubes consist of three materials: the innermost is steel (with wall thickness 51 cm), which absorbs EM and hadronic showers; this is surrounded by 15 cm of polyethylene to stop neutrons; the outer layer is 5 cm thick lead, which absorbs the photons produced by neutron capture in the polyethylene. Collectively, the shielding, concrete walls and new scrapers reduce background hits by a factor of 40–100 [55].

Muon Tracking System

An exploded view of the muon tracking system is shown in Fig. 3.16. The central system covers $|\eta| \lesssim 1.0$, where the tracking detector dominates the precision of momentum determination. The forward systems cover $1 \lesssim |\eta| \lesssim 2$, and are of greater importance in measuring muon momenta, since the central tracker is less effective for particles produced at narrow polar angles. Both central and forward muon systems consist of three layers of detection components, labelled A–C, with layer A placed within the toroid magnets, and layers B and C outside. The outer layers are separated by $\sim$1 m, to improve the precision of the extrapolated muon trajectory. In the central region, the detectors are proportional

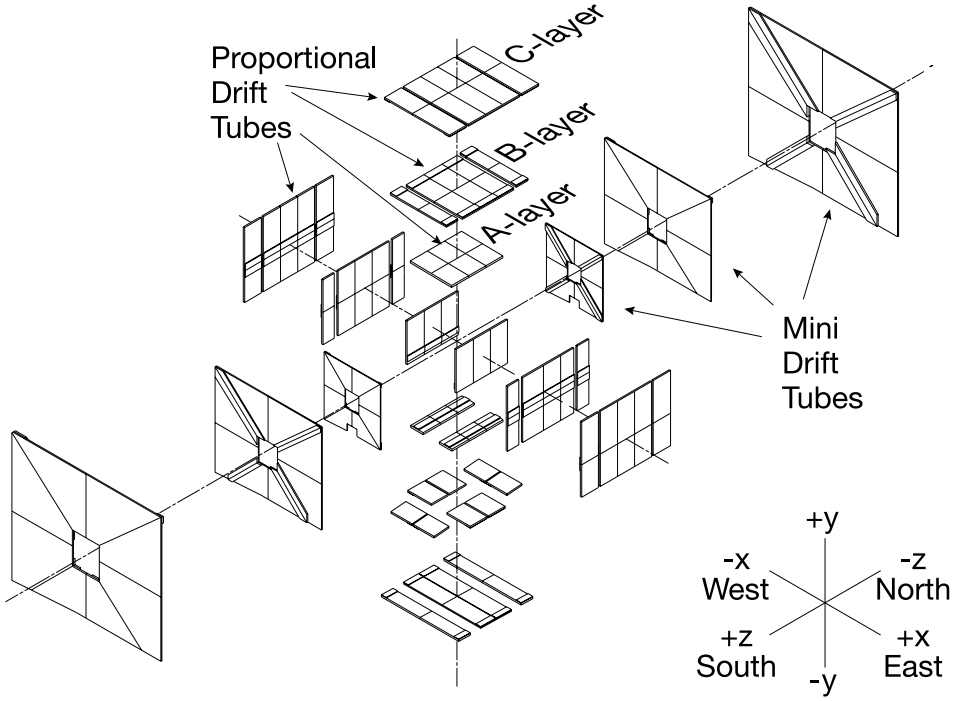

Figure 3.16: Exploded isometric view of the muon tracking system at D0. Shown are the three layers of PDTs in the central region, and the three layers of MDTs in the forward regions, as described in the text.

drift tubes (PDTs); in the forward region, mini drift tubes (MDTs); both of these are described below.

a) Proportional Drift Tubes

The fundamental detection element (cell) of the PDT system is a rectangular aluminium tube, with a square cross-section of width 10.1 cm, and a typical length of 5.6 m. A 50 μm gold-plated tungsten anode wire is stretched down the long axis of the tube, equidistant from all four rectangular sides, and maintained at a voltage of 4.7 kV. Cathode pads are inserted in the upper and lower internal surfaces, and operate at 2.3 kV. The cell cross-section and the resulting electric field in the tube are shown in Fig. 3.17. The precision with which the wires are located at the end surfaces of the tube is ± 130 μm, with a characteristic gravitational sag of 0.6 mm over the wire length. The tubes are filled with a

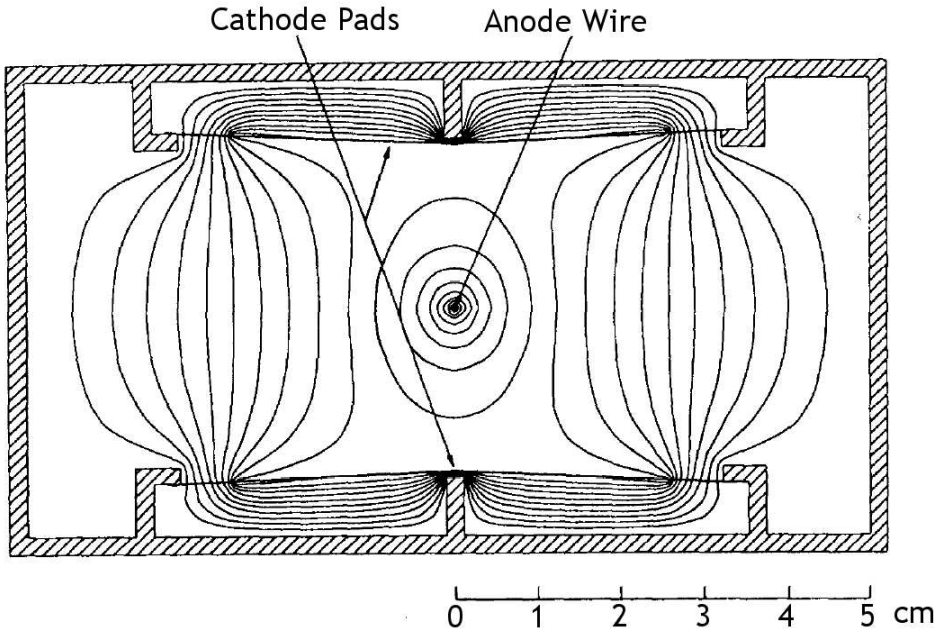

Figure 3.17: Cross-section of a single muon PDT cell, showing the electrical field induced by the anode wire and the four cathode pads.

mixture of argon gas (84%), methane (8%) and CF_4 (8%). A muon passing though a tube causes ionisation, with the resulting electrons drifting toward the detection surfaces over a maximum time of $\sim$450 ns. Signals from the anode and cathode are then extracted at one end of the tube, and transported to the read-out electronics.

Coordinate information is collected in the form of several variables, for use in subsequent event reconstruction. The electron drift time is measured, and corresponds to a spatial resolution of around 1 mm in the cross-sectional plane, including an uncertainty contribution of 0.4 mm from electron diffusion in the gas. In addition, the time difference ΔT between signals at the tube ends from two adjacent cells is recorded, and used to determine the coordinate along the wire direction (ξ) with a resolution of 10–50 cm. This variation in precision arises from uncertainties introduced as the signals traverse the connection wires to reach the read-out electronics: a longer signal path length yields a coarser resolution. For tubes in the A layer, the ξ coordinate measurement is improved by using signals from the cathode pads. These form a repeating pattern of zig-zag tracks

along their surfaces, resulting in a characteristic relation between electron drift time and ξ position. Combined with drift time information from the anode, and an approximate longitudinal position from the ΔT value, the ξ-coordinate can be measured to within ± 3 mm. This facility is generally not present in the outer two layers of PDTs, mainly due to cost, but also motivated by the reduced benefit for muons with hits in multiple layers. A few B and C layer tubes are instrumented for cathode pad use, since they are useful to monitor the electron gain, and therefore the PDT performance, over the passage of time.

The PDT cells are length-ways abutted into decks, typically 24 tubes wide. In layers B–C, and in the bottom plane of layer A, three decks are stacked on top of each other to form a full 'drift chamber' of 72 tubes. For the top and side layer A planes, four decks form a single chamber of 96 cells. Ninety-six of these drift chambers (totalling 6624 read-out channels) are then arranged into the planes shown in Fig. 3.16, resulting in full three-layer coverage for around 55% of the central region, and 90% coverage with at least two layers. Most of the excluded areas correspond to the bottom planes, due to obstruction from structural supports. The gas mixture within the drift chambers is circulated and filtered to remove contaminants from the electrodes, with the full volume of around 100 m^3 circulating once every $\sim$8 hours.

b) Mini Drift Tubes

The repeating element in the MDT system is a rectangular stainless-steel drift tube, with a cross-section of 80×10 mm^2 and a typical length of 1–5 m. This tube is compartmentalised length-ways into eight individual 9.4×9.4 mm^2 drift cells by an aluminium 'comb', with a grounded anode wire running down the centre of each, as shown in Fig. 3.18. The aluminium comb (0.6 mm thick) and steel housing (0.15 mm thick) collectively comprise the cathode, operated at -3.2 kV, which is insulated by a 1 mm thick PVC envelope. The anodes are identical with those in the PDTs, and are located by plastic end-caps (which also provide an airtight seal) and at least one spacer per metre of wire length. The tubes are filled with CF_4 (90%) and CH_4 (10%) gas, providing maximum drift time of around 60 ns, and a muon detection efficiency of more than 99%. The overall efficiency of the system is reduced to around 95% by inter-tube gaps and losses to the PVC cladding and

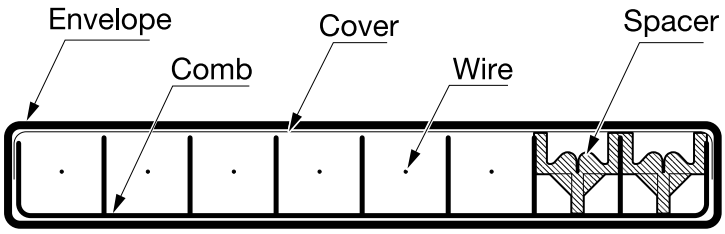

Figure 3.18: Cross-section of a single muon MDT element, showing the eight individual drift cells as described in the text.

end-caps. The electron drift time from the anodes is measured as the time difference between the bunch crossing and the signal reception, and read out with a digitised time bin of $\sim$19 ns, limiting the spatial resolution to around 0.8 mm.

The MDT system is constructed by combining individual cells into octant planes, as shown in Fig. 3.16. Each octant in layer A (B, C) houses four (three) stacked decks of tubes, precisely mounted between plastic blades on an aluminium honeycomb, and is fully enclosed by a Faraday cage of aluminium sheeting. An octant deck generally comprises 32–48 individual drift tubes, for a total of 6080 tubes, or 48,640 channels, in the entire forward muon detector. The 18 m^3 of MDT gas is circulated and filtered at a rate of 0.5 system volumes per day.

Scintillation Counters

The muon tracking system relies on correctly associating muon signals with a specific bunch crossing, in order to determine the electron drift time. For Run II accelerator operating conditions, with a time between bunch crossings of 396 ns, scintillation counters are required to fulfill this role. In addition, these counters are used to reject cosmic ray signals, by examining the time ordering of signals as particles traverse the detector. Based on these uses, the performance requirements are: a fast signal read-out and fine time resolution (of order $\sim$10 ns); and a high detection efficiency. The spatial resolution need only be fine enough to unambiguously associate a muon signal to the appropriate PMT or MDT.

The layout of the scintillation system is shown by an exploded view in Fig. 3.19. The

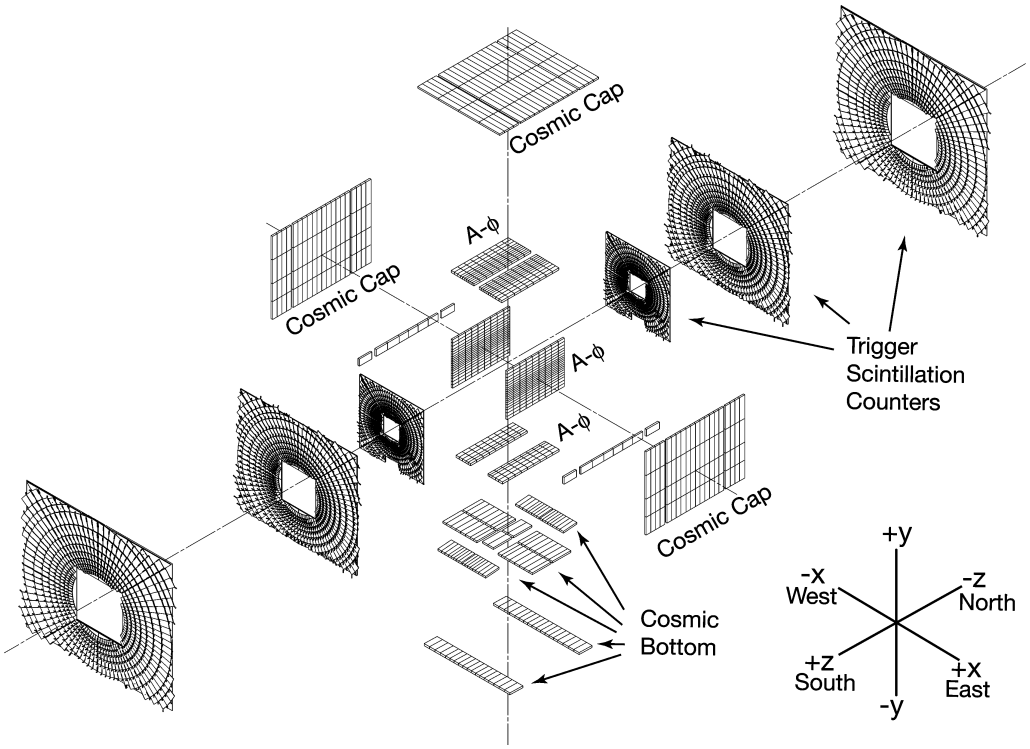

Figure 3.19: Exploded isometric view of the muon scintillation counters. Shown are the two layers (cosmic and A-ϕ) of counters in the central region, and the three layers of pixel counters in the forward regions, as described in the text.

central region ($|\eta| \lesssim 1$) consists of two layers of counters: the cosmic layer surrounding the outermost PDTs (named for its original use when installed in the later part of Run I); and the A-ϕ counters inside the central toroid. In the forward region ($1 \lesssim |\eta| \lesssim 2$), the scintillating system comprises three layers of 'pixel' counters. The following sections detail the design and arrangement of these three counter types.

a) Cosmic Counters

Cosmic counters are attached to the outside of the layer C PDTs, forming three large planes on the top and (z, y) sides of the detector (the 'cosmic cap'), and several smaller planes placed on the underside to negotiate the structural elements. The cosmic cap [57] was installed late in Run I, with additional counters installed in the shutdown prior to Run II [35, 55]. The counters from different locations operate on the same principles, with

some slight design differences which will not be examined in detail.

The cosmic cap consists of 240 individual counters, each of which is a plane of Bicron 404A scintillator: 12.7 mm thick, 62.5 cm wide (i.e. slightly wider than six PDT cells) and around 204–282 cm long (i.e. slightly more than half a PDT length). These dimensions are chosen so that a plane of 4×2 counters will cover a single PDT chamber, with a slight overlap to minimise dead regions. Muons passing through the Bicron will excite the material to produce photons, which are then captured by wavelength shifting fibres (1 mm diameter) running parallel to the long edge of the counter. Fibres from each end of the counter run to the middle and are connected to one of two photomultiplier tubes (PMTs) which convert the photons into an electrical signal. Each counter thus has two signal channels, read out in a 50–100 ns time window (depending on the position of the counter) corresponding to the expected arrival time of high momentum muons from a bunch crossing. A counter 'fires' when the electrical output from a PMT exceeds a certain voltage threshold in a single read-out period; both channels must fire simultaneously in order to activate the level one trigger. Four fibres are placed together in machined grooves (4 mm wide, 1.75 mm deep) with 4 mm separation, covering half of the surface: two fibres from a groove are connected to each PMT. The edges of the scintillator are polished and covered in aluminium to contain photons and increase the light yield; the upper and lower surfaces are covered in 0.5 mm aluminium sheeting for optical isolation, with a hole cut in the top sheet for fibre access. The total efficiency of the cosmic cap counters is estimated as exceeding 99% [57], with typical light yields of 18–30 photons per PMT [35].

The additional 132 cosmic counters (the so-called 'cosmic bottom') installed for Run II cover a smaller area than those in the cosmic cap (around 40×200 cm^2), but are otherwise very similar in construction. They are arranged in several planes to give the broadest coverage possible considering the substantial obstruction of the detector supports. The long sides of the counters are parallel to the z-axis, such that each one subtends around 4.5° in ϕ —corresponding to a single CFT trigger sector. Of the cosmic-bottom counters, 68 have the fibres arranged in vertical grooves (i.e. the wires are stacked vertically, instead of running side-by-side), which are separated by 6-10 cm: the light yield and efficiency of these scintillators is comparable with the horizontal-fibre counters.

b) A-ϕ Counters

The A-ϕ counters line the inner surfaces of the layer A PDTs, inside the toroid magnet. The construction and material is similar to the cosmic counters: a 12.7 mm thick Bicron scintillation plane, with WLS fibres running length-ways from either end to the centre, for collection in a single PMT. In this case the grooves are vertical, each housing six 1 mm diameter fibres, with $\sim$4.5 cm between grooves.

Each counter is 84.5 cm long, such that each quadrant plane of the PDT system is fully covered by nine end-to-end barrels of A-ϕ counters, separated by 10 mm gaps. A single barrel comprises twenty counters per quadrant, with three different widths used ($\sim$36 cm, $\sim$27 cm and $\sim$23 cm) to maintain a ϕ coverage of $\sim 4.5^\circ$ per counter, as illustrated in Fig. 3.20. The counters overlap by around 3% of their ϕ width to maximise detection efficiency. The bottom plane is interrupted by the calorimeter support, giving partial coverage with only ten counters per barrel: in total there are 630 counters in the full A-ϕ system.

The photo multiplier tubes are shielded from the strong magnetic fields by a cylinder of 6 mm thick lead and 1.2 mm thick μ-metal (a nickel-iron alloy with very high magnetic permeability). The light yield for a muon is around 18 photons, and the time resolution of a single counter is around 0.8 ns, corresponding to a total system resolution of 2.5 ns. The time window for muons from bunch crossings is 24 ns wide, allowing direct use of A-ϕ information by the level 1 trigger, as described at the end of the following section.

c) Pixel Counters

The scintillation system in each forward region comprises three layers of pixel counters: layer A is mounted on the internal (low $|z|$) surface of the end toroid; layer B is mounted on the outer surface of the toroid; layer C is mounted on a dedicated steel structure close to the end of the collision hall. The layers are formed by 'fish scale' interleaving of individual trapezoidal cells, as shown in Fig. 3.21 for one of the 12×10 m^2 C layers. The counters are arranged in $\sim$10–12 concentric circles per layer, giving 4214 units in the entire six layer system.

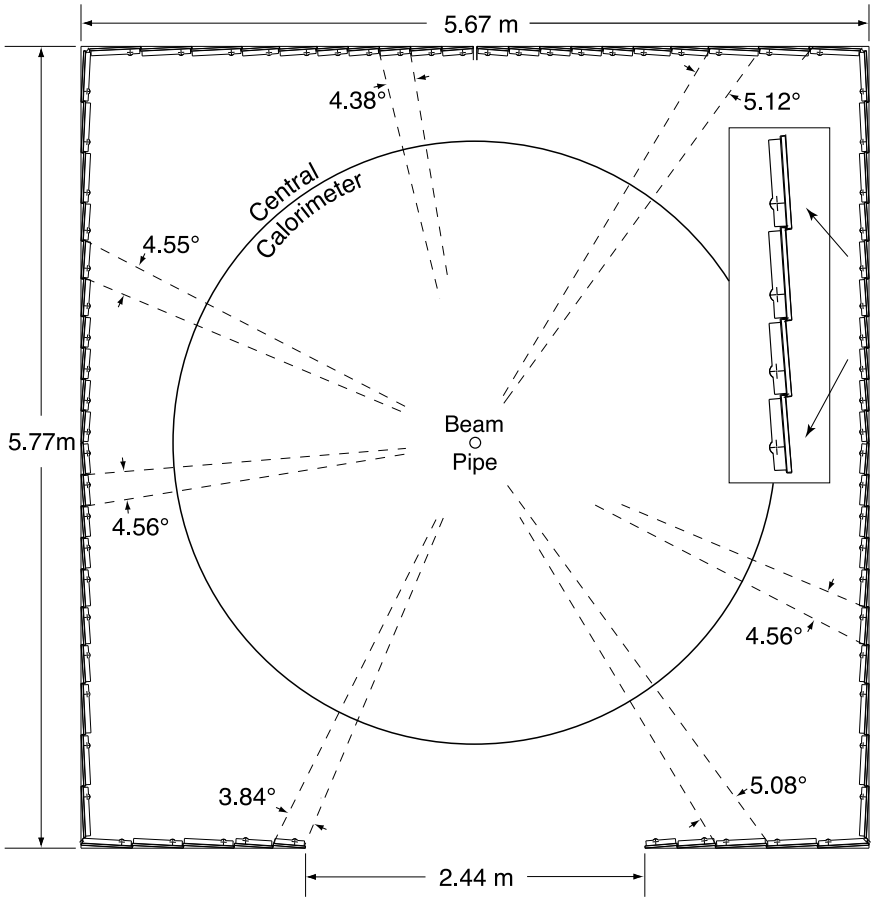

Figure 3.20: End view of the muon A-ϕ counters in a single barrel, with a close-up of the counter arrangement inset. The coverage in ϕ is shown for counters in seven different locations.

The size of individual counters varies by location, in order to maintain a ϕ resolution of 4.5° (to match the CFT trigger design), with the η segmentation varying from 0.07 to 0.12. The smallest counters have an area of 9×14 cm^2, with the largest being 60×110 cm^2. A typical counter design is shown in Fig. 3.22: the active material is a trapezium shaped plane of 12.7 mm thick Bicron scintillator, with the broad edge and one of the side edges terminated by a wavelength shifting bar, 4.2 mm across and 12.7 mm thick. At the corner where these WLS bars meet, they are bent by $\sim45^\circ$ to guide the signal photons into a photomultiplier tube; their other ends are terminated by aluminium tape to improve reflectivity. The scintillator and WLS bars are covered in light-tight material, and mounted

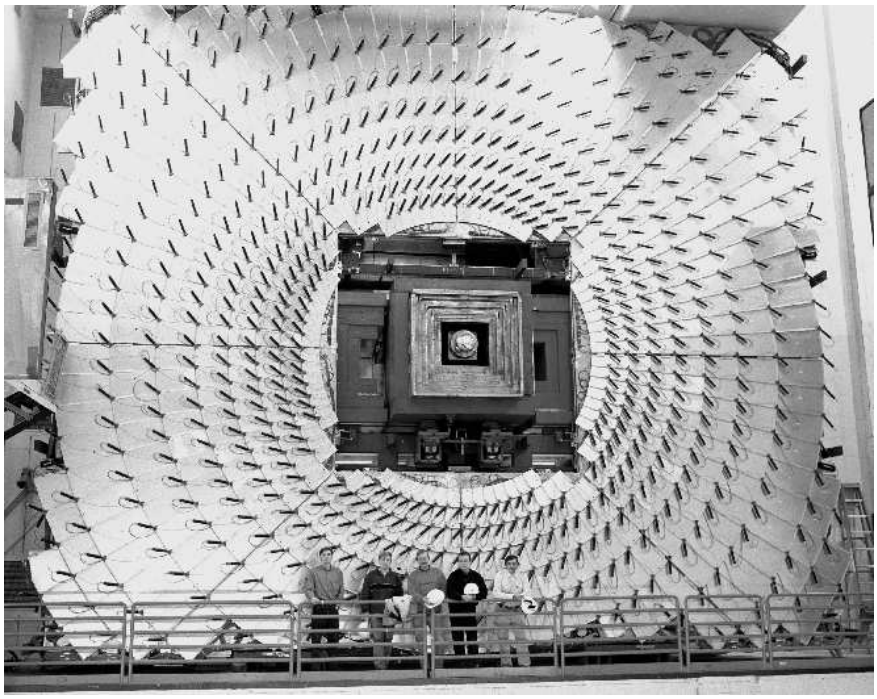

Figure 3.21: Photograph of one C-layer of pixel scintillation counters, showing the fish scale interleaving of counters. The shielding around the beampipe can also be seen.

in an aluminium box. The photo-tubes are magnetically insulated in a similar manner to the A-ϕ counter PMTs, and typically receive 70–240 photons per muon interaction, with yields decreasing for the larger counters due to attenuation in the scintillating material and the WLS bars. For 150 of the smaller counters, twelve 1 mm diameter WLS fibres are used to coat the Bicram edges, instead of the thicker WLS bar; in this way the available detection area is maximised. For these counters, light yield is measured to be 60–110 photons per particle.

Following installation, the performance of different sized pixel counters was tested: peak efficiency was found to be $> 99.9\%$, with time resolutions of 0.5–1.0 ns. The collective time resolution for all counters combined is 2.2 ns, much smaller than the acceptance window of 30 ns in which muons from bunch crossings are detected. Reliability is excellent, with generally only 1–3 counters inactive during most physics runs, and consistent signal timing over several years of running.

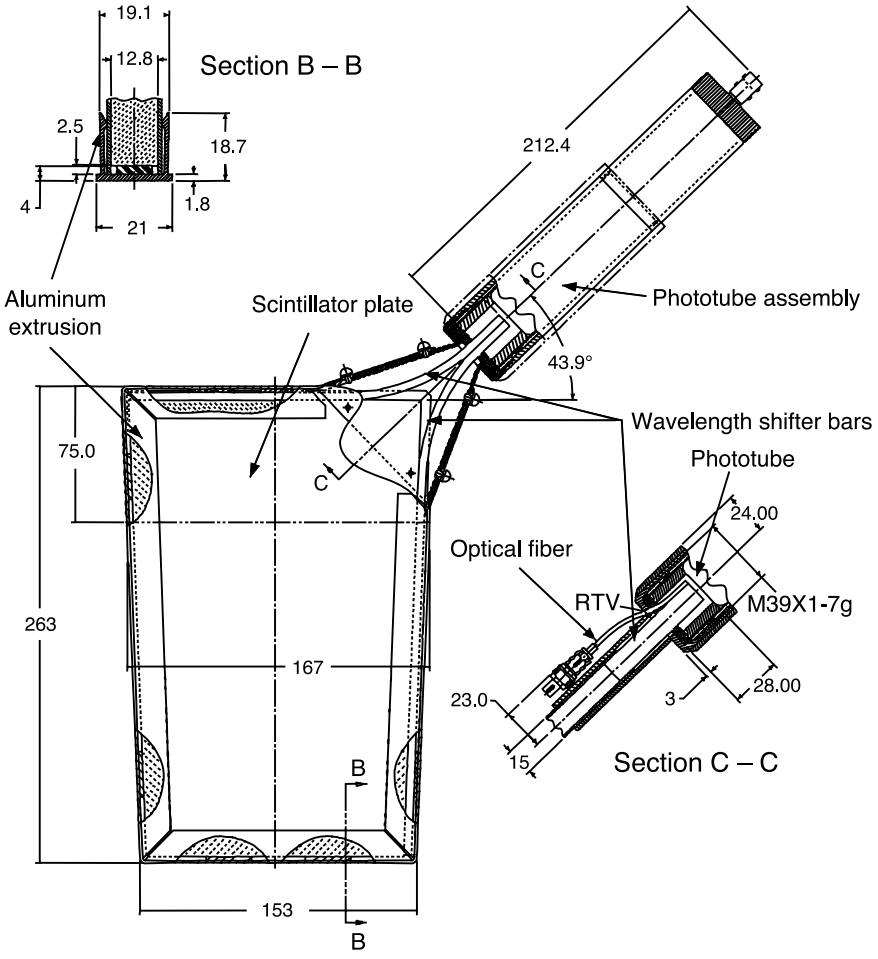

Figure 3.22: Structure of a typical pixel counter (dimensions in mm).

Signals from A-ϕ and pixel counters are treated similarly by the read-out electronics. The output from a PMT, collected in each timing window, is first tested by an amplitude discriminator with a variable voltage threshold. Signals above this threshold are then passed to the level one trigger to provide a fast and relatively pure indication of muon presence (around 50% of all such signals are reconstructed as muons in the full offline algorithm). Amplitude and timing information is then sent to level two triggers for finer discrimination (with purity $\sim$80%), and to the data acquisition system for storage.

3.2.6 Luminosity Monitor

Although the luminosity monitor is not used directly in the analysis described in later chapters, it is an important component of the detector, enabling the luminosity (both instantaneous and integrated) to be measured and tracked over the course of data collection. For some physics measurements, such as determining the cross-section for a particular process, a precise calculation of the luminosity is essential. Even if this is not the case, the integrated luminosity of a data set is a quantitative measure allowing comparisons between different studies and experiments to be made; the future event yield, and therefore precision, for a particular study at D0 can also be extrapolated as a function of the (increasing) volume of data.

The purpose of the luminosity monitor (LM) is to determine the average number of inelastic collisions per bunch crossing, $\hat{N}_{LM}$, from which the Tevatron luminosity at D0 can be determined. Multiple collisions usually occur in a single bunch crossing (i.e. $\hat{N}_{LM} > 1$), which can be difficult to distinguish from each other. To remove this complication, the fraction of crossings with *no* inelastic collisions is counted, from which $\hat{N}_{LM}$ is extracted under assumption of Poisson statistics. The luminosity is then calculated by the relation

$$\mathcal{L} = \frac{f\hat{N}_{LM}}{\sigma_{NL}}, \tag{3.4}$$

where f is the bunch crossing frequency and σ_{NL} is the effective inelastic cross section for the LM. The detector consists of two circular planes of 24 scintillating wedges, located at $z = \pm 140$ cm in the narrow angle range $2.7 < |\eta| < 4.4$. Photons produced in each wedge are collected and sent to PMTs to produce an electrical signal, which is amplified and passed to the electronic read-out system for identification of $p\bar{p}$ collisions.

Precise luminosity determination requires the removal of background events from the beam halo. This is done by examining timing information, and relies on the 0.3 ns time resolution of the LM detector. Each event detected by both planes of the LM is assumed to be from a $p\bar{p}$ interaction; the z position of the hypothetical collision (z_v) is determined from the time difference between hits in the north and south LM planes, via the relation

$z_v = \frac{c}{2}(t_N - t_S)$. Here $t_{N(S)}$ is the time of flight between the bunch crossing and detection by the north (south) LM plane, with the particles travelling at close to the speed of light, c. Events from colliding beam interactions are selected by requiring $|z_v| < 100$ cm, which is large enough to capture almost all signal events (the collision region is limited to $\sigma_z \approx 30$ cm, as described in Section 3.1.2).

3.3 Triggering and Data Acquisition (DAQ)

Some of the basic principles of triggering have already been introduced in the previous section: the detector is exposed to a far greater rate of $p\bar{p}$ interactions than it can ever capture to data storage media. The average bunch crossing frequency is ∼1.7 MHz, with multiple interactions per crossing taking the event rate up to 5 MHz; in contrast, the maximum rate of the full detector read-out system is around 100 Hz. Therefore only approximately one out of every hundred thousand interactions can be collected and stored for use in analysis. Finding the most useful 0.001% of events is the task of the trigger system, which works in three distinctive levels (L1–L3), with the rate of surviving events being reduced after each level, allowing the complexity of succeeding triggers to be increased.

Event information from the detector is arranged in a number of 'data blocks' (of 1–20kB in size), corresponding to different detector sub-systems and geographical sectors. Each block is sent to a single read-out 'crate' containing the microprocessor boards required for level one and two triggering; additional crates house dedicated triggering electronics. There are sixty-three crates in total located in a moveable counting house (MCH) which can be moved on tracks to maintain contact with the detector if the latter is ever removed from the collision hall (e.g. for major upgrades). An entire event is therefore divided over several dozen different processing crates, and only unified for level three triggering and storage. Each crate is synchronised with the 53.1047 MHz 'tic rate' (the RF-bucket crossing frequency) of the Tevatron, to ensure that the different parts of an event are correctly matched for subsequent recombination.

The level one (L1) trigger comprises various hardware tests from the fastest detection components. It examines all events, with a maximum output rate of ∼2 kHz. The level

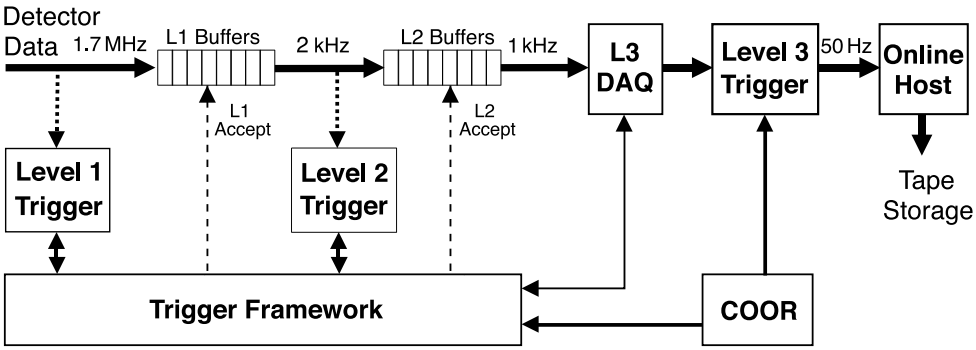

Figure 3.23: Data flow diagram for the trigger and DAQ system, as described in the text.

two (L2) trigger tests events selected by L1, using both hardware and firmware from in-built microprocessors in each crate. This allows more complex physics 'objects' to be examined following partial reconstruction (for example, track finding algorithms); in addition, the consistency of signals over separate components is tested (e.g. associating muon hits to central tracks). The maximum output rate from the L2 system is $\sim$1 kHz, corresponding to the limited input rate of the level three (L3) trigger. This final stage is a fully programmable software trigger, operated on a 'farm' of microprocessors, and performing a full reconstruction of electrons, muons, charged hadrons, particle jets and missing energy within a single complete event. Important properties such as invariant mass or angular isolation are determined and used to reduce the final rate of selected events to 50–100 Hz: these are then stored by a robotic tape system in the Fermilab computing facility, about 3 km from the detector. The flow of data can be seen in Fig. 3.23.

Loss-less data flow is maintained through first-in-first-out (FIFO) buffers, which hold successive events as those ahead of them are tested by each trigger. The system is flexible enough to operate successfully under a wide range of luminosities, since each trigger can be 'prescaled' to adjust the fraction of events it selects: in low luminosity running, pass requirements can be loosened, and additional triggers added. The level 3 data acquisition system (L3DAQ) controls the flow of data from the read-out crates to the L3 farm where each complete event is examined by a single processor. The online host receives the events

from the farm for storage and distribution to real time monitoring and logging programs. Overall control of the various triggering systems and data acquisition is performed by the central coordination program (COOR): for example, setting the appropriate list of individual triggers used for a particular run.

Since the L1 and L2 trigger systems operate on small parts of events, corresponding to a particular sector of one detector sub-system, the event testing is undertaken by a number of individual triggers, as shown in Fig 3.24. Each of these searches for a number of different event signatures, called 'trigger terms' —for example, at least one track with a transverse momentum exceeding 2.5 GeV/c. These terms are then combined into trigger bits, each of which tests a number of term conditions to produce a Boolean output. The trigger framework (TFW) gathers the bits from each individual trigger, and logically combines them to decide whether or not the event should be retained at the next level; in total it can receive up to 128 trigger bits. It is also used to prescale certain triggers to control the event accept rate. At this point it should be mentioned that the event selection described in Chapter 4 makes no specific trigger requirements: events from all triggers are used. However, the nature of the analysis means that most selected events will satisfy single-muon triggers, with another significant contribution from displaced-vertex triggers using tracking information. As such, the emphasis in the following description is on muon and tracking triggers, with the other triggers mentioned for completion.

3.3.1 Level One Triggers

As shown in Fig. 3.24, there are four separate trigger types forming the L1 system. The central tracking trigger (L1CTT) combines data from the central and forward pre-shower (CPS, FPS) detectors and the CFT system to search for tracks exceeding certain transverse momentum thresholds. The muon trigger (L1MUO) uses data from the scintillation counters to perform the same task for muons, and can be combined with the L1CTT in a simple track matching scheme. These are both discussed in more detail below. The other triggers are: the calorimeter trigger (L1CAL), which passes events which satisfy certain energy deposition requirements; and the forward proton detector trigger (L1FPD), which

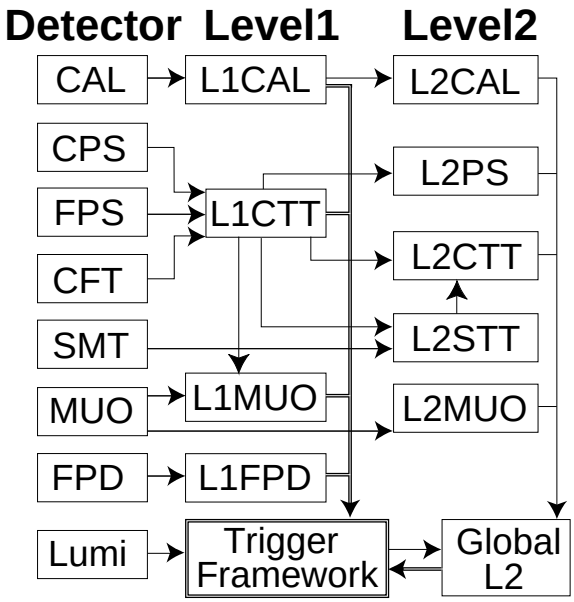

Figure 3.24: Data flow diagram for the L1 and L2 trigger system. The individual triggers are described in the text.

selects events with protons or antiprotons scattered at very small angles to the beampipe. The trigger framework selects events to pass to level two based on a set of trigger terms.

Level One Central Track Trigger (L1CTT)

The read-out from the central fiber and pre-shower systems in a 132 ns window is sent to the L1CTT [58, 59] for testing. Triggering in the central region uses the axial CFT and CPS layers to search for tracks with $p_T > 1.5$ GeV/c. Additional information is collected regarding 'clusters' (mini showers of particles detected in the CPS detectors), track-cluster matching, track-muon association, and CFT occupancy: these data are passed for use in L1MUO, L2SMT, L2CTT and L2PS triggers. The algorithm for track finding is complex [35], but the starting point is a search for tracks which have hits in all eight axial CFT doublet-layers, within a single 4.5° azimuthal wedge (see Fig. 3.25). The six surviving tracks with the highest p_T in each wedge (i.e. up to 480 tracks) are called 'track seeds', and are sent to the L1MUO (see next section), and to processing boards for additional L1CTT testing. Information from all wedges is then combined, with additional

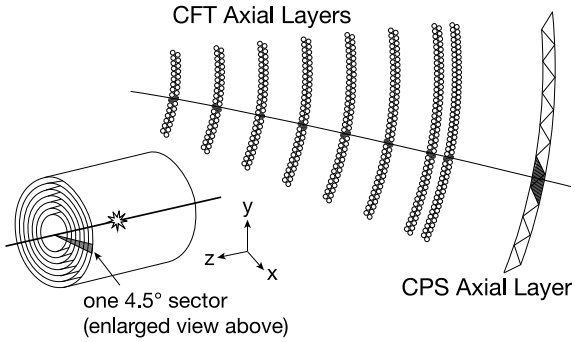

Figure 3.25: Detection components used in the L1CTT axial trigger. The six highest p_T tracks with hits in all eight axial CFT doublet layers form the track seeds, for use in later processing.

discrimination, producing a set of around 60 trigger terms sent to the TFW, one example of which is: at least one track with $p_T > 5$ GeV/c, with a confirming hit/cluster in the CPS.

The FPS detector provides the TFW with another set of trigger terms, based on clusters of hits in the four scintillation planes. The stereo layers of the CPS also store hit information, but this is not used until level two and later.

Level One Muon Trigger (L1MUO)

The L1MUO trigger uses data from the wire chambers, scintillation counters and tracks from L1CTT, to search for signals consistent with a muon event [60]. Logical testing of outputs from ∼60,000 muon channels is combined with the track seeds from L1CTT, within detector sectors corresponding to octants in the central, north or south muon detectors. Again, the details are complex, but the main principle is testing for signal consistency as a muon candidate traverses the detector volume. One algorithm tests scintillator hits for consistency with the central track seeds. A second algorithm matches scintillator hits to track 'stubs' (or 'centroids') reconstructed from hits in each layer of drift chambers. Different trigger purities are provided by requiring hit association in more or fewer layers, passing a total of up to 32 trigger terms to the TFW.

3.3.2 Level Two Triggers

The L2 trigger comprises five detector sub-systems, in addition to a global filter (L2Global) which combines signals from the L1 trigger terms, with additional discrimination, to produce composite physics objects including information from several detector components. These objects can then be tested to select events for L3 at the maximum accept rate of 1 kHz. Data from the calorimeter, tracker and muon system, and signals from the TFW, are sent to dedicated L2 crates for processing.

The L2CAL uses shower pattern finding algorithms to identify photon, electrons and hadronic jets, and measure the missing transverse energy ($\not\!\!E_T$) associated with neutrinos. The level two pre-shower (L2PS) trigger finds clusters with good spatial resolution, which can then be matched to calorimeter objects for improved electron-photon separation, background rejection and detection efficiency. At level two, the FPS detector provides the only tracking information in the forward region.

The L2MUO trigger takes the muon candidates from L1MUO, and improves the selection using additional timing, tracking and calibration data. The level two tracking triggers (L2STT and L2CTT) are discussed in more detail below. The global trigger combines information from all L2 sub-systems to make accept decisions from higher level testing of objects. For example, one L2 trigger bit might require a calorimeter tower with transverse energy $E_T > 3$ GeV, matched to a central track with $p_T > 5$ GeV/c.

Level Two Silicon Tracking Trigger (L2STT)

At level two, the SMT information is used to improve the selection and measurement of tracks from L1CTT. Apart from giving an independent set of hits, which can remove fake tracks wrongly reconstructed by the L1CTT, it also provides a higher momentum resolution, and allows the track impact parameter to be measured. Here, the impact parameter (IP) is the distance-of-closest-approach in (r, ϕ) of an extrapolated track with respect to the beam. If this is significantly greater than zero, it indicates the presence of a long lived particle which travelled far from the primary vertex, before decaying to produce the track particle. This is a strong signature of a B meson event, therefore this ‘displaced secondary

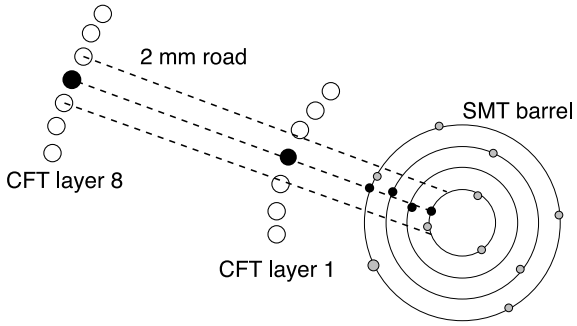

Figure 3.26: Track finding by the L2 silicon tracking trigger (L2STT). At least three hits in the axial SMT ladders must be associated with each track from L1CTT; the track parameters are then recalculated without the CFT hits in layers 2–7.

vertex' trigger is valuable in B physics analyses.

The starting point for event testing by L2SMT is the set of tracks from L1CTT. For each one, the tracking algorithm searches for SMT axial ladder hits within an extrapolated ϕ 'road', 2 mm wide, as shown in Fig. 3.26. If hits from at least three of the four SMT layers can be associated with a L1CTT track, the track parameters are recalculated using the SMT hits plus hits from the inner and outer CFT layers. The associated impact parameter is divided by its uncertainty to form a significance measure, which is used to produce trigger terms; this uncertainty is around 50 μm for low p_T particles, reducing to 20 μm for $p_T > 5$ GeV/c. The resulting track parameters, the χ^2 of the fit, and pre-shower cluster information from L1CTT are then passed to L2CTT.

Level Two Central Tracking Trigger (L2CTT)

The L2CTT takes tracks from L1CTT and performs additional measurements to provide more detailed information to L2Global. The azimuthal angle of tracks at the beam-line (ϕ_0) and at the third layer of the EM calorimeter (ϕ_{em3}) is recorded, and the tracks are tested for several isolation criteria. A p_T-ordered track list is then sent to the global trigger. Tracks from L2STT are processed similarly, except the isolation is measured without being tested; both p_T-ordered and IP significance-ordered lists are sent to L2Global.

3.3.3 Level Three Triggers

The L3 trigger is a high level software facility providing multiple tools for reconstructing physics objects [61]. All data blocks from a single event are collected, fully digitized, and sent to one of several hundred computers in the L3 farm. Here the trigger bits from L1 and L2 are passed through a series of additional filters, each one searching for one or more higher level criteria, such as a minimum invariant mass, or a certain confidence that a calorimeter object is an electron. The filters used, and the particular threshold values of these filters, are set by the L3 trigger list; this is chosen based on the current areas of interest in particle physics, so that a wide range of different events pass the L3 trigger to be written to tape. The L3 trigger takes events from L2 at 1 kHz, and passes final selected events to be stored at 50–100 Hz. The reconstruction proceeds by object-specific algorithms, called tools; the most relevant of which for this analysis are discussed below.

Level Three Muon Tool

The sample of muon candidates from L2 is improved by a number of cross checks, including the use of tracking and calorimeter data. The timing of scintillator hits along a muon track is used to distinguish prompt (from $p\bar{p}$ interaction) and out-of-time (background) hits; cosmic ray events are similarly excluded. Tracking software combines hits from multiple layers to produce a three dimensional track: thresholds are set on the number of hits required in each layer to define a valid muon. The tracks from 'local muons' (those associated only with hits in the muon system) are extrapolated to the central tracker, and where possible associated with a single central track under some best-fit prescription. The resulting 'global muons' have more precise momenta, and can be associated with specific production vertices. The presence of minimum ionising particle (MIP) trails in the calorimeter provides additional data regarding muon trajectories and isolation.

Level Three Tracking Tools

Tracks in the central detector are reconstructed using a number of different methods, each having certain advantages. One particular type of tracking algorithm (an 'outside-in' 'link-and-tree' method) is described below. Track fitting is also used at level three to determine the position of the initial $p\bar{p}$ interaction, which can be combined with the individual track information to trigger on displaced secondary vertices, in an extension of the level two test. The z vertex of an event can also be measured from either CFT or SMT hits, with the former favoured due to the higher resulting purity and efficiency; the resolution of this measurement is around 0.5 mm [35].

For the level three trigger, and for all offline track reconstruction, the read-out information for tracks is dealt with more thoroughly, redefining the concept of a 'hit'. In level one and two, a hit is associated to a given read-out channel if its signal magnitude exceeds a certain voltage (SMT) or light yield (CFT). However, since a charged particle can leave signals in several neighbouring strips (SMT) or fibres (CFT) in an individual detection element, it is important to be able to combine these signals into one measurement for higher level processing. This is done by a process of *clustering* [62], which first associates all adjoining read-out signals which exceed a certain voltage (or light yield) threshold, and then allocates a hit to this cluster, with coordinates given by the magnitude-weighted average of the signal positions. For all subsequent discussion, this average cluster measurement is what is meant by a hit. Computer simulated tracks are used to determine the spatial resolution of hits in a particular element, by plotting the difference between the measured coordinate and the genuine particle position, and fitting to an appropriate function (usually Gaussian in form). The results show that hits are correctly located to within $\sim$10 μm, with no systematic bias in any direction [63].

The CFT-only link-and-tree tool starts from the outermost axial-doublet layer of the CFT, successively linking clusters from adjacent layers to form track candidates, provided that the radius of curvature is consistent at each cluster addition, and exceeds a certain minimum value corresponding to a threshold p_T. At each layer, many possible clusters can be associated with the existing track, leading to a proliferation of possible tracks in

the early stages. However, as the path length increases, the curvature becomes better defined and fewer hits will fulfill the requirements at each layer. Eventually, there will be no way to 'legally' extend any tracks to the next layer (for some tracks this could mean that the innermost layer has been reached), and the process terminates. The longest track produced by this iterative procedure is then retained as a track candidate, and the algorithm continues with the next outer layer cluster. A similar tool builds tracks from SMT hits, but in this case the requirements for track extension are that Δz and $\Delta\phi$ values between layers must be consistent within certain limits. The longest tracks are fitted to a helix, with the best-fit case saved as a track candidate. This type of track fitting and filtering is a lightweight version of the full offline reconstruction methods, which are described in the next chapter.

3.3.4 Monitoring and Storage

All events which pass successfully through the three levels of trigger requirements are transfered to the online host (see Fig. 3.23), which receives data at approximately 10 MB/s corresponding to 50 Hz and 200 kB/event. At this stage, an event is simply a collection of digitized detector signals, called a raw data chunk (RDC). Each event is labelled according to the specific triggers which it passed, which is important in some analyses: for example, care must be taken if using displaced secondary vertex triggers in lifetime measurements, since they automatically bias the sample in favour of longer lived particles. The main task of the online host is to transfer the final data to the robotic tape drives, providing a buffer in case of interruptions or a slow connection. Data is stored using the 'sequential access via metadata' (SAM) system, which controls the transfer of files between different mass storage devices and between different computing systems, providing valuable book-keeping facilities to keep track of data. Each file is associated with a metadata list, which contains file information such as the store and run number, the date and time of transfer to SAM, the trigger list used etc. The metadata information is generated by the online host.

The second major task of the online host is to provide monitoring capabilities, so that data quality can be checked, in near real time, by experts in the control room. Whenever

possible, a copy of each event is sent be distributed to a collection of online analysis and monitoring tools (called EXAMINES). This allows distributions of various important kinematic and topological event properties to be inspected, and compared to expectations; such parameters include E_T, ϕ and η for individual particles, and total multiplicities of electrons, muons, jets, taus and global tracks.

Chapter 4

Event Reconstruction and Selection

At the end of the previous chapter, the collection and storage of raw detector signals was described. From this point onwards, the analysis is continued using custom designed software, which converts the signals from several thousand readout channels into meaningful data. Firstly, the basic signatures of particles are extracted, by allocating channels to their physical detector and location, and using timing information to associate signals in different detector elements to a single particle trajectory. Additional information from signal magnitudes is also used to perform specific detector-dependent measurements. This process of rebuilding the underlying particle behaviour from a snapshot of raw signals is called *reconstruction*, and leads to the concept of 'objects', which are specific particle types or classes (such as muons, electrons, hadron jets, and charged particle tracks) inferred by the reconstruction software. The first part of this chapter describes this software.

A second important process in particle physics analysis is the identification and selection of appropriate particles and events of interest. The interaction of protons and antiprotons is a quantum process, with a wide range of possible outcomes in terms of the number, type and behaviour of the secondary particles produced. The subsequent decays of particles are also purely probabilistic, meaning that a particular combination of particle production and decay will only occur a fraction of the time. As more data is collected, it becomes possible to gather significant samples of rarer events, but the challenge of

separating the few interesting events from the massive background sample requires more ingenious solutions. Massive reductions in background can be made by simple topological or kinematic event requirements, but at some point all criteria will also start to remove signal events, and there is inevitably a pay-off between reducing background and maintaining a large signal sample. The second part of this chapter describes the search for excited B mesons, by iterating over all events in the Run IIa data set, and selecting those which fulfill certain characteristics indicative of the required meson decays. In addition, some variables and methods are introduced which allow the signal to background ratio to be enhanced. The data sample corresponds to a total integrated luminosity of 1.35 fb^{-1}, as collected in Run IIa by the D0 detector during 2002–2006. The data were selected without any explicit trigger requirement, although most events satisfy inclusive single-muon triggers.

4.1 Event Reconstruction

In order to make use of the raw detector data, it must be reconstructed into its constituent physics objects: muons, tracks, jets, electrons and so on; certain parameters of these objects can then be determined, such as charge, momentum, energy and orientation. Up to this point, the reconstruction process transcends any particular study, and so is performed centrally to produce useable data formats for further specialised reconstruction and analysis by individual research groups. The program used to reconstruct physics events is called D0RECO [64], which is used to produce a 'thumbnail' (TMB) file [65], although other file types can also be generated. Raw detector data is distributed offline to be reconstructed by D0RECO, on CPU production farms both on-site at Fermilab and on location around the world. Reconstruction is a multiple-stage process, as summarised below.

The raw data corresponding to each detector sub-system is first unpacked from its compressed format in SAM, and the read-out channels are mapped onto their physical detector location using geometry files, which take into account the most recent element alignment studies. Additional information relating to the signal magnitude and timing is also extracted, using a database of calibration constants. These give the expected noise

level and gain for every channel, which allows the signal voltage to be converted into a more meaningful measure. This process is particularly important for the calorimeter, where the energy deposits are measured directly through the voltage in each channel (in contrast to the tracking detector, where the magnitude of each 'hit' is less important in momentum determination). As such, a dedicated calorimeter calibration run is performed at the end of each $p\bar{p}$ store, to produce conversion constants entered into a calibration database; other components have less frequent calibration runs. The final result of this stage is a set of signals mapped both to their three dimensional coordinate, and to their corrected magnitude.

The next stage is the generation of particle tracks, using the hit information from the SMT and CFT detectors. This requires a combination of CPU-intensive track-fitting algorithms, which are described in more detail in Section 4.1.1. The results are track 'chunks', sections of track with associated parameters, which are then used by subsequent stages starting with vertex reconstruction. Here, the tracks are examined collectively to search for points where two or more particles may have originated from a common process (e.g. the decay of a neutral particle into two charged ones). Firstly, the primary interaction vertex (the initial $p\bar{p}$ interaction) is located by fitting to a set of suitable tracks; secondary vertices are then found, corresponding to particle decays away from the beampipe. Since vertexing is an important part of this analysis, with many uses in event selection, it is described in more detail in Section 4.3.1.

Once tracks and vertices have been found, higher-level object based reconstruction can take place. Electrons, photons, neutrinos (via $\not\!\!E_T$), muons and jets are identified from track, vertex, calorimeter and muon system information. More advanced algorithms reconstruct τ lepton candidates, and distinguish between different jet types (corresponding to an initial light quark (u,d,s), b quark or c quark). Sections 4.1.2 and 4.1.3 describe muon reconstruction in more detail, since along with track finding, muon identification is an important reconstruction tool used in this analysis.

Over time, as additional studies are completed, improvements into the reconstruction process can be made, resulting in a new version of D0RECO. These may involve new tracking algorithms, improved calibration or detector alignment databases, better object

ID packages, and so on. The new versions of the reconstruction software can be used by individuals as soon as the improvements are implemented, but for increased data set stability, the official release version used to reconstruct the data is only updated occasionally; currently these major updates are initiated only every few years, as a result of the stable operation associated with a mature experiment. Following an update of the official version, all previously reconstructed data from the same detector era is reprocessed with the new code. The data set for the analysis here presented is mainly comprised of the *p17* release, the most recent for Run IIa data. Around 10% of the data was reconstructed using the previous *p14* release, but the changes between these versions are not significant for track reconstruction or muon identification.

In addition to running over raw detector data, D0RECO is also used to reconstruct simulated events, as described in Chapter 5. Here, the 'raw' data is produced by interfacing a physics simulation program with a computerised model of the D0 detector. Using the same reconstruction code for both real and computer generated events makes the resulting simulation more realistic. All generated data is reconstructed with the *p17* version of D0RECO.

4.1.1 Track Reconstruction

The reconstruction of tracks is a non-trivial process, utilising multiple CPU-intensive algorithms to infer the trajectories of several hundred charged particles, from a snapshot of hits in the central tracking detector. Additional complications arise from detector noise (which can give fake hits), inefficiencies (leading to missing hits) and the unknown curvature of the particle tracks in the magnetic field. The current tracking scheme was converged upon by examining a number of custom built algorithms, and comparing performance over a range of instantaneous luminosities, particle momenta and event types. The performance is measured by a combination of quality indicators (e.g. tracking efficiency, fake rate) and resource use (e.g. CPU time and memory useage), using dedicated samples of simulated events, in conjunction with real detector data [66].

The general approach to tracking can be considered as comprising two phases. Firstly,

pattern recognition methods associate hit combinations which are likely to have originated from a single charged particle; following this, these hit combinations are fitted to produce a track, which is the best-fit to the true particle trajectory. In practice, there is an element of track fitting in the pattern recognition software, and vice versa. The selected tracking method uses two independent complementary algorithms, each producing a list of track candidates. These are the Histogram Track Finding (HTF) algorithm, which has better efficiency at high p_T, and works well in the forward regions and at high luminosity; and the Alternative Algorithm (AA), which has a lower fake rate, and higher efficiency for tracks with low p_T or a large impact parameter. The two lists are combined, and the pool of tracks compared and filtered to select the 'best' candidates under a number of tests. Finally, the surviving tracks are refitted with a third tracking algorithm, the Global TRacking (GTR) Refit, which takes into account effects such as interaction with detector material. This combination was determined to give the best tracking results over a range of different requirements.

The HTF Algorithm

The Histogram Track Finding [67] method uses a Kalman road-finder [68], adapted to perform under the high detector occupancies and hit multiplicities typically found in the D0 detector. Two similar approaches are used to build tracks, one uses SMT hits only, the other uses CFT hits only. In both cases, the final stage is extrapolation into the other tracking system to look for global tracks. First, Hough transforms (described below) are made to move hits from the arbitrary detector coordinate space into a more meaningful 'track' space; the track candidates are then selected using a histogramming method, in preparation for final selection by the Kalman filter.

The trajectory of a particle of charge q in a magnetic field B can be completely defined in the transverse plane by three quantities: the curvature $\rho = 1/r = qB/p_T$, the distance-of-closest-approach d_0 to the origin and the direction ϕ at this point-of-closest-approach. In the case where $d_0 \ll 1$, the description simplifies into two parameters, meaning that each track can be plotted as a point, or more correctly a finite region (due to experimental uncertainties), in (ρ, ϕ) space. Similarly, in the longitudinal direction, a track (with a small

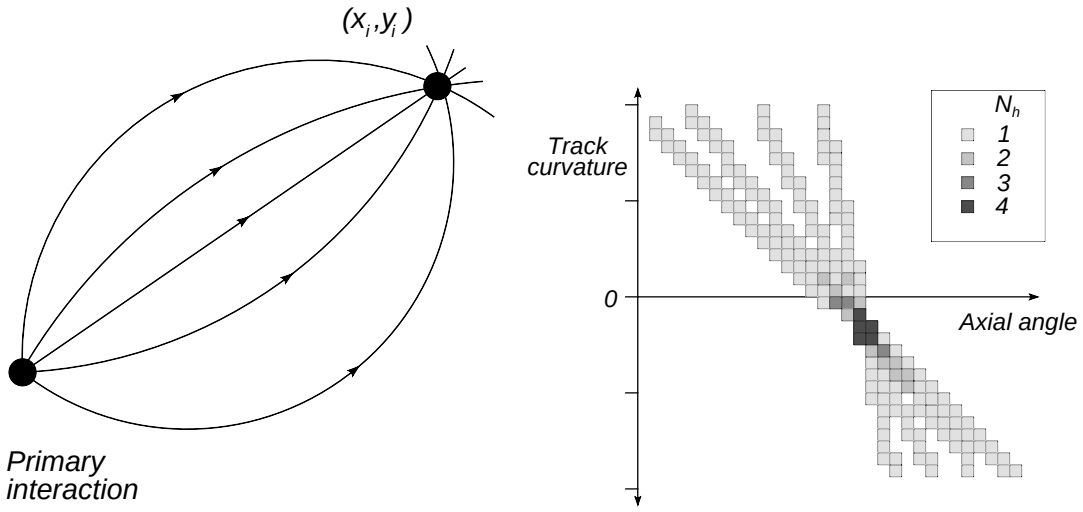

(a) (b)

Figure 4.1: Track finding in the HTF algorithm, as described in the text. (a) Each hit is associated with a range of possible tracks from the primary interaction, with a characteristic relation between the initial axial angle and the curvature; (b) hits from the same track will form converging bands in (ρ, ϕ) space, allowing tracks to be identified by a histogramming method.

impact parameter) can be defined by its z position at the point-of-closest-approach (z_0), and the inclination $C = dz/dr$. The HTF algorithm relies on this parameterisation, using a Hough transform which takes hits in detector space (x, y, z) and maps then into track space. In practice this is done separately for transverse $(x, y) \rightarrow (\rho, \phi)$, and longitudinal $(r, z) \rightarrow (z_0, C)$ transforms.

In the transverse case of the resulting coordinate system, each hit (x_i, y_i) corresponds to a band in (ρ, ϕ), since it could be associated with any one of a family of trajectories which pass through points $(0, 0)$ and (x_i, y_i), as illustrated by Fig. 4.1(a). A single hit is used to fill a two dimensional histogram in (ρ, ϕ), by incrementing all bins through which its band passes. This process is then repeated for all hits in the SMT (or CFT) to construct the full transverse histogram. Since each track corresponds to a small region in

(ρ, ϕ), all hits/bands from a common track will intersect at that point to produce a highly-populated bin: the signature of a real particle trajectory. Figure 4.1(b) shows the results from populating a histogram with the bands corresponding to four hits from a common track. The band convergence can be seen and quantified by the region with a greater number of hits, N_h. Unsuitable track candidates are removed by requiring some minimum bin population, $N_h^{min} = 4(7)$ for the SMT (CFT) case. This is the basic principle behind the Hough transform filter, which heavily reduces combinatorics to produce a set of track 'templates', each of which comprises a number of hits, and a set of approximate track parameters. The efficiency is reduced for tracks with large impact parameters as a result of the assumption that d_0 is small for all real tracks.

The Kalman filter takes the resulting templates and performs a more complete track search, starting with a pair of hits (in two or three dimensions), and determining the appropriate set of track parameters $(\rho, d_0, \phi, z_0, C)$ and their uncertainties. The algorithm then iteratively loops over all potential hits in the next detection layer, in a road finding method similar to the one described in Section 3.3.3. Only those hit additions which keep the track parameters consistent (under some adjustable prescription) are allowed to form extended track candidates. The process continues until a full set of tracks has been formed. The assumption that d_0 is small is no longer required, so that all tracks are constructed without bias.

The overall approach of the HTF algorithm is as follows:

- The SMT case:
  - Perform the $(x, y) \rightarrow (\rho, \phi)$ Hough transformation using only SMT hits, build the histogram and form track templates by enforcing $N_h^{min} = 4$;
  - Perform the $(r, z) \rightarrow (z_0, C)$ Hough transformation and histogram selection on the surviving templates, to form a set of possible 3D tracks;
  - Build the SMT tracks using the 3D Kalman filter;
  - Extrapolate the tracks into the CFT if possible.

- The CFT case:
  - Perform the $(x, y) \rightarrow (\rho, \phi)$ Hough transformation using only CFT hits, build the histogram and form track templates under the criterion $N_h^{min} = 7$;
  - Apply the (x, y) 2D Kalman filter to remove background tracks;
  - Perform the $(r, z) \rightarrow (z_0, C)$ Hough transformation over all resulting 2D tracks to form 3D CFT track templates;
  - Apply the (r, z) 2D Kalman filter to further clean-up the sample;
  - Build the final tracks candidates using the full 3D Kalman filter;
  - Extrapolate the tracks into the SMT if possible.

This is a simplified description: the full algorithm uses additional filtering tools and imposes specific requirements to remove fake tracks (tracks which do not correspond to real particle trajectories) and ghost tracks (cases where more than one track is allocated to the hits from a single particle trajectory). The tracks from SMT and CFT approaches are combined, with repeated candidates removed, and passed into the collective HTF-AA pool.

The Alternative Algorithm

The AA method [69] starts with hits in the innermost layer of the SMT detector, and constructs possible tracks by iteratively adding hits from radially increasing layers of SMT and CFT. As a result of the axial-stereo structure of the tracking detector, each hit has one or more associated stereo hits: i.e. a single (r, ϕ) measurement can correspond to more than one possible z coordinate measurement. The track candidates thus formed will be well defined in the transverse (axial) plane, but have multiple possible projections in the (r, z) plane. Such combination of axial and stereo hits leads to reduced combinatorics, allowing more advanced track finding methods to be used within the allowable time-frame. A second approach starting with CFT hits allows tracks with no SMT hits to be identified: this will be described later.

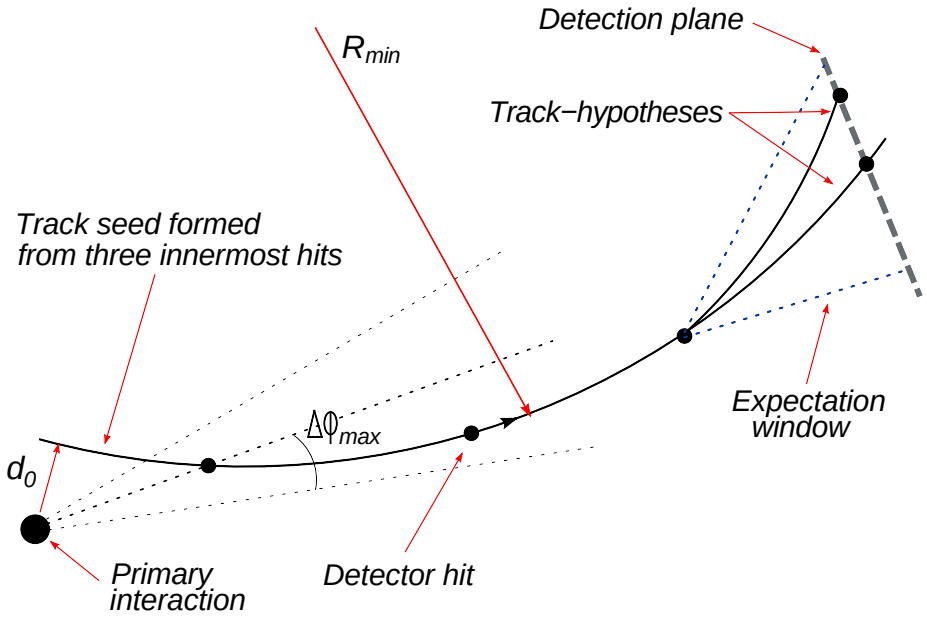

Figure 4.2: Overview of the AA track finding procedure, as described in the text. The track seed is formed from hits in the three innermost layers, with selections imposed on d_0, R_{min} and $\Delta\phi_{max}$, as well as the fit χ^2. Track hypotheses are then formed by searching within an expectation window at each subsequent detector layer.

The AA tracking method is illustrated schematically in Fig. 4.2. The starting point for a track candidate is a set of three axial SMT measurements, each with at least one associated stereo measurement. The first can be any hit in layers 1–6 of the SMT barrels, or in the F-disks; the second is selected in any downstream layer, and must lie within an angle $\Delta\phi_{max} = 0.08$ rad of the first hit; a third hit is selected in any following layer. At this point the track parameters can be measured and tested, the transverse radius of curvature must exceed $R_{min} = 30$ cm (corresponding to $p_T^{min} = 180$ MeV/c) and the transverse distance-of-closest-approach to the beam must be less than $d_0^{max} = 2.5$ cm. The goodness-of-fit of the track hypothesis is also tested by using the uncertainties of the hit coordinates to construct a χ^2 parameter: all tracks selected must satisfy the requirement $\chi^2_{max} = 16$.

Once an initial track hypothesis has been selected it is extended outward to the next

detection layer, by searching for hits in this layer which lie within a certain 'expectation window'. This window corresponds to any hit which can be added to the track hypothesis giving an increase in the track χ^2 of 16 or less. If there are several such hits, all possible track hypotheses are constructed; if there are no hits fulfilling this requirement, a 'miss' is allocated, provided that the expectation window is completely covered by active, functional detector material. The hit-miss concept is important here and in subsequent vertexing and event selection: an *inside* miss occurs when a track is associated with hits on both sides of the miss; *forward* misses are those radially outlying all track hits, and *backward* misses correspond to the layers radially within the first hit. Misses are defined separately for axial and stereo layers.

This extrapolation process is continued until the final layer of the CFT, or until three consecutive misses are allocated to the end of a track. By the time that all detection layers have been used, many of the possible (r, ϕ) stereo projections are excluded by repeated misses in the (r, z) expectation window. However, some transverse track hypotheses are still associated with multiple (r, z) trajectories. One final set of requirements must be met by each track candidate, after which they are passed on to the common HTF-AA pool for further selection. The criteria imposed on each track are as follows:

- At least four total measurements which contain both axial and stereo hits;
- ≤ 3 total inside misses;
- ≤ 6 total (forward + backward) misses;
- ≤ 2 inside misses in the SMT system;
- $N_{\text{hits}} \geq 5N_{\text{misses}}$;
- If there are any inside misses, then:
  - ≤ 4 total (inside + forward) misses;
  - ≤ 3 total (inside + backward) misses.

To allow tracks with fewer than three SMT hits to be found, a similar approach is made starting with the innermost layer of the CFT detector. In this case, the axial-stereo combinatorics are much greater, due to the large number of fibres extending over a wide range in z. Without additional constraints, this proliferation of track hypotheses would swamp the algorithm and slow reconstruction to unreasonable rates. However, by using the SMT-constructed tracks in the same event, the location of the primary interaction(s) can be measured. This information is used to filter CFT tracks by requiring them to pass within 1.5 cm (in both transverse and longitudinal projections) of one of these interaction points. Otherwise, the construction of track hypotheses continues as above, from the inner to outer layers of CFT. Once the outer layer has been reached, or at least three consecutive misses have been recorded, the track is extrapolated inwards to collect as many SMT hits as possible. All resulting candidates which satisfy the above list of criteria are passed to the HTF-AA pool.

Filtering the HTF-AA Track Candidates

All track candidates from both tracking algorithms discussed above are collected for further selection [69]. The first stage is to order the tracks according to their 'quality', using several hit-miss parameters. Tracks are then tested in order, and passed to the next stage if they fulfill certain 'shared-hit' criteria. The $p\bar{p}$ interaction point is then used to improve the ordering of tracks, and a second shared-hit test is made to select final tracks to be passed to the final reconstruction algorithm, GTR.

Track candidates are primarily ordered by decreasing number of hits; within this scheme by increasing number of misses, and fine tuned by ordering according to increasing χ^2 of the fit. The highest quality track hypothesis under this ordering is then chosen for the next track reconstruction step, and all the hits associated with it are flagged as having been used. Subsequent track hypotheses are tested in order, with specific requirements relating their total number of axial hits (N_{total}) and the number of hits which have already been flagged as used by a previous track hypothesis (N_{shared}):

- $N_{\text{shared}} \leq \frac{2}{3} N_{\text{total}}$;

- $N_{\text{shared}} \leq \frac{1}{5} N_{\text{total}}$ *or* $(N_{\text{total}} - N_{\text{shared}}) \geq 4$.

In this way, different tracks can be associated with a single common hit, as can occur with the high multiplicities of the D0 environment; limits are placed on this allowance to increase the confidence that a track corresponds to a real charged particle trajectory. Some additional criteria are applied to short tracks, or those with misses.

The track hypotheses which pass the shared-hit tests enter a second pool for a refined ordering process. Here, tracks passing close to the primary interaction point(s) are promoted up the list by performing the operation $N_{\text{hits}} \rightarrow N_{\text{hits}} + 2$ for all track candidates with small values of d_0. The list is then ordered in the same way as above, and the selection and shared-hit test is repeated. The results will be different as a consequence of the new hypothesis order. The biasing in favour of tracks passing close to the interaction point strongly suppresses fake tracks.

The Global TRacking (GTR) Refit

The GTR algorithm [70] takes the track candidates from the filter, and refits them with an improved calculation of their track parameters and the associated uncertainties (in terms of covariance matrices). It uses a Kalman fit road-finding technique, similar to the Kalman filter described for HTF, but whereas the filter simply calculates a track χ^2 for use in pattern finding, the full Kalman fit also determines several other important variables [71]. The Kalman fit is effectively a multi-dimensional χ^2 minimisation, used in conjunction with an 'interacting propagator' [72, 73] which takes the parameters (and uncertainties) for an incompletely fitted track, and predicts the location of a measurement on the next detector surface encountered. The propagator takes into account particle interactions in the detector material which are neglected in the earlier track finding algorithms, and is therefore an important component of GTR, though it can be considered as a black box by the Kalman fit.

The first stage is constructing a model of the detector in terms of *surfaces*, which represent the SMT by planes, and the CFT by cylinders. From this model, a set of *paths* is formed, representing the routes through the detector surfaces which may be traversed

by a particle from the $p\bar{p}$ interaction. Track *seeds* are then formed by looking at hits in the innermost few surfaces, and approximate parameters and errors are calculated. At this point, the interacting propagator and the Kalman fit are introduced. The former predicts the 'future' trajectory of a particle from the track seed, solving the equation of motion in the magnetic field and including multiple-scattering and energy losses. The fit then associates hits close to the predicted location to the track seed, forming one or more hypotheses provided that the fit χ^2 does not increase too much. The new track parameters and uncertainties are calculated, and the process continues until the last surface on a path is reached. Missed hits are allowed, but the fit takes into account the probability of a miss occurring, for later use.

The final stage is a filtering process, using information from the fit to select the best candidates for tracks. The fit χ^2, the number of misses and their probabilities, and the number of shared hits, are all used; the result is a refined list of tracks, with well known parameters, which comprise the final reconstructed tracks for the event.

It should be noted that the GTR algorithm is not limited to track fitting inside the solenoid. Information from the pre-shower detectors and muon chambers is also used. The complex magnetic fields and the large amount of detector material in these outer layers adds additional complexity to the track propagator software. The predictions of track parameters are tested by comparing them to the local parameters determined in the muon or pre-shower systems. Computer simulated events are also used to refine and calibrate the propagator model; in particular, large samples of muons are generated to test the effect of multiple-scattering.

Tracking Performance

The combined use of the three different algorithms improves tracking performance over a wide range of particle momenta and luminosities. The efficiency for correctly reconstructing muon tracks in $Z \rightarrow \mu\mu$ events is around 85–90%, even with several 'minimum bias' events overlaid onto the signal event of interest. These are generic events which would not normally pass trigger requirements, but are collected since they come from the same bunch-crossing as a triggered interaction. Since the number of $p\bar{p}$ interactions

per crossing is proportional to the instantaneous luminosity, tracking in the presence of several minimum bias events is a good measure of performance at higher luminosities. The fake rates are consistently below 2% for all data collected in Run IIa, increasing to 3–4% for the highest luminosities in Run IIb. Another measure of tracking proficiency is the mis-reconstruction (mis-reco) rate: the fraction of tracks which are wrongly associated with one or more hits or misses. In these cases, while the tracks do represent real charged particles, their parameters may be distorted by the missing or mis-allocated hits. The mis-reco rate is typically 7–8% for Run IIa conditions, which means that over 90% of tracks are reconstructed from correct and complete hit information [74]. Fake rates and mis-reco rates are determined using a combination of methods, over both simulated and real data. The transverse momentum resolution of the combined SMT and CFT systems is given by:

$$\Delta p_T = 0.002 \cdot (p_T)^2, \tag{4.1}$$

where the units of momentum are GeV/c [75]. This results in typical resolutions of 5 GeV/c at a particle momentum 50 GeV/c.

One additional tracking aspect must be introduced here: this is a systematic effect known as the D0 momentum scale uncertainty, which results in the track curvatures being mis-measured by a small amount. This translates into a small shift in the transverse momenta, relative to the true particle value. In turn, it can influence the invariant masses and momenta of the parent particles, which are reconstructed by combining the charged particle tracks. The origin of the shift is not well understood, but believed to arise from some combination of mis-modelling of the the magnetic field (shape and normalisation) and the detector material. In this analysis, the effect is compensated for by applying an *ad hoc* correction to all measured masses, based on the D0 and world average value of the B^+ mass, as described in Section 4.3.6.

4.1.2 Muon Reconstruction

As with central track reconstruction, offline muon identification and tracking uses methods similar to those used by the trigger system, but taking advantage of the extended processing time-frame: more complex algorithms are used to yield muon samples with higher efficiency and purity, and more precise track information.

The first stage is to find muons within each layer (A–C) by associating multiple signals from drift chamber wires and scintillation counters into short tracks, called *segments*. These segments are then matched between layers, first in the region outside of the toroid magnets (layers B and C), followed by extrapolation through the magnet material to match to A layer segments, forming local muon *tracks*. Following this process, the muon tracks are extended inward to search for matching central tracks from the SMT and CFT systems. If a match is found, the muon trajectory is refitted with all information to form a global muon object, giving much improved momentum resolution.

Reconstructing Local Muon Segments

The first stage in local muon reconstruction is mapping the 'hits' in the drift chambers into a convenient coordinate system for each octant-layer, with a transverse plane perpendicular to the wire direction, and longitudinal coordinate (ξ) along the wire. As described in Section 3.2.5, the ξ coordinate of a muon can be measured to within $\sim$3 mm by the PDTs, and the drift time allows the interaction distance from the wire to be measured. However, these two measurements do not uniquely define an interaction point: only a circular locus about the wire arising from the rotational symmetry of the system; this is shown in Fig. 4.3. In practice, the electric field lines mean that the drift time loci are elliptical, and of course extended into three dimensions by the finite ξ resolution.

The signal information is used to build up an array of hit loci, separately for each layer (A–C) and octant of the central and forward muon systems; from this array, segments are constructed by successively associating suitable hits in a linked list method [76]. This can be visualised as plotting trajectories which touch the circles from multiple wire hits, as shown in Fig. 4.3. In reality, the task is complicated by such effects as the non-circular

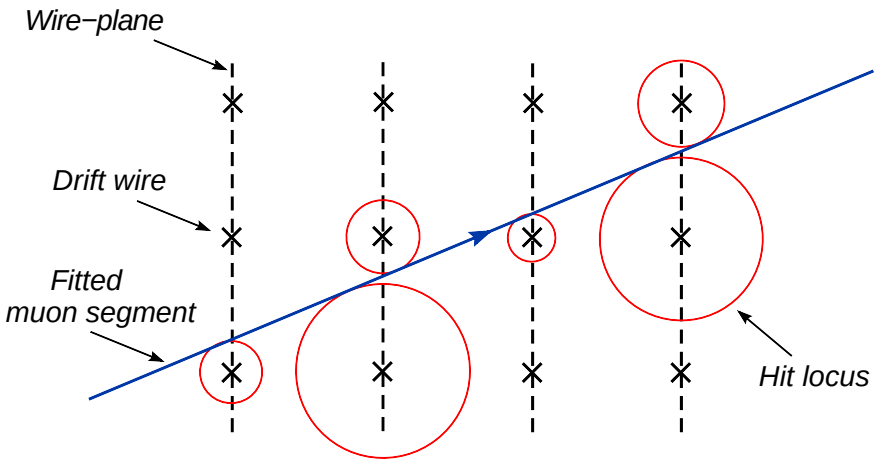

Figure 4.3: Illustration of muon segment reconstruction from drift chamber hits. Each hit is associated with a locus of possible muon coordinates, with the longitudinal position and radius set by drift chamber signals and scintillator timing. Muon segments are built by searching for matched hits between detection planes, as described in the text.

shape of loci, the presence of the toroidal magnetic field, and missing hits. The end result is a list of segments containing three or more hits within a single detection layer; these must be distributed over at least two planes of wires, out of the 3–4 planes per layer. The hits in each resulting hypothetical trajectory are then fitted to an appropriate track, separately in the transverse plane, and along the wire direction. A filter then selects the best four segments per octant-layer according to the number of associated hits, and the χ^2 of the transverse fit, for each segment.

At this stage, the scintillation counter information is used to improve the timing data for a muon candidate: each segment is extrapolated into the counter system for that layer, and scintillator hits within a reasonable (tuneable) distance of the expected muon position are associated to that segment. This is particularly important in the forward region, since the MDTs do not measure the ξ coordinate of hits, and so the drift time is poorly translated into a transverse locus (i.e. the circle becomes a broad torus). In these cases, the trajectories are refitted with the new timing information taken into account, although the position of scintillator hits is not used. Additional constraints can be placed by associating

the segments with a vertex from the tracking detector.

Matching Segments Between Layers

Since layers B and C both lie outside the toroid magnet, segments can be matched straightforwardly between these layers, and the resulting set of hits used to perform a better fit over a longer distance. This is undertaken by the same algorithm which builds the segments for each layer, as described above. For each octant, segments in layer B are extrapolated into layer C, and any segments in that layer which match in position and angle, within tuneable limits, are adjoined and refitted into a two-layer local segment. The constituent single-layer segments are discarded, but those segments which cannot be matched between layers are retained. A final filter then selects the best BC segment candidates per octant, by transverse χ^2 comparison, to pass to the next stage in reconstruction.

Another algorithm [77] then matches A layer segments with BC segments, and performs a fit to produce muon tracks and their corresponding parameters, uncertainties and χ^2. The first step is to pair each BC segment to all A segments in the same octant region, and test the compatibility within each pair by enforcing a number of requirements on the coordinates and orientations of the segments. The A segment must also point back towards the primary interaction point, within some reasonable range to account for secondary muon production from long lived particles. Any pairs surviving these selections are then entered into a fitting program, which generates a set of track parameters, and the error matrix, for each hit in A and BC layers. This takes into account energy loss and deflection due to multiple-scattering in the thick toroid magnets, as well as the effect of the magnetic field itself.

Matching Muons to Central Tracks

Local muons and central tracks are matched in one of two ways. For muons with segments both inside and outside the toroid, the track is extrapolated inward to the central tracking system, and any combination of central and muon tracks which pass a maximum χ^2 threshold are considered as global muon candidates. The combined track parameters and

uncertainties are computed from a weighted combination of the two matched tracks [78]. For local muons without segments on both sides of the toroid, the extrapolation is reversed: central tracks are extended outward and associated with compatible segments, with the combined track assigned the same parameters as the central track [70].

The muon type is quantified by the quantity 'nseg', which is either a positive (for local muons matched to central tracks) or negative (for unmatched local muons) integer, with magnitude 1 (A-segment only), 2 (BC-segment only) or 3 (A and BC matching segments). If there are no muon segments, but there is evidence that a track may be a muon, it is assigned a value nseg $= 0$: here the required signature is either a single hit in the muon system, or an MTC muon (see Section 4.1.3). In the event selection for this analysis, all muons are required to be matched (nseg ≥ 0), with some additional constraints placed on those with fewer segments, as described fully in section 4.3.3. In total, central track matching is performed with an estimated efficiency of 85–96%, depending on the angular isolation and nseg value of the muon [79, 80].

4.1.3 Muon Tracking in the Calorimeter (MTC)

As emphasized in Section 3.2.5, muon identification is very important for this analysis, and is aided by the wide coverage, high precision, and tracking capabilities of the dedicated muon detectors. However, some muons will traverse this system without producing a local muon segment, and so can not be identified in the absence of additional selection tools. In such cases, the calorimeter can provide the required information to tag particles as muons. This is because the typical interaction behaviour of muons in the calorimeter material is different from electrons, photons and hadronic objects. By examining the signal profile associated with each particle, and using appropriate algorithms, muons can be distinguished and the useable event sample enlarged. This identification process is carried out by the Muon Tracking in the Calorimeter (MTC) package [81], described below.

Electrons and photons produce particle showers in the innermost (EM) layers of the calorimeter, which are fully captured by the active material. Hadronic objects produce deeper showers which can extend to the outlying layers, but which have a distinctive

energy profile: this is the distribution of energy deposited per layer in a tower, which peaks when the number of ionising particles in a shower reaches its maximum. On the other hand, muons are much less likely to shower, instead causing minimal ionisation in each layer traversed in the calorimeter. Also, energy from muons is deposited relatively uniformly with longitudinal distance, so most energy is lost in the hadronic modules, which are significantly thicker than the EM modules. Therefore, the presence of several energy depositions in a single tower, where the signals are consistent with an MIP, is a clear indication of a muon.

A sample of possible muon candidates is first collected by a simple energy-deposit counting method. A two dimensional histogram is constructed in detector (η, ϕ) coordinates, with each bin corresponding to a single tower. Here the coordinate origin is the primary interaction point of the event. In each bin, a 'hit' is allocated whenever energy of 100 MeV or more is deposited in a single layer of the hadronic calorimeter modules. Since muons are expected to leave hits in several consecutive layers, a candidate is required to leave either three (out of four possible) hits in the CC, or four (out of six possible) hits in the EC.

The above method does not allow muons which cross between towers, so is supplemented with a 'supertower' selection. Here, another two dimensional histogram is constructed, but this time each bin contains 2×2 towers in (η, ϕ), any of which can contribute a hit. The same requirement of hits in 3/4 (4/6) layers for CC (EC) candidates is enforced, with the additional criterion that:

$$N_{\text{hits}} \leq N_{\text{layers}} + 1 \ , \tag{4.2}$$

i.e. each layer can only contribute a single hit, except for one layer, which can contribute two (to allow for tower crossing effects). This removes narrow showers from the sample, which will in general produce hits in adjacent (η, ϕ) cells over multiple layers.

Particles fulfilling the above selections are called calorimeter muons. The purity of this sample is improved by constructing a discriminant based on the observed energy profiles of signal (muon-like) and background-like samples. The signal sample comprises

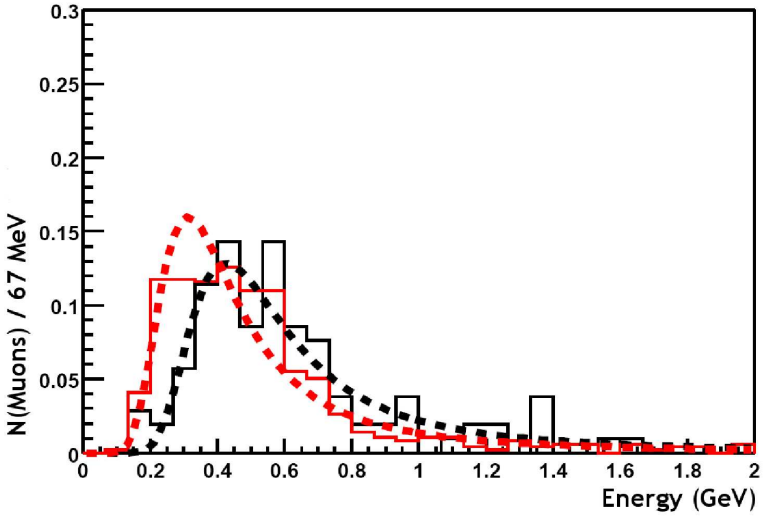

Figure 4.4: Muon energy deposits in a single layer of the hadronic calorimeter, for both background (red) and $Z \rightarrow \mu\mu$ signal (black) samples, as defined in the text. The solid lines give the bin content, the dashed lines show the fit to a Landau distribution. The histograms have been rescaled to determine the normalised distributions.

calorimeter muons from $Z \rightarrow \mu\mu$ events, where both muons are identified by the muon system, and the pair have opposite charge and an invariant mass within 15 GeV/c^2 of the Z mass. The background-like sample comprises calorimeter muons with a matching track from the central tracking detector, but no hits in the muon system.

For each layer l, a histogram of the energy deposited per particle is produced for signal and background samples, which are then fitted to a Landau distribution, $S_l(E_l)$ for signal, and $B_l(E_l)$ for background. The fitted histograms for a single layer (the outermost fine-hadronic layer in the forward calorimeter) can be seen in Fig. 4.4. From these distributions, a calorimeter muon can be tested for consistency with the signal sample, with the following relation:

$$P(\bar{E}) = \frac{\prod_l S_l(E_l)}{\prod_l S_l(E_l) + \prod_l B_l(E_l)} \, , \tag{4.3}$$

where $\bar{E} = (E_1, E_2, ...E_n)$ is a vector giving energy deposits per layer, associated with the muon. The resulting quantity $P(\bar{E})$ is called the energy signature: its distribution for

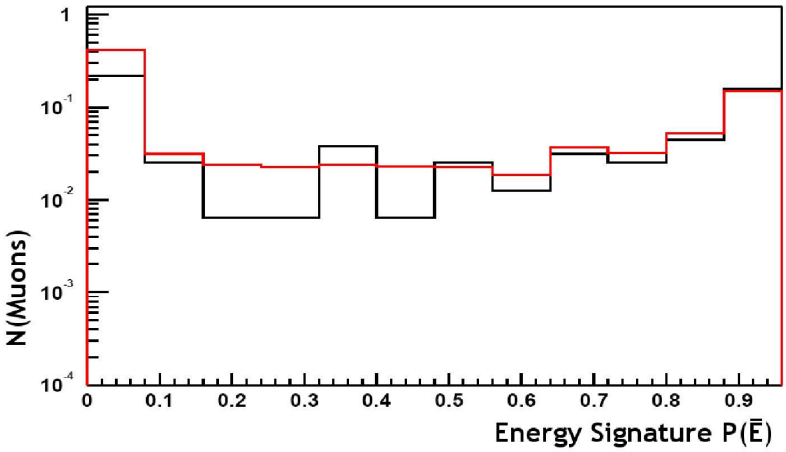

Figure 4.5: Normalised distribution of energy signature (defined in Eq. 4.3) for calorimeter muons. The signal (black) and background (red) samples show different distributions, and the requirement $P(\bar{E}) > 0.5$ is enforced to enhance the muon purity.

signal and background samples is shown in Fig. 4.5. The requirement $P(\bar{E}) > 0.5$ is then enforced to improve the purity of calorimeter muons. The performance has been tested by running the algorithm over around one million events containing a local isolated muon. The angular separation of the calorimeter and local muons is shown by the two plots in Fig. 4.6; these plots illustrate both the resolution (by the signal peak width) and the purity (by the relative peak and background areas) of the final calorimeter muon sample.

4.2 Event Selection: Introduction

Having reconstructed the fundamental physics objects of importance to this analysis, the process of selecting suitable events can be undertaken. In this analysis, two distinct systems of excited neutral B mesons are investigated. These are the B_J states (also called B^{**}), corresponding to a $(b\bar{d})$ quark composition; and the B_{sJ} (B_s^{**}) states, corresponding to $(b\bar{s})$. As such, there are two corresponding data samples. The remainder of this chapter describes the methods used to select signal events for each sample, using the tools and concepts introduced in the previous sections. Many of the selection criteria are common

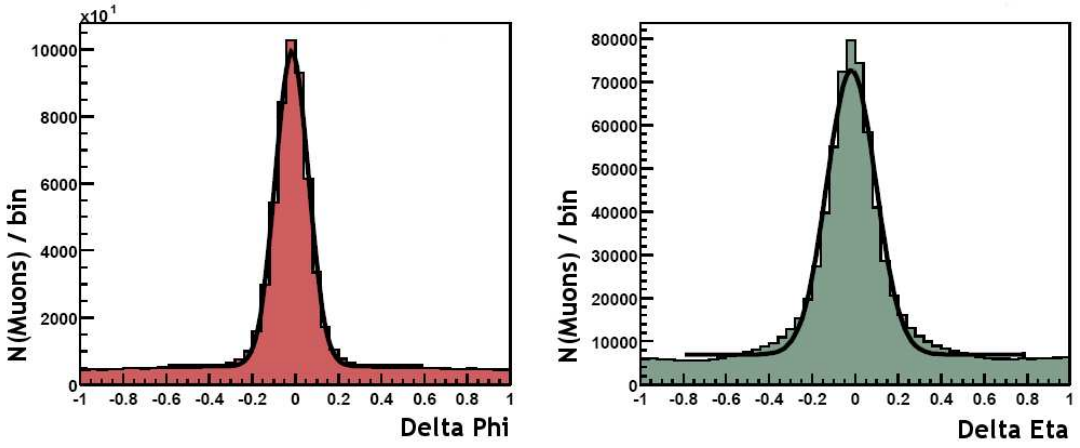

Figure 4.6: Purity and tracking performance of MTC algorithm. Shown are the differences in muon track ϕ (left) and η (right) between calorimeter muons and local muons.

to both samples.

The search for narrow B_J mesons is performed by examining events containing the final states $B^{+(*)}\pi^-$. This sample includes the following decays:

$$B_1 \rightarrow B^{*+}\pi^-,\ B^{*+} \rightarrow B^+\gamma; \tag{4.4}$$

$$B_2^* \rightarrow B^{*+}\pi^-,\ B^{*+} \rightarrow B^+\gamma; \tag{4.5}$$

$$B_2^* \rightarrow B^+\pi^-. \tag{4.6}$$

In the case of the B_{sJ} states, if the mass $M(B_{sJ})$ is large enough the main decay channel should be $B_{sJ} \rightarrow B^{(*)}K$. This is because the $B_s\pi$ channel is forbidden by isospin conservation, as described in Section 1.5.3. The search for narrow B_{sJ} mesons is therefore performed by examining events with $B^{+(*)}K^-$ decays:

$$B_{s1} \rightarrow B^{*+}K^-,\ B^{*+} \rightarrow B^+\gamma; \tag{4.7}$$

$$B_{s2}^* \rightarrow B^{*+}K^-,\ B^{*+} \rightarrow B^+\gamma; \tag{4.8}$$

$$B_{s2}^* \rightarrow B^+K^-. \tag{4.9}$$

Here, and in all future descriptions of particles and reactions, charge conjugated events

are implied, meaning that the corresponding antiparticles $\bar{B}^{**}_{(s)}$ formed from $b\bar{d}(\bar{s})$ quarks are selected through the conjugate decay processes.

In both the B_J and the B_{sJ} searches, it follows that the initial event selection is geared to reconstructing B^+ mesons. In order to minimise uncertainties in the final analysis, it is important to develop a B^+ selection method which will yield a large sample, with maximally enhanced signal-to-background ratio. This method is described in the following section.

4.3 B^+ Selection

The B^+ meson is reconstructed in the exclusive decay $B^+ \rightarrow J/\psi K^+$ with J/ψ decaying to $\mu^+\mu^-$. This channel takes advantage of D0's high efficiency and broad coverage in the muon system, as outlined in Chapter 3. The first stage is to construct J/ψ candidates from suitable pairs of muons; this necessitates the use of a vertexing technique which reconstructs short-lived, neutral particles from their charged decay products, as described below.

4.3.1 Vertex finding

The vertexing algorithm takes as its input a pair of tracks (t_1, t_2), corresponding to two particles, (p_1, p_2). It then performs certain tests (described below) to calculate the likelihood that these particles were produced at a common vertex. In this way, particles such as the J/ψ, which cannot be directly observed in the tracking detector, can be inferred from their decay products. In addition, the parameters of these reconstructed particles, such as their momenta, can be determined by suitable combination of the properties of the daughter particles. Thereby, the parent particles can be defined, and associated with their own trajectories. By iterating this procedure for the newly defined particles, it is possible to rebuild an entire event; starting from those charged particles which live long enough to produce hits in the tracking detector, and ultimately reconstructing those particles which were produced in the $p\bar{p}$ collision and the subsequent hadronisation process. This method

forms the basis for all event reconstruction in the following sections, so it is important to understand how the vertexing algorithm operates.

Tracks observed by the detector, as described in Section 4.1.1, are defined only between the first and last hits with which they are associated. However, it is possible that a track t_i may represent an incomplete portion of the trajectory of the particle, p_i, which created it. This is because the detector is not 100% efficient, and hits are not necessarily produced in every silicon layer through which a charged particle passes. To account for such effects, the vertexing method extrapolates both tracks beyond their end-points, determining the mutual distance-of-closest-approach for their hypothetical three dimensional trajectories. At this point, a preliminary selection is made to exclude those particles which do not closely approach each other. Track pairs are removed from the sample if they do not approach eachother within 0.3 cm in the (r, ϕ) plane, or within 0.5 cm in the z direction. This is a very loose selection criterion, removing only particle combinations which are extremely unlikely to have originated from a common vertex.

The hypothesis that the particles p_1 and p_2 originate from a common vertex, V, can now be further tested. The vertex is assigned a coordinate corresponding to the average of the track position vectors at the point-of-closest-approach. Each track will therefore be a distance ξ from the vertex, at the closest approach. Since there is some uncertainty associated with each track trajectory, a χ^2 parameter can be defined for each track, with respect to its associated vertex, which is given by:

$$\chi^2(t_i, V) = \left(\frac{\xi_T(t_i)}{\sigma[\xi_T(t_i)]}\right)^2 + \left(\frac{\xi_L(t_i)}{\sigma[\xi_L(t_i)]}\right)^2. \tag{4.10}$$

Here $\xi_T(t_i)$ is the projection of the track-vertex distance on the plane perpendicular to the beam direction, and $\sigma[\xi_T(t_i)]$ is its uncertainty. Similarly, $\xi_L(t_i)$ is the projection of the track-vertex distance along the beam direction, with uncertainty $\sigma[\xi_L(t_i)]$.

The $\chi^2(V)$ for a vertex is then the sum of $\chi^2(t_i, V)$, for all tracks associated with it. In the case described here, we are dealing only with two-track vertices, but this calculation

can be extended for vertices with any number of tracks:

$$\chi^2(V) = \sum_{i=1}^{n} \left[\chi^2(t_i, V)\right] . \tag{4.11}$$

This parameter is a measure of the probability that the particles' paths coincide at some point in the detector. The χ^2 for a vertex is a parameter which is frequently used in the reconstruction process; it is not restricted to cases where the decay particles are charged (as in the above description). Note, however, that this does not identify production vertices as opposed to particle crossings: these topologies are isomorphic at this point, but are distinguished next, using additional vertex and track parameters.

As outlined above, the tracks are allowed to form vertices beyond their end-points (by extrapolation), or along their length. There are thus two cases in which a pair of tracks can be wrongly attributed to a common vertex, with a small χ^2. The first is track crossings, where the 'vertex' is in reality just a close pass of two particles. The second occurs when a track is extrapolated beyond the trajectory of the underlying particle; any vertices found in this way will not correspond to real particle decays, and should be discarded. These cases can be suppressed by making use of the hit information for the tracks, as illustrated schematically in Fig. 4.7. As a result, these tests can only be performed for those tracks directly observed in the detector; i.e. those produced by charged particles. Neutral particles reconstructed from their charged daughters are also assigned tracks, but these parent particle tracks are not associated with hits, and have to be tested using different methods. The selection criteria for forming vertices with charged-particle tracks are enumerated below:

1. $N_{\text{misses}}^{\text{upstream}}(t_i) \leq 4$,

   i.e. the number of upstream misses for each track cannot exceed four. Upstream misses are those occurring between the start-point of a track, and the vertex with which it is associated. If $N_{\text{misses}}^{\text{upstream}}(t_i)$ is large, then the extrapolation distance is large, and the probability of wrongly attributing a vertex to the track is increased. In Fig. 4.7, track t_1 has one upstream miss, and the event would therefore pass this selection. Misses along the length of a track (i.e. inside misses) can also be

significant, but these are addressed at a later stage.

2. $N_{\text{hits}}^{\text{downstream}}(t_1) + N_{\text{hits}}^{\text{downstream}}(t_2) \leq 2$,

   i.e. the total number of downstream hits for both tracks cannot exceed two. Downstream hits are those occurring before the vertex, and are hence indicative that the particle existed prior to the point-of-closest-approach, and that the apparent vertex is in fact a track crossing. However, tracks with downstream hits are not excluded automatically, as it is possible that a track can be wrongly associated with one or more hits in the tracking detector. In these cases, tracks can be extended beyond the production or decay vertices of the particle which produced them; thus giving a vertex the appearance of a track crossing, as shown for track t_2 in the example in Fig. 4.7. To correct for such over-extended tracks, a small number of downstream hits are allowed for each vertex. Vertices with large total $N_{\text{hits}}^{\text{downstream}}$ are assumed to be crossings, and excluded.

4.3.2 The Primary Vertex and Impact Parameters

At this point, it is appropriate to define and describe the primary vertex (PV) for an event. This coordinate represents the point in space at which the initial $p\bar{p}$ interaction occurred; it cannot be directly measured, since it is always within the beampipe. Instead, it is reconstructed from a set of selected tracks, and the beamspot position. The latter is the intersection volume of the two particle beams, which cross at the centre of the detector environment. The beam spot is generally rather small in the (r, ϕ) plane, but can be extended for several centimetres along the beam direction (see Section 3.1.2 for details).

A sample of tracks is then selected, and used to fit the primary vertex. Here the emphasis is on excluding from the fit any tracks which may introduce a bias in the PV position. For example, tracks produced by the decay of long-lived particles will not originate at the $p\bar{p}$ interaction, and so are removed from the fit. Tracks which interact with the detector material are also removed. Once a suitable set of tracks has been determined for an event, the PV position is determined by a χ^2 fit over all the tracks. The minimisation function,

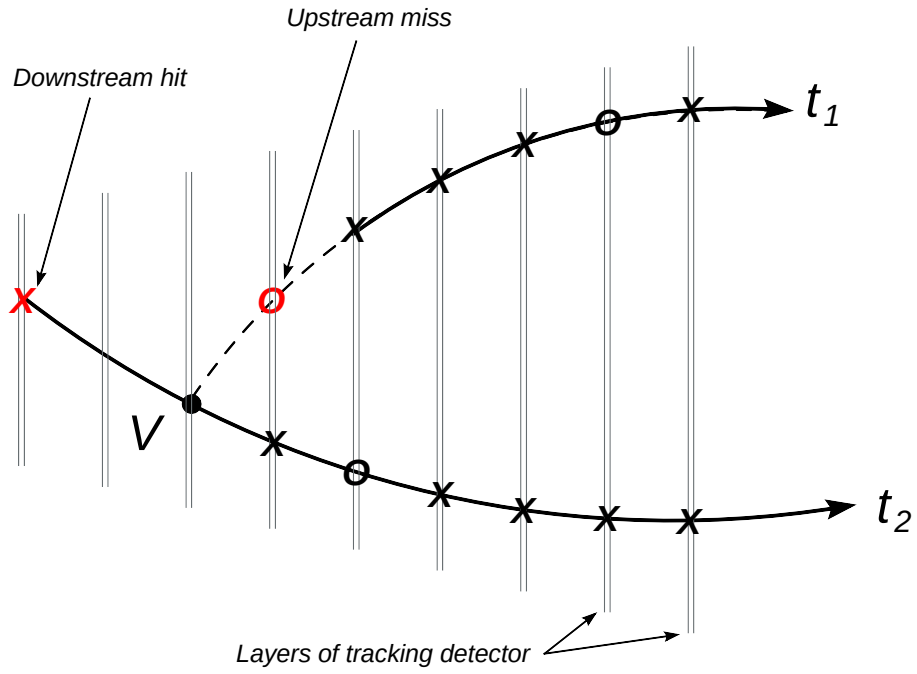

Figure 4.7: Event topology selections designed to remove pairs of tracks which do not correspond to a particle production vertex. Layers of the tracking detector are shown schematically, with hits (X) and misses (O) for each track. Requirements on the number of downstream hits, and upstream misses, are described in the text.

as well as the procedure for selecting suitable tracks, is described in full in Ref. [82]. In this way, the primary vertex can be located with a resolution of 35 μm along the beam direction [35].

Once the PV has been defined and its position determined for a given event, it is possible to measure the impact parameter (IP) of any track. This is the distance-of-closest-approach of the track to the primary vertex. By combining the impact parameter with its uncertainty, an IP significance, S, can be determined. This is analogous with the vertex χ^2 defined in Section 4.3.1; it is a well defined statistical parameter, quantifying the likelihood that a track originated at the original $p\bar{p}$ interaction. For any track i, the

significance S_i is defined as:

$$S_i = \sqrt{\left[\frac{\delta_T}{\sigma(\delta_T)}\right]^2 + \left[\frac{\delta_L}{\sigma(\delta_L)}\right]^2}, \tag{4.12}$$

where δ_T (δ_L) is the projection of the track impact parameter on the plane perpendicular to (along) the beam direction, and $\sigma(\delta_T)$ [$\sigma(\delta_L)$] is its uncertainty. This parameter is very useful in the reconstruction of excited B meson candidates, as will become clear in the later sections of this chapter. Having established a number of essential discriminatory parameters and reconstruction tools, we now list the specific criteria used for J/ψ event selection.

4.3.3 $J/\psi \rightarrow \mu\mu$ Events

The dominant tool in distinguishing J/ψ candidates from background events, is the ability to identify particles as muons. This takes place when a local muon (i.e. one detected using only information from the muon system) is associated with a track from the central tracking detector, forming a global muon. The topology of muon hits is then used as an indicator of the confidence in this association.

The first stage in J/ψ reconstruction is to take pairs of tracks, both of which must be identified as global muons, with opposite charge. The tracks must form a common vertex, according to the criteria described in Section 4.3.1, but no explicit constraint is placed on the vertex χ^2 at this point. Both tracks must be associated with at least one hit in the CFT detector, and at least one of the muons must have two or more hits in the SMT detector. In addition, at least one muon must have segments inside and outside the toroid magnet (nseg $= 3$), and both muons must have transverse momentum (p_T) greater than 1.0 GeV/c.

To demonstrate the effectiveness of these requirements, a small sub-sample (around 3%) of the Run IIa data is used to construct signal-like and background-like distributions for significant variables. The starting point is a very loose di-muon selection, comprising any muon pairs which form a common vertex and have opposite charge. The J/ψ-signal sample is then defined by all muons satisfying $2.95 < M(\mu\mu) < 3.25$ GeV/c^2, and the background sample comprises muons in the two sideband regions, $2.2 < M(\mu\mu) <$

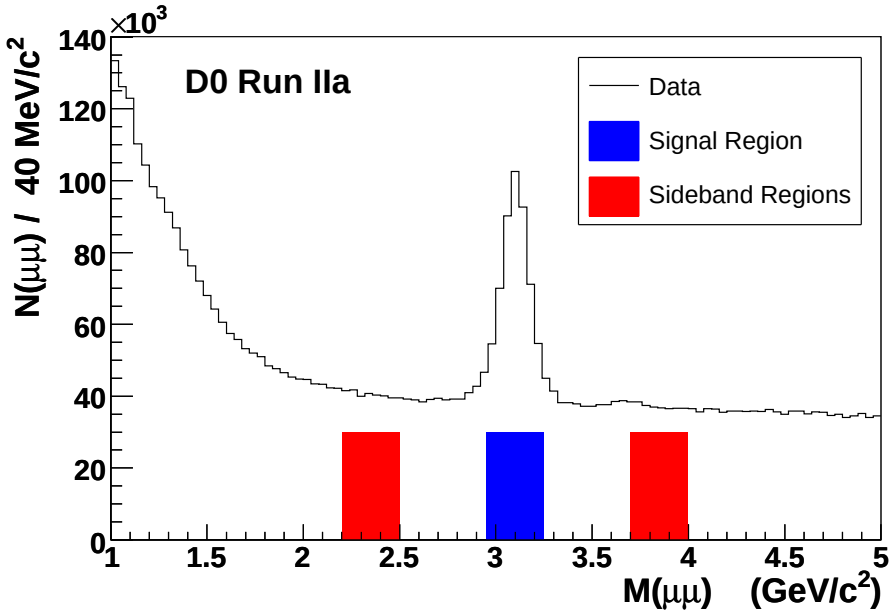

Figure 4.8: Di-muon invariant mass for a sub-sample of Run IIa data, under loose selection requirements. Shown are the J/ψ-signal and sideband regions used to demonstrate the discriminatory power of certain variables in this section.

2.5 GeV/c^2 and $3.7 < M(\mu\mu) < 4.0$ GeV/c^2. The resulting di-muon invariant mass distribution is shown in Fig. 4.8, annotated with the signal and sideband regions.

It is now possible to examine the distributions of the selection variables, for both signal and background samples. Figure 4.9 shows such a plot for the muon transverse momentum, demonstrating that signal-like events are associated with larger $p_T(\mu)$ than background-like events, and motivating the exclusion of muons with $p_T < 1.0$ GeV/c. In this histogram, the number of background entries has been normalised to match the size of the signal sample. Note that this requirement is not intended to be optimal, only to reduce the background fraction to a reasonable level, in preparation for subsequent optimisation of the $B^+ \to J/\psi K^+$ selection. Figure 4.10 shows the equivalent plot for the 'nseg' variable, demonstrating that small numbers of matched muon segments are associated with background-dominated samples, while the requirement nseg $= 3$ results in a signal-enhanced sample.

Following the application of such global criteria, additional constraints are placed on

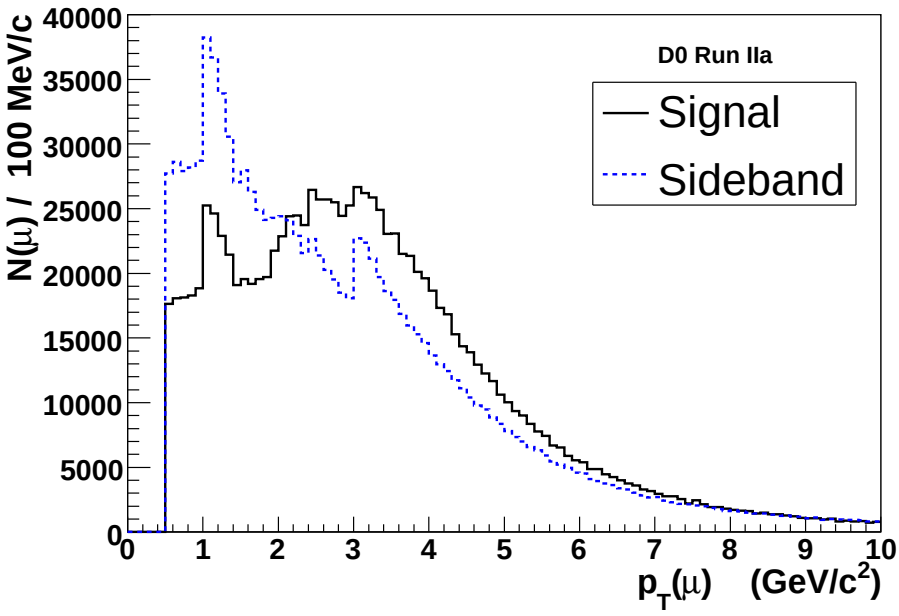

Figure 4.9: Muon transverse momenta for J/ψ-like and background samples, showing the characteristic 'harder' (i.e. higher-p_T) distribution for the J/ψ events. The two samples are defined by the di-muon invariant mass, as shown in Fig. 4.8, and the sideband histogram has been renormalised to match the number of events in the signal sample. The apparent structure in the distribution is a consequence of the different trigger requirements used in accepting single and di-muon events.

some candidates according to nseg(μ_1, μ_2). These selections are enumerated below, with motivation for their inclusion.

1. If nseg$(\mu_i) \geq 1$, then $p_T(\mu_i)$ must exceed 1.5 GeV/c,

   i.e. a tighter transverse momentum requirement is imposed if a muon has a reconstructed segment in any of the drift chambers. Any muons produced by a J/ψ decay, in the central tracking region, will only survive to produce hits in the muon system if they have a relatively high p_T; therefore this requirement predominantly removes background muons.

2. If nseg$(\mu_i) = 0$ then the following conditions are enforced:

   (a) $\chi^2(\mu_i) < 25$ and $\chi^2(\mu_j) < 25$,

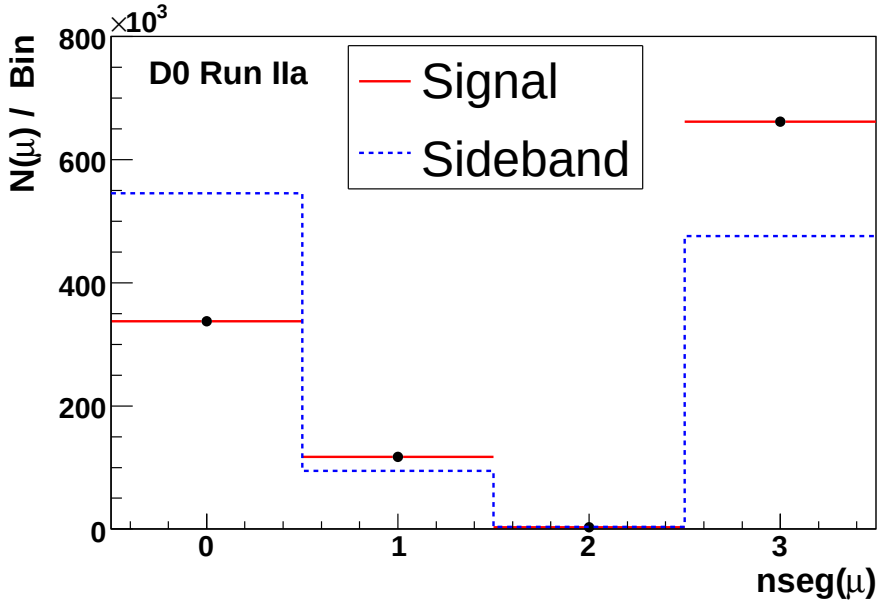

Figure 4.10: Number of matched muon segments ('nseg') for J/ψ-like and background samples, showing the enhancement of signal (background) at high (low) values of this variable. The two samples are defined by the di-muon invariant mass, as shown in Fig. 4.8, and the sideband histogram has been renormalised to match the number of events in the signal sample.

i.e. both tracks are required to come from the assigned J/ψ decay vertex, with an explicit probability. This is still a rather loose selection: the full power of the χ^2 parameter is used at a later stage.

(b) $P_{total}(\mu_i) < 7.0$ GeV/c,

i.e. the muon with nseg $= 0$ must be 'soft' (low momentum). High momentum muons are expected to produce multiple hits in the muon drift chambers; in this case, the absence of reconstructed segments would be indicative of a poorly understood event, which should thus be excluded. On the other hand, it is normal for low momentum muons to produce no drift chamber hits.

(c) $p_T(\mu_j) > 2.5$ GeV/c,

i.e. the other muon (which has nseg $= 3$) must have an even higher transverse momentum than otherwise enforced. High p_T particles are associated with

smaller uncertainties in their track parameters. This requirement therefore compensates for the larger uncertainties which are associated with μ_i, as a result of its lack of muon hits.

(d) $p_T(\mu_1 + \mu_2) > 4.0$ GeV/c

i.e. the transverse momentum of the combined $\mu_1\mu_2$ (J/ψ) system must exceed 4.0 GeV/c. Since the J/ψ candidates should come from decays of B hadrons, we expect them to have relatively high p_T. This is an additional compensation for the increased uncertainties in the μ_i information.

(e) $P[\bar{E}(\mu_i)] \geq 0.015 * N_{layers}(\mu_i)$

Since there is no information from the muon drift chambers, we require that the calorimeter identifies a muon which is associated with the central track. This uses the MTC (Muon Tracking in the Calorimeter) package, as described in Section 4.1.3. By enforcing the additional requirement that the energy signature $P(\bar{E})$ exceeds 0.015 per layer of the hadronic calorimeter, the purity of the muon sample is improved, at the expense of a reduction in efficiency.

For illustrative purposes, the final $\mu\mu$ invariant mass is shown in Fig. 4.11, using the same sub-sample of data as used in constructing the loose sample of Fig. 4.8. Clearly, the background has been significantly reduced, giving a much-improved signal-to-background ratio for subsequent reconstruction of B mesons.

Since the aim of the reconstruction process is to find B mesons, the selection takes into account the known signatures of events containing a b quark. In particular, the short observed lifetimes can be used to determine an interaction volume close to the primary vertex, which B mesons are highly unlikely to pass beyond. All ground state B mesons observed to date show similar lifetimes of around 1.6 ps, with the exception of the B_c, which has a lifetime of around 0.5 ps [11]. Therefore, even in highly energetic events, the B meson will decay within a distance of several centimetres: the typical decay length for a 100 GeV B^+ meson is 1 cm. The orbitally excited B mesons, and the J/ψ meson, are too short lived to travel any observable distance between production and decay, and so in all events of interest, the $\mu\mu$ vertex should be close to the primary vertex. For this reason,

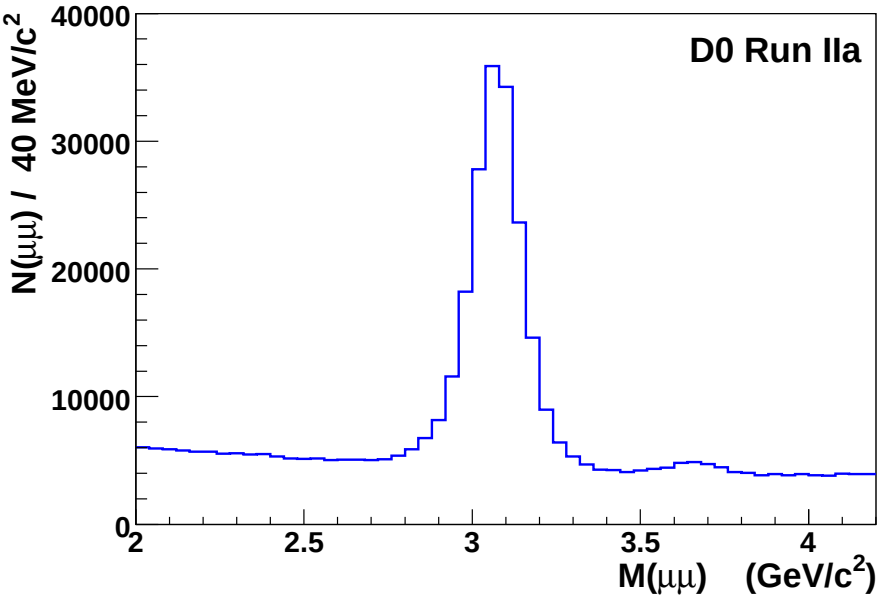

Figure 4.11: Di-muon invariant mass for a sub-sample of Run IIa data, after application of all J/ψ selection requirements. This can be compared to Fig. 4.8, showing the same distribution before application of the J/ψ-enhancing criteria.

J/ψ candidates are only accepted if they decay within 10.0 cm of the primary vertex for the event. The probability of a signal event failing this requirement is negligible at the Tevatron collision energy. On the other hand, there are many background processes which can produce $\mu\mu$ vertices at large distances from the PV.

Each pair of muons fulfilling the above requirements is then used to construct a J/ψ candidate. The J/ψ three-momentum is formed by vector addition of the momenta of the daughter muons, and its decay vertex is defined as the production vertex of the muon pair. The J/ψ is assigned an invariant mass, $M(J/\psi)$, under the assumption that the daughter particles have the muon mass as defined by the Particle Data Group (PDG) [11]. The additional condition $2.80 < M(J/\psi) < 3.35$ GeV/c^2 is then required of all candidates.

Having assigned the appropriate PDG masses to the muons, and measured their momenta in the detector, their kinematics are now completely defined. However, there is an

associated uncertainty on these momenta which will propagate through the reconstruction process. To reduce this uncertainty, the momenta of the muons are corrected using the J/ψ mass [11] as a constraint.

The selection requirements described above are rather loose, being designed to keep a large fraction of the signal, while removing only those events which are very unlikely to originate from real J/ψ decays. The tightening and fine tuning of criteria is undertaken at the next iteration of the reconstruction process; that is, when B^+ mesons are examined in decays to $J/\psi K^+$. In this way, the selection is tuned to be optimised for B^+ events, which may contain J/ψ candidates which differ (in their distributions of discriminating variables) from those found in generic events. The natural extension of this argument would be to wait one more stage, and tune the selections for the various excited states B_J and B_{sJ}. However, this type of optimisation relies upon large, well defined samples of signal and background events. In the case of the excited B mesons, such samples do not exist. This is partly due to the low expected signal yields of these rarely produced events, and partly because the states are not well understood at this time.

4.3.4 Optimising $B^+ \to J/\psi K^+$ Selection

The next stage in event selection is to reconstruct B^+ candidates by searching for combinations of $J/\psi K^+$, which are observed as coming from a common vertex. Since the J/ψ decays at the point of production, this means looking for K^+ mesons which are produced at the same point as the muon pair.

For any event containing a J/ψ candidate, an additional charged track is selected. This track must form a common vertex, V_B, with the muon pair, with $\chi^2(V_B) < 40$ as defined in equation (4.11). In addition, it must fulfill the following criteria:

1. $p_T > 0.5$ GeV/c;

2. $p_{total} > 0.7$ GeV/c;

3. At least two measurements in SMT.

From each set of three particles fulfilling these requirements, a B^+ candidate is constructed, with its invariant mass calculated under the assumption that the additional particle has the K^+ PDG mass. Conditions are imposed on both the production and decay vertices of the B^+ mesons. The requirement that the B^+ is produced at the PV is enforced by requiring that the impact parameter significance S_B is less than $\sqrt{40}$ [see Eq. (4.12)]. In addition, the B^+ is expected to travel an observable distance in the detector prior to decay. This is enforced by using the decay length significance, Γ_B, which is defined for any particle i as:

$$\Gamma_i = [l_{xy}/\sigma(l_{xy})]_i, \tag{4.13}$$

where l_{xy} is the decay length of the particle in the plane perpendicular to the beam direction, and $\sigma(l_{xy})$ is the associated uncertainty. The B^+ must then pass the selection $\Gamma_B > 3$. In this way, much of the background arising from direct production (i.e. production at the $p\bar{p}$ interaction) is eliminated.

The surviving B^+ candidates are then further selected to create the final B^+ signal sample, using the optimised tagging procedure described in this section. This likelihood ratio (LR) method provides a simple way of combining several discriminating variables into a single variable with increased power to separate signal and background, i.e. to "tag" signal events. It is described fully in reference [83].

The LR method takes a set of discriminating variables, $x_1, x_2, ..., x_n$, each of which is associated with a probability density function (PDF) for both signal $[f_i^s(x_i)]$ and background $[f_i^b(x_i)]$ samples. Here the PDF is the expected shape of the x_i distribution for the appropriate sample. A variable is termed discriminating if it shows observably different distributions in signal and background samples. An event E can be ascribed a probability that it comes from background, even for a single variable: if $x_i(E) = A$, then this probability is proportional to the ratio $y_i = f_i^b(A)/f_i^s(A)$. However, the selection is far more powerful when several variables are used simultaneously to form a combined tagging

variable, y, defined by:

$$y = \prod_{i=1}^{n} y_i; \qquad y_i = \frac{f_i^b(x_i)}{f_i^s(x_i)} \tag{4.14}$$

For some events, a particular variable x_i can be undefined. In this case, the corresponding variable y_i is set to unity. The selection is then made by requiring events to fulfill $y < y_0$; where y_0 can be varied to select the required tagging purity or efficiency.

In the case where the discriminating variables are independent, this selection procedure can be shown to give the best possible tagging performance; that is, it maximises the signal efficiency when compared to the background efficiency. Mathematical proofs of this assertion are given in references [83] and [84]. In practice, the discriminating variables are not fully independent, but by selection of suitable variables, the dependencies can be reduced to a level where the selection closely approaches the optimal level. The six variables chosen to participate in this optimised selection are:

1. The transverse momentum of the kaon, $p_T(K)$;
2. The minimum transverse momentum of the two muons, $p_T(\mu_{\text{soft}})$;
3. The B^+ decay length significance, Γ_B, defined in (4.13);
4. The B^+ impact parameter significance, S_B, defined in (4.12);
5. The kaon impact parameter significance, S_K;
6. The χ^2 of the B^+ decay vertex, defined in (4.10) and (4.11);

Correlation tests between the variables chosen for this analysis are described in Appendix A, and summarised here. The Pearson product-moment correlation coefficient, $r = \sigma_{xy}/(\sigma_x\sigma_y)$, is calculated for each pair of discriminating variables, (x, y) [85]. Here σ_{xy} is the covariance of the two variables, and $\sigma^2_{x(y)}$ is the variance of $x(y)$, defined in the usual way. The results are shown in Table A.1. Although correlation is not necessarily caused by dependence, small values of r are indicative of independent variables, while large values correspond to linear dependencies, and are undesirable. Almost every pair

of variables show negligible correlation, with only two r values having magnitude greater than 0.1. Hence the likelihood ratio method is expected to give near optimal selection in this case.

The probability density functions for both signal and background samples are extracted from data. The events are divided into three samples, according to the mass of the B^+ candidate, $M(B^+)$. The central sample includes all events satisfying $5.19 < M(B^+) < 5.34$. Two background data sets are defined: a low mass sample with $4.98 < M(B^+) < 5.13$, and a high mass sample with $5.40 < M(B^+) < 5.55$; i.e. the background selections are symmetrical about the central mass region. The use of such equidistant 'sideband' backgrounds helps to better model the parameters of the background events in the central mass region (i.e. under the B^+ mass peak), which cannot be isolated from signal events.

At this point, it is convenient to take the logarithm of both sides of equation (4.14), in order to separate the PDFs for each discriminating variable into different terms:

$$-\log_{10}(y) \;=\; \sum_{i=1}^{n} \left\{ \log_{10}[f_i^s(x_i)] - \log_{10}[f_i^b(x_i)] \right\} . \tag{4.15}$$

Here the minus sign is introduced as a convention to ensure signal events are identified by more positive values of this parameter. The probability density functions are now constructed from the distribution of each variable, $\log_{10}(x_i)$, for background and signal samples. For the background, the PDF is simply the distribution for all events in the two sidebands. For the signal sample, the PDF is formed by subtracting the background distribution multiplied by 0.5 from the distribution of events in the central mass band. The resulting distributions for each discriminating variable are shown in Fig. 4.12.

The combined tag parameter is then formed by combining these probability density functions (six signal, six background) according to equation (4.15), giving the distribution as shown in Fig. 4.13. The selection of signal events is enforced by requiring $-\log_{10}(y) > 0.08$. This value maximises the signal efficiency with respect to the background, i.e. it gives the largest value of $S/\sqrt{S+B}$, where S, B are the number of signal and background events respectively.

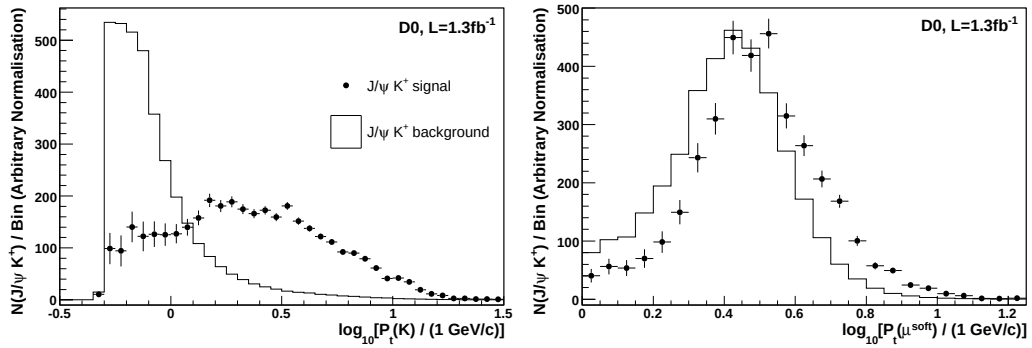

(a) $\log_{10}[p_T(K)]$; (b) $\log_{10}[p_T(\mu_{\rm soft})]$;

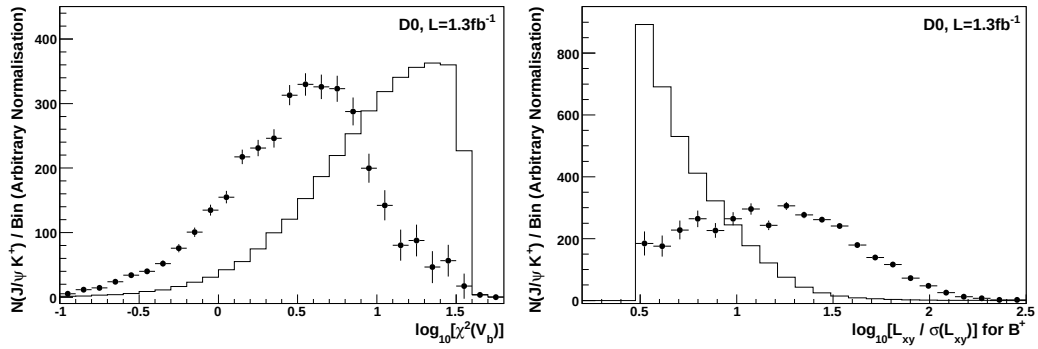

(c) $\log_{10}[\chi^2(V_B)]$; (d) $\log_{10}(\Gamma_B)$;

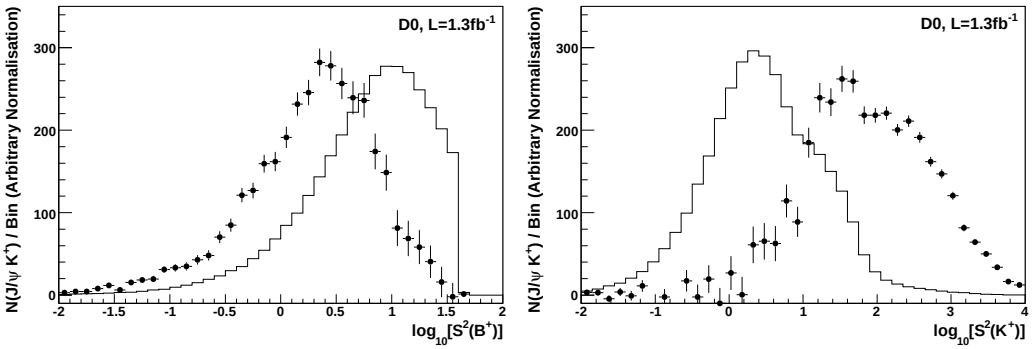

(e) $\log_{10}[S^2(B^+)]$; (f) $\log_{10}[S^2(K)]$;

Figure 4.12: Distributions of the discriminating variables used as inputs for the combined tag selection of B^+ candidates, extracted from Run IIa data. Shown separately are contributions from both signal-like (data points) and background-like (histogram) $J/\psi K^+$ combinations, as described in the text.

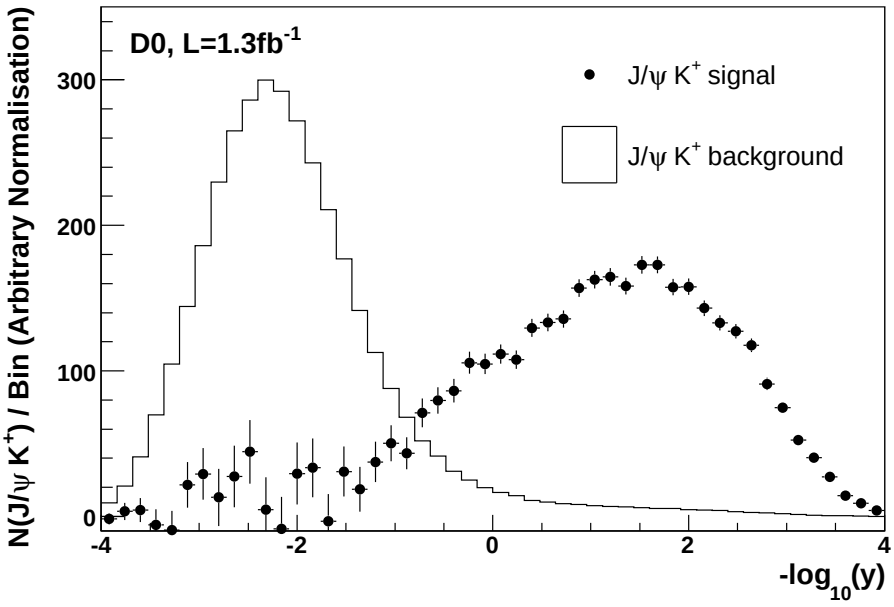

Figure 4.13: Distribution of $-\log_{10}(y)$ from Run IIa data, where y is the combined tagging variable, defined by (4.14). The separation of signal-like (data points) and background-like (histogram) $J/\psi K^+$ combinations can be clearly seen.

4.3.5 Fitting the $B^+ \to J/\psi K^+$ Invariant Mass Distribution

The B^+ candidates fulfilling all the requirements outlined in the previous sections form the starting sample for a search for the excited $L = 1$ mesons, B^{**} and B_s^{**}. However, before reconstructing these excited states, an additional requirement is imposed on the mass of the $B^+ \to J/\psi K^+$ system, in order to remove candidates with masses far from the central value of the resonance. This constraint should remove sideband background events which have survived the combined tagging selection.

In order to maximise the effect of such a mass window, and to better understand the different sources of background, it is necessary to examine the $J/\psi K^+$ invariant mass distribution, which is shown in Fig. 4.14. In addition to the binned data points, this figure also shows the function used to fit the shape of the distribution, which is described in this section.

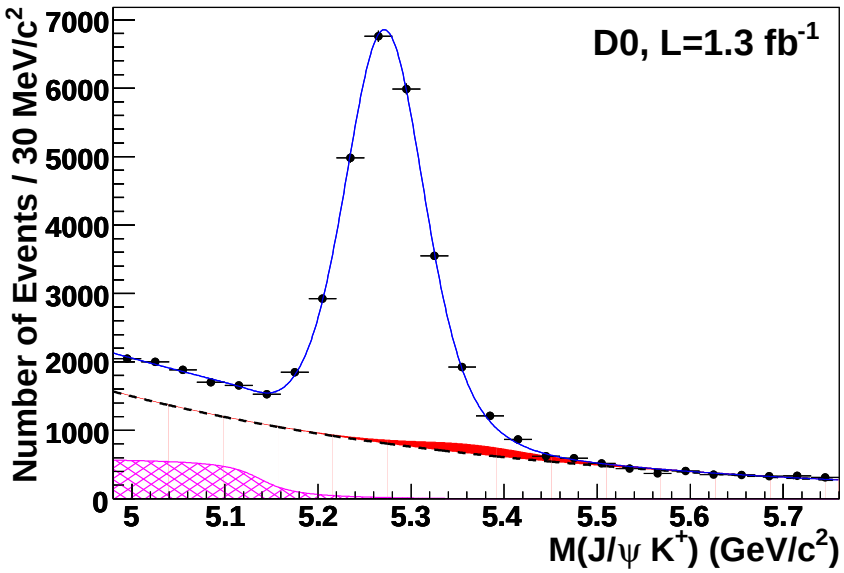

Figure 4.14: Invariant mass distribution of $J/\psi K^+$ events. The solid line shows the sum of signal and background contributions, as described in the text. The contribution of $J/\psi\pi^+$ events is shown by the solid filled area and the $J/\psi K^{+*}$ contribution is shown by the hatched area. The dashed line shows the exponential function modeling the combinatorial background.

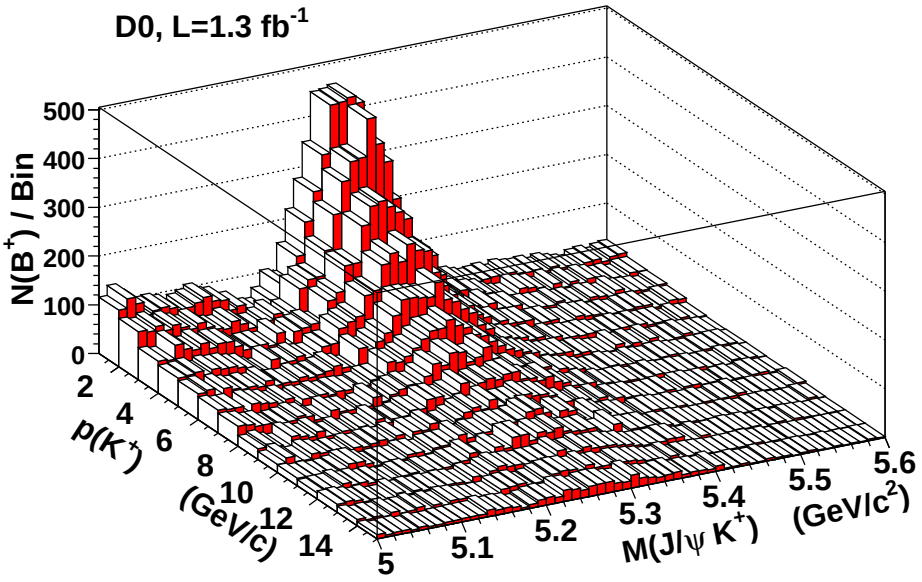

Figure 4.15: Two-dimensional distribution of $M_{J/\psi K}$ and p_K in $B^+ \to J/\psi K^+$ events, showing the characteristic broadening of the resonance as the kaon transverse momentum increases.

An unbinned maximum likelihood (UML) method is used to fit a generalised probability density function $f_{tot}(M_{J/\psi K}, p_K)$ to the two dimensional distribution in the $J/\psi K^+$ mass $M_{J/\psi K}$, and the kaon momentum p_K. Although the result of interest is the one dimensional projection of this fit onto the $M_{J/\psi K}$ axis, given by the solid line in Fig. 4.14, the total momentum of the kaon is an important factor in the shape of the fitting function. This is because higher momentum tracks are associated with a poorer mass resolution, as quantified by Eq. (4.1). This behaviour can be seen in Figure 4.15, which shows the two-dimensional distribution of J/ψ events in bins of $(M_{J/\psi K}, p_K)$. This plot is for illustrative purposes only, since the fit to data uses an unbinned method.

The sum of contributions from four sources is considered in the fit:

$$\begin{aligned} f_{tot}(M_{J/\psi K}, p_K) &= f_{J/\psi K}(M_{J/\psi K}, p_K) + f_{J/\psi \pi}(M_{J/\psi K}, p_K) \\ &+ f_{J/\psi K^*}(M_{J/\psi K}) + f_{comb}(M_{J/\psi K}) \end{aligned} \tag{4.16}$$

The functional forms of these contributions are now described, with motivation for their inclusion in the fitting procedure. The relative normalisation of each of the component functions is allowed to vary in the fit.

1. $f_{J/\psi K}(M_{J/\psi K}, p_K)$

   This function models the $B^+ \to J/\psi K^+$ signal peak, forming the dominant contribution to the fit. The mass distribution is parameterised by a Gaussian function, $G[M_{J/\psi K}, M_B, \sigma_B]$, with the resolution depending on the kaon momentum:

   $$\sigma_B = \sigma_0 \cdot \{1 + a_K \cdot E_K\}. \tag{4.17}$$

   Here σ_0 and a_K are free parameters in the fit. Although the above expression relates the B^+ width to the kaon energy, E_K, this quantity is in turn completely defined by the momentum through the relation $E_K = \sqrt{\bar{p}_K^2 + m_K^2}$, since the kaon mass m_K is fixed at the PDG value [11]. The central value, M_B, of the B^+ mass is also a free parameter. Finally, the normalisation of this contribution is scaled by a p_K-dependent factor N_1, to account for the sample kinematics, i.e. the fact that the $B^+ \to J/\psi K^+$ signal candidates are not evenly distributed in p_K (as is clear from Fig. 4.15). This factor is quadratic in E_K, with the particular parameterisation determined separately for three energy ranges, quantified by three coefficients a_1–a_3 which participate in the fit:

   $$\begin{aligned} N_1 =& 1 + \frac{a_1}{3}(E_K - 3) + \frac{a_2}{9}(E_K - 3)^2 && E_K < 3\ \text{GeV}/c^2, \\ =& 1 + \frac{a_3}{7}(E_K - 3) && 3\ \text{GeV}/c^2 < E_K < 10\ \text{GeV}/c^2, \\ =& 1 + a_3 && E_K > 10\ \text{GeV}/c^2. \end{aligned} \tag{4.18}$$

   The resulting two-dimensional fitting function for this component is shown in binned-format in Figure 4.16.

2. $f_{J/\psi\pi}(M_{J/\psi K}, p_K)$

   It is possible that the additional track which forms a vertex with the $\mu\mu$ pair might

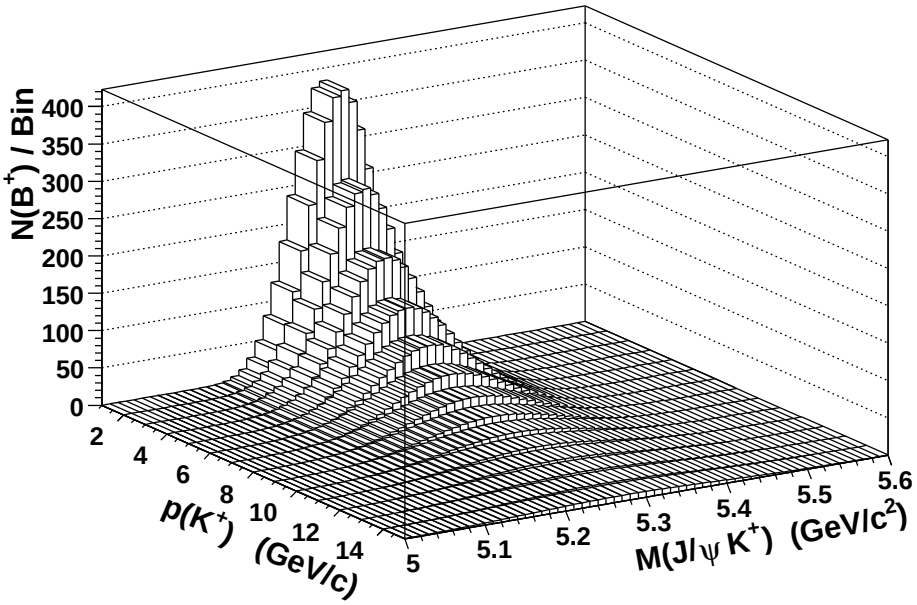

Figure 4.16: Two-dimensional binned representation of the $(M_{J/\psi K}, p_K)$ fitting function, as used to model the shape of the $B^+ \to J/\psi K^+$ signal peak in data. This component forms the largest source of B^+ candidates, and takes into account both the worsening resolution and reduced number of events, as the kaon momentum increases.

be a pion misidentified as a kaon, while still arising from an underlying B^+ event. As such, a contribution from $B^+ \to J/\psi\pi^+$ decays is allowed in the fit. In the reconstruction process, the energy of the additional particle is calculated under the assumption that it has the kaon mass; this assumption is also used in calculating the B^+ invariant mass. As a result, the $J/\psi\pi^+$ signal in the mass distribution will be shifted to a higher mass, M_R:

$$M_R^2 = (E_{J/\psi} + E_K)^2 - (\bar{p}_{J/\psi} + \bar{p}_K)^2, \tag{4.19}$$

$$M_R^2 - M_B^2 = 2E_{J/\psi} \cdot (E_K - E_\pi) + m_K^2 - m_\pi^2, \tag{4.20}$$

where $E_\pi = \sqrt{\bar{p}_K^2 + m_\pi^2}$ is the true energy of the pion. This shift from the true B^+

mass will therefore be strongly dependent on the kinematics of the event. For this contribution, the mass distribution is again fitted by a Gaussian function, with central value M_R, and width σ_R. The resolution of this 'reflected' peak is expected to be worse than for the $J/\psi K$ resonance because the track energies are higher. Since the mass shifts are relatively small in this case, a simple linear extrapolation is used to determine $\sigma_R = \sigma_B \cdot M_R/M_B$. Again, a quadratic E_K-dependent scale-factor is applied to account for the kinematics of the $J/\psi\pi^+$ sample, with the parameterisation as in Eq. (4.18), and the coefficients a_1–a_3 constrained to be the same for both $J/\psi K^+$ and $J/\psi\pi^+$ mass peaks. The resulting contribution to the B^+ mass fit is shown by the solid filled area in Fig. 4.14.

3. $f_{J/\psi K^*}(M_{J/\psi K})$

   There is a second source of background events arising from genuine B^+ decays. These are decays to excited kaon states, $K^*(892)$ and $K_1(1270)$, which in turn can decay into final states containing ground state kaons. For such events, since there are additional undetected particles in the decay chain, there will be energy missing from the B^+ decay. Such partially reconstructed events are therefore expected to contribute mainly to the low-mass background. The effect of these events on the $J/\psi K^+$ mass distribution is estimated from a dedicated Monte Carlo simulation, described in Section 5.5.3, and the resulting shape is shown by the hatched area in Fig. 4.14. The majority of these background events come from decays $B^+ \to J/\psi K^{+*}$, with $K^{+*} \to K\pi$; the resulting mass distribution is broad, with a threshold near $M(B) - M(\pi)$. No dependence on the kaon momentum is included in $f_{J/\psi K^*}$, and the only free parameter in the fit is the relative contribution of events.

4. $f_{comb}(M_{J/\psi K})$

   This final function represents the contribution from non-resonant, combinatorial backgrounds. Examples are particles pairs incorrectly assumed to come from a common vertex, in spite of the precautions highlighted in Section 4.3.1. The resulting mass distribution is expected to be a continuous, slowly changing function of mass; it is modeled by an exponential function, with the decay constant inserted in

the fit as a free parameter. This is shown by the dashed line in Fig. 4.14. Again, no dependence is attributed to the kaon momentum.

The UML fit is performed over the range $4.98 < M_{J/\psi K} < 5.76$ GeV/c^2, in order to ensure a stable fit over the background component. In total, the $B^+ \to J/\psi K^+$ and $B^+ \to J/\psi \pi^+$ mass peaks contain 23287 ± 344 (stat) events, comprising 22445 ± 340 $(J/\psi K^+)$, and 854 ± 92 $(J/\psi \pi^+)$ candidates. The B^+ invariant mass returned by the fit is:

$$M(B^+) = 5271.6 \pm 0.4 \text{ (stat) MeV}/c^2. \tag{4.21}$$

Based on the results of this fit, the requirement $5.19 < M(B^+) < 5.36$ GeV/c^2 is imposed on all events which are used in $B^{**}_{(s)}$ reconstruction. This represents the central region of the $J/\psi K^+$ signal, with a range of approximately $2\sigma_G$ on either side of the central mass. Here $\sigma_G = 41.8 \pm 0.4$ MeV/c^2 is the width of the B^+ mass peak when fitted with a single Gaussian function. This selection reduces the number of candidates in the signal sample to:

$$N[B^+ \to J/\psi(K^+, \pi^+)] = 20915 \pm 293 \text{ (stat.)} \pm 200 \text{ (syst.) events.} \tag{4.22}$$

This number is later used to determine the relative production rates of the B^{**} and B^{**}_s states. Two sources of systematic uncertainty are investigated. To test the effect of the particular fitting range, the upper and lower limits are varied, and the change in $N(B^+)$ assigned as the associated uncertainty. In addition, the form of the fitting function is adjusted in several ways, and an uncertainty is derived from the effect of these changes. For example, the parameters of the $J/\psi K^*$ component are varied within their $\pm 1\sigma$ uncertainty limits, as determined from the fit to simulated data.

4.3.6 Comparing D0 Masses to the World Average

Having made a precise measurement of the B^+ mass using a large, signal-enhanced sample, there is an additional effect which must be discussed. This is the so-called D0 momentum scale uncertainty, which results in a small discrepancy between the masses measured by the experiment, and the world averages listed by the Particle Data Group [11].

Determining the invariant masses of particles, reconstructed from multiple tracks, relies on unbiased measurements of the track momenta. Any systematic deviations on these measurements will propagate through the reconstruction process, moving detected masses away from their true values. Hence it is important to test the detector response to certain well studied reference particles, such as the B^+ meson. The B^+ mass recorded by the PDG is 5279.1 ± 0.5 MeV/c^2; which can be compared to the D0 measured mass in Eq. (4.21), showing a shift downward from the true mass by $\epsilon_M(B^+) = 7.5$ MeV/c^2. In the absence of a full understanding of this effect, a correction is applied under the assumption that the shift for a given mass measurement, $\epsilon_M(m)$, is proportional to the mass m. Any masses measured in this analysis will therefore be manually adjusted upwards, to compensate for this effect, by an amount:

$$\epsilon_M(m) = \epsilon_M(B^+) \cdot \frac{m}{M(B^+)} \tag{4.23}$$

Since neither the cause or the behaviour of the momentum scale uncertainty are fully understood, a systematic uncertainty equal to the value of the shift is assigned to each mass corrected in this way.

4.4 Selecting B^{**} Candidates

Once the selection of B^+ candidates has been made, the search for orbitally excited $L = 1$ mesons can begin. For convenience, the expected decays of the B^{**} states (4.4–4.6) are

repeated here:

$$B_1 \to B^{*+}\pi^-,\ B^{*+} \to B^+\gamma; \tag{4.4}$$

$$B_2^* \to B^{*+}\pi^-,\ B^{*+} \to B^+\gamma; \tag{4.5}$$

$$B_2^* \to B^+\pi^-. \tag{4.6}$$

The photon emitted during the de-excitation of B^{*+} to the ground state is not used in the reconstruction process. The difficulty in correctly tagging photons from this decay would reduce both the purity and efficiency of the event selection. The mass difference $M(B^+) - M(B^{*+})$ is well defined and precisely measured as 45.78 ± 0.35 MeV/c^2, which corresponds to the energy E_γ of the photon emitted. As a result, all three of the B^{**} decays above are found by reconstructing $B^+\pi^-$ combinations, with the knowledge that those decays proceeding via the singly excited B^{*+} meson will be missing an energy of E_γ.

For every B^+ event, defined by the criteria in the previous section, an additional particle is selected. This must correspond to a track in the detector with opposite charge to the B^+, and with at least one hit in each of the CFT and SMT components. This track is then assigned the mass of the pion [11]. Since the B^{**} mesons decay at the production point, the additional track is required to originate from the primary vertex by applying the condition on its significance $S_\pi < \sqrt{6}$ [see Eq. (4.12)]. In addition, the pions from this decay are expected to be distinguishable from background tracks by their large transverse momenta. As such, the additional track is required to fulfill $p_T(\pi) > 0.75$ GeV/c. Both of these kinematic cuts were fixed in a preliminary study which contained a smaller dataset, corresponding to 300 fb^{-1} of integrated luminosity.

For illustrative purposes, the transverse momentum distribution of the pion, in signal and background samples, is shown in Fig. 4.17. Here the background sample is defined by all $B\pi$ combinations with opposite charges, which fulfill the track quality cuts (number of SMT and CFT hits), and which have an invariant mass satisfying $(5.28 < M(B^+\pi^-) < 5.58)$ GeV/c^2 or $(5.83 < M(B^+\pi^-) < 6.13)$ GeV/c^2. This sideband p_T distribution is compared to the signal distribution estimated from simulation (see Section 5.2.1), since

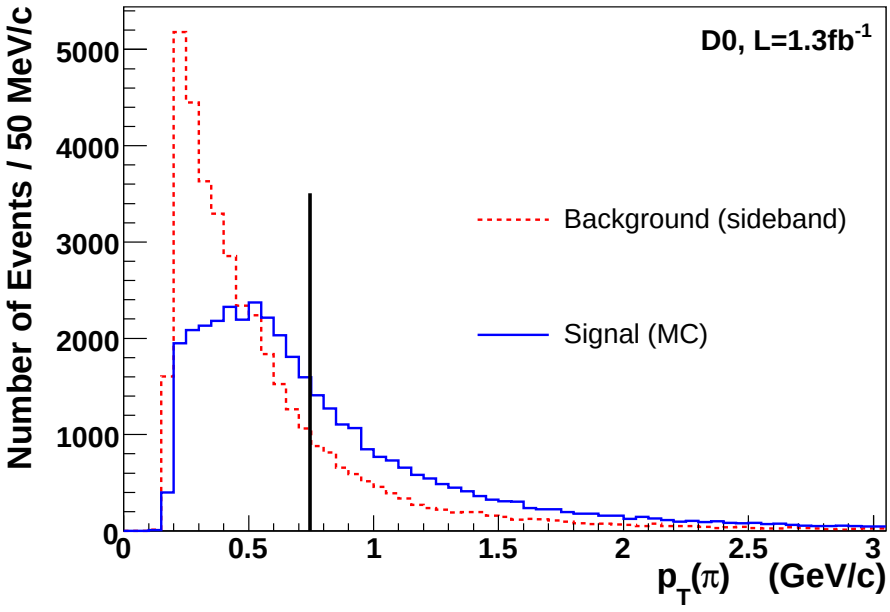

Figure 4.17: Pion transverse momentum distributions, in B^{**} decay, for signal and background samples. The background sample is defined by sidebands in the invariant mass $M(B^+\pi^-)$; the signal sample is taken from simulation. The vertical solid line shows the requirement $p_T > 0.75$ GeV/c, enforced to remove background in the final B^{**} sample.

it is not possible to isolate the signal contribution in data. As shown in the figure, the background is dominant for transverse momenta below 0.6 GeV/c, with the relative contribution of signal events increasing for larger p_T.

The B^{**} candidates are then reconstructed in the standard way: The four-momenta of the B^+ and the selected pion are added to produce the B^{**} four-momentum vector. The three-momentum of the resulting object is then corrected using the PDG B^+ mass as a constraint, and is in turn used to calculate the $(B^+\pi^-)$ invariant mass.

All suitable pions in an event are allowed to be reconstructed with the B^+, i.e. no constraint is placed on the multiplicity of B^{**} candidates per B^+. The alternative would be to select only the 'best' n pions per B^+, for a small value of n. However, this method relies on additional knowledge of what makes a candidate 'good', without which the requirement is unlikely to remove background events preferentially over signal events. Since

there will be significant background tracks with both low impact parameter significance, and high p_T, neither of these quantities appear suitable for labeling the best pion candidates. Instead, this analysis relies on a high pion detection efficiency giving a large yield, so that the signal and background components of the mass distribution can be separated in the fitting procedure.

Figure 4.18 shows the distribution of the B^{**} multiplicity for the resulting signal sample. Also shown is the same plot for like-charge $B\pi$ combinations, which will contain no signal events. The background histogram is normalised to contain the same number of events as the signal, for comparison. This plot demonstrates that in order to maximise the number of signal events, a large number of background events are also collected.

For each $B^+\pi^-$ combination satisfying the above criteria, the mass difference ΔM is computed:

$$\Delta M = M(B^+\pi^-) - M(B^+). \tag{4.24}$$

The distribution of ΔM can then be examined and fitted by a suitable parameterisation, as detailed in Chapter 6.

4.5 Selecting B_s^{**} Candidates

The selection of B_s^{**} events is very similar to the procedure used for B^{**} candidates, with the exception that instead of searching for appropriate $B\pi$ pairs, we reconstruct BK combinations. Since no method to distinguish light charged mesons is utilised in this analysis, this effectively means assigning the kaon mass to the selected tracks, and not the pion mass. The relevant decays (4.7–4.9), are repeated here for convenience:

$$B_{s1} \to B^{*+}K^-,\ B^{*+} \to B^+\gamma; \tag{4.7}$$

$$B_{s2}^* \to B^{*+}K^-,\ B^{*+} \to B^+\gamma; \tag{4.8}$$

$$B_{s2}^* \to B^+K^-. \tag{4.9}$$

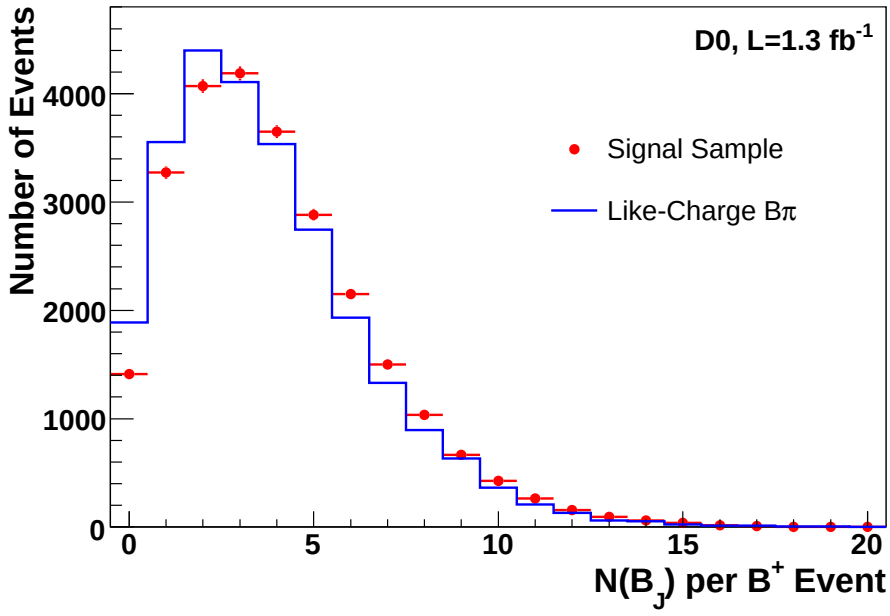

Figure 4.18: Multiplicity of B^{**} candidates per B^+ event. Shown separately are distributions for the signal sample, and the like-charge $B\pi$ sample as described in the text. The scale is only valid for the signal sample. The large multiplicities demonstrate the necessity of an effective mass-fitting method to resolve the signal component.

As explained in the previous section, no attempt is made to reconstruct the photon in $B^{*+} \to B^+\gamma$ decays, so events reconstructed from decays (4.7) and (4.8) will have a missing energy of $E_\gamma = 45.78 \pm 0.35$ MeV.

The selection proceeds in the same way as for B^{**} events: an additional track is selected, with charge opposite to the B^+, at least one hit in each of the CFT and SMT components, and impact parameter significance $S_K < \sqrt{6}$. This track is assigned the kaon mass, and is allowed into the signal sample if it passes the transverse momentum threshold $p_T > 0.60$ GeV/c. This final kinematic requirement is somewhat looser than the 0.75 GeV/c required for the pions in B^{**} decay, in order to increase the signal efficiency. This will compensate for the lower expected production rate of B_s^{**} particles, allowing sufficient yield to distinguish signal from background in the mass fit.

The B_s^{**} candidates are then reconstructed from the selected B^+K^- combinations,

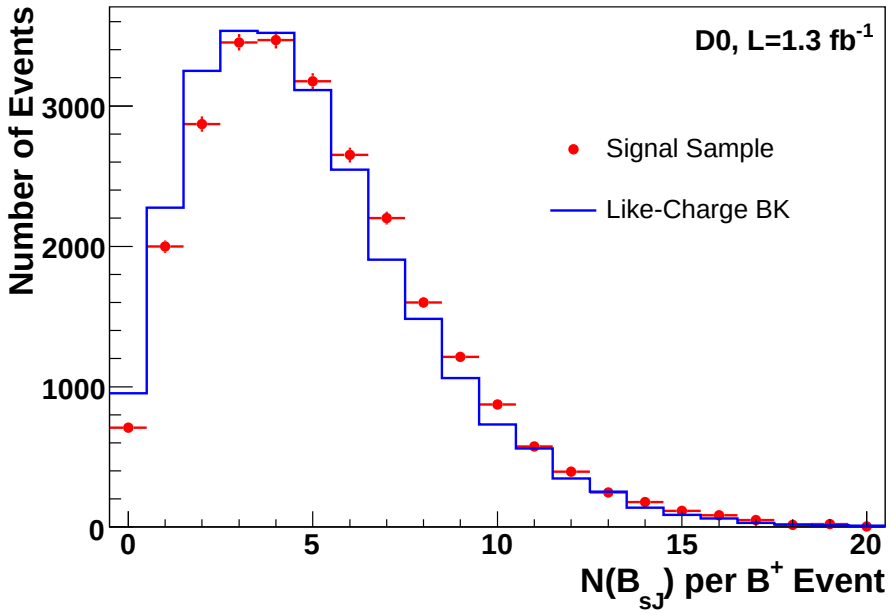

Figure 4.19: Multiplicity of B_s^{**} candidates per B^+ event. Shown separately are distributions for the signal sample, and the like-charge BK sample as described in the text. The scale is only valid for the signal sample.

with their momentum corrected using the B^+ mass constraint, and the invariant mass $M(B^+K^-)$ is determined.

Since all suitable kaons are allowed to form potential B_s^{**} candidates, the multiplicity $N(B^+K^-)$ per B^+ event is again a quantity worth examining. Figure 4.19 shows the distribution of this parameter, for the signal sample, and the like-charge BK sample. The background histogram is normalised to contain the same number of events as the signal.

For each event in the resulting sample, the quantity ΔM_s is then calculated:

$$\Delta M_s = M(B^+K^-) - M(B^+) - M(K^-). \tag{4.25}$$

Note that the masses of both daughters are subtracted from the total invariant mass, which is not the case for ΔM. The expected mass range of B_s^{**} states is close to the production threshold $\Delta M_s = 0$, therefore it is useful to arrange the scale in this way.

4.6 Summary of Selection Criteria

The selection of events containing orbitally excited mesons requires a large B^+ sample, with high purity. The initial selection of $\mu\mu K^+$ candidates is kept loose, allowing the combined tagging method to remove background with near optimal performance. The subsequent selection of $B^{**}_{(s)}$ candidates is targeted at maintaining a high detection efficiency, rather than maximising the signal-to-background ratio. In this way a statistically significant sample of signal events can be collected, with the subsequent mass fitting procedure used to isolate signal and background contributions.

Table 4.1 summarises all the selection criteria applied in the selection of B^+ candidates. Table 4.2 shows the additional requirements imposed on B^{**} and B^{**}_s events. For definitions of the selection variables, and motivation for these selections, please see Sections 4.3.3–4.3.5. New or unusual terminology is explained by the footnotes.

Table 4.1: Summary of all B^+ selection criteria.

Objects of Interest	Requirement
All muon pairs μ_1, μ_2 forming a common vertex $(i = 1, 2)$.	$p_T(\mu_i) > 1.0$ GeV/c $N^{hits}_{CFT}(\mu_i) \geq 1$ $N^{hits}_{SMT}(\mu_1) \geq 2$ or $N^{hits}_{SMT}(\mu_2) \geq 2$ nseg$(\mu_1) = 3$ or nseg$(\mu_2) = 3$ if nseg$(\mu_i) \geq 1$ then $p_T(\mu_i) > 1.5$ GeV/c
Muon pairs where nseg$(\mu_i) = 0$, nseg$(\mu_j) = 3$.	$\chi^2(\mu_i) < 25$ and $\chi^2(\mu_j) < 25$ $p_{total}(\mu_i) < 7.0$ GeV/c $p_T(\mu_j) > 2.5$ GeV/c $p_T(\mu_i) + p_T(\mu_j) > 4.0$ GeV/c $P[\bar{E}(\mu_i)] \geq 0.015 * N_{layers}(\mu_i)$
Reconstructed J/ψ candidates.	$l_{PV}(J/\psi) < 10$ cm [a] $2.80 < M(J/\psi) < 3.35$ GeV/c^2
Kaon in decay $B^+ \rightarrow J/\psi K^+$.	$p_T(K) > 0.5$ GeV/c $p_{total}(K) > 0.7$ GeV/c $N^{hits}_{SMT}(K) \geq 2$
Reconstructed B^+ candidates.	$\chi^2(V_B) < 40$ $S(B^+) < \sqrt{40}$ $\Gamma_B > 3$ [b] $-\log_{10}(y) > 0.08$ [c] $5.19 < M(B^+) < 5.36$ GeV/c

[a] The distance between the $J/\psi \rightarrow \mu\mu$ decay vertex and the primary interaction point.
[b] The decay length signifi cance, defi ned in Eq. (4.13).
[c] The combined tag parameter, defi ned in Eq. (4.15).

Table 4.2: Summary of all B^{**} and B_s^{**} selection criteria.

System of Interest	Requirement
B^{**} candidates, reconstructed in decays to $B^+\pi^-$	$p_T(\pi^-) > 0.75$ GeV/c $S(\pi^-) < \sqrt{6}$ $N_{SMT}^{hits}(\pi^-) \geq 1$ $N_{CFT}^{hits}(\pi^-) \geq 1$
B_s^{**} candidates, reconstructed in decays to B^+K^-	$p_T(K^-) > 0.60$ GeV/c $S(K^-) < \sqrt{6}$ $N_{SMT}^{hits}(K^-) \geq 1$ $N_{CFT}^{hits}(K^-) \geq 1$

Chapter 5

Event Simulation

GENERATING SAMPLES OF SIMULATED EVENTS is a very important aspect of particle physics analysis. It allows detector and reconstruction effects to be disentangled from the underlying particle properties and behaviour. This is possible because the true parameters of a simulated event (for example, the masses, energies, momenta and trajectories of the generated particles) are known, which is not the case for real data. As a result of these additional constraints, valuable information can be extracted, such as the experimental mass resolution or the detection efficiency for a particular event type. In addition, simulation allows the distributions of kinematic variables for specific signal or background sources to be investigated, without contamination from other types of events.

Both of these features are exploited for the purposes of this analysis. The specific uses of simulated events are described in Sections 5.3–5.5. In the introductory sections, the basic principles of simulation are outlined, with descriptions of the main $B^{**}_{(s)}$ samples produced by the event generator.

5.1 Overview of the Simulation Methods

All processes involving B mesons are simulated using the PYTHIA Monte Carlo (MC) event generator [86]. This program allows realistic and complete multi-particle events to be generated from simulated $\bar{p}p$ collisions. For all samples generated in this analysis, the generator parameters, such as the collision energy, are tailored to match the specific

conditions found at the D0 detector. The properties of the relevant orbitally excited $B^{**}_{(s)}$ states are manually adjusted to give reasonable values, based on preliminary studies at D0, and on theoretical considerations, as described later in this section.

Of the particles involved in the simulated events, only the very short lived $B^{**}_{(s)}$ mesons are allowed to decay in the PYTHIA software. For all other particles, the EVTGEN decay package is utilised [87]. This is designed specifically to simulate the decays of B hadrons, as realistically as possible given current knowledge of the underlying physics. In some cases, it is necessary to isolate a particular decay chain, by manually setting the appropriate branching fractions to unity. In other cases, it is desirable to replicate the true behaviour of particle decay, in which case the default branching ratios from EVTGEN are retained.

At this stage, before the most computationally intensive phases of simulation, the events can be filtered to create custom samples containing only the desired events; kinematic requirements can also be imposed, for example, to remove low energy particles which would not survive the subsequent reconstruction and event selection.

The interface of the PYTHIA generator and the EVTGEN decay package works under the assumption that particles are produced and decay in vacuo. This is clearly not the case within a colliding beam experiment, where the various detector components will interact with the particles. The detector effects include those required to observe and measure the particles, such as loss of energy due to ionisation of the tracking chamber material. In addition, there are unwanted effects, such as interaction with the detector structure or wiring components, or with the material in the solenoid and toroid magnets. All of these aspects are taken into account by putting events through a full GEANT simulation of the D0 Run IIa detector [88].

Next, the output from the detector simulation is further processed to account for several effects. These include noise from the tracking detector components and detector inefficiencies. A contribution from 'zero bias' events, extracted from real data, is also overlaid on the simulation. These events are those which would be observed with a totally inclusive trigger, typically having low transverse energy and multiplicity. They represent a true sample of $p\bar{p}$ interactions, without the biasing property of the physics trigger.

Zero bias events must be considered because at the current Tevatron luminosities, there are usually multiple $p\bar{p}$ interactions per bunch crossing; if any of these passes the trigger requirements, the other interactions will also be accepted into the data sample: and the simulation must be able to account for this important effect.

Finally, the simulated data is passed through the D0 reconstruction software, in exactly the same way as real data. This is followed by the analysis-specific event selection and reconstruction process described in Chapter 4. This completes the discussion of the general methods used to generate simulated events. In the following section, the details of some important MC samples are described.

5.2 Simulated Data for Orbitally Excited B Mesons

5.2.1 B^{**} Events

Following initial investigation of the $\Delta M = M(B^+\pi^-) - M(B^+)$ distribution, it appears that all three decays (4.4–4.6) may contribute to the B^{**} signal. As such, all three are included in the simulation: one half of all events are $B_1 \to B^{*+}\pi^-$; the other half are B_2^* events which decay with equal probability into $B^+\pi^-$ and $B^{*+}\pi^-$ channels, following theoretical expectations. Subsequent decays are forced to match those investigated in the data: $B^{*+} \to B^+\gamma, B^+ \to J/\psi K^+, J/\psi \to \mu\mu$.

It is important to set the generated masses as close as possible to the true particle values, since the mass resolution and efficiency are strongly dependent on particle momenta, which are determined by the mass of the decaying B^{**} state. Since no precise measurements have been made on this system, the masses are fixed according to values obtained from preliminary fits over the data. These are found to be:

$$M(B_1)_{\text{sim}} = 5720.0\,\text{MeV}/c^2\,, \tag{5.1}$$

$$M(B_2^*)_{\text{sim}} = 5745.0\,\text{MeV}/c^2\,. \tag{5.2}$$

All other relevant particle masses are set according to the Particle Data Group world averages [11].

It is not possible to use the same method to determine the physical widths of the B^{**} states, since the resonances observed in the ΔM distribution will be smeared by the limited mass resolution of the detector. This is an unknown effect at this stage: it being one of the objects of the simulation to measure and quantify it. Fortunately, neither the detection efficiency nor the resolution are found to be significantly influenced by the specific choice of widths (within the reasonable bounds determined by theoretical predictions). The widths of both B_1 and B_2^* are fixed to be:

$$\Gamma(B_1)_{\text{sim}} = \Gamma(B_2^*)_{\text{sim}} = 5.0 \text{ MeV}/c^2 \, . \tag{5.3}$$

Some loose kinematic requirements are imposed on the events, to increase the proportion which survive the event selection. All final state particles are required to have an absolute pseudorapidity $|\eta| < 2.2$. In addition, the following transverse momenta criteria are enforced:

- $p_T(\mu) > 2.0$ GeV/c ;
- $p_T(K^+) > 0.5$ GeV/c ;
- $p_T(\pi^-) > 0.6$ GeV/c .

Under these conditions, with parameters fixed as above, a sample of $47,330$ B^{**} events was generated. The ΔM distribution at the generator level, before the detector simulation, is shown in Fig. 5.1(a). Also shown, in Fig. 5.1(b), is the equivalent distribution for events which have passed through the full detector simulation and been reconstructed by the D0 software. There are several important ways in which the distribution is modified by this process. Firstly, the B_2^* signal is divided into two peaks; this is because the photon in decays $B^{*+} \rightarrow B^+\gamma$ is not reconstructed, and so $B_2^* \rightarrow B^{*+}\pi^-$ events are detected with missing mass corresponding to the photon energy of 45.78 ± 0.35 MeV. The B_1 signal is also displaced to lower mass by this effect, hence the resulting three peak structure.

Secondly, the number of events is much reduced, as a result of the combined inefficiencies inherent at each stage of detection and reconstruction. Only around $\sim 17\%$

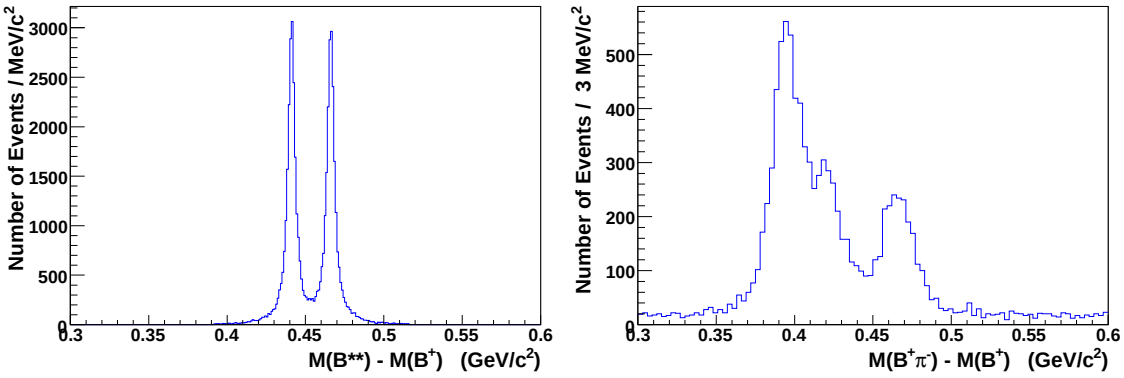

(a) Generated ΔM distribution;

(b) Reconstructed ΔM distribution;

Figure 5.1: ΔM distribution for simulated B^{**} events, showing the difference between generated masses, and those reconstructed following detector interaction, track finding and event selection.

(8109) of signal events survive to be observed. Note that this number cannot be interpreted as the absolute detection efficiency, since the generated events have already passed kinematic selections and so do not fully represent real data. Detection efficiencies are discussed in some detail in Section 5.4.

The constant background of around 1–2 events per MeV/c^2 is due to mis-reconstructed candidates, where a pion and B^+ are associated which did not arise from a common B^{**} decay. The majority of zero bias events are removed by the vertexing requirements, since they will generally originate several centimetres apart along the beampipe. Finally, the original narrow ($\Gamma = 5$ MeV/c^2) Breit-Wigner resonances have been smeared by the detector response, which has limited mass resolution. This effect is examined in Section 5.3.1.

The pseudorapidity and transverse momentum requirements listed above, while increasing the number of useful events in the simulation, do lead to some loss of information. In order to examine the distribution of $p_T(\pi)$, as shown in Fig. 4.17, an additional smaller sample ($\sim$ 19K events) of B^{**} MC data was generated with no selections imposed on the pion. The kinematic requirements must also be taken into account when calculating the reconstruction efficiencies, as described later.

5.2.2 B_s^{**} Events

The preliminary studies of the ΔM_s distribution indicate that the main decay of interest is $B_{s2}^* \to B^+K^-$, with a possible $B_{s1} \to B^{*+}K^-$ contribution, and little or no signal from $B_{s2}^* \to B^{*+}K^-$ events. Following these findings, a sample of 17508 B_{s2}^* events was generated, with all particles decaying through the B^+K^- channel. The B_{s2}^* mass is fixed according to an exploratory fit over the data:

$$M(B_{s2}^*)_{\text{sim}} \;=\; 5839.0 \text{ MeV}/c^2 \; . \tag{5.4}$$

The width of this resonance is fixed at 5.0 MeV/c^2. Again, the exact value of the generated width is not found to influence the resulting mass resolution or efficiency measurements.

As with the B^{**} sample, the decays are forced to match those investigated in the data: $B^+ \to J/\psi K^+, J/\psi \to \mu\mu$, with masses of these particles fixed at the default PYTHIA values. The same kinematic criteria are also imposed at the generator level, with the substitution $\pi^- \to K^-$.

The ΔM_s distribution of B_{s2}^* events from the generator is shown in Fig. 5.2(a). The same distribution for fully reconstructed events is shown in Fig. 5.2(b), showing the effect of the detector response. Here there is no missing energy, since all decays are direct to the ground state B^+, and are thus fully reconstructed. Only $\sim 17\%$ (2853 events) of the generated sample survives the event selection process. In addition, the characteristic smearing of the mass peaks is also observed, as investigated fully in Section 5.3.2.

The search for a possible B_{s1} signal, as described in Section 6.3.4, requires that the experimental mass resolution be determined for $B_{s1} \to B^{*+}K^-$ decays. This is expected to be better than the corresponding quantity for B_{s2}^* decays, since the momenta of daughter particles will be smaller for the less massive B_{s1} state. For this purpose, a test sample of $\sim 10,000$ simulated events is generated for this decay, with the mass fixed according to preliminary fits:

$$M(B_{s1})_{\text{sim}} \;=\; 5828.0 \text{ MeV}/c^2 \; . \tag{5.5}$$

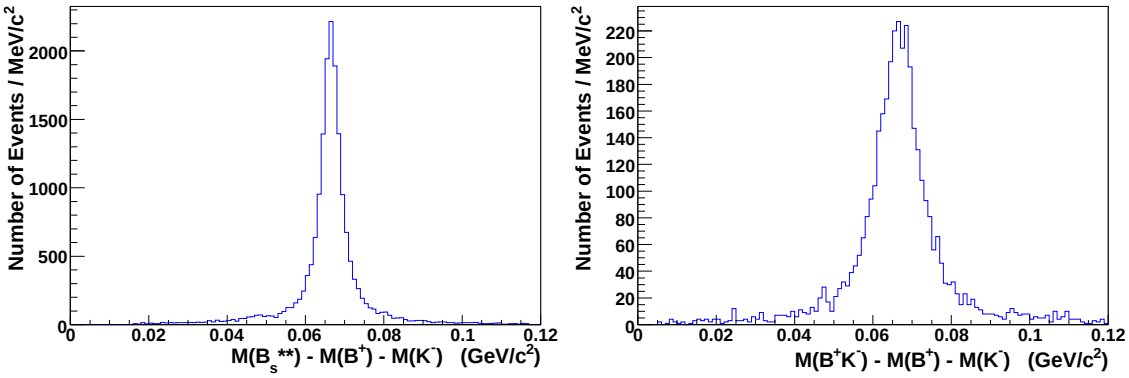

(a) Generated ΔM_s distribution;

(b) Reconstructed ΔM_s distribution;

Figure 5.2: ΔM_s distribution for simulated B^*_{s2} events, showing the difference between generated masses, and those reconstructed following detector interaction, track finding and event selection.

Here the proximity to the production threshold can distort the shape of the mass resonance, which will influence the measured detection efficiency. The test sample is not used to measure the efficiency, however, and so the choice of width is not crucial; it is fixed to be 0.1 MeV/c^2.

This completes the description of the main samples of simulated data, as used to measure experimental mass resolutions (Section 5.3), detection efficiencies (Section 5.4), and the effect of 'reflections' from mis-identified tracks (Section 5.5).

5.3 Experimental Mass Resolution of the $B^{**}_{(s)}$ States

The detection and reconstruction of particle physics events is associated with a finite mass resolution: the measured mass of a particle can be different from its true value, as evident from Figures 5.1 and 5.2. For a given event type, there will be an associated detector response function, which is the probability density function for the mass difference, $M_{\text{true}} - M_{\text{detected}}$. The particular shape and parameters of this function will be different for each analysis, since they are strongly influenced by event topology and kinematics.

Since the power of the $B^{**}_{(s)}$ analysis rests with the ability to accurately model and fit the shape of signal peaks in the $\Delta M_{(s)}$ distributions, the smearing effect of the detector response must be determined and used as an input to the fitting procedure. The measured resonance shapes are then expressed as the convolution of true physical peak shapes with the detector response function; this is discussed fully in Chapter 6, for example in Eq. (6.3).

The procedure for measuring the detector response function is as follows. The appropriate sample of simulated data is passed through the full event selection and reconstruction algorithm, described in the previous chapter. For each event which survives to be 'detected', the measured invariant mass $M[B^+\pi(K)]$ is compared to the generated mass $M(B^{**}_{(s)})$, and the difference is calculated:

$$y = M[B^+\pi(K)] - M[B^{**}_{(s)}] \, . \tag{5.6}$$

The distribution of this variable is then fitted with a suitable parameterising function, and the most likely parameters of this function are determined by χ^2 minimisation. In practice, a double-Gaussian function is found to be an appropriate model for all particles investigated in this chapter, although alternative models are investigated.

The double-Gaussian function, when normalised as a probability density function, has three degrees of freedom: the widths of the wide (σ_1) and narrow (σ_2) Gaussian curves, and the relative normalisation of the two components, $S = \mathrm{Norm(narrow)}/\mathrm{Norm(wide)}$:

$$\begin{aligned} Res(y;\sigma_1,\sigma_2,S) &= \frac{1}{\sqrt{2\pi}\sigma_1}\cdot\frac{1}{S+1}\exp\left(\frac{-y^2}{2\sigma_1^2}\right) \\ &+ \frac{1}{\sqrt{2\pi}\sigma_2}\cdot\frac{S}{S+1}\exp\left(\frac{-y^2}{2\sigma_2^2}\right) \, . \end{aligned} \tag{5.7}$$

This function assumes that the detector response is symmetrical about the true masses of the particles, with no systematic shifts. This is tested in the fit by allowing the mean of the double-Gaussian function to be a free parameter. This should converge to zero for $B^{**}_{(s)}$ events which decay directly to B^+, where there is no missing energy. For events with decays proceeding via B^{*+}, the central values should converge to -45.78 MeV/c^2, since

the reconstructed mass will be displaced by the energy of the missing photon.

5.3.1 B^{**} States

As emphasized in the previous section, the detector response can be different for each type of event. In the B^{**} system, there are three decays of interest (4.4–4.6), therefore the mass resolution for each of these decays should be measured independently. Since the photon in B^{*+} de-excitation is not detected, the event topology for all B^{**} decays is effectively identical; any differences in mass resolution will arise from kinematic effects, namely the momenta of the daughter particles. Higher momenta particles are associated with broader resolution functions (i.e. larger Gaussian widths $\sigma_{1,2}$). As a result, the highest energy transition $B_2^* \to B^+\pi^-$ is expected to have the broadest detector response, followed by $B_2^* \to B^{*+}\pi^-$ decays, with the finest mass resolution corresponding to $B_1 \to B^{*+}\pi^-$ events.

For each event type, the distribution of $M(B^+\pi^-) - M(B^{**})$ is constructed, and fitted by a double-Gaussian function (5.8). The results of the fit are shown in Fig. 5.3, and the converged values of the three resolution parameters are listed in Table 5.1. Also tabulated here are the χ^2 values at convergence, and the number of degrees of freedom of the fit (d.o.f.).

Table 5.1: Mass resolution parameters for the three B^{**} decays, determined directly from the fit over simulated data.

Decay	σ_1 (MeV/c^2)	σ_2 (MeV/c^2)	S	χ^2/d.o.f.
$B_1 \to B^{*+}\pi$	17.9 ± 2.5	7.4 ± 0.2	6.5 ± 1.8	$78/49$
$B_2^* \to B^{*+}\pi$	15.0 ± 2.0	7.4 ± 0.5	2.5 ± 1.0	$48/46$
$B_2^* \to B^{+}\pi$	24.5 ± 9.4	8.8 ± 0.3	8.3 ± 3.0	$64/47$

Some increase in the Gaussian widths is apparent for the highest energy transition; however, the resolution parameters are found to be relatively consistent for the three decays, while the relative uncertainties on the parameters σ_1 and S are large: greater than 10% and 20% respectively.

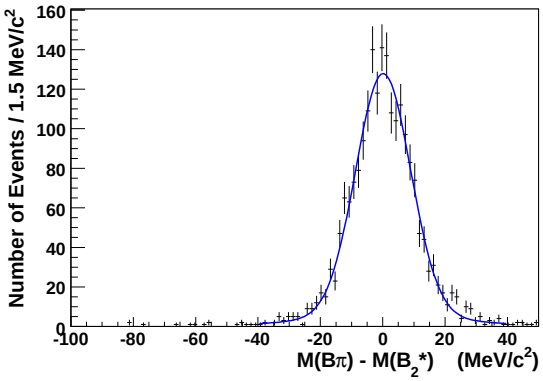

(a) $B_2^* \to B^+\pi^-$ events;

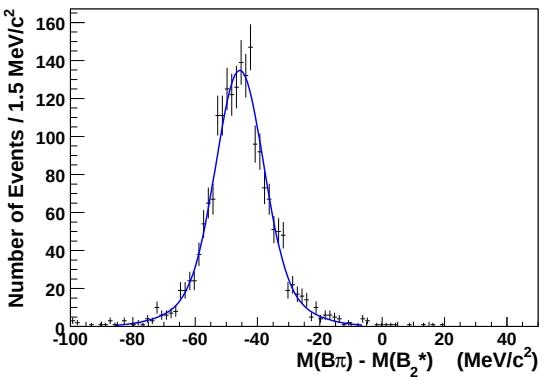

(b) $B_2^* \to B^{*+}\pi^-$ events;

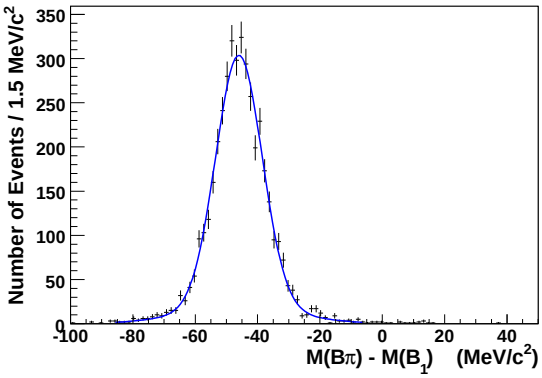

(c) $B_1 \to B^{*+}\pi^-$ events;

Figure 5.3: Detector response distributions for each B^{**} decay, fitted by double-Gaussian functions as described in the text.

The central values (μ) of the double-Gaussian functions converge to values consistent with those expected: the direct decay to B^+ has a detector response centered at zero; while the indirect decays via B^{*+} have response functions centered at the missing photon energy.

$$\begin{aligned} \mu(B_2^* \to B^+\pi^-) &= 0.15 \pm 0.22 \text{ (stat.) MeV}/c^2 \,, \\ \mu(B_2^* \to B^{*+}\pi^-) &= -45.7 \pm 0.2 \text{ MeV}/c^2 \,, \\ \mu(B_1 \to B^{*+}\pi^-) &= -46.0 \pm 0.1 \text{ MeV}/c^2 \,. \end{aligned} \tag{5.8}$$

This gives confidence that the event selection and reconstruction does not introduce any systematic shifts into the mass measurement, further to the effect of the D0 momentum

scale uncertainty described in Section 4.3.6.

The closeness of the resolution parameters for the three decays, with respect to the respective uncertainties, provides motivation for fitting all three decays with a single resolution function; the increased sample size should reduce the uncertainties from the minimisation. A systematic uncertainty arising from this simplification is estimated by repeating the mass fits with and without separate resolution functions for the three transitions. The resulting changes in the fit parameters are very small compared to the other systematic effects, as described in Section 6.2.5. The detector response distribution and fitting function is shown in Fig. 5.4, with the following parameters obtained from the minimisation:

$$\sigma_1 = 17.6 \pm 1.1 \text{ (stat.) MeV}/c^2 , \tag{5.9}$$

$$\sigma_2 = 7.5 \pm 0.2 \text{ MeV}/c^2 , \tag{5.10}$$

$$S = 3.8 \pm 0.5 \text{ MeV}/c^2 . \tag{5.11}$$

In this fit, two identical double-Gaussian functions, defined by the above parameters (σ_1, σ_2, S), are used to model the data: one for the decays to B^+, and one for decays to B^{*+}. The central positions of these two curves are allowed to vary in the fit, as are their relative normalisations. The χ^2/d.o.f. of the fit at convergence is $128/90$. Repeating the fit with a single-Gaussian parameterisation of each peak results in a χ^2/d.o.f. of $285/92$. Such a large increase in χ^2 indicates that this alternative fitting scheme is unsuitable. In contrast, the goodness-of-fit of the double-Gaussian fit indicates that this model is satisfactory for the purposes of this analysis.

Before using these parameters in the ΔM fit, the agreement of data and simulation must be investigated. This is the subject of Section 5.3.3. Having accounted for any differences, the effect of the detector response on all B^{**} resonances in ΔM is modelled by the unified double-Gaussian function $Res(y; \sigma_1, \sigma_2, S)$. To test the influence of this simplification, the ΔM fit is repeated with each resonance parameterised by its own mass resolution function. The change in results is used to determine a set of systematic uncertainties arising from the choice of resolution parameterisation, as outlined in

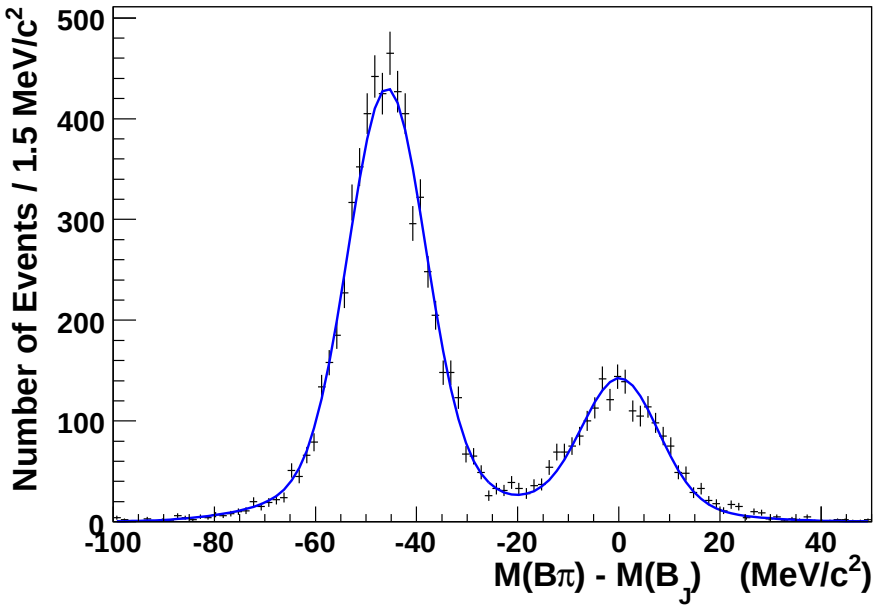

Figure 5.4: Detector response for all B^{**} events, fitted to the sum of two double-Gaussian functions, as described in the text.

Section 6.2.5.

5.3.2 B^{**}_s States

In the case of the B^{**}_s states, the shape of the resonances for both $B^*_{s2} \rightarrow B^+K^-$ and $B_{s1} \rightarrow B^{*+}K^-$ decays must be determined, being important inputs to the ΔM_s fitting procedure. This requires that the mass resolution parameters be determined in the usual way; the distribution of $y = M(B^+K^-) - M(B^{**}_s)$ is constructed for each decay, and fitted to determine the three relevant parameters of the double-Gaussian response function.

The results of the independent fits over the two decay samples are shown in Fig. 5.5, and the resulting converged parameters are listed in Table 5.2. In this case, there is a clear improvement in the detector resolution for the B_{s1} mass, compared to the B^*_{s2}. This is anticipated as a result of the much reduced phase-space available to the former, resulting in lower energy daughter particles, which are detected with greater momentum precision. Unlike the case for the B^{**} system, it is clearly not reasonable to replace these two different functions with a single combined response.

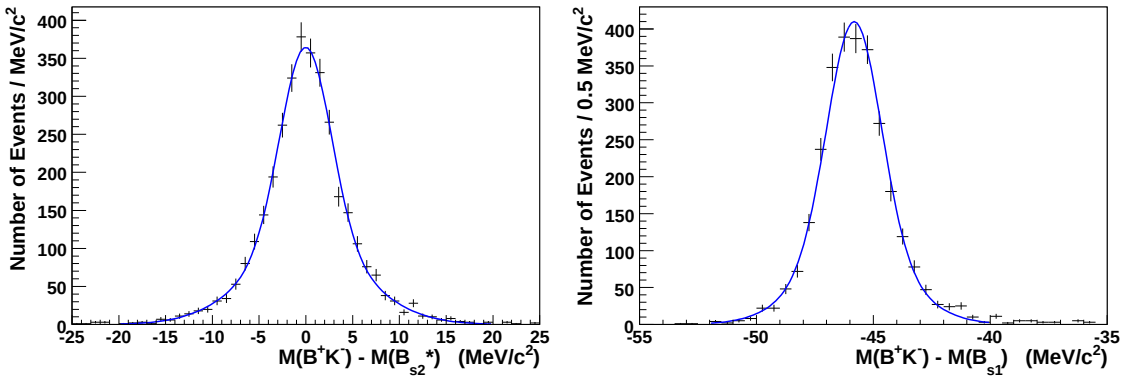

(a) $B^*_{s2} \to B^+K^-$ events; (b) $B_{s1} \to B^{*+}K^-$ events;

Figure 5.5: Detector response distributions for each B^{**}_s decay, fitted by double-Gaussian functions as described in the text.

Table 5.2: Mass resolution parameters for B^{**}_s decays, determined directly from the fit over simulated data.

Decay	σ_1 (MeV/c^2)	σ_2 (MeV/c^2)	S	χ^2/d.o.f.
$B_{s1} \to B^{*+}K$	2.2 ± 0.2	1.1 ± 0.1	3.6 ± 1.0	$32.3/19$
$B^*_{s2} \to B^+K$	6.2 ± 0.3	2.7 ± 0.2	1.2 ± 0.2	$31.3/35$

Fitting the y distribution with a single Gaussian function yields a χ^2/d.o.f. of $89/21$ for the B_{s1} case, and $171/37$ for the B^*_{s2}. This parameterisation is therefore discarded as unsuitable, and the double-Gaussian is used to model the detector mass resolution for all subsequent fits over the ΔM_s distributions.

As mentioned in the concluding part of Section 5.3.1, it is important to compare the results of simulation and data, to check for consistency. This is the subject of the following section.

5.3.3 Agreement between Data and Simulation

Since we do not yet have a complete understanding of all fundamental particle processes, or the computational power to fully model all detector effects, the results of simulation may diverge from the true particle behaviour. In particular, the mass resolution in data

may differ from the Monte Carlo predictions found in the previous section. The possibility of a data/simulation discrepancy must be investigated, with corrections and appropriate systematic uncertainties applied if necessary. In this case, the disagreement is evaluated by examining the $B^+ \to J/\psi K^+$ mass distributions for real and simulated data; these are fitted using a binned χ^2 minimisation, with a single Gaussian function parameterising the signal. The widths determined by the fit for real and simulated data are then compared.

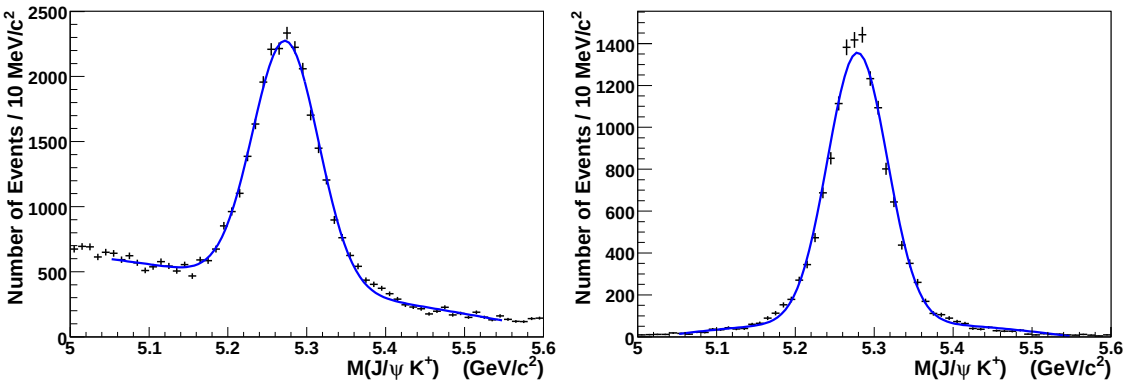

(a) Real data; (b) Simulated data;

Figure 5.6: Comparison of B^+ invariant mass in real and simulated data. The solid lines show the sum of contributions for signal (Gaussian function) and background (second order polynomial) components.

Figure 5.6 shows the resulting distributions, with the fitting functions overlaid. In both cases, a second order polynomial is included to model the contribution of background; the fits are performed in the range $5.05 < M(B^+) < 5.55$ GeV/c^2, covering 50 bins of equal width. The Gaussian widths converge to the following values:

$$\sigma_{\text{MC}}(B^+) = 37.8 \pm 0.4\,\text{MeV}/c^2\,, \tag{5.12}$$

$$\sigma_{\text{data}}(B^+) = 41.8 \pm 0.4\,\text{MeV}/c^2\,. \tag{5.13}$$

The simulation therefore underestimates the mass resolution by $9.6 \pm 1.4\%$. To correct for this effect, all widths $\sigma_{1,2}$ determined from simulation are manually increased by 10%. The final mass resolution parameters for all decays, taking this correction into account,

are listed in Table 5.3. Note that the $B^*_{s2} \to B^{*+}K^-$ decay is included for completeness: any searches for this resonance use the mass resolution parameters as determined for $B^*_{s2} \to B^+K^-$ transitions.

Table 5.3: Mass resolution parameters for $B^{**}_{(s)}$ decays, including corrections to account for disagreement of simulation and data.

Decay	σ_1 (MeV/c^2)	σ_2 (MeV/c^2)	S
$B_1 \to B^{*+}\pi$	19.7 ± 2.8	8.1 ± 0.2	6.5 ± 1.8
$B^*_2 \to B^{*+}\pi$	16.5 ± 2.2	8.1 ± 0.5	2.5 ± 1.0
$B^*_2 \to B^{+}\pi$	27.0 ± 10.3	9.7 ± 0.3	8.3 ± 3.0
All B^{**} decays	19.4 ± 1.2	8.3 ± 0.2	3.8 ± 0.5
$B_{s1} \to B^{*+}K$	2.4 ± 0.2	1.3 ± 0.1	3.6 ± 1.0
$B^*_{s2} \to B^{*+}K$	6.8 ± 0.3	3.0 ± 0.2	1.2 ± 0.2
$B^*_{s2} \to B^{+}K$	6.8 ± 0.3	3.0 ± 0.2	1.2 ± 0.2

Since the disagreement in mass resolution between real data and simulation is not fully understood, and may differ in the $B^{**}_{(s)}$ states, a conservative systematic uncertainty is assigned to the choice of $\sigma_{1,2}$ in all fits over the ΔM_s distributions. The fits are repeated with and without the 10% correction in widths, and the uncertainty on each free parameter is assigned to be the change in its converged value under this variation. This is found to be one of the smallest sources of systematic uncertainty, as summarised in Sections 6.2.5 and 6.3.5.

5.4 Detector Efficiencies for the $B^{**}_{(s)}$ States

One of the principal objectives of this analysis is to determine the production rates of the orbitally excited states, relative to that of the B^+ meson. This measurement requires knowledge of the detection efficiencies for all $B^{**}_{(s)}$ decays under study, expressed as a fraction of the B^+ detection efficiency, as justified later in Section 7.3.1. These efficiencies are also necessary to extract the true branching ratios R_1 and R_2 from the number of events in each B^{**} resonance in the ΔM distribution, as described in Section 7.2.

Since all $B^{**}_{(s)}$ events in this analysis are reconstructed through the $B^+\pi^-(K^-)$ channel, it is sufficient to determine the efficiency of correctly detecting and identifying the additional pion (kaon). This efficiency will be affected by any kinematic selections on the π (K), and by detector effects such as the spatial limits of the tracking system. The following pages outline how the detection efficiencies are extracted from the simulation, including systematic uncertainty studies and corrections for data/simulation disagreement.

5.4.1 Overview

The efficiency of detecting any particle is found by counting the fraction of generated events which pass through all selections to be correctly identified and reconstructed. For a given sample of generated events, if X B^+ candidates and Y $B^{**}_{(s)}$ candidates are correctly reconstructed, then the efficiency of detecting the additional pion (kaon) is simply the ratio Y/X. The correctness of the reconstruction is tested by 'truth-matching', checking that each particle in the decay chain corresponds to the appropriate generated particle. This determination can only be made using simulated data, where the true sample content is known.

Before this process is undertaken, the simulated data must be reweighted on an event-by-event basis, to ensure that the particle transverse momentum distributions match real data. This is important because the additional track is required to pass a p_T selection, and so any differences in data and MC will skew the efficiency measurement. The reweighting method is the same for B^{**} and B^{**}_s events, and is outlined below.

Reweighting the Simulated Data

To estimate the extent of the disagreement in data and simulation, and correct for this effect, the p_T distributions of B^+ mesons in real and simulated data are compared. The simulated sample is custom generated, with approximately $100,000$ $B^+ \to J/\psi K^+$ events, of which around $20,000$ survive the reconstruction process. No constraints are placed on the origin of the B^+ mesons. The data sample comprises all B^+ events which pass the likelihood ratio selection (see Section 4.3.4), with no additional mass window constraint.

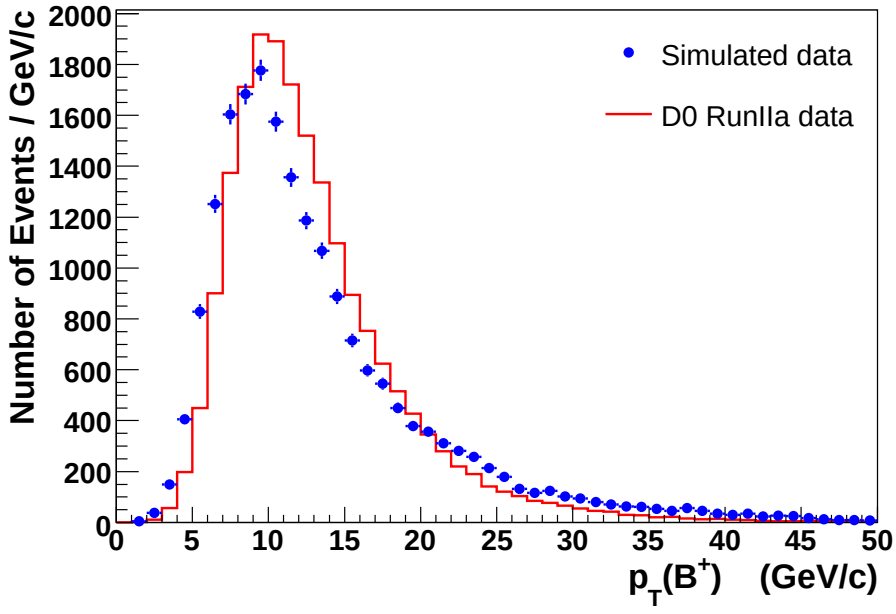

Figure 5.7: B^+ transverse momentum distributions for data (solid line) and for Monte Carlo simulation (crossed points). The data histogram has been normalised to match the number of events in the simulation.

Both samples are therefore composed of generic B^+ events, so that a fair comparison of the transverse momenta distributions can be made.

The distributions of $p_T(B^+)$, for both data and the simulation, are shown in Fig. 5.7. The data histogram has been normalised to match the number of events in the Monte Carlo sample. The simulation has more events both at low (< 8 GeV/c), and high (> 20 GeV/c) transverse momentum than the data. To correct for this effect, a reweighting function is built by dividing the data histogram by the simulation histogram, producing the plot shown in Fig. 5.8. The resulting histogram is then fitted to a fourth order polynomial function, $F(p_T)$, shown by the solid line. For transverse momenta beyond the fitting range, below 3 GeV/c or above 50 GeV/c, the reweighting function is fixed at unity.

Having established the reweighting function, it is now used to assign each reconstructed $B^{**}_{(s)}$ and B^+ candidate with a weight, according to its transverse momentum,

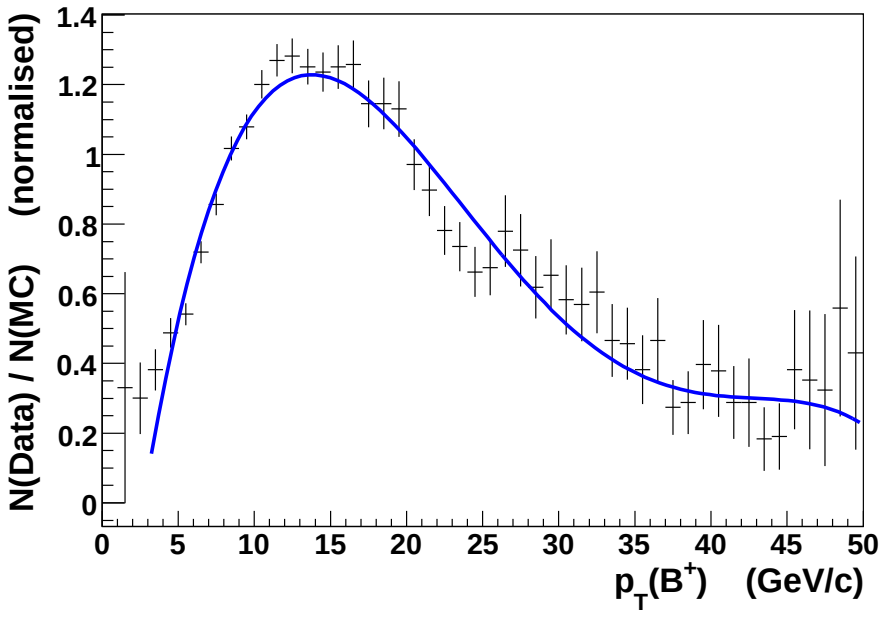

Figure 5.8: Result of dividing the p_T distribution of generic B^+ events in data, by that from simulation. The solid line shows the fit by a fourth order polynomial function, as described in the text.

$w_i = F(p_T)$. The reconstruction efficiency for any $B^{**}_{(s)}$ state is then calculated by:

$$\varepsilon_{\text{rec}} = \frac{\sum w_j}{\sum w_k} \,, \tag{5.14}$$

where the index j labels all the appropriate $B^{**}_{(s)}$ events, and k labels all B^+ events, which are detected after the full simulation, selection and reconstruction algorithms.

Since this is another example of an *ad hoc* correction, such as the mass shifts described in Section 4.3.6, a conservative systematic uncertainty is assigned to the reweighting process. This is taken to be the difference in efficiencies calculated with and without the reweighting process.

Generator-Level Effects

The above method would be sufficient to determine the detection efficiencies, if the Monte Carlo simulation were generated without any kinematic or topological constraints on the

pion (kaon) from $B^{**}_{(s)}$ decay. However, as described in Section 5.2.1, there are generation requirements $p_T(\pi^-, K^-) > 0.6$ GeV/c, and $|\eta(\pi^-, K^-)| < 2.2$. The sample is therefore enhanced with particles which are detected and reconstructed more readily than in data: the excluded high pseudorapidity tracks would be outside the detector range, and the low p_T events would fail the event selection.

To account for this enhancement, an additional *generator-level* efficiency is determined, which is the fraction of total events generated which survive the pion (kaon) requirements enforced by PYTHIA. This must be determined separately for the B^{**} and B^{**}_s systems. In each case, two samples of 5000 events are generated; one sample has the usual kinematic requirements on the $\pi^-(K^-)$, the second has these requirements removed. To produce such samples, a much larger number, N_{gen} of initial events are generated from simulated $\bar{b}b$ production, which are then filtered to remove all but the $B^{**}_{(s)}$ decays of interest. The generation efficiency for each process is then determined by taking the ratio:

$$\varepsilon_{\text{gen}} = \frac{N_{\text{gen}}(\text{Without } \pi^-(K^-) \text{ requirements})}{N_{\text{gen}}(\text{With } \pi^-(K^-) \text{ requirements})} \,. \tag{5.15}$$

The overall detection efficiency is then given by the product of the reconstruction efficiency from Eq. (5.14), and the generation efficiency from Eq. (5.15). The calculations and final determined values are given in Sections 5.4.2–5.4.3.

Allocating Systematic Uncertainties

The sources of systematic uncertainty on the efficiency measurement are the same for both systems under investigation, and are summarised in Tables 5.5 and 5.7. The effect of reweighting is assigned a 100% uncertainty, equal to the total change in measured efficiency caused by applying the reweighting function.

The uncertainty of the impact parameter resolution in the simulation is estimated to be approximately 10% [89]. This can influence the measurement of the selection efficiency of the pion (kaon) from the $B^{**}_{(s)}$ decay, since one of the selection criteria relates to the impact parameter significance, $S_{\pi,K} < \sqrt{6.0}$ [see Eq. (4.12)]. To test for the effect of such an uncertainty, the efficiency is recalculated with the IP significance requirement

varied by $\pm 10\%$, i.e. with selections $S_{\pi,K} < \sqrt{4.8}$ and $S_{\pi,K} < \sqrt{7.2}$. The corresponding systematic uncertainty is then taken to be half of the total change in measured efficiency under these variations.

The track reconstruction efficiency for particles with low transverse momentum is measured in Ref. [90], and good agreement between data and simulation is found. This comparison is valid within the uncertainties of branching fractions of different B semileptonic decays, which is about 7%. As such, a 7% relative uncertainty is assigned to every efficiency measurement, to account for possible disagreement in simulation.

This completes the description of the procedure for calculating the relative detection efficiencies, and their associated uncertainties. The following sections detail the determination of these quantities for the $B^{**}_{(s)}$ states.

5.4.2 B^{**} States

Using the sample of simulated events defined in Section 5.2.1, the number of correctly reconstructed B^+ and B^{**} candidates, for each separate transition, are determined with and without the reweighting procedure. The results are summarised in Table 5.4. The efficiencies are calculated by division of the appropriate numbers, according to Eq. (5.14); all weights are defined to be unity for the non-reweighted case. The uncertainties are given by the expression for binomial behaviour:

$$\sigma = \sqrt{\frac{\varepsilon(1-\varepsilon)}{N_{\text{trials}}}}\,, \tag{5.16}$$

where N_{trials} is the number of B^+ mesons correctly reconstructed, which is the number of trials in which a B^{**} event can be detected.

The generation efficiency is also calculated separately for each decay, using Eq. (5.15). Here the numbers N_{gen} in the calculations are the total number of events produced at the generator level, required in order to create 5000 of the particular B^{**} transition of interest. The uncertainties are calculated using the binomial expression for each fraction $5000/N_{\text{gen}}$ and then combined to determine the effect on the generation efficiencies. The results are

Table 5.4: Calculation of reconstruction efficiencies for separate B^{**} decays. The rows show the number of each event type, with and without reweighting, and the corresponding efficiency. The columns divide the sample into the different decays of interest.

	Without Reweighting			With Reweighting		
Process	$N(B^+)$	$N(B^{**})$	ε_{rec}	$N(B^+)$	$N(B^{**})$	ε_{rec}
$B_1 \to B^{*+}\pi^-$	6516	4202	0.645(6)	6576.9	4318.7	0.657(6)
$B_2^* \to B^{*+}\pi^-$	3003	2020	0.673(9)	3023.6	2019.8	0.668(9)
$B_2^* \to B^{+}\pi^-$	3106	2104	0.677(8)	3103.8	2074.9	0.669(8)

as follows:

$$\varepsilon_{\text{gen}}(B_1 \to B^{*+}\pi^-) = \frac{3,588,222}{7,318,033} = 0.490 \pm 0.010\,, \tag{5.17}$$

$$\varepsilon_{\text{gen}}(B_2^* \to B^{*+}\pi^-) = \frac{2,316,866}{4,471,143} = 0.518 \pm 0.010\,, \tag{5.18}$$

$$\varepsilon_{\text{gen}}(B_2^* \to B^{+}\pi^-) = \frac{2,297,330}{4,082,162} = 0.563 \pm 0.011\,. \tag{5.19}$$

The total detection efficiency for each transition is the product of the generation efficiency with the reweighted reconstruction efficiency from Table 5.4. The uncertainties from systematic effects described in Section 5.4.1 are included, with the full breakdown of sources given in Table 5.5. The overall detection efficiency for all B^{**} decays is then estimated by a weighted average of the individual process efficiencies, with each B_2^* decay having weight unity, and the B_1 decay having weight two.

$$\varepsilon_1 \equiv \varepsilon(B_1 \to B^{*+}\pi^-) = 0.322 \pm 0.028 \text{ (syst.)} \tag{5.20}$$

$$\varepsilon_2 \equiv \varepsilon(B_2^* \to B^{*+}\pi^-) = 0.346 \pm 0.029 \text{ (syst.)} \tag{5.21}$$

$$\varepsilon_3 \equiv \varepsilon(B_2^* \to B^{+}\pi^-) = 0.377 \pm 0.031 \text{ (syst.)} \tag{5.22}$$

$$\varepsilon_0 \equiv \varepsilon(B_J \to B^{(*)+}\pi^-) = 0.342 \pm 0.029 \text{ (syst.)} \tag{5.23}$$

Table 5.5: Systematic uncertainties of the detector efficiencies for each B^{**} decay. The rows without $\pm$ symbols indicate the efficiencies measured under some variation in the procedure, for example in the absence of reweighting, or under a different requirement for impact parameter significance (S_π). Rows with $\pm$ symbols show the extracted uncertainty from each source.

Source	ε_1	ε_2	ε_3	ε_0
Without reweighting	0.316	0.349	0.381	0.340
With reweighting	0.322	0.346	0.377	0.342
σ(reweighting)	± 0.006	± 0.003	± 0.004	± 0.002
$S_\pi < \sqrt{4.8}$	0.305	0.329	0.357	0.323
$S_\pi < \sqrt{7.2}$	0.331	0.356	0.386	0.351
σ(IP uncertainty)	± 0.013	± 0.014	± 0.015	± 0.014
σ(7% tracking)	± 0.023	± 0.024	± 0.026	± 0.024
σ(binomial)	± 0.007	± 0.008	± 0.009	± 0.008
Total	± 0.028	± 0.029	± 0.031	± 0.029

5.4.3 B^{**}_s States

The above methods are now repeated for the B^{**}_s system, with the simplification that only one detection efficiency needs to be determined: for the $B^*_{s2} \to B^+K^-$ decay. The other two decays are not observed with sufficient significance to motivate a measurement of the branching ratios or relative production rate, as quantified in Section 6.3.4.

Passing the simulated B^*_{s2} data sample through the reconstruction code, the number of correctly detected B^+ and B^*_{s2} events is determined, both with and without reweighting by transverse momentum. These numbers, and the resulting efficiencies, are shown in Table 5.6.

The generation efficiency is again determined by looking at the initial sample sizes required in order to yield 5000 final events, with and without any kinematic selections on the kaon from B^*_{s2} decay. The results are as follows:

$$\varepsilon_{\text{gen}}(B^*_{s2} \to B^+K^-) \;=\; \frac{6,364,746}{9,152,075} = 0.695 \pm 0.014\,, \tag{5.24}$$

Combining the reconstruction efficiency with this generation factor, and taking into account the systematic uncertainties summarised in Table 5.7, the overall detection efficiency for $B^*_{s2} \to B^+K^-$ is calculated as:

$$\varepsilon_s \equiv \varepsilon(B^*_{s2} \to B^+K^-) = 0.518 \pm 0.044 \text{ (syst.)} \tag{5.25}$$

Table 5.6: Calculation of reconstruction efficiencies for $B^*_{s2} \to B^+K^-$ decays.

$B^*_{s2} \to B^+K^-$	$N(B^+)$	$N(B^*_{s2})$	ε_{rec}
Without reweighting	4587	3406	0.743(6)
With reweighting	4710.9	3508.5	0.745(6)

Table 5.7: Systematic uncertainties on the B^*_{s2} detection efficiency. See Table 5.5 for an explanation of the layout.

Source	ε_s	$\delta\varepsilon_s$
Without reweighting	0.516	—
With reweighting	0.518	—
σ(reweighting)	—	$\pm$0.002
$S_K < \sqrt{4.8}$	0.491	—
$S_K < \sqrt{7.2}$	0.535	—
σ(IP uncertainty)	—	$\pm$0.022
σ(7% tracking)	—	$\pm$0.036
σ(binomial)	—	$\pm$0.011
Total	—	$\pm$0.044

5.5 Background Shapes in Mass Distributions.

Understanding the shapes of backgrounds in B^+, B^{**} and B_s^{**} mass distributions is an important tool in this analysis. For the orbitally excited states, it is crucial, allowing the effect of so-called reflections to be examined. These occur in cases where several physics signals share a common topology, with the only difference coming from the specific particle types involved in the decay. In searching for one of these signals, it is possible to accidentally collect a significant number of other unwanted signal events, by mis-identifying a differentiating particle. For these events, the wrong mass will be attributed to the mis-identified particle, and so the position of the resonance will be shifted ('reflected') in mass. Since this type of background comes from resonant behaviour, it can lead to auxiliary peaking in the mass distribution. An example of this has already been described in Section 4.3.5, where the pion track in $B^+ \to J/\psi\pi^+$ decays can be wrongly attributed to be a kaon, leading to a second, albeit small, peak in the $J/\psi K^+$ invariant mass spectrum.

As detailed in the previous chapter, event selection for all orbitally excited B mesons in this analysis is based on B^+X^- reconstruction; where $X \equiv \pi$ for the B^{**} system, and $X \equiv K$ for the B_s^{**} system. Since no identification tools are used to distinguish pion and kaon tracks, mis-identifications can be common, and so there can be cross-contamination of the samples. The following sections describe the use of simulation to measure the effect of such contamination on the $\Delta M_{(s)}$ distributions.

5.5.1 Reflections from B_s^{**} in the ΔM Distribution

The effect of mis-identified B_s^{**} events on the ΔM distribution is estimated by passing the main B_{s2}^* simulated data sample through the B^{**} selection and reconstruction software. The resulting shape in ΔM is shown by the data markers in Fig. 5.9, where there is a clear peak in the region $0.2 < \Delta M < 0.45$ GeV/c^2. However, the number of events in this distribution must be scaled to appropriately represent real data. This is done as follows.

The number of B_{s2}^* signal candidates yielded by the ΔM_s fit, following event selection and reconstruction with the B_s^{**} software, is 125 ± 25 for D0 Run IIa data [see

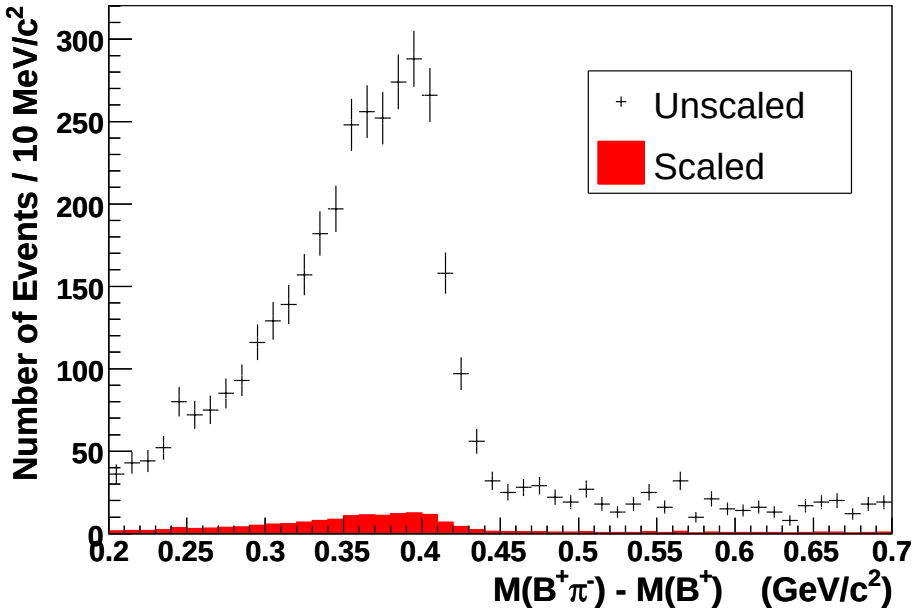

Figure 5.9: Reflections from B^*_{s2} decays in the ΔM distribution. The data points show the effect of passing the B^*_{s2} simulated event sample through the B^{**} reconstruction code. The filled histogram is the same shape, but scaled to match the number of B^*_{s2} events in data.

Eq. (6.31)], and 2853 ± 22 for the B^*_{s2} simulated sample (see Section 5.2.2). Therefore the distribution in Fig. 5.9 must be scaled by a factor $125/2853 = 0.044$ to replicate the true number of B^*_{s2} events in the data, as shown in the same figure by the filled histogram. In Section 6.2.2, this scaled histogram is considered in assigning an appropriate background model to the ΔM fit.

No attempt is made to model the effects of reflections from B_{s1} or $B^*_{s2} \to B^{*+}K^-$ decays, following the low significance of these signals determined in Section 6.3.4.

5.5.2 Reflections from B^{**} in the ΔM_s Distribution

The impact of reflections on the ΔM_s distribution from $B^{**} \to B^{(*)+}\pi^-$ events, where the pion is incorrectly tagged as a kaon, is estimated by passing the B^{**} simulated sample through the B^{**}_s reconstruction software. The ΔM_s distribution resulting from this procedure is shown by the markers in Fig. 5.10. A broad distribution can be seen, with

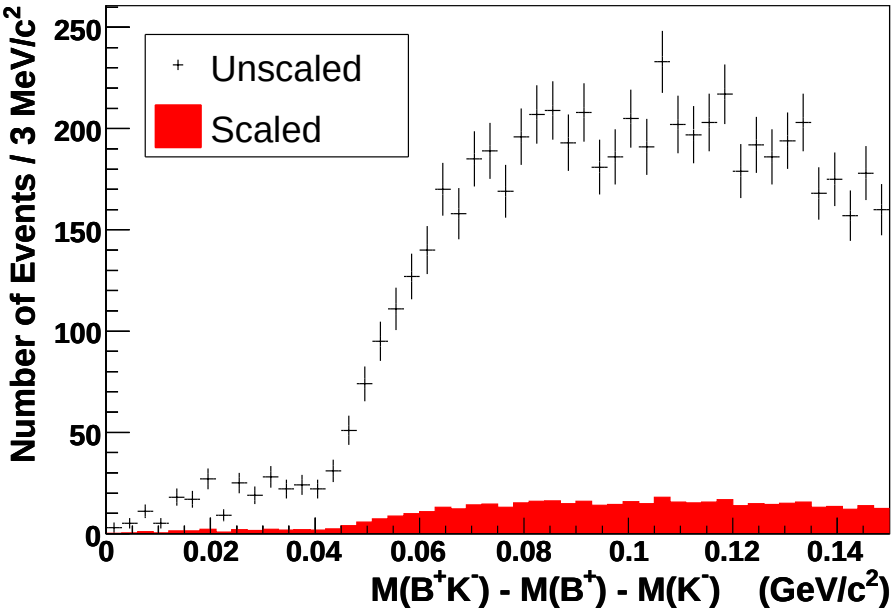

Figure 5.10: Reflections from B^{**} decays in the ΔM_s distribution. The data points show the effect of passing the B^{**} simulated event sample through the B_s^{**} reconstruction code. The filled histogram is the same shape, but scaled to match the number of B^{**} events in data.

a threshold at $\Delta M_s = 0.05$ GeV/c^2, and no narrow peaks. In the same figure, the distribution is also shown after having been scaled to match the number of B^{**} events found in real data, by the filled histogram. In this case, passing the simulated data through the B^{**} reconstruction yields 8109 ± 170 final events, while running over the D0 Run IIa data sample yields 662 ± 91 events [see Eq. (6.19)], so the required scale factor is ~ 0.077. This scaled distribution is used in Section 6.3.2 to motivate the choice of background parameterisation in the ΔM_s fit.

5.5.3 Backgrounds in the B^+ Mass Distribution

As part of the B^+ mass fitting procedure, described in Section 4.3.5, a contribution is allowed from partially reconstructed B^+ decays to $J/\psi K^{+*}(892)$ and $J/\psi K_1(1270)$. In both cases, the excited kaons can decay to K^+, producing an event difficult to distinguish from the desired ($J/\psi K^+$) signal, but with missing energy from the other undetected

daughter particle(s) of the higher mass kaon. Events of this type can form a significant fraction of the total B^+ candidates, although most are expected to occur below the $J/\psi K^+$ resonance, as a result of the missing energy. The following relative branching ratios are given by the Particle Data Group [11]:

$$\Gamma(B^+ \to J/\psi K^+) = [(1.008 \pm 0.035) \times 10^{-3}] \times \Gamma_{\text{tot}}, \quad (5.26)$$

$$\Gamma[B^+ \to J/\psi K^{+*}(892)] = [(1.41 \pm 0.08) \times 10^{-3}] \times \Gamma_{\text{tot}}, \quad (5.27)$$

$$\Gamma[B^+ \to J/\psi K_1^+(1270)] = [(1.8 \pm 0.5) \times 10^{-3}] \times \Gamma_{\text{tot}}. \quad (5.28)$$

The effect of such partially reconstructed decays is estimated by a dedicated simulation, in which B^+ mesons are generated and required to decay exclusively into channels (5.27) and (5.28); the relative branching ratios are fixed at the central values quoted above. In turn, the K^{+*} and $K_1^+(1270)$ states from B^+ decays are forced to decay into final states containing a charged kaon or pion, i.e. those channels which may be mis-interpreted as true $J/\psi K^+$ signal events. The relative branching ratios of these decays are again fixed at the PDG values, as listed in Table 5.8. All other particles are allowed to decay naturally, with no requirements on the decay path. In this way, a wide range of possible background sources are investigated simultaneously.

The generated events are passed through the full detector simulation, as described in Section 5.1; the simulated data sample is then used as an input for the B^+ selection and reconstruction code. The resulting $J/\psi K^+$ mass distribution from this process is shown in Fig. 5.11. This shape is parameterised by the following threshold function:

$$f_{J/\psi K^*}(M_{J/\psi K}) = N\{\text{arctan}(-34.327[M_{J/\psi K} - 5.138]) + 1.4454\} \quad (5.29)$$

where the three numerical parameters are determined by a fit to the simulated data in Fig. 5.11, shown by the solid line. The value of the normalisation N depends only on the size of the simulation: it is included as a free parameter in the fit over the B^+ mass in data, since the fraction of events from partially reconstructed decays is not known. For invariant masses greater than 5.365 GeV/c^2, the contribution from this source of background is fixed to be zero.

Table 5.8: Relative branching ratios of K^{+*} and $K_1^+(1270)$ states, fixed in the simulation of partially reconstructed B^+ decays.

Decaying Particle	Decay Channel i	$\Gamma_i/\Gamma_{\rm tot}$
$K^{+*}(892)$	$K^0\pi^+$	0.666
	$K^+\pi^0$	0.333
	$K^+\gamma$	0.001
$K_1^+(1270)$	ρ^+K^0	0.2800
	ρ^0K^+	0.1400
	$K^{0*}\pi^+$	0.1067
	$K^{+*}\pi^0$	0.0533
	$K^+\omega$	0.1100
	$K^+\pi^+\pi^-$	0.1444
	$K^0\pi^+\pi^0$	0.1244
	$K^+\pi^0\pi^0$	0.0412

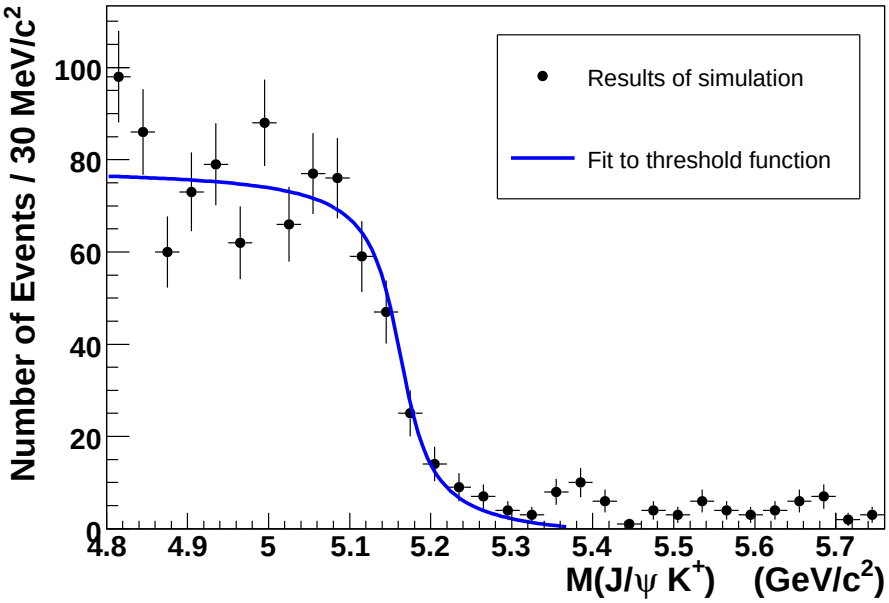

Figure 5.11: Contribution to the B^+ mass distribution from partially reconstructed decays to $J/\psi K^{+*}$, determined from simulation. The data markers show the results of passing the $J/\psi K^{+*}[K_1(1270)]$ Monte Carlo data through the B^+ reconstruction code; the solid line shows the fit by a threshold function, as described in the text.

5.6 Summary

This concludes the description of the simulation methods used in this analysis. In the following chapter, the experimental mass resolution parameters determined here are used as an input to the $\Delta M_{(s)}$ fits. In Chapter 7, the results of these fits are then combined with the efficiency measurements to extract the $B^{**}_{(s)}$ decay branching ratios and relative production rates. The information regarding reflections and partially reconstructed decays is used in selecting suitable background parameterisations for the B^+ (Section 4.3.5), B^{**} (Section 6.2.2), and B^{**}_s (Section 6.3.2) mass distributions.

In all cases where simulation is used, the level of agreement with real data has been carefully considered. For all measurements made using Monte Carlo samples, corrections have been applied to minimise any such discrepancy, and conservative systematic uncertainties are allocated to these shifts.

Chapter 6

Fitting the Mass Distributions

In CHAPTER 4, the procedures for constructing the ΔM and ΔM_s distributions were established. In order to extract the $B^{**}_{(s)}$ properties from each distribution, an appropriate general fitting model is first constructed, consisting of separate signal and background components. The physical parameters, such as masses and branching ratios, are included as parameters in the model; their most likely values are then determined by fitting the model to the data, and finding the 'best-fit' under some statistical prescription. The methods and results of this fitting scheme are described in this chapter.

The type of fit will depend on the particular case, although for both distributions discussed in this chapter, binned fits are used. The bin widths in the $\Delta M_{(s)}$ histograms are chosen to be 10 MeV/c^2 for B^{**} states, and 3 MeV/c^2 for B^{**}_s states; these values are comparable to the expected widths of the respective resonances. In this way, the loss of detail inherent in any such binned distribution is minimised; while the number of events in each bin is kept as high as possible.

Where possible, the model is fitted to the data by χ^2 minimisation, as this method returns a meaningful goodness-of-fit measurement. However, this approach assumes that the population of each bin is distributed normally. For low-content bins this assumption is no longer valid; instead the Poisson distribution is the correct model, and a maximum likelihood fit must be utilised. These considerations are important for the $\Delta M_{(s)}$ fits, as will become clear later in this chapter.

For each bin i involved in the fit, the expected number of events f^i_{total} must be determined, given the current parameter values of the theoretical model. This process requires some numerical method for integrating the continuous fitting function $f_{\text{total}}(\Delta M_{(s)})$ over the width of the bin. This is done most precisely by a numerical method, whereby precision is only limited by the computer performance:

$$f^i_{\text{total}} = \int_{x^i_{min}}^{x^i_{max}} f_{\text{total}}(x)dx, \tag{6.1}$$

where x^i_{min}, x^i_{max} are the upper and lower limits of the bin in $\Delta M_{(s)}$. The drawback of such a method is the extended timescale involved for each iteration of the fit. For simple functions, such as background-only fits, Eq. (6.1) is used to determine the expected number of events in each bin. For all fits involving signal models, an approximate method is used instead:

$$f^i_{\text{total}} = f_{\text{total}}\left(\frac{x^i_{min} + x^i_{max}}{2}\right) \tag{6.2}$$

For the binning schemes and fit models used in this analysis, Eq. (6.2) yields best-fit parameters effectively identical to those from the full integration method. Any differences are much smaller than the quoted uncertainties from the fit, with no systematic movement from the central values.

The models used to parameterise the background contributions are determined by examining real and simulated data, as explained in Sections 6.2.2 and 6.3.2. On the other hand, the physical shapes of the signal resonances are described by theory, and are the same for all $B^{**}_{(s)}$ decays. The corresponding parameterisation, and the effect of the detector mass resolution on the observed signal peaks, is detailed in the following section.

6.1 Signal Parameterisation

All four states under consideration are predicted by theory to have narrow widths in the mass distributions, as explained in Chapter 2. The B^{**} mesons are expected to have physical widths of order 10 MeV/c^2, while the B^{**}_s states have smaller widths of order

1 MeV/c^2. In both cases, the widths are comparable to the associated detector mass resolution. As a result, both the physical resonance shape, and the mass smearing effect of the detector response, must be considered when fitting the signal peaks.

Since this section describes signal parameterisation for both ΔM and ΔM_s distributions, the general mass difference $x = \{\Delta M, \Delta M_s\}$ is introduced for convenience. Each signal peak in x is parameterised by the convolution of a relativistic Breit-Wigner function with the experimental resolution in x:

$$D(x; x_0, \Gamma, \bar{R}) = \frac{1}{N_0} \int Res(x, x'; \bar{R}) \cdot BW(x'; x_0, \Gamma) dx'. \tag{6.3}$$

where x_0 is the central mass difference of the appropriate $B^{**}_{(s)}$ transition, Γ is its width, and N_0 is a normalisation factor. The resolution is parameterised by a double-Gaussian function, defined by the parameters $\bar{R} = (\sigma_1, \sigma_2, S)$, which are determined from simulation separately for each transition, as described in Section 5.3:

$$\begin{aligned} Res(x, x'; \sigma_1, \sigma_2, S) &= \frac{1}{\sqrt{2\pi\sigma_1}} \cdot \frac{1}{S+1} \exp\left(\frac{-(x-x')^2}{2\sigma_1^2}\right) \\ &+ \frac{1}{\sqrt{2\pi\sigma_2}} \cdot \frac{S}{S+1} \exp\left(\frac{-(x-x')^2}{2\sigma_2^2}\right) \end{aligned} \tag{6.4}$$

The relativistic Breit-Wigner function takes into account threshold effects, using the standard expression for an $L = 2$ decay:

$$BW(x; x_0, \Gamma) = \frac{x_0 \Gamma(x)}{(x^2 - x_0^2)^2 + x_0^2 \Gamma^2(x)}, \tag{6.5}$$

$$N_0 = \int \frac{x_0 \Gamma(x)}{(x^2 - x_0^2)^2 + x_0^2 \Gamma^2(x)} dx, \tag{6.6}$$

$$\Gamma(x) = \Gamma \frac{x_0}{x} \left(\frac{k}{k_0}\right)^{2L+1} F^{(L)}(k, k_0) \ \ (L = 2). \tag{6.7}$$

The variables k and k_0 are the magnitudes of the pion (kaon) three-momentum in the $B^{**}_{(s)}$ rest frame when the $B^{**}_{(s)}$ state has a squared four-momentum equal to x^2 and x_0^2 respectively. $F^{(2)}(k, k_0)$ is the Blatt-Weiskopf form factor for $L = 2$ decay [91]:

$$F^{(2)}(k, k_0) = \frac{9 + 3(k_0 r)^2 + (k_0 r)^4}{9 + 3(kr)^2 + (kr)^4}, \tag{6.8}$$

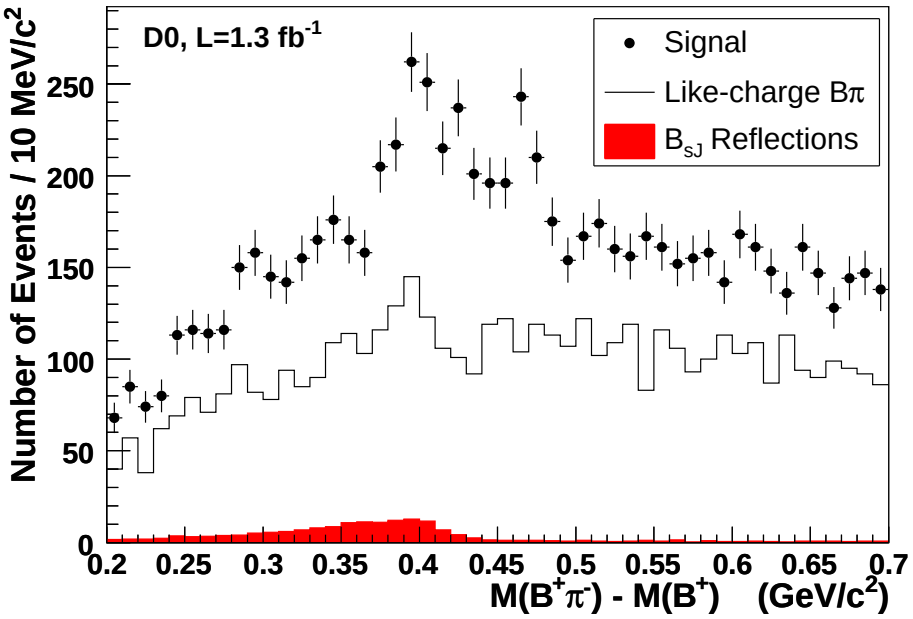

Figure 6.1: Unfitted ΔMdistribution. Shown separately are the data points from the signal sample, the shape of the like-sign background, and the reflections from B_s^{**} events, as described in the text.

where $r = 5$ (GeV/c)$^{-1}$ is a typical hadron momentum scale.

This completes the description of the signal mass peak parameterisation. For each distribution $\Delta M_{(s)}$, it remains to formulate a primary fitting hypothesis, develop a model for fitting the background, and choose an appropriate fitting scheme. These topics are the subject of the following sections.

6.2 B^{**} Mass Distribution

6.2.1 Choice of Fitting Hypothesis

The ΔM distribution for the selected event sample is shown by the data points in Fig. 6.1. First inspection suggests that the distribution exhibits some complex structure in the range $0.37 < \Delta M < 0.49$ GeV/c^2, corresponding to an excess of events relative to the smooth, featureless shape outside of this range.

Since theory predicts that the B_1 and B_2^* are produced in similar numbers, and that the latter state decays equally into $B^+\pi$ and $B^{*+}\pi$, the primary fitting hypothesis is a three-peak signal, corresponding to decays (4.4–4.6). The contribution from each transition is allowed to vary in the fit, so that the total signal contribution is parameterised by:

$$\begin{aligned} f_{\text{sig}} &= N\{f_1 \cdot D(x; x_1, \Gamma_1, \bar{R}_1) \\ &+ (1-f_1)[f_2 \cdot D(x; x_2, \Gamma_2, \bar{R}_2) + (1-f_2) \cdot D(x; x_3, \Gamma_3, \bar{R}_3)]\} \end{aligned} \tag{6.9}$$

Here the fractions f_1 and f_2 are free parameters in the fit, as is the total number of events, N. The first term corresponds to decays $B_1 \to B^{*+}\pi$, the second to $B_2^* \to B^{*+}\pi$, and the third to $B_2^* \to B^+\pi$.

The mass resolution parameters $\bar{R}_i$ for each decay are listed in Table 5.3. However, the study described in section 5.3 shows that the detector response to the combined signal is well modelled by a single function $Res(\sigma_1, \sigma_2, S)$, with $\sigma_1 = 19.4$ MeV/c^2, $\sigma_2 = 8.3$ MeV/c^2, $S = 3.8$. This reduces the number of required resolution parameters from nine to three. Various tests of the resolution parameterisation are performed, and the results are used to assign a systematic uncertainty to this source, as described in section 6.2.5.

The decay widths of the three transitions are predicted by theory to be close, so they are fixed to be equal in the fit $\Gamma_1 = \Gamma_2 = \Gamma_3 = \Gamma$. With the current dataset and mass resolution, the fit is found to be insensitive to values of Γ below 25 MeV/c^2. As a result, the physical width for all transitions is fixed to be 10 MeV/c^2, following theoretical expectations. A systematic uncertainty is assigned to this choice by fitting over a range of different widths, and looking at the variation in the converged values of the free parameters.

The central values in Eq. (6.9) correspond to the mass differences:

$$\begin{aligned} x_1 &= M(B_1) - M(B^{*+}), \\ x_2 &= M(B_2^*) - M(B^{*+}), \\ x_3 &= M(B_2^*) - M(B^+) \end{aligned} \tag{6.10}$$

The PDG mass difference $M_\gamma = M(B^{*+}) - M(B^+) = 45.78 \pm 0.35$ MeV/c^2 is a precisely

measured quantity. As a result, the fit is further constrained by the condition $x_3 = x_2 + 45.78$ MeV/c^2. The uncertainty on this measurement is taken into consideration when determining the systematic uncertainties in the ΔM fit.

The positions of the peaks are thus defined by the two parameters (x_1, x_2). The value of the mass splitting $M(B_2^*) - M(B_1)$ is of special interest in comparison with theory, as is the mass difference between the B_1 and B^+ mesons. The fit is redefined following these considerations, in terms of the parameters $[x_1 + M_\gamma, x_2 - x_1]$. In this way, any systematic uncertainties associated with the B^+ reconstruction do not contribute in the mass splitting measurement.

To summarise, the fit over the signal takes the following ten parameters as arguments:

A. Five fixed parameters in the fit:

   a) Three mass resolution parameters, (σ_1, σ_2, S), fixed from simulation;

   b) $\Gamma = 10$ MeV/c^2 fixed following theoretical predictions;

   c) $M_\gamma = M(B^{*+}) - M(B^+) = 45.78 \pm 0.35$ MeV/c^2 fixed at the PDG value.

B. Five free parameters in the fit:

   a) f_1: fraction of total signal events in the B_1 peak;

   b) f_2: fraction of B_2^* events in the $B_2^* \to B^{*+}\pi$ peak;

   c) $x_1 + M_\gamma = M(B_1) - M(B^+)$;

   d) $x_2 - x_1 = M(B_2^*) - M(B_1)$, i.e. mass splitting between the excited states;

   e) N: total number of signal events in the three peaks.

6.2.2 Backgrounds

Having described the parameterisation of the B^{**} signal peaks, and chosen a fitting hypothesis, we now find a suitable function to model the contribution of background events to the ΔM distribution. This section describes the different sources of background events, along with their characteristic ΔM shape. An appropriate fit function $f_{\text{bckg}}(\Delta M)$ can then

be chosen. To facilitate this study, two additional histograms are overlaid onto Fig. 6.1, corresponding to different background sources, described below.

Since the pion multiplicity per B^+ can be large, the dominant background in the B^{**} sample is expected to come from combinatorial events, where pions are produced independently of the B mesons. These type of events should occur in approximately equal rates for positively and negatively charged pions. Therefore, it is possible to estimate their effect on the mass distribution by looking at like-charge combinations $(B^+\pi^+, B^-\pi^-)$, which will contain no signal component. The resulting histogram is overlaid on Fig. 6.1, and shows a smooth, broad shape, with no significant structure. The signal distribution shows a similar shape, except in the region $[0.37 < \Delta M < 0.49]$ GeV/c^2, which is interpreted to be the ΔM signature of decays (4.4–4.6).

In addition to the combinatorial background, it is possible that some B_s^{**} events can be mis-identified as B^{**} candidates. These events are topologically identical with the signal, so their contribution will not be suppressed by the standard selections. They decay into B^+K^- final states, as shown in decays (4.7–4.9), and so any kaons falsely identified as pions will contaminate the B^{**} sample. The effect of this B_s^{**} reflection on the ΔM distribution is determined from simulation, the details of which are given in section 5.5.1. The results are shown by the filled histogram in Fig. 6.1: a low, broad shape in ΔM, with a threshold at ~ 0.42 GeV/c^2.

Taken in combination, the two background histograms closely fit the shape of the ΔM distribution for the signal sample, outside the region of excess events. However, the opposite-charge sample contains around 50 more events per bin than the like-charge sample, over most of the range of the distribution. This surfeit of events is attributed to non-resonant $B\pi$ production, combined with a contribution from the two broad $L = 1$ states B_0^* and B_1'. All theories predict large widths for these states (> 100 MeV/c^2), as summarised in Chapter 2.

All background sources are therefore expected to contribute broad, smooth distributions in ΔM. These can be modelled as a whole by single polynomial function, with no need for threshold effects or background resonances. The lowest order polynomial which models the like-charge sample is chosen; this is determined to be $p(4)$, by a χ^2

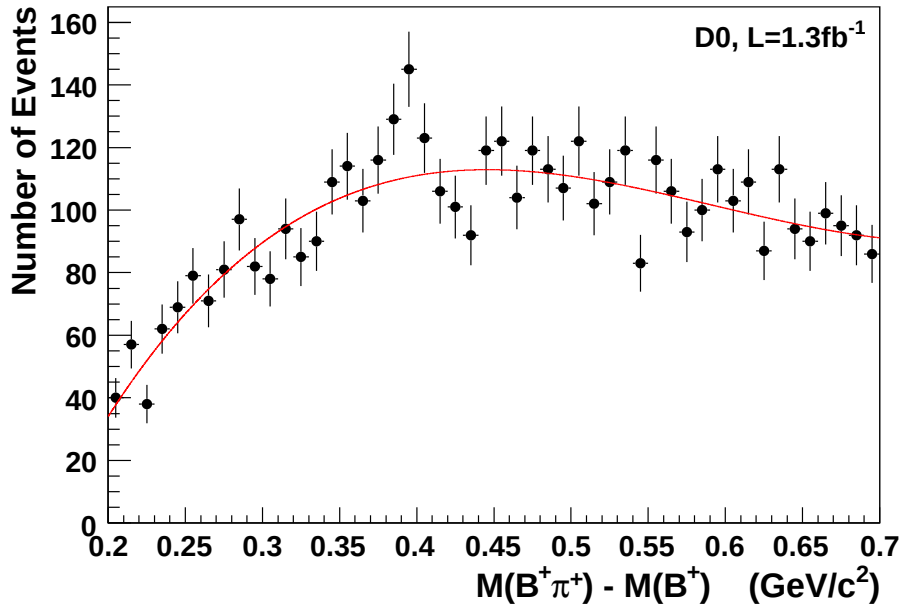

Figure 6.2: ΔM distribution for like-charge $B\pi$ events. The solid line shows the result of a χ^2 fit to a fourth order polynomial, as described in the text.

minimisation fit, as shown by the curve in Fig. 6.2. The background parameterisation is then:

$$f_{\text{bckg}} = a_0 + a_1 x + a_2 x^2 + a_3 x^3 + a_4 x^4, \tag{6.11}$$

where all five coefficients a_i are free parameters in the fit.

6.2.3 Results

The combined signal and background model $f_{\text{tot}} = f_{\text{sig}} + f_{\text{bckg}}$ for the ΔM distribution is fitted to the data by χ^2 minimisation. This is carried out using the MINUIT package [92] over a fitting range of $0.2 < \Delta M < 0.7$ GeV/c^2, covering 50 bins of equal width 10 MeV/c^2. Once the fitting procedure has converged on a stable minimum, the MINOS processor is used to determine parameter errors. This takes into account both parameter correlations and non-linearities, and is useful in handling problems where either of these factors are significant. For the fit over ΔM, the uncertainties calculated by MINOS are

symmetric about the converged value of each parameter, with magnitudes very close to the parabolic errors calculated by the usual MINUIT algorithm. As such, all statistical uncertainties quoted for the ΔM fit are taken from the parabolic values.

The χ^2 fit is appropriate because the observed (N_i) and expected (λ_i) populations of each bin can be used to construct a statistic, Q_i, which is normally distributed with mean 0 and variance 1:

$$Q_i = \frac{(N_i - \lambda_i)^2}{[\sigma(\lambda_i)]^2} = \frac{(N_i - \lambda_i)^2}{\lambda_i^2} \tag{6.12}$$

Here it is assumed that the contents of each bin are normally distributed. This becomes a statistically sound assumption for $N_i > 50$, which is the case for all bins used in the fit. The sum of Q_i for all bins will then be distributed according to the χ^2 distribution, with the appropriate number of degrees of freedom (d.o.f.) [93]. In this way, the data is used to find the parameter values most likely to result in the observed distribution. In addition, the χ^2 statistic can be used to find the statistical significance of a particular fit parameterisation, with respect to alternative models.

The fit converges with a χ^2 of 32.9, with 40 degrees of freedom corresponding to the 50 data points, minus the ten free parameters (five signal, five background). The fitting function is shown overlaid onto the data points in Fig. 6.3. The three distinct peaks can be seen, corresponding to the transitions as labelled on the figure.

The values of the mass parameters determined from the fit are:

$$x_1 + M_\gamma = 441.0 \pm 2.4 \text{ MeV}/c^2 , \tag{6.13}$$

$$x_2 - x_1 = 26.2 \pm 3.1 \text{ MeV}/c^2 . \tag{6.14}$$

These cannot yet be directly associated with the physical parameters of the B^{**} states, as there are systematic effects associated with the reconstruction process, which must be considered. All mass measurements must be shifted upward to correct for the D0 momentum scale uncertainty by an amount ϵ_M, according to Equation (4.23). This process

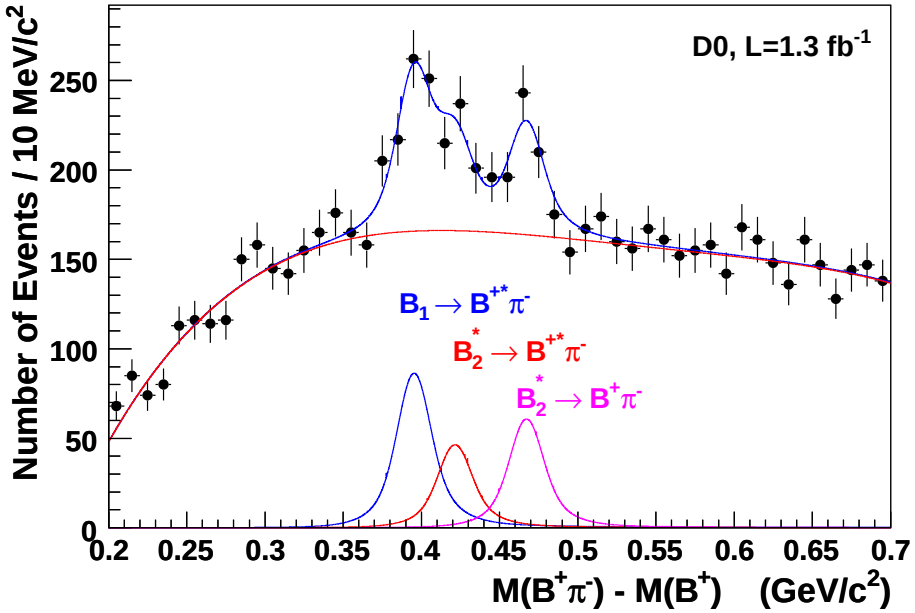

Figure 6.3: Signal-plus-background fit over the ΔM distribution. Shown separately are the contributions from background and the three signal components, which are labelled by their respective decays.

yields:

$$\begin{aligned} M(B_1) - M(B^+) &= x_1 + M_\gamma + \epsilon_M(x_1 + M_\gamma) \\ &= 441.0 + 7.5\left(\frac{441.0}{5271.6}\right) \\ &= 441.6\ \text{MeV}/c^2 \end{aligned} \tag{6.15}$$

$$\begin{aligned} M(B_2^*) - M(B_1) &= x_2 - x_1 + \epsilon_M(x_2 - x_1) \\ &= 26.2 + 7.5\left(\frac{26.2}{5271.6}\right) \\ &= 26.2\ \text{MeV}/c^2 \end{aligned} \tag{6.16}$$

These corrections are taken to have a 100% systematic uncertainty. The absolute masses of the B_1 and B_2^* mesons are calculated from these mass differences in Section 7.1. This calculation requires knowledge of the parameter correlations, in order to determine the combined uncertainties. The correlation coefficients between the parameters are shown

in Table 6.1.

The normalisation and signal composition fractions returned by the fit are:

$$f_1 = 0.449 \pm 0.063 \,, \tag{6.17}$$

$$f_2 = 0.436 \pm 0.086 \,, \tag{6.18}$$

$$N = 662 \pm 91 \text{ events.} \tag{6.19}$$

The total number of events, N, is used to determine the production rate of the B^{**} states, relative to the B^+ rate. This is described in Section 7.3.1. The fractions f_1 and f_2 define the observed composition of the B^{**} sample, and are used to calculate the associated branching ratios in Section 7.2.

Table 6.1: Correlation coefficients of the B^{**} parameters in the ΔM fit.

Source	M_1 [a]	M_{21} [b]	f_1	f_2	N
M_1	1.00	-0.659	0.394	-0.355	-0.233
M_{21}	-0.659	1.00	-0.205	0.377	0.277
f_1	0.394	-0.205	1.00	-0.361	-0.342
f_2	-0.355	0.377	-0.361	1.00	0.064
N	-0.233	0.277	-0.342	0.064	1.00

[a] $M_1 = M(B_1) - M(B^+)$ (MeV/c^2).
[b] $M_{21} = M(B_2^*) - M(B_1)$ (MeV/c^2).

6.2.4 Signal Significance and Alternative Fitting Hypotheses

The above results are only valid within the assumption that the ΔM distribution exhibits a three-peak structure. To check the validity of this assumption, the three-peak fitting hypothesis is tested against other parameterisations of the data. Of particular interest are three alternative hypotheses:

A. The data is consistent with a background-only parameterisation;

B. The data is consistent with a single mass peak;

C. The data is consistent with a two-peak hypothesis.

Each of these possibilities is investigated by fitting over the modified parameterisation. The change in the χ^2 parameter under different fit models, δ, gives a quantitative measure of the confidence with which each hypothesis can be ruled out, with respect to the primary fitting model. The technique used for this hypothesis testing is now outlined.

The χ^2 change δ is itself distributed as a χ^2 function with the number of degrees of freedom equal to the difference in dimensionality (i.e. number of free parameters) between the two hypotheses, m. The significance of the increase in likelihood under the primary hypothesis is then equal to the area under the χ^2 probability density function $P_m(x)$ [93]:

$$\alpha \equiv \int_{\delta}^{\infty} P_m(x)dx \; . \tag{6.20}$$

where:

$$P_m(x) = \frac{1}{2^{m/2}\Gamma(m/2)} x^{(m/2)-1} e^{-x/2} \; , \tag{6.21}$$

and Γ is the Gamma function. This p-value is converted to the conventional particle physics significance measure by use of the error function [94]:

$$n_\sigma = 2\sqrt{\frac{2}{\pi}} \int_{1-\alpha}^{\infty} e^{-t^2} dt \; . \tag{6.22}$$

Here n_σ is the displacement, in units of σ, from the mean of a normal distribution, which corresponds to a tail area of α. This machinery is now used to assess the significance of the signal peaks.

For the background-only hypothesis, the parameterisation is straightforward: the ΔM distribution is fitted to a fourth order polynomial. This is shown in Fig. 6.4(a). It is clear that the data is poorly modelled by this function, with the χ^2/d.o.f. of the fit increasing to $98.5/(50-5)$. This corresponds to $\delta = 65.6$, with $m = (10-5)$, when compared to the three-peak fit. Using Eqs. (6.20, 6.22), this infers that this alternative hypothesis can be rejected with a statistical significance of 7.1σ, with respect to the primary hypothesis.

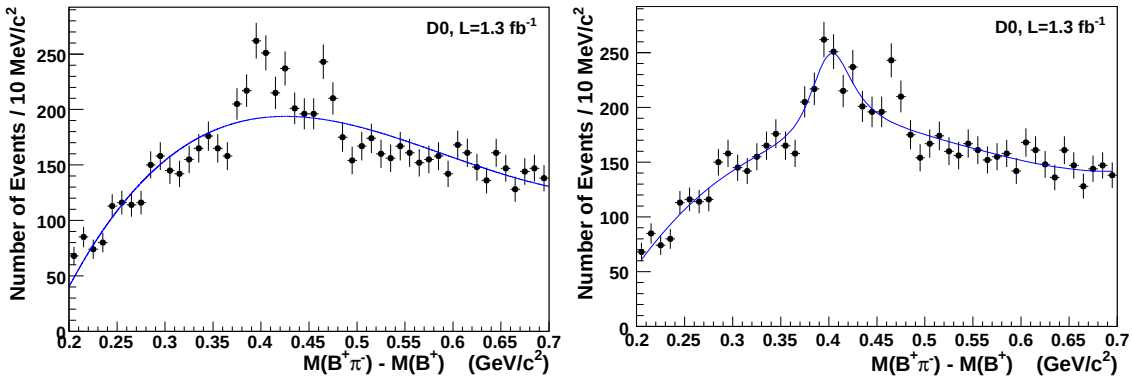

(a) Background-only hypothesis;

(b) One-peak hypothesis;

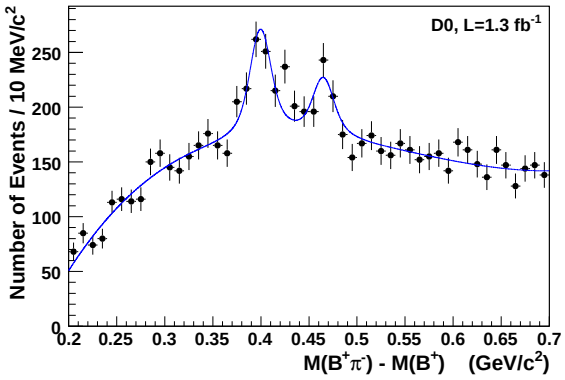

(c) Two-peak hypothesis;

Figure 6.4: Alternative fitting hypotheses for the ΔM distribution, as described in the text.

The above test gives very strong evidence that there is some resonant behaviour in the signal sample, inconsistent with background effects. We next examine the confidence of the claim that there are multiple signal resonances, by comparing to the fit over a single mass peak. In this case, the peak is modelled by the usual convolution of Breit-Wigner function with the detector resolution. The position, normalisation, and physical width of the peak are all free parameters in the fit, the results of which are shown in Fig. 6.4(b). The χ^2/d.o.f. for this fit is $52.9/(50-8)$, corresponding to $\delta = 20.0, m = (10-8)$. This gives a confidence of 4.1σ that the data is inconsistent with a single resonance, with

respect to the primary hypothesis. The signal converges to a width 44.9 ± 2.6 MeV/c^2, with central value 451.0 ± 6.9 MeV/c^2.

Finally, the two-peak hypothesis is tested by removing the $B^*_{s2} \to B^{*+}\pi$ signal contribution. This corresponds to the central resonance in Fig. 6.3, which is the least statistically significant of the three peaks. The other two peaks are parameterised in the usual way, with the positions and relative normalisations allowed to vary, and both widths fixed at 10 MeV/c^2. Figure 6.4(c) shows the result of the fit. Here, χ^2/d.o.f.$= 41.2/(50-9)$, which corresponds to $\delta = 8.3, m = (10-9)$; giving 2.9σ significance for the $B^*_{s2} \to B^{*+}\pi$ peak.

In summary, the data is highly inconsistent with a background-only hypothesis, and there is strong evidence $(> 4\sigma)$ that the signal corresponds to multiple peaks. However, there is not sufficient evidence to distinguish the two- and three- peak hypotheses with a high level of confidence.

6.2.5 Systematic Uncertainties

The systematic uncertainties in the ΔM fit are determined from a number of different sources. These are summarised in Table 6.2, and described in this section. As long as a parameter is allowed to vary in the ΔM fit, the effect of its variation on the other parameters is quantified, and included in the statistical uncertainties calculated by MINUIT. Systematic uncertainties arise when parameters are fixed at positions which may differ from their true values, or where the fitting model does not fully replicate the true behaviour of the transition. To estimate the uncertainties arising from a particular fixed parameter, the fit is repeated over a range of different (fixed) values. The 1σ uncertainty on each free parameter is then taken to be half of its total variation under these fits. This effectively averages the positive and negative systematic uncertainties, which are found to be comparable in all cases. The five fixed parameters in the ΔM fit are listed at the end of Section 6.2.1.

For example, the physical mass width of all three decays is fixed at 10 MeV/c^2 in the

fit. Had a different width been chosen, the free parameters may have converged to different values. Since the true width is unknown, the best we can do is repeat the fit over many different values of Γ, and look at the variation in the converged signal parameters. Following theoretical predictions, the range of widths used in this study is $0 < \Gamma < 20$ MeV/c^2. This source gives the most significant contribution to the systematic uncertainties on the B^{**} properties. Primarily, this is because the width is not well constrained by theory or experiment, so the variation is over a very large range.

Another fixed parameter in the fit is the mass difference $M(B^{*+}) - M(B^{+}) = 45.78 \pm 0.35$ MeV/c^2. Unlike the B^{**} width, this quantity is well measured, and the associated systematic uncertainty is extracted by repeating the fit with the parameter value taken to its one standard deviation limits.

The mass resolution parameters were measured by simulation, and hence their accuracy relies on good agreement of simulation with data. As described in Section 5.3.3, studies have shown that simulation underestimates decay widths of B mesons by up to 10% compared to data. The resolution parameters σ_1, σ_2 used in the fit include a 10% correction to account for this effect. The fit is repeated without this correction; the fit is

Table 6.2: Systematic uncertainties of the B^{**} parameters determined from the ΔM fit. The rows show the various sources of systematic error as described in the text. The columns show the resulting uncertainties for each of the five free signal parameters.

Source	δM_1 [a]	δM_{21} [b]	δf_1	δf_2	δN
Background parameterisation	0.15	0.15	0.009	0.008	19
Bin widths/positions	0.85	0.70	0.006	0.024	12
Value of Γ	0.75	0.55	0.022	0.029	138
B^{+*} mass uncertainty	0.30	0.25	0.004	0.004	6
Momentum scale	0.60	0.03	—	—	—
Resolution uncertainty	0.20	0.05	0.007	0.004	10
Total	1.30	0.90	0.026	0.039	140

[a] $M_1 = M(B_1) - M(B^{+})$ (MeV/c^2).
[b] $M_{21} = M(B_2^{*}) - M(B_1)$ (MeV/c^2).

also performed with each decay parameterised by a separate resolution function, as determined in Section 5.3.1. The total systematic uncertainty assigned to the mass resolution is based on changes in the fit parameters under both these modifications.

In addition, a 100% systematic uncertainty is assigned to the mass shifts calculated in Eqs. (6.16–6.17), which are corrections to the D0 momentum scale uncertainty.

The choice of binning scheme is tested by fitting over different numbers of bins in the range $0.2 < \Delta M < 0.7$ GeV/c^2. Finally, the choice of background parameterisation is examined by replacing the model with a third or fifth order polynomial function.

6.2.6 Consistency Checks

There are two simple tests which can be performed to check the reliability and stability of the mass fitting procedure and the associated statistical analysis. The first is to fit the ΔM distribution for background samples, allowing a contribution from a 'signal' peak. The central value and width of this peak are fixed at $\Delta M = 451$ MeV/c^2, $\Gamma = 44.9$ MeV/c^2, following the results of the one-peak alternative modelling of the signal data, described in Section 6.2.4. The number of events contained by the peak is a free parameter in the fit. For true background-only samples, the fit should converge to give a low statistical significance of the peak, with the number of events consistent with zero.

Two different background samples are investigated. The first is the like-charge sample, which is certain to be free of signal contamination. The second is defined by all unlike-charge events with impact parameter significance $S_\pi > 4$, i.e. events where the pion is extremely unlikely to originate at the primary vertex [see Eq. (4.12)]. The ΔM distributions for these two samples, and the results of the fit to signal and background models, are shown in Fig. 6.5. In each case, the results of the one-peak fitting hypothesis are shown by the solid line; and the background-only fit by the dashed line.

For the like-charge $B\pi$ combinations, the one-peak fit converges to give $N = 50^{+66}_{-50}$ 'signal' events. The χ^2 is 28.4, compared to 31.1 for the background-only hypothesis. The only additional degree-of-freedom is the number of signal events, since the position and width of the peak are fixed, therefore $m = 1$. Using equations (6.20–6.22), this statistical

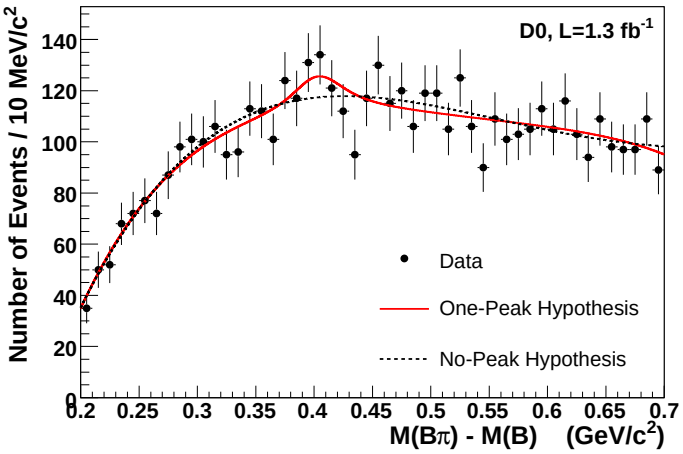

(a) Like-charge $B\pi$ combinations;

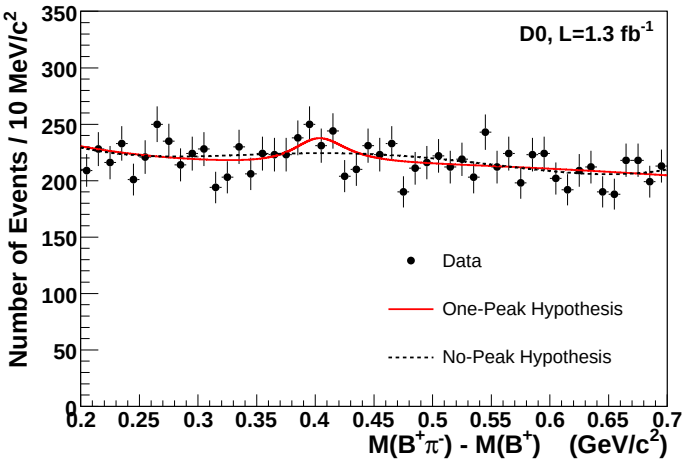

(b) Pions not produced at PV

Figure 6.5: Testing for B^{**} signal events in background samples. Two independent background-only samples are fitted to a single-peak hypothesis, with results as described in the text.

significance of the peak is determined to be 1.6σ. This represents a low confidence that the signal hypothesis is true, as is desired in such a background sample.

Similarly, for the sample containing pions not compatible with primary vertex production, the following results are obtained. The number of events in the peak converges

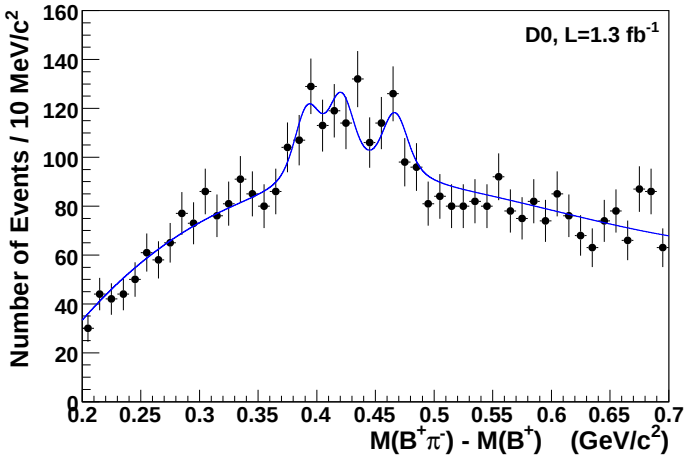

(a) $B^+\pi^-$ combinations;

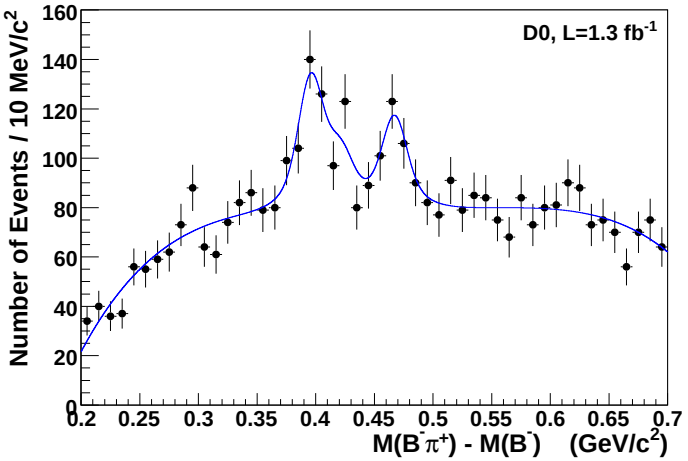

(b) $B^-\pi^+$ combinations;

Figure 6.6: Fitting ΔM over sub-samples of the B^{**} signal data. The two samples are defined by the pion charge, and fitted to the usual three-peak hypothesis, with results as described in the text.

to $N = 166 \pm 88$; with the χ^2 decreasing from 42.8 to 39.2 when the peak contribution is introduced. The statistical significance of the 'signal' contribution is then 1.9σ. Once more, this expresses a low confidence that the one-peak hypothesis is correctly modelling the data.

The second test of the fitting procedure is to divide the signal data set into two appropriate sub-samples, and repeat the fit. This will check that the resulting converged parameter values are consistent in each sample, and with the values obtained from the full data fit. Since the number of signal events is rather small, further sub-division is expected to reduce the precision with which the B^{**} properties can be measured, and so some deviation from the reported values of masses and branching ratios is expected. Nevertheless, these movements should be reasonable with respect to the parameter uncertainties. The division into two sub-samples is made according to the charge of the pion in the B^{**} decay; the fit is performed as with the full data set, and the results are shown in Fig. 6.6.

Table 6.3 lists the converged values and associated statistical uncertainties for the free parameters over the two sub-sample fits, and the full data fit. Here the masses are those directly returned by the fit, and have not been shifted to correct for the D0 momentum scale uncertainty. The peak positions remain stable, with only small increases in uncertainty. The fractions f_1 and f_2 show larger shifts, but are consistent within one standard deviation, since the uncertainties have markedly increased. The number of signal events in each sample is consistent with equal decays into $B^+\pi^-$ and $B^-\pi^+$ combinations.

Table 6.3: Measured B^{**} parameters for independent sub-samples of data. Shown are the converged values and statistical uncertainties for each of the five signal parameters in the ΔM fit. The two sub-samples are defined by the sign of the pion charge.

Sample	M_1 [a]	M_{21} [b]	f_1	f_2	N
$B^+\pi^-$ events	437.8 ± 2.7	28.9 ± 3.3	0.334 ± 0.086	0.544 ± 0.118	304 ± 52
$B^-\pi^+$ events	441.5 ± 2.7	25.6 ± 3.6	0.482 ± 0.076	0.340 ± 0.114	374 ± 62
$B^+\pi^- + B^-\pi^+$	441.0 ± 2.4	26.2 ± 3.1	0.449 ± 0.063	0.436 ± 0.086	662 ± 91

[a] $M_1 = M(B_1) - M(B^+)$ (MeV/c^2).
[b] $M_{21} = M(B_2^*) - M(B_1)$ (MeV/c^2).

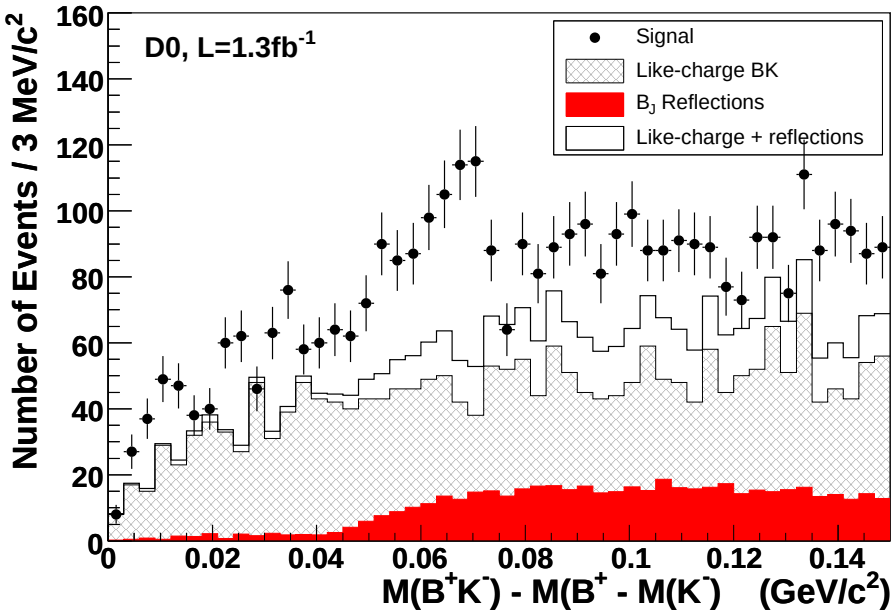

Figure 6.7: Unfitted ΔM_s distribution. Shown separately are the data points for the signal sample, the shape of the like-sign background (cross-hatched histogram), the reflections from B^{**} events (filled histogram), and the sum of contributions from like-sign and reflection backgrounds (unshaded histogram), as described in the text.

6.3 B_s^{**} Mass Distribution

6.3.1 Choice of Fitting Hypothesis

The data markers in Figure 6.7 show the distribution of ΔM_s for the B_s^{**} signal sample. In this case, the choice of a fitting hypothesis is complicated by the closeness of the production threshold to the region of interest. It is possible that one or more of the $B_s^{**} \to B^{(*)+}K^-$ decays can be kinematically forbidden, if the invariant mass of the excited state is less than the combined mass of the daughter particles. In addition, the contribution of phase-space factors to the production and decay rates will become significant. These phase space suppressions are described in more detail in Section 6.3.4. At this point, it is sufficient to appreciate that the three transitions (4.7–4.9) may not correspond to three observable signal peaks in the ΔM_s distribution.

Following this statement, the preliminary study of Fig. 6.7 suggests that there is a single region of excess events, at $\Delta M_s \approx 67$ MeV/c^2. There is no indication of a signal at higher ΔM_s, suggesting that this excess corresponds to the highest energy transition, $B_{s2}^* \to B^+K^-$. If the signal were instead associated with the decay $B_{s2}^* \to B^{*+}K^-$, an additional peak would be expected from the decay to the ground state, shifted to higher ΔM_s by $M(B^{*+}) - M(B^+) \approx 46$ MeV/c^2. This second peak would be subject to reduced phase-space suppression and therefore contain a significant number of events. In the absence of such a peak, this alternative hypothesis is excluded. Similarly, if the signal were associated with the $B_{s1} \to B^{*+}K^-$ decay, two additional peaks would be expected in the higher ΔM_s region, since all theories predict $M(B_{s1}) < M(B_{s2}^*)$, with an expected mass splitting usually around 12–15 MeV/c^2 (see Table 2.6).

The primary fitting hypothesis therefore assumes that there is one signal peak in the ΔM_s distribution, arising from decays of B_{s2}^* to the ground state. The signal is then parameterised according to:

$$f_{\text{sig}} = N \cdot D(x; x_0, \Gamma, \bar{R}). \tag{6.23}$$

Here x_0 is the central value of the signal in $x \equiv \Delta M_s$, Γ is the physical decay width, and $\bar{R}$ are the three mass resolution parameters (σ_1, σ_2, S) for the decay. The number of events in the signal peak is given by N.

The experimental mass resolution of this decay is determined in Section 5.3.2 to be well modelled by a double Gaussian function, with parameters $\sigma_1 = 6.8$ MeV/c^2, $\sigma_2 = 3.0$ MeV/c^2, $S = 1.2$. The physical width is predicted by theory to be around 1 MeV/c^2, as shown in Table 2.6. The fitting procedure is not sensitive to values of Γ smaller than the mass resolution, and so the width is fixed to be 1.0 MeV/c^2 in the fit. A systematic uncertainty is assigned to this choice in the usual manner, by refitting under a number of different widths and measuring changes in the final fitted parameters.

The central value of the signal is then directly related to the absolute B_{s2}^* mass according to:

$$x_0 = M(B_{s2}^*) - M(B^+) - M(K^-), \tag{6.24}$$

where it is assumed that the measured value has been corrected to account for the D0 momentum scale uncertainty.

This completes the description of the signal fitting hypothesis, which is completely defined by the following six parameters:

A. Four fixed parameters in the fit:

   a) Three mass resolution parameters, (σ_1, σ_2, S), fixed from simulation;

   b) $\Gamma = 1.0$ MeV/c^2 fixed following theoretical predictions.

B. Two free parameters in the fit:

   a) $x_0 \equiv \Delta M_s(B^*_{s2}) = M(B^*_{s2}) - M(B^+) - M(K^-)$;

   b) N: total number of signal events in the peak.

6.3.2 Backgrounds

Since the decays of B^{**}_s are topologically isomorphic with B^{**} events, very similar background sources are anticipated. The difference arises in parameterising the resulting background shape, since the proximity to the production threshold requires that the condition $N(0) = 0$ be enforced; where $N(\Delta M_s)$ is the number of events at a given point in the distribution. The two overlaid histograms in Fig. 6.7 represent background contributions to the ΔM_s distribution, which are now discussed.

The contribution from combinatorial background is estimated from the ΔM_s distribution for like-charge combinations (B^+K^+, B^-K^-), shown by the solid line in Fig. 6.7. The number of events per bin is relatively constant for $\Delta M_s > 0.04$ GeV/c^2, with a gradual 'turn-off' below this mass.

The effect of reflections from B^{**} events is taken into account, shown by the filled area in Fig. 6.7. This corresponds to a pion from a B^{**} decay being mis-identified as a kaon, and is modelled by simulation, as described in section 5.5.2. The contribution of such events is more significant than for the equivalent reflections in the B^{**} distribution, as can be seen by examination of the respective histograms in Figures 6.1 and 6.7. This is

because the production rates are significantly smaller for the excited B_s states, which is determined quantitatively in section 7.3.2.

The reflections show threshold behaviour at $\Delta M_s = 0.04$ GeV/c^2. Taken in combination with the combinatorial background, the resulting distribution gives a good fit to the shape of the signal histogram, except for an excess in the region $0.05 < \Delta M_s < 0.07$. This is interpreted as arising from $B_{s2}^* \to B^+K^-$ decays.

Non-resonant BK production, as well as decays of the wide $L = 1$ states B_{s0}^* and B_{s1}', will also contribute to the background. As discussed in section 6.2.2, the distributions are difficult to model, but expected to be smooth, broad and featureless, with the exception of the threshold turn-off at $\Delta M_s = 0$.

The prescription for modelling the background shape in B_s^{**} decays is as follows: the simplest possible function is chosen which will model the shape of the like-charge distribution, i.e. the function with the fewest parameters. The same functional form is then used to parameterise the background shape for the signal sample. However, the particular values of any background parameters are allowed to vary in the fitting procedure, to account for contributions from the reflections, broad states, and non-resonant production.

The like-charge distribution is shown in Fig. 6.8, along with the results of a likelihood fit to the chosen parameterisation, a modified power-law function:

$$F_{\text{bckg}}(\Delta M_s) \;=\; c \cdot (\Delta M)^k + d \cdot \Delta M. \tag{6.25}$$

Here the parameters c, d and k all participate in the fit. The dimensionless 'scale factor' k is the dominant controlling variable in the shape of the curve. As a result, it should not change significantly in subsequent fits over the signal sample, in contrast to the fine tuning parameters c and d. The soundness of the background model can therefore be tested by keeping this scale factor fixed at the value determined by the like-charge sample, $k = 0.55 \pm 0.04$. This test is used to estimate a systematic uncertainty arising from background parameterisation, as described in section 6.3.5.

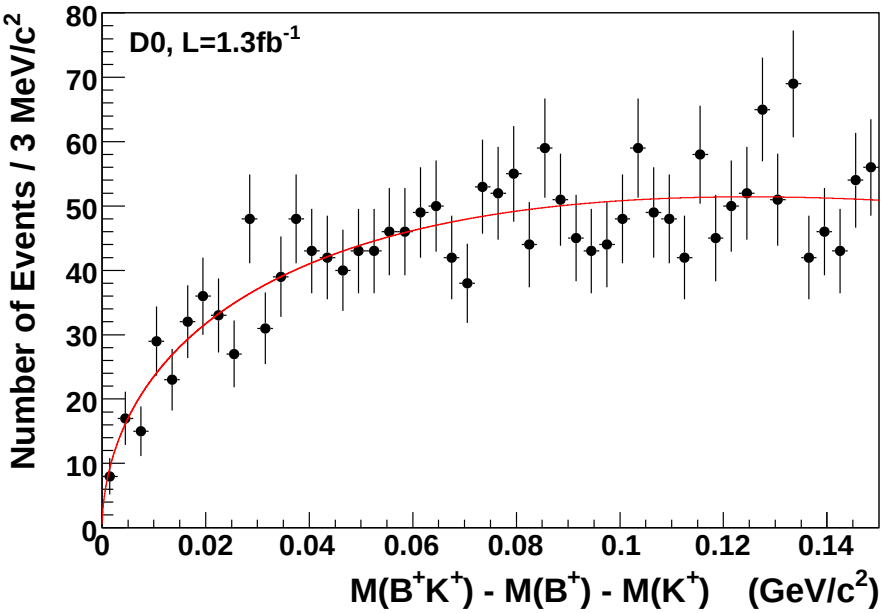

Figure 6.8: ΔM_s distribution for like-charge BK events. The solid line shows the result of a likelihood fit to a power-law function, as described in the text.

6.3.3 Results

Inspection of Fig. 6.7 shows that several bins near the production threshold contain fewer than 25 events each. If the fit is to extend over this region, then a χ^2 fit is no longer appropriate, since the assumption of Gaussian behaviour becomes invalid in small populations. For a stable description of the background contribution, it is preferable to include all data points below the signal region, including these low-content bins. Therefore, a binned maximum likelihood fit is used to determine the signal and background parameters by a fit to the data points. The fit is performed over a range of $0 < \Delta M_s < 150$ MeV/c^2, covering 50 bins of width 3 MeV/c^2, using the MINUIT package, with error calculations from the MINOS algorithm.

The maximum likelihood method tunes the five free parameters in the fit to obtain the values most likely to yield the observed data distribution. The number of events N_i in each bin should follow a Poisson distribution [95], with the mean $\lambda_i = f^i_{\text{total}}$ determined by the model. The likelihood for each bin is the probability of it containing N_i events,

given the current model and parameter values. The total likelihood L for the fit is then the product of L_i for all bins in the fitting range:

$$L_i = \frac{e^{-\lambda_i}\lambda_i^{N_i}}{N_i!}, \tag{6.26}$$

$$L = \prod_{i=1}^{50} L_i = \frac{e^{-\sum\lambda_i}\prod\lambda_i^{N_i}}{N_1!...N_{50}!}. \tag{6.27}$$

It is conventional to take natural logarithms to separate the different terms in this expression; we also multiply by (-1) to convert the problem into a minimisation, following the requirements of MINUIT.

$$-ln(L) = \sum_{i=1}^{50} \left[\lambda_i - N_i ln(\lambda_i) + ln(N_i!)\right]. \tag{6.28}$$

This function must then be minimised with respect to the set of 50 expected bin contents, λ_i, which in turn are determined by the five free parameters of the function $f_{\text{total}}(x)$. The third term in Eq. (6.28) depends only on the observed bin contents, and will not change in the minimisation process. As a result it can be subtracted without affecting the parameter convergence. Hypothesis testing is also unchanged by this transformation, since the significant quantity is the change in log likelihood over different fitting models. Hence the actual parameter minimised by MINUIT is:

$$-ln(\mathcal{L}) = -ln(L) - \sum_{i=1}^{50} ln(N_i!) = \sum_{i=1}^{50} \left[\lambda_i - N_i ln(\lambda_i)\right]. \tag{6.29}$$

The fitting function resulting from this minimisation is shown by the solid line in Fig. 6.9, with the contributions of signal and background shown separately. The final converged values for the free signal parameters are:

$$\Delta M_s(B_{s2}^*) = 66.7 \pm 1.1 \text{ MeV}/c^2, \tag{6.30}$$

$$N(B_{s2}^*) = 125 \pm 25 \text{ events}. \tag{6.31}$$

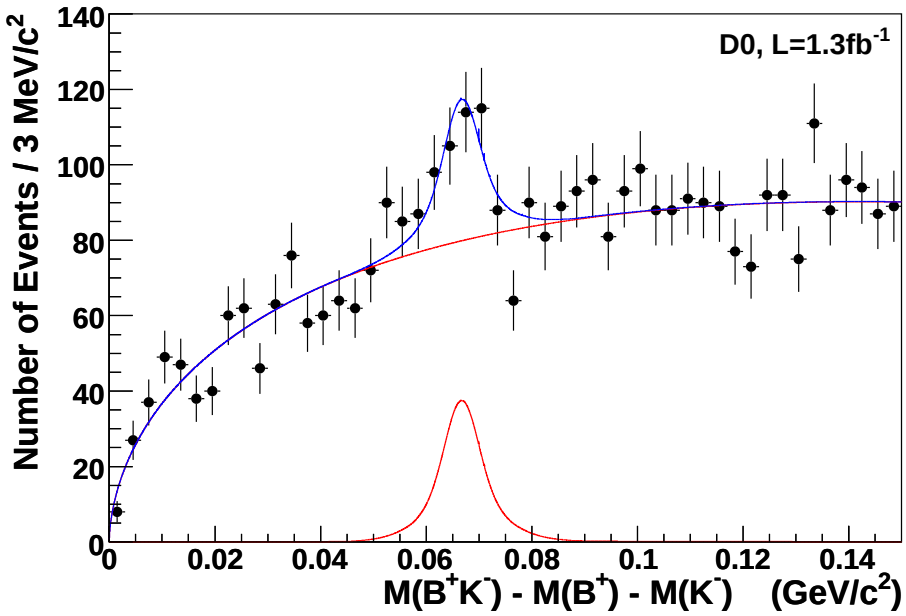

Figure 6.9: Signal-plus-background fit over the ΔM_s distribution. Shown separately are the contributions from background and signal components as described in the text.

The mass is again shifted upwards to account for the D0 momentum scale uncertainty:

$$\begin{aligned} M(B^*_{s2}) - M(B^+) - M(K^-) &= \Delta M_s(B^*_{s2}) + \epsilon_M[\Delta M_s(B^*_{s2})] \\ &= 66.7 + 7.5\left(\frac{66.7}{5271.6}\right) \\ &= 66.8\ \text{MeV}/c^2, \end{aligned} \tag{6.32}$$

where a 100% systematic uncertainty is assigned to this mass shift. In Chapter 7, this mass difference is converted into an absolute mass measurement, using the PDG masses of B^+ and K^-. In addition, the number of signal events is used to determine the B^*_{s2} production rate relative to the B^+.

The dimensionless scale factor k modelling the background shape is determined to be $k = 0.59 \pm 0.03$. This is consistent with the value obtained by fitting over the like-charge distribution (0.55 ± 0.04).

6.3.4 Signal Significance and Alternative Fitting Hypotheses

The decision to model the signal contribution to the ΔM_s data distribution by a single peak would appear to go against the theoretical expectations. In addition, strong evidence of a multiple-peak signal has been found in the corresponding distribution for B^{**} decays, as described in Section 6.2. As a result, it is important to investigate other fitting hypotheses, and to understand how the divergence from the (naïvely) expected three-peak structure arises.

Significance of $B^*_{s2} \rightarrow B^+K^-$ Signal

Before looking at alternative signal models, the statistical significance of the observed peak is tested. This is performed by fitting the ΔM_s distribution with a background-only parameterisation: using $f_{\text{back}}(\Delta M_s)$ as defined in Eq. (6.25). All three parameters are allowed to vary in the fit, and the results are shown in Fig. 6.10. The significance of the signal peak is then calculated using a likelihood ratio method, which compares the likelihoods of the null hypothesis H_0 (without B^*_{s2} signal) and the primary fitting hypothesis H_1 (with B^*_{s2} signal), to form the ratio:

$$\mathcal{L}_{0/1} = \frac{\mathcal{L}(H_0|\text{data})}{\mathcal{L}(H_1|\text{data})} \, . \tag{6.33}$$

The parameter $-2ln(\mathcal{L}_{0/1}) = 2[ln(\mathcal{L}_1) - ln(\mathcal{L}_0)]$ has the form of a χ^2 distribution, with the number of degrees of freedom equal to the difference in dimensionality between the two hypotheses, $m = (5-3)$ [96]. For the two models under examination, $-2ln(\mathcal{L}_{0/1}) = 26.8$, which corresponds to an area under the χ^2 probability density function of:

$$\alpha \equiv \int_{26.8}^{\infty} P_2(x)dx = 1.515 \times 10^{-6} \, . \tag{6.34}$$

Using Eq. (6.22), this yields a significance of 4.8σ.

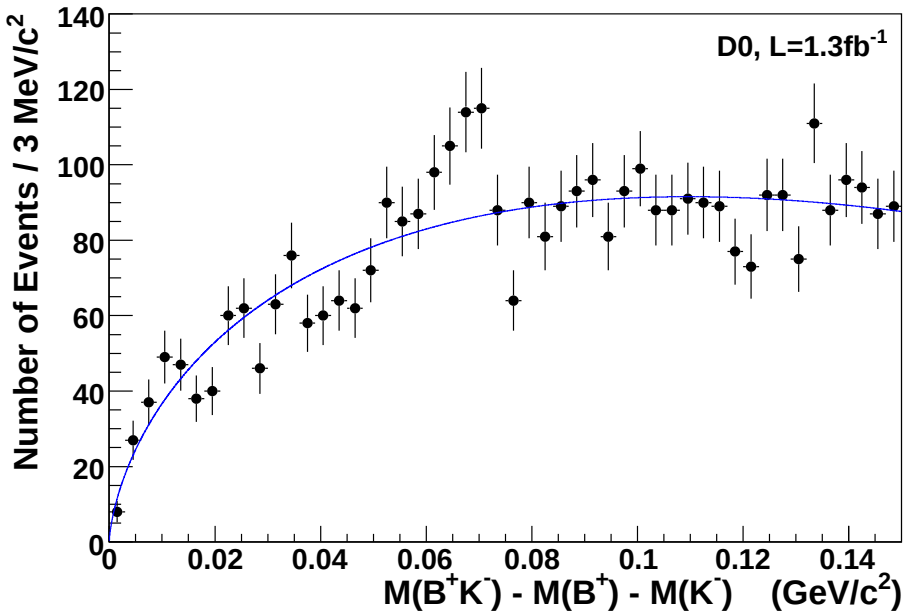

Figure 6.10: ΔM_s distribution fitted to a background-only model.

$B^*_{s2} \to B^{*+}K^-$ Signal

As discussed in Chapter 2, the B^*_{s2} meson has two possible decays into the ground state B^+. The signal in the ΔM_s distribution is associated with the direct decay to B^+K^-. The other possible decay proceeds via the singly excited B^{*+} meson, and so should result in a peak in the data distribution corresponding to $\Delta M_s \approx 66.7 - [M(B^{*+}) - M(B^+)] \approx 21$ MeV/c^2. Having measured the mass of this excited state, it is possible to determine the expected number of $B^*_{s2} \to B^{*+}K^-$ events, by calculating the phase space suppression factor, using the expression in Ref. [1]:

$$\frac{Br(B^*_{s2} \to B^+K^-)}{Br(B^*_{s2} \to B^{*+}K^-)} = \frac{0.4}{0.6} \cdot \left(\frac{p}{p^*}\right)^5 , \tag{6.35}$$

where p (p^*) is the momentum of the kaon in the $B^*_{s2} \to B^+K^-$ ($B^{*+}K^-$) decay, in the B^*_{s2} rest frame. These momenta are calculated using the standard expressions for two-body decay. Taking the PDG world average masses for the B^+ and kaon, and the B^*_{s2} mass as determined in Chapter 7, we obtain $p = 252.4$ MeV/c, $p^* = 138.4$ MeV/c; the suppression factor is then ~ 13.4.

In addition to this phase space ratio, the detection efficiency for the decay to $B^{*+}K^-$ will be reduced with respect to the higher energy transition, for the reasons explained in Section 7.2. As a result, fewer than ten $B^*_{s2} \to B^{*+}K^-$ events are expected in the data, distributed over several bins. With the number of background events in the sample, such an excess is not expected to be observed with any statistical significance.

To test this expectation, the fit is repeated with an additional contribution from $B^*_{s2} \to B^{*+}K^-$ decays. This central value of the second peak is fixed to be 45.78 MeV/c^2 lower than the primary signal peak, with the number of events as a free parameter. The mass resolution is taken to be the same as the direct B^*_{s2} decay, and the physical width is fixed at zero. The background is parameterised as usual, with all three parameters participating in the fit. The likelihood fit converges to give $N = 0$ events in the second peak, which therefore has no statistical significance with respect to the primary hypothesis. All other converged parameters are consistent with their one-peak values.

$B_{s1} \to B^{*+}K^-$ Signal

It remains to investigate the hypothesis that there is an additional signal in the data, corresponding to the $B_{s1} \to B^{*+}K^-$ decay. All theories predict $M(B^*_{s2}) > M(B_{s1})$, therefore the characteristic resonant peak of this transition should correspond to $\Delta M_s < 21$ MeV/c^2. A recent result by the CDF collaboration reported the observation of an excess of events at an invariant mass corresponding to $\Delta M_s = 10.73 \pm 0.21$ (stat.) ± 0.14 (syst.) MeV/c^2, and interpreted as the $B_{s1} \to B^{*+}K^-$ resonance [97].

To test for the presence of a B_{s1} signal in the data, a two-peak hypothesis is used to fit the ΔM_s distribution. Here the B_{s1} peak is assigned a vanishingly small physical width, by appropriate use of the dirac delta function; its shape is then parameterised by the double-Gaussian detector resolution function determined in Section 5.3.2. The relevant resolution parameters from Table 5.3 are summarised here:

$$\begin{aligned} \sigma_1(B_{s1}) &= 2.2 \pm 0.2 \text{ (stat.) MeV}/c^2, \\ \sigma_2(B_{s1}) &= 1.3 \pm 0.1 \text{ (stat.) MeV}/c^2, \\ S(B_{s1}) &= 3.6 \pm 1.0. \end{aligned} \tag{6.36}$$

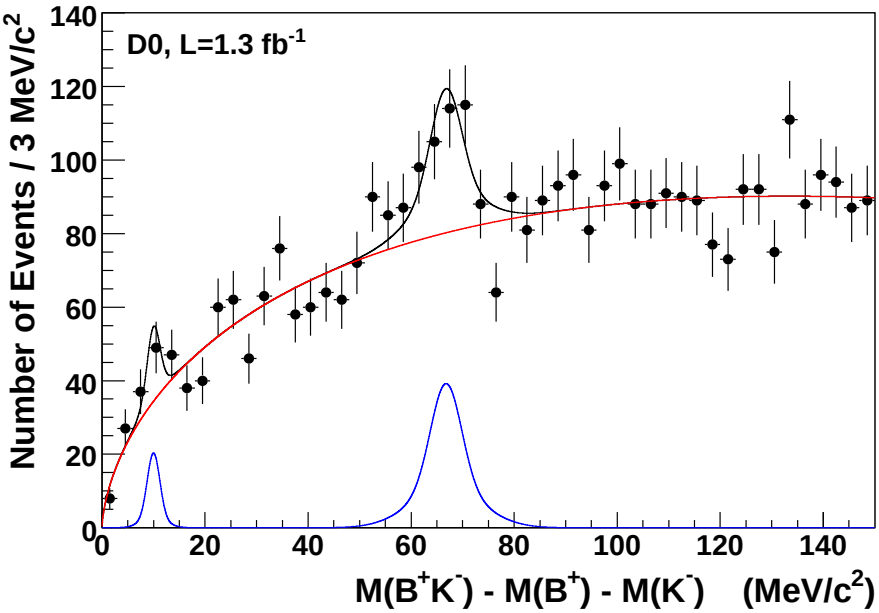

Figure 6.11: ΔM_s data distribution fitted to a two-peak hypothesis. Shown separately are contributions from background and the two signal peaks, as described in the text.

The resolution for a B_{s1} signal is thus considerably finer than that for the B^*_{s2} signal; this is expected due to the lower associated momenta of the final state particles.

The resulting fit over the data is shown in Fig. 6.11, giving the following parameters for the B_{s1} signal:

$$\begin{aligned} \Delta_s(B_{s1}) &= M(B_{s1}) - M(B^{*+}) - M(K^-) \\ &= 11.5 \pm 1.4 \text{ (stat.) MeV}/c^2, \qquad (6.37) \\ N &= 25 \pm 10 \text{ (stat.) events.} \qquad (6.38) \end{aligned}$$

The central mass of this resonance is therefore consistent with the value reported by CDF. However, the likelihood ratio with respect to the single-peak fit is only 5.4, with $m = 2$. Using the relations defined in Section 6.2.4, the significance of the B_{s1} signal is determined to be 1.8σ. Hence with the current data, the observation by CDF can be neither confirmed or excluded.

The B_{s2}^* parameters returned by the fit have values consistent with the primary hypothesis, demonstrating the stability of the fitting procedure:

$$M(B_{s2}^*) - M(B^+) = 66.8 \pm 1.4 \text{ (stat.) MeV}/c^2, \quad (6.39)$$

$$N(B_{s2}^*) = 130 \pm 30 \text{ (stat.) events}, \quad (6.40)$$

$$k = 0.68 \pm 0.02. \quad (6.41)$$

The background scale factor k is changed slightly, which is expected, since it is sensitive to the background at low ΔM_s. Future investigation of the B_{s1} meson will rely on developing stable models for the background shape close to the threshold.

6.3.5 Systematic Uncertainties

The allocation of systematic uncertainties to the fitting procedure proceeds analogously to the method described in Section 6.2.5. The summary of all sources and their contributions to the systematic errors on the signal parameters are summarised in Table 6.4.

The effect of selecting a particular binning scheme is tested by repeating the fit with 55, 60 and 65 bins instead of 50. The uncertainty on the two signal parameters is taken as half the total range of that parameter's converged values under these variations.

Similarly, the physical width $\Gamma(B_{s2}^*)$ is fixed at several values in the range $0 < \Gamma < 2$ MeV/c^2, and the fit repeated, to determine the systematic uncertainties associated with this source. Unlike the B^{**} decays, the B_{s2}^* width is well constrained by theory, and so the contribution to the uncertainty is much smaller.

The background parameterisation is not an arbitrary polynomial function, as was used for the B^{**} mass fit. Instead it was developed according to the shape of the like-charge BK distribution. As a result, attempting to fit with other background models is not a fair way to allocate a systematic uncertainty. Instead, the signal fit is undertaken with the scale factor k fixed at the value determined from the like-charge fit; the change in parameter values is then used to assign an uncertainty in the usual way.

The contribution from possible disagreement between data and simulation in the mass resolution measurement is determined by fitting with and without the 10% correction in

the parameters (σ_1, σ_2), as described in Section 5.3.3. Finally, the mass shift applied to correct for the D0 momentum scale uncertainty is assigned a 100% systematic error.

Table 6.4: Systematic uncertainties of the B^*_{s2} parameters determined from the ΔM_s fit. The rows show the different sources as described in the text, the columns show the effect on the two free signal parameters.

Source	$\delta M(B^*_{s2})$ (MeV/c^2)	δN
Background parameterisation	0.0	3
Bin widths/positions	0.3	7
Value of Γ	0.3	5
Momentum scale	0.1	0
Resolution uncertainty	0.1	3
Total	0.4	10

6.3.6 Consistency Checks

As with the B^{**} analysis, the signal fitting procedure is tested to ensure that it gives reasonable results over background samples, and consistent results over independent sub-samples of data. Two background data sets are defined in the usual way: a like-charge BK sample, with all other requirements identical with signal selection; and a sample containing kaons with $S_K > 4$, i.e. incompatible with primary vertex production [see Eq. (4.12)]. The two resulting ΔM_s distributions are fitted to a one-peak hypothesis, with the central value fixed at 66.7 MeV/c^2, following the results of the signal fit [Eq. (6.30)]. The width is again fixed at 1 MeV/c^2, and the number of events in the peak is a free parameter in the fits. The results are compared to those from a background-only fitting hypothesis, to ascertain the statistical significance of the peaks; for true background samples, this should be low.

Figure 6.12 shows the data histograms, and the resulting fits to one-peak and background-only fits. For the like-charge distribution, the number of events converges to $N = 0^{+12}_{-0}$, with no increase in likelihood when the peak is introduced. This means that there is no

statistical support for the one-peak model, relative to the background-only hypothesis. For the $S_K > 4$ sample, the number of events in the peak is determined as $N = 4^{+15}_{-4}$, with a corresponding likelihood ratio of 0.05, giving a statistical significance of 0.2σ for the signal peak. Again, this gives negligible support for the one-peak model, as is expected for these samples.

To check for consistency between fits over independent datasets, the signal events are divided into two sub-samples, according to the sign of the kaon charge. The one-peak fit is then performed over both ΔM_s distributions, with the central value and normalisation as free parameters, and the width fixed at 1 MeV/c^2 as usual. The results of these fits are shown in Fig. 6.13; the final values of the signal parameters and the background scale factor k are listed in Table 6.5. Note that the masses in this table are those returned directly by the fit, with no correction factors. The largest deviation is the central value of the peak in the B^-K^+ sample, but this is still consistent with the full fit result, within ~ 1.5 standard deviations. The number of events are consistent with equal decay rates into B^+K^- and B^-K^+ channels.

Table 6.5: Measured B_s^{**} parameters for independent sub-samples of data. Shown are the converged values and statistical uncertainties for each of the two signal parameters, and the background scale factor, in the ΔM_s fit. The two sub-samples are defined by the sign of the kaon charge.

Sample	$\Delta M_s(B^*_{s2})$ [a]	N	k
B^+K^- events	67.2 ± 0.6	78 ± 18	0.50 ± 0.07
B^-K^+ events	62.6 ± 2.0	52 ± 17	0.69 ± 0.03
$B^+K^- + B^-K^+$	66.7 ± 1.1	125 ± 25	0.59 ± 0.03

[a] $\Delta M_s(B^*_{s2}) = M(B^*_{s2}) - M(B^+) - M(K^-)$ (MeV/c^2).

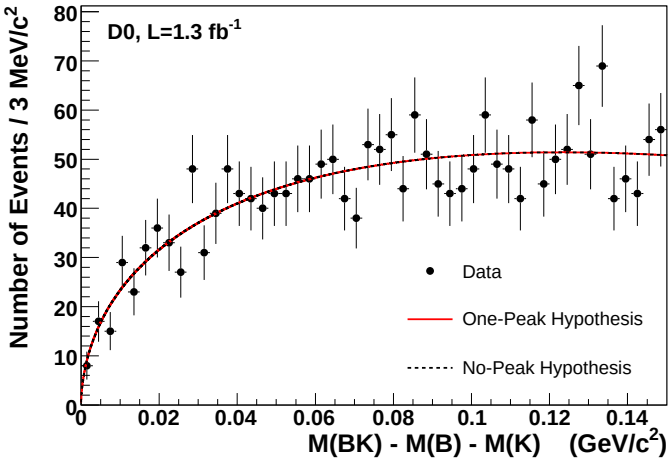

(a) Like-charge BK combinations;

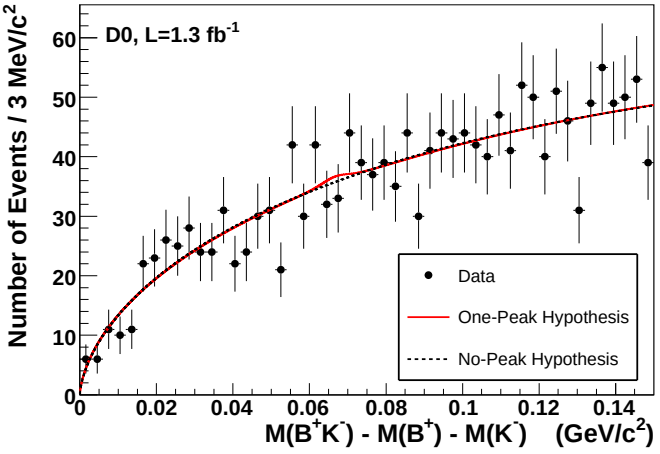

(b) Kaons not produced at PV

Figure 6.12: Testing for B_s^{**} signal events in background samples. Two independent background-only samples are fitted to a single-peak hypothesis, with results as described in the text.

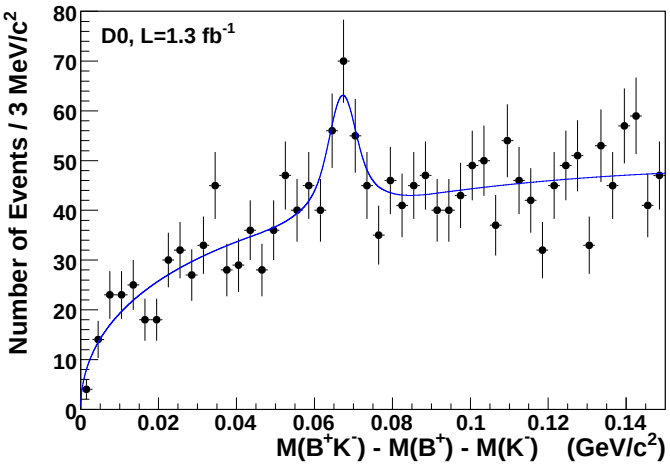

(a) B^+K^- combinations;

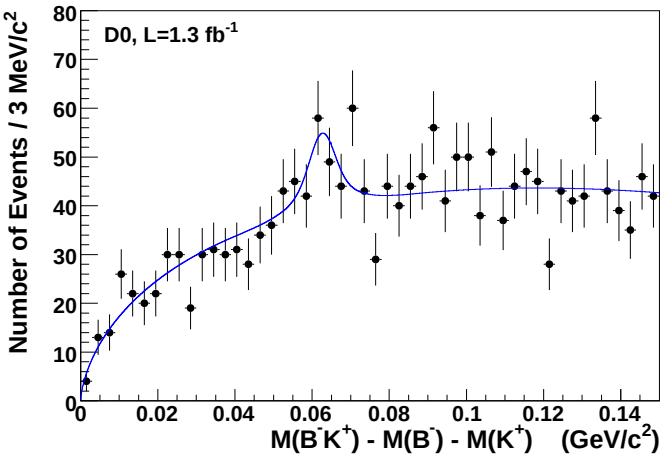

(b) B^-K^+ combinations;

Figure 6.13: Fitting ΔM_s over sub-samples of the B_s^{**} signal data. The two samples are defined by the kaon charge, and fitted to the usual one-peak hypothesis, with results as described in the text.

Chapter 7

Results

THE FIT OVER THE MASS DISTRIBUTIONS, in combination with the findings of the event simulation, provide all the information required to extract the masses, decay branching ratios, and production rates of the $B^{**}_{(s)}$ states. This chapter enumerates the final determined values, with statistical and systematic uncertainties.

7.1 $B^{**}_{(s)}$ Masses

The previous chapter measured the position of the B^{**} mass peaks in the ΔM distribution, with the results from the fitting procedure given by Eq. (6.14). These mass splittings were corrected to compensate for the systematic underestimation of masses in D0's tracking algorithm (6.16–6.17). The systematic uncertainties were also determined, and summarised in Table 6.2. Taking all this information in combination, the final mass splittings in the B^{**} system are found to be:

$$M_1 \equiv M(B_1) - M(B^+) = 441.6 \pm 2.4 \text{ (stat.)} \pm 1.3 \text{ (syst.) MeV}/c^2 \,, \quad (7.1)$$

$$M_{21} \equiv M(B_2^*) - M(B_1) = 26.2 \pm 3.1 \text{ (stat.)} \pm 0.9 \text{ (syst.) MeV}/c^2 \,. \quad (7.2)$$

The absolute mass of the B_1 meson is calculated by the addition of M_1 to the world average B^+ mass, listed by the Particle Data Group [11] as 5279.1 ± 0.5 MeV/c^2. The B_2^* mass is calculated by the addition of M_1, M_{21} and $M(B^+)$. The uncertainty on the absolute mass must take into account the correlation between the two mass splittings.

From Table 6.1, the correlation coefficient of these parameters is $\rho = -0.659$, which is used to calculate the combined statistical and systematic uncertainties according to:

$$\sigma^2(B_2^*) = \sigma^2(M_1) + \sigma^2(M_{21}) + 2\rho \cdot \sigma(M_1)\sigma(M_{21}) \; . \tag{7.3}$$

This gives the final masses as:

$$M(B_1) \;=\; 5720.7 \pm 2.4 \text{ (stat.)} \pm 1.3 \text{ (syst.)} \pm 0.5 \text{ (PDG) MeV}/c^2 \; , \tag{7.4}$$

$$M(B_2^*) \;=\; 5746.9 \pm 2.4 \text{ (stat.)} \pm 1.0 \text{ (syst.)} \pm 0.5 \text{ (PDG) MeV}/c^2 \; . \tag{7.5}$$

The B_{s2}^* meson is observed as a peak in the ΔM_s distribution, shown in Fig. 6.9. Including the small mass shift of Eq. 6.33, and the systematic uncertainty from Table 6.4, the fitting procedure returns the following mass difference:

$$M(B_{s2}^*) - M(B^+) - M(K^-) = 66.8 \pm 1.1 \text{ (stat.)} \pm 0.4 \text{ (syst.) MeV}/c^2 \; . \tag{7.6}$$

The world average mass of the charged kaon, listed by the Particle Data Group, is 493.677 ± 0.016 MeV/c^2. The B_{s2}^* absolute mass is extracted by addition of the B^+ and K^- masses to Eq. 7.6, yielding the following result:

$$M(B_{s2}^*) = 5839.6 \pm 1.1 \text{ (stat.)} \pm 0.4 \text{ (syst.)} \pm 0.5 \text{ (PDG) MeV}/c^2 \; . \tag{7.7}$$

7.2 B^{**} Branching Ratios

In addition to measuring the positions of the B^{**} resonances in the ΔM distribution, the fitting procedure also returns the relative normalisations of each peak, in terms of the fractions f_1 and f_2. The former is the fraction of total signal events in the $B_1 \to B^{*+}\pi^-$ peak; the latter is the fraction of B_2^* events in the $B_2^* \to B^{*+}\pi^-$ peak. Including the systematic uncertainties from Table 6.2, the observed fractions are then:

$$f_1 \;=\; 0.449 \pm 0.063 \text{ (stat.)} \pm 0.026 \text{ (syst.)} \; , \tag{7.8}$$

$$f_2 \;=\; 0.436 \pm 0.086 \text{ (stat.)} \pm 0.039 \text{ (syst.)} \; . \tag{7.9}$$

To convert the observed composition fractions f_1 and f_2 into meaningful physical quantities, the detection efficiencies for each decay must be taken into account. The motivation for this requirement is as follows. The three decays are associated with different transition energies, x_1–x_3. The energies, and hence transverse momenta, of the daughter pions will therefore have different distributions for each decay:

$$\bar{p}_T(B_1 \to B^{*+}\pi) \;<\; \bar{p}_T(B_2^* \to B^{*+}\pi) \;<\; \bar{p}_T(B_2^* \to B^{+}\pi)\,, \tag{7.10}$$

where $\bar{p}_T(X)$ is the mean transverse momentum of pions from a particular transition, X. Since the reconstruction process imposes a requirement $p_T(\pi) > 0.75$ GeV/c, it will preferentially select the higher energy transitions. As a result, the observed signal composition will be skewed away from the true B^{**} composition, with more events in the higher energy peaks. To correct for this effect, we utilise the pion detection efficiencies as listed in Equations (5.20–5.23).

The branching ratios of the B^{**} states are then calculated to be:

$$R_1 \;=\; \frac{Br(B_1 \to B^{*+}\pi)}{Br(B_J \to B^{(*)}\pi)} = f_1 \cdot \frac{\varepsilon_0}{\varepsilon_1} = 0.477 \pm 0.070 \pm 0.064\,, \tag{7.11}$$

$$R_2 \;=\; \frac{Br(B_2^* \to B^{*}\pi)}{Br(B_2^* \to B^{(*)}\pi)} = f_2 \cdot \frac{\varepsilon_3}{\varepsilon_2} = 0.475 \pm 0.094 \pm 0.071\,. \tag{7.12}$$

Here the first quoted uncertainty is statistical, propagated from the $f_{1,2}$ parabolic errors determined by the ΔM fit. The second uncertainty is systematic, from the combination in quadrature of contributions from $f_{1,2}$ and the efficiency measurements, as summarised in Table 7.1.

7.3 Measuring Relative Production Rates

7.3.1 B^{**} States

In addition to the B^{**} masses, and the composition fractions f_1 and f_2, the number of B^{**} events is also returned by the ΔM fitting procedure. Taking systematic uncertainties into

Table 7.1: Summary of systematic uncertainties on the B^{**} branching ratios.

Source	Value	$\pm$ (syst.)	δR_1 (syst.)	δR_2 (syst.)
f_1	0.449	0.026	0.028	—
f_2	0.436	0.039	—	0.042
ε_0	0.342	0.029	0.040	—
ε_1	0.322	0.028	0.041	—
ε_2	0.346	0.031	—	0.043
ε_3	0.377	0.029	—	0.037
Total	—	—	0.064	0.071

account from Table 6.2, the total number of orbitally excited B mesons observed is:

$$N(B^{**}) = 662 \pm 91 \text{ (stat.)} \pm 140 \text{ (syst.) events.} \tag{7.13}$$

Converting this number into a total production cross-section would be very difficult, requiring detailed knowledge of detector, trigger and reconstruction efficiencies, in addition to a precise measurement of the integrated luminosity of the data sample. Such a complex measurement is outside the scope of this analysis. However, it is possible to determine the relative production rate of the B^{**} mesons, as a fraction of the B^+ production rate.

The number of B^+ mesons detected in the D0 Run IIa data sample, decaying to the $J/\psi K^+$ channel, is measured as $20915 \ \pm 293 \ \pm 200$ [see Eq. (4.22)]. This is used to determine the ratio:

$$R = \frac{Br(b \to B^{**} \to B^{+(*)}\pi^-)}{Br(b \to B^+)} = \frac{\mathcal{T}(B^{**})}{\mathcal{T}(B^+)} \, . \tag{7.14}$$

Here $\mathcal{T}(X)$ is the true number of events of each type contained in the data. The ratio of production rates is thereby reduced to a ratio of event numbers, since all measurements use an identical data sample, namely the full D0 Run IIa dataset. However, the true number of events is unknown; this equation must be rearranged in terms of the *observed*

number of events $[N(B^+), N(B^{**})]$ by the relation:

$$\begin{aligned}\frac{\mathcal{T}(B^{**})}{\mathcal{T}(B^+)} &= \frac{N(B^{**})}{N(B^+)} \cdot \left[\frac{N(B^+)}{\mathcal{T}(B^+)}\right] \cdot \left[\frac{\mathcal{T}(B^{**})}{N(B^{**})}\right] \\ &= \frac{N(B^{**})}{N(B^+)} \cdot \left[\frac{\eta(B^+)}{\eta(B^{**})}\right] . \end{aligned} \tag{7.15}$$

Here $\eta(X)$ is the ratio of the observed number of events to the total number of events, of type X, i.e. the absolute detection efficiency. In Section 5.4, the ratio of efficiencies $\varepsilon_0 = \eta(B^{**})/\eta(B^+)$ is determined collectively for all B^{**} decays to be $0.342 \pm 0.008 \pm 0.029$ (5.23). The relative production rate is then calculated by:

$$\begin{aligned} R &= \frac{N(B^{**})}{N(B^+) \cdot \varepsilon_0} = \frac{20915}{662 \times 0.342} \\ &= [9.25 \pm 1.30 \text{ (stat.)} \pm 2.10 \text{ (syst.)}] \, \% . \end{aligned} \tag{7.16}$$

Here the statistical uncertainty is propagated from the parabolic errors on the number of B^{**} and B^+ events, as returned by the mass fits. The systematic uncertainty takes into account contributions from $N(B^{**})$, $N(B^+)$ and ε_0.

Since decays into neutral modes $B^0\pi^0$ cannot be detected, this ratio only accounts for decays into charged $B\pi$ combinations. However, isospin conservation allows this measurement to be extended to include the neutral states, by scaling by a multiplicative factor of $3/2$. There will be small phase space effects, since the neutral pions are around 4.6 MeV/c^2 less massive than the charged pions. This will slightly increase the B^{**} decay rate into $B^0\pi^0$, pushing the multiplicative factor from 1.50 to 1.51. This is far smaller than the uncertainties quoted on the production rate measurement, and so we neglect the effects of the mass difference $M(\pi^\pm) - M(\pi^0)$ for the purposes of this calculation:

$$\begin{aligned} R_{B^{**}} &= \frac{Br(b \to B^{**0} \to B^{(*)}\pi)}{Br(b \to B^+)} = \frac{3 \cdot N(B^{**})}{2 \cdot N(B^+) \cdot \varepsilon_0} \\ &= (13.9 \pm 1.9 \pm 3.2) \, \% . \end{aligned} \tag{7.17}$$

7.3.2 B_s^{**} States

Exactly the same procedure can be used to determine the B_{s2}^* production rate, using the number of B^+ and B_{s2}^* events detected in the data, and the relative detection efficiency, ε_s. Taking into account the systematic uncertainties in Table 6.4, the final number of observed B_{s2}^* events is determined as:

$$N(B_{s2}^*) = 125 \pm 25 \text{ (stat.)} \pm 10 \text{ (syst.) events.} \tag{7.18}$$

The ratio of efficiencies for detecting B_{s2}^* compared to B^+ events is determined to be 0.518 ± 0.044 [see Eq. (5.25) and Section 5.4.3]. Following the same reasoning as used for the B^{**} states, the relative production rate is then calculated as:

$$\begin{aligned} R_{B_{s2}^*} &= \frac{Br(b \to B_{s2}^{*0} \to B^+K^-)}{Br(b \to B^+)} = \frac{N(B_{s2}^*)}{N(B^+) \cdot \varepsilon_s} \\ &= (1.15 \pm 0.23 \pm 0.13)\,\% \,. \end{aligned} \tag{7.19}$$

The statistical uncertainties are propagated from the parabolic errors on $N(B^+)$ and $N(B_{s2}^*)$ determined by the mass fits. The systematic uncertainty is the combination in quadrature of the relative uncertainties on these event numbers and the efficiency.

The extension to include decays into neutral states B^0K^0 is less straightforward than the B^{**} calculation, since the relative phase-space suppression factor departs significantly from unity, and cannot be neglected. The neutral kaon has mass 497.648 ± 0.022 MeV/c^2 [11], and is therefore around 4 MeV/c^2 more massive than the charged kaon. As a result it will be produced with a smaller momentum in the B_{s2}^* rest frame. The suppression due to phase space is proportional to the fifth power of the ratio of momenta:

$$\frac{Br(B_{s2}^* \to B^+K^-)}{Br(B_{s2}^* \to B^0K^0)} = \left[\frac{p(K^-)}{p(K^0)}\right]^5 = 1.16 \,, \tag{7.20}$$

where the kaon momenta are calculated from the standard expressions for two-body decay, using the B^+ and kaon masses from the Particle Data Group, and the B_{s2}^* mass in (7.7). The uncertainty on this factor is less than 0.001, much smaller than the other uncertainties in the calculation.

Excluding this suppression, isospin conservation implies that the neutral states are produced at the same rate as both charged channels combined. Therefore the relative production rate including decays to neutral kaons is calculated to be:

$$\begin{aligned} R_{B^*_{s2}} &= \frac{Br(b \to B^{*0}_{s2} \to BK)}{Br(b \to B^+)} = \left(1 + \frac{1}{1.16}\right) \cdot \frac{N(B^*_{s2})}{N(B^+) \cdot \varepsilon_s} \\ &= (2.14 \pm 0.43 \pm 0.24)\ \% \ . \end{aligned} \tag{7.21}$$

The ratio of the production rates of B^*_2 and B^*_{s2} can also be estimated, by comparing Eq. (7.17) to Eq. (7.21), and using the observed fraction R_1 in Eq. (7.11) to factor out the contribution of B_1 states:

$$\frac{R_{B^*_2}}{R_{B^*_{s2}}} = \frac{R_{B^{**}}(1 - R_1)}{R_{B^*_{s2}}} = 3.40 \pm 0.94 \pm 0.96 \ . \tag{7.22}$$

This is consistent with the fractional production rates observed over all B_d and B_s mesons, as given in Table 2.1, which gives an equivalent measure $f_d/f_s = 3.59 \pm 0.40$. Here the uncertainty is an estimate, since it assumes no correlation between f_d and f_s.

7.4 Summary of Results

Taking into account theoretical considerations, and the results of the dedicated event simulations described in Chapter 5, several measurements have been extracted from the $\Delta M_{(s)}$ fitting procedures.

For the B^{**} system, the data exhibits a multiple-peak structure with a high degree of statistical confidence. The three-peak fitting hypothesis is motivated by theoretical expectations, and shown in Fig. 6.3. Several alternative fits are attempted, of which only the two-peak hypothesis (with the central $B^*_2 \to B^{*+}\pi$ signal removed from the fit) is consistent with the data. If this alternative hypothesis were true, the measured B_1 and B^*_2 masses would not change, but the branching ratio R_2 in (7.12) would no longer be correct. As such, it is important to understand that the recorded branching ratios and production rates extracted from the ΔM fit are valid only within the assumption that the three-peak fitting hypothesis is truly representative of the data.

The masses of both B_1 and B_2^* mesons are measured directly, and their values are found to be:

$$M(B_1) = 5720.7 \pm 2.4 \text{ (stat.)} \pm 1.3 \text{ (syst.)} \pm 0.5 \text{ (PDG) MeV}/c^2 \,, \qquad (7.4)$$

$$M(B_2^*) = 5746.9 \pm 2.4 \text{ (stat.)} \pm 1.0 \text{ (syst.)} \pm 0.5 \text{ (PDG) MeV}/c^2 \,. \qquad (7.5)$$

The decay branching ratios, and the relative production rate of these states are measured as:

$$R_1 = \frac{Br(B_1 \to B^{*+}\pi)}{Br(B^{**} \to B^{(*)}\pi)} = 0.477 \pm 0.070 \pm 0.064 \,, \qquad (7.11)$$

$$R_2 = \frac{Br(B_2^* \to B^*\pi)}{Br(B_2^* \to B^{(*)}\pi)} = 0.475 \pm 0.094 \pm 0.071 \,, \qquad (7.12)$$

$$R_{B^{**}} = \frac{Br(b \to B^{**0} \to B^{(*)}\pi)}{Br(b \to B^+)} = (13.9 \pm 1.9 \pm 3.2)\ \% \,. \qquad (7.17)$$

The ΔM fit is found to be insensitive to the values of the B^{**} widths, which are expected to be comparable to, or smaller than, the characteristic experimental mass resolution of the D0 detector for these states.

For all measurements except the production rate, the uncertainties are dominated by the parabolic errors returned by the mass fit. These arise from limitations in the sample size, i.e. statistical effects. The largest uncertainty on the production rate measurement is the systematic uncertainty on the number of B^{**} events, which is in turn dominated by the effect of fitting with a range of different physical widths for the excited states. The sources of uncertainty are well understood, and proposals for increasing the precision of future measurements are discussed in Chapter 8.

For the B_s^{**} system, the data is best modelled by the combination of background and a one-peak signal hypothesis, corresponding to $B_{s2}^* \to B^+K^-$ decays, and shown in Fig. 6.9. Alternative single-peak hypotheses are inconsistent with theoretical considerations, which would then predict additional peaks at higher ΔM_s, which are not observed.

On the other hand, the absence of observed resonances at lower ΔM_s is explained by phase-space suppression; this effect is marked as a result of the proximity to the production threshold $\Delta M_s = 0$. The observation of the B^*_{s2} meson is therefore only valid within the assumption that the signal peak can be attributed to resonant behaviour in $B^*_{s2} \to B^+K^-$ decays. There are, however, convincing theoretical arguments for this assumption.

The B^*_{s2} mass and relative production rate determined in this analysis are then:

$$M(B^*_{s2}) = 5839.6 \pm 1.1 \text{ (stat.)} \pm 0.4 \text{ (syst.)} \pm 0.5 \text{ (PDG) MeV}/c^2 \,, \qquad (7.7)$$

$$R_{B^*_{s2}} = \frac{Br(b \to B^{*0}_{s2} \to BK)}{Br(b \to B^+)} = (2.14 \pm 0.43 \pm 0.24)\ \% \,. \qquad (7.21)$$

For both of these results, the precision is limited by the statistical uncertainties from the ΔM_s fit, which is to be expected since only 125 ± 25 signal events are observed in the data set. Projections of future precision of B^*_{s2} measurements at D0 are described in Chapter 8.

Fits with additional signal peaks are also attempted on the data. No evidence is found for $B^*_{s2} \to B^{*+}K^-$ decays, which is consistent with the expected phase-space suppression, calculated from Eq. (6.35). There is some indication (1.8σ significance) for an additional peak at $\Delta M_s = 11.5$ MeV/c^2, which can be attributed to $B_{s1} \to B^{*+}K^-$ decays. However, with the current data set, the two-peak hypothesis can be neither confirmed nor excluded.

Chapter 8

Conclusions

THE FINAL OUTCOME OF THE $B^{**}_{(s)}$ studies, as described in this thesis, is a large improvement in the precision and volume of measurements in the orbitally excited B meson systems. For the first time, the mass splittings and relative contributions of the three $B^{**} \to B^{(*)}\pi$ transitions have been allowed to vary in the parameterised fit over data. The narrow $j_q = \frac{3}{2}$ states have been examined with minimal theoretical input, and without making significant assumptions regarding the $j_q = \frac{1}{2}$ resonances, except that they are broad, with widths in excess of 100 MeV/c^2. The resulting mass measurements are significantly more precise than previous experimental values, which should provide strong discriminatory power in examining theoretical predictions.

In the B^{**}_s system, the early evidence for resonant behaviour in the BK invariant mass distribution [14] has been confirmed, and the precision significantly improved. The results show consistency with the concurrent analysis by CDF [97], and the observed proportion of B^*_2 and B^*_{s2} candidates agrees with the experimental hadronisation fractions for d and s quarks. The measurement of production rates in both sets of narrow states will further improve knowledge of B meson sample compositions at hadronic colliders, an essential ingredient in many future analyses at the Tevatron, LHC and beyond.

In this concluding chapter, three aspects of the results are discussed. Firstly, the consistency with previous experimental measurements and theoretical predictions is examined. Secondly, the impact of the publication of this new set of results is described, in

terms of several new theoretical calculations which have been recently released. Thirdly, some possible improvements and extensions to these studies are reviewed, with speculation as to the future prospects of these measurements.

8.1 Consistency with Previous Results and Predictions

The previous experimental and theoretical results have already been summarised in this thesis, in Chapters 1 and 2 respectively. In the following text the major results are tested for consistency with a number of different sources, with single uncertainties covering all sources for ease of comparison; for more detail and for a full list of references please refer to the original chapters.

8.1.1 Masses of Orbitally Excited States

Of the previous experimental results, the earliest evidence for resonant $B\pi$ behaviour from LEP gave approximate B^{**} masses of 5680–5730 MeV/c^2, as shown in Eq. (1.7)–(1.9). Here, the measured mass represents the mean position of the full four-state resonance, which is consistent with our results for the narrow states. The OPAL collaboration also observed a single resonance in the BK invariant mass distribution, interpreted as an unknown B_s^{**} transition, and consistent with the B_{s2}^* peak of this analysis.

Subsequent studies at LEP, and an early publication by CDF, used theoretical models to constrain the relative peak positions in the mass fits. The results of these measurements are shown in rows 3–6 of Table 8.1. The B_1 masses presented by OPAL and L3 are significantly higher than the D0 result, although distinguishing the broad states from the combinatorial background may have distorted the masses in these early results, as explicitly stated in the OPAL publication. Of the exclusive studies, both ALEPH and CDF found B^{**} masses consistent with the current D0 result.

As mentioned in Chapter 6, CDF have recently published a study of the B_s^{**} system, finding two peaks interpreted as $B_{s2}^* \rightarrow BK$ and $B_{s1} \rightarrow B^*K$ transitions [97]. The

measured mass of the higher energy resonance coincides with the D0 result for B^*_{s2}; furthermore, the B_{s1} mass peak reported by CDF is consistent with the findings of this thesis under a two-peak fit hypothesis (see Section 6.3.4). CDF have also released preliminary results for a B^{**} study, in which a three-peak structure is found, and interpreted as the allowed transitions of the $j_q = \frac{3}{2}$ narrow states, as observed by D0. The masses are given in Table 8.1: there is some disagreement between the recent CDF and D0 measurements, regarding the mass splitting of the states, although until a final result is published by CDF it is difficult to interpret this discrepancy.

Table 8.1: Comparisons between these results and the findings of previous studies, as detailed in Chapter 1. In each case, the quoted uncertainties combine statistical and systematic effects. Units are MeV/c^2 throughout.

Source	$M(B_1)$	$M(B_2^*)$	$M(B_2^*) - M(B_1)$	$M(B_{s2}^*)$
This result	5720.7 ± 2.8	5746.9 ± 2.6	26.2 ± 3.2	5839.6 ± 1.3
OPAL [14, 15]	5738 ± 9	—	—	5853 ± 15
L3 [16]	5756 ± 8	—	—	—
ALEPH [17]	—	5739 ± 10	—	—
CDF [18]	5710 ± 20	—	—	—
CDF [97]	—	—	—	5839.6 ± 0.7
CDF [98] [a]	5725.3 ± 2.4	5740.2 ± 1.9	14.9 ± 2.7	—

[a] Preliminary result.

The equivalent comparisons can also be made with the various theoretical predictions listed in Chapter 2, as shown in Table 8.2. Unfortunately, most calculations do not quote uncertainties, or only give order-of-magnitude estimates for higher order corrections. The results favour the relativistic constituent quark model of Ebert, Galkin and Faustov [27], which gives good agreement for all three states. Ref. [28] uses a similar model, which also agrees reasonably well with the data. The observed mass splitting between the B^{**} states is somewhat larger than expected by most approaches, although no uncertainties are quoted on the theoretical values. The predicted splitting $M(B_2^*) - M(B_1) \approx 50$ MeV/c^2 from the lattice approach can be almost entirely ruled out, since there is very strong statistical significance for a multi-peak structure, with a separation too broad to be assigned

to the two B_2^* transitions alone.

Table 8.2: Experimentally determined masses of the B_1, B_2^* and B_{s2}^* mesons, compared to the expectations of various theoretical models, outlined in Chapter 2. Uncertainties and units follow the convention of Table 8.1.

Source	$M(B_1)$	$M(B_2^*)$	$M(B_2^*) - M(B_1)$	$M(B_{s2}^*)$
This result	5720.7 ± 2.8	5746.9 ± 2.6	26.2 ± 3.2	5839.6 ± 1.3
F+M [1] [a]	5780	5794	14	5899
E,H,Q [2] [b]	5759	5771	12	5861
I [24] [c]	5700	5715	15	—
E,G,F [27] [d]	5719	5733	14	5844
DP+E [28] [e]	5700	5714	14	5820
K [29] [f]	$5770\ ^{+39}_{-47}$	$5822\ ^{+52}_{-57}$	52	$5878\ ^{+36}_{-42}$

[a] Falk and Mehen (1996) —Leading-order corrections to HQET.
[b] Eichten, Hill and Quigg (1994) —HQET with quark-potential model.
[c] Isgur (1998) —Non-relativistic quark model.
[d] Ebert, Galkin and Faustov (1997) —Relativistic quark model.
[e] Di Pierro and Eichten (2001) —Relativistic quark model.
[f] Khan *et al.*(2001) —Lattice QCD calculation.

In general, predictions appear to be converging with experiment over time, with deviations from this pattern occurring whenever a new calculational approach is introduced. There are still some interesting disagreements between theories, such as the spin-orbit inversion predicted by several groups; this has not yet been experimentally tested, since the broad state properties have yet to be measured reliably. For such a study to be possible, the combinatorial background in $p\bar{p}$ collisions must be understood at a sufficient level that its contribution can be disentangled from the full four-state B^{**} resonance.

8.1.2 Branching Ratios and Production Rates

Several of the early B^{**} studies included a measurement of the production rate of $B_{u,d}^{**}$ states as a fraction of the total rate for all $B_{u,d}$ ground state production, denoted $R_{u,d}^{**}$ and defined in Eq. (1.6). Since this includes the effect of all four $L = 1$ states, it cannot be directly compared with the production rate reported in this thesis. Nevertheless, it is still worth examining the results, to see if any light can be shed on the relative contribution of

broad and narrow states. The values from these previous studies are:

$$\begin{aligned} R^{**}_{u,d} &= [\,27.9 \pm 7.7\,]\,\%, && \text{(ALEPH [12])} \\ &= [\,31 \pm 11\,]\,\%, && \text{(ALEPH [17])} \\ &= [\,35 \pm 8\,]\,\%, && \text{(DELPHI [13])} \\ &= [\,28 \pm 7\,]\,\%, && \text{(CDF [18])} \\ R^{**}_{d} &= [\,27.0 \pm 5.6\,]\,\%, && \text{(OPAL [14])} \end{aligned} \tag{8.1}$$

where the two ALEPH results correspond respectively to inclusive and exclusive selections, and the CDF result is from the early model-dependent publication. The consistency of the results from CDF and LEP indicates that this relative rate is similar for $e^+e^- \to Z \to b\bar{b}$ and $p\bar{p} \to b\bar{b}$ production mechanisms. Assuming that decays to $B\pi$ dominate for both narrow and wide states, the typical production rate of $\sim (30 \pm 8)\%$ from the above studies can be compared to the D0 result of $(13.9 \pm 3.7)\%$ for the narrow states only. This exercise suggests that the narrow and wide states are produced in approximately equal rates; however, the large uncertainties mean that the wide:narrow production ratio of 4:8 predicted by spin counting arguments cannot be ruled out. In general, care should be taken when interpreting such comparisons, due to the large theory-dependency implicit in many of the early results.

The decay branching ratio R_2, giving the fraction of B^*_2 decays which proceed via the $B^*\pi$ channel, has not been previously measured, although the preliminary result from CDF indicates consistency with $R_2 = 50\%$. The D0 result of $(47.5 \pm 11.8)\%$ from Eq. (7.12) is also close to one-half, which fits in with the theoretical expectations summarised in Section 2.4.

From a spin counting argument, the production rate of B_1 should represent a fraction $3/8 \equiv 37.5\%$ of total B^{**} meson production. Although this cannot be directly associated with the quantity $R_1 = (47.7 \pm 9.5)\%$ in Eq. (7.11), since only a single decay channel is investigated, it does indicate that the observed composition of the B^{**} sample is consistent with spin counting predictions, in addition to the simple state counting prediction of 50%.

8.2 Impact of Publication

Since the release of the B^{**} and B_s^{**} results in December 2007 and February 2008 respectively, the studies have been cited by over a dozen other publications. Some of these are experimental reviews of Tevatron results, but many are theoretical works, giving updated or completely new predictions for the masses of these orbitally excited states. The new calculations use the experimental $B_{(s)}^{**}$ masses as constraints, allowing other parameters to be floated and giving a more complete understanding of both the physical system of states, and the approaches which are likely to be most fruitful in determining masses.

The paper by Badalian, Simonov and Trusov [99] uses a chiral Lagrangian to calculate $B_{(s)}^{**}$ masses by investigating the coupling between the excited states and the ground state mesons to which they decay. In this scheme, the mixing between $B'_{(s)1}$ and $B_{(s)1}$ states can influence the masses of all four particles in the $L = 1$ multiplet. By fitting to data, this mixing is determined to be minimal, and the following masses predicted:

$$\begin{aligned} M(B_1) &= 5726 \text{ MeV}/c^2, & (5720.8 \pm 2.8) \\ M(B_2^*) &= 5742 \text{ MeV}/c^2, & (5746.9 \pm 2.6) \\ M(B_{s2}^*) &= 5843 \text{ MeV}/c^2, & (5839.6 \pm 1.3) \end{aligned} \tag{8.2}$$

where the value in parentheses is the corresponding D0 measurement. A second chiral Lagrangian approach has been utilised by Zhong and Zhao [100], where the focus is on determining the various decay amplitudes of excited states. Using the experimental masses from D0 and CDF as inputs, several relative branching ratios are constructed, which agree with the results of this thesis. The B_2^* mass indicates a relative decay branching ratio of:

$$R_2 \equiv \frac{\Gamma(B_2^* \to B^*\pi)}{\Gamma(B_2^* \to B^{(*)}\pi)} = 0.47 \,, \tag{8.3}$$

which is very close to the D0 result of 0.475 ± 0.118. Note that the calculations do not use this experimental value as a constraint: it follows entirely from the chiral model with

the observed mass as an input. The corresponding result in the B_s^{**} system is:

$$R_{s2} \equiv \frac{\Gamma(B_{s2}^* \to B^* K)}{\Gamma(B_{s2}^* \to B^{(*)} K)} = 0.06 \; . \tag{8.4}$$

This strong suppression is consistent with the non-observation of a $B_{s2}^* \to B^* K$ resonance by either CDF or D0. Finally, both B^{**} masses are used to construct the strong decay width ratio:

$$R_1 \equiv \frac{\Gamma(B_1 \to B^* \pi)}{\Gamma(B^{**} \to B^{(*)} \pi)} = 0.34 \; , \tag{8.5}$$

which can be compared to the D0 value of 0.477 ± 0.095. All of these calculations neglect the effects of di-pion decays, as do the rates R_1 and R_2 from this thesis.

There have also been multiple recent publications which use lattice QCD methods. The European Twisted Mass collaboration [101] gives predictions for both broad and narrow states in the orbitally excited systems, in terms of the splitting $\Delta(B_{(s)}^{**}) = M(B_{(s)}^{**}) - M(B_{(s)})$:

$$\begin{aligned} \Delta(B_1) &= 513 \pm 8 \text{ MeV}/c^2, & (441.6 \pm 2.7) \\ \Delta(B_2^*) &= 524 \pm 8 \text{ MeV}/c^2, & (467.8 \pm 2.6) \\ \Delta(B_{s2}^*) &= 512 \pm 14 \text{ MeV}/c^2. & (473.0 \pm 1.6) \end{aligned} \tag{8.6}$$

Again, the values in parentheses are the D0 results, where the B_{s2}^* uncertainty includes a contribution from the B_s^0 mass listed by the Particle Data Group [8]. These values show that the lattice approach is still far from perfected, but the splitting between the $j_q = \frac{3}{2}$ states is now significantly closer to the experimental value than the earlier prediction by Khan *et al.* [29], given in Table 8.2. A different lattice calculation by the BGR collaboration does give values of Δ which are more consistent with data, although only the average mass is quoted for each j_q doublet [102].

In summary, the rate of publication in this field has significantly increased in the year following the release of $B_{(s)}^{**}$ results from the Tevatron experiments. Input from these studies has aided in improving calculation methodology and given new insight regarding

the decay ratios and widths of these states. In addition, the results have been incorporated into the latest version of the HERWIG event generator, which will help computer simulations of $b\bar{b}$ production to more closely match data [103].

8.3 Future Prospects

8.3.1 Improved Precision of Current Measurements

On examination of the uncertainties attributed to each of the measurements listed in Section 7.4, the dominant contribution comes in almost all cases from the statistical uncertainty associated with the mass fitting procedure. The exception is the B^{**} production rate, where the large systematic uncertainty on the number of events is associated with the unknown decay widths which were fixed in the fit. The statistical contribution is expected to reduce according to the relation $\sigma_{\text{stat}} \propto 1/\sqrt{N}$, where N is the number of events detected; it can therefore be extrapolated over time, as shown in Fig. 8.1. In this case, the anticipated future precision of the B_2^* mass measurement is shown, but the behaviour will be similar for all statistically dominated measurements. In constructing this figure, the projected improvements in the systematic uncertainties are not shown: they will be discussed later.

The reduction in the statistical contribution assumes that the number of B^{**} events scales in proportion to the recorded integrated luminosity; this is not necessarily true, for a number of reasons. Primarily, the typical instantaneous luminosities achieved by the Tevatron have increased significantly over the last few years (see Fig. 3.4 for an illustration of this in Run IIa alone). During periods of very high luminosity, the B physics triggers become less efficient, and are heavily prescaled to allow other trigger types to share the DAQ rate. Consequently, the number of B hadrons per pb^{-1} will be reduced for Run IIb running. On the other hand, the trigger lists have recently been updated (March 2008) and subsequent studies have observed significant increase in the number of J/ψ candidates, with rates up 17% in total, and $\sim 40\%$ at high luminosity running [104]. There is therefore hope that the final 4 fb^{-1} of data collected will be at least as fruitful as Run IIa. As a result

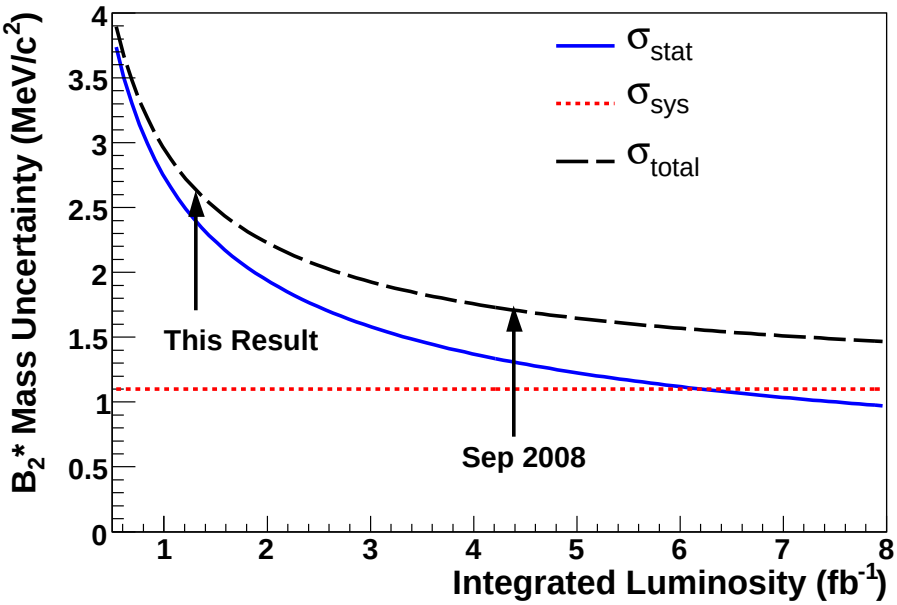

Figure 8.1: Projected future precision of the B_2^* mass measurement, showing the $1/\sqrt{L}$ behaviour of the statistical contribution, as described in the text. The anticipated improvements in systematic uncertainty are not shown.

of these complications, the curve in Fig. 8.1 should be interpreted as an estimate of future performance.

Figure 8.1 shows that at the time of writing, the volume of data collected by D0 has already increased threefold compared to the Run IIa data set covered by this thesis. The total luminosity recorded by end of running is expected to be 8 fb^{-1} or above. As such, simply repeating the studies with no other improvements would give precisions of 1.5 MeV/c^2 or better on the B^{**} masses, and 0.8 MeV/c^2 on the B_{s2}^* mass.

In addition to this direct scaling with the volume of data, there are some systematic uncertainties which will also be reduced as the sample size increases. In particular, it is anticipated that the mass fit will become sensitive to the value of the B^{**} width, Γ. This expectation follows the recent preliminary result by CDF [98], which measures $\Gamma = 22.7^{+5.0}_{-10.7}$. Such a width would be larger than the corresponding mass resolution of Eqs. (5.9–5.11), and so the analysis technique presented in this thesis should be sensitive to it, provided that the number of events is large enough to give stable convergence. The

effect of varying the fixed width in the ΔM fit, which currently represents the largest source of systematic uncertainties across the whole set of parameters, would thereby be removed. In particular, the systematic uncertainty on the B^{**} production rate would immediately reduce from 3.2% to 1.3%.

A second significant source of systematic uncertainty is the binning scheme. Rewriting the mass fitting code to work with an unbinned fit would remove this contribution, although the arbitrary fitting range would still contribute, and the statistical uncertainties of an unbinned fit could be increased. It is certainly an option worth investigating, which together with the above improvements, could push the total mass uncertainties of the $B^{**}_{(s)}$ states below 1 MeV/c^2.

8.3.2 Additional Observations

The B_{s1} state recently reported by CDF, which is not observed with high significance at D0, is the immediate target in terms of new measurements in the excited B meson system. Assuming that the 25 ± 10 events currently seen in the second BK mass peak of Fig. 6.11 correspond to the B_{s1} state, the extrapolation to the full dataset is expected to yield around 60 such candidates, which would correspond to a significant observation considering the statistical uncertainty on this figure. However, to minimise the systematic effects, additional studies must be made to improve the understanding of backgrounds, particularly close to the production threshold. Clearly, the uncorrelated $B\pi$ production does not fully explain the shape of the distribution, since the wrong-sign samples in Figures 6.1 and 6.7 contain appreciably lower populations than the right-sign samples. As well as the predicted effect of reflections, it is necessary to disentangle the remaining contribution of the broad $L = 1$ transitions from the non-resonant correlated $B\pi$ production, described below. Future studies of the broad states in the B^{**} system may also help to constrain the distribution at low ΔM_s.

During hadronisation, the flavour of the b quark (i.e. b or $\bar{b}$) will affect the charges of the particles close to it, because the q which pairs up with the bottom quark must be produced from the QCD vacuum in tandem with a $\bar{q}$ [105]. This will in turn form a

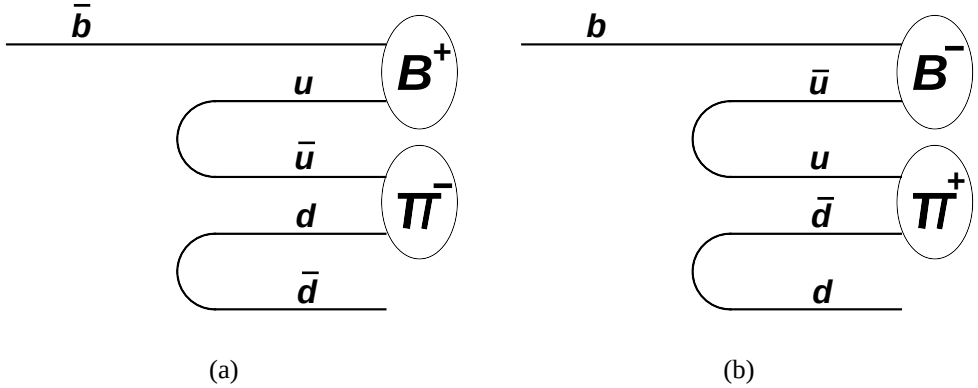

Figure 8.2: Correlated $B\pi$ production during hadronisation, giving preferential opposite-charge combinations as expected for the B^{**} signal. Understanding and modelling such backgrounds is essential if the broad $L = 1$ states are to be isolated and studied.

hadron, with a charge dependent on the flavour of the B spectator quark. This is illustrated schematically in Fig. 8.2, which shows that the result is the same $B^+\pi^-$ correlation as expected for the B^{**} decays. Modelling this behaviour is not straightforward, and it is anticipated that information from simulation will need to be combined with observations in other B and D mass distributions in order to assign a background shape to this component.

Having produced templates of the expected contributions of uncorrelated and correlated backgrounds, and reflections from mis-identified light mesons, the remaining distribution of excess events in the $B\pi$ invariant mass can then be fitted to a four-state (i.e. five-peak) structure, with the positions, widths and relative normalisations of each peak allowed to participate in the minimisation. If this fit can be successfully performed, the resulting information on the broad states will allow the spin-orbit puzzle to be solved, and provide additional valuable information regarding relative production rates. The corresponding measurements in the B_s^{**} system may also be feasible, although the phase-space distortion and suppression of the broad states may limit the precision of results.

Once the $L = 1$ orbitally excited states have been observed and their properties extracted, the natural progression would be to begin investigation of the first set of radially excited states, corresponding to more massive versions of the $L = 0$ B and B^* mesons. These states cannot decay to $B^{(*)}\pi$ as a result of parity and angular momentum conservation laws, therefore the dominant decays are expected to be to $B^{(*)}\pi\pi$. The challenge of reconstructing an additional pion will need to be addressed by improving background rejection. One possibility is to utilise a combined likelihood method, as described in Section 4.3.4, using information from the studies of orbitally excited states.

8.4 Final Words

The understanding of mass excitations in B mesons is in its early stages, with many of the low lying states yet to be observed, and several properties still not precisely known. However, the results of this thesis present a significant improvement on the previous results, and provide the foundations for future progress in both the experimental and theoretical realm. With the continued running of the mature Tevatron experiments, together with the bright future represented by upcoming experiments such as LHCb, there is good reason to believe that the excited B mesons may become as well understood as the ground states are currently. The existence of mesons with precisely measured masses over a number of different internal quark arrangements will present a strong set of constraints for theoretical calculations; this will allow non-perturbative QCD methods to be fine tuned, in analogy with the development of quantum electrodynamics through precise measurements of hydrogen energy levels.

Appendix A

Testing for Correlation between the B^+ Discriminating variables

In section 4.3.4, a likelihood method was used to combine six discriminating variables into a single 'tagging' parameter, in order to optimise the selection of B^+ candidates. As mentioned in the text, and described in more detail in references [83] and [84], this method provides an optimised selection only in the case where the discriminating variables are independent. Where there are dependences between variables, the optimal selection requires the use of multi dimensional probability density functions $f^b(x_1, ..., x_n)$ and $f^s(x_1, ..., x_n)$. These are complicated to use in practice, and so the usual method is to aim to use variables which are minimally dependent; in this case, the procedure closely approaches optimal performance. Such is the approach used for this analysis; as a result it is useful to inspect the six chosen discriminating variables. In this appendix, each pair of variables (x, y) is tested for linear dependence by calculating the Pearson product-moment correlation coefficient [85], defined as:

$$r = \frac{\sigma_{xy}}{\sigma_x \cdot \sigma_y} \tag{A.1}$$

Where σ_{xy} is the covariance of variables (x, y), and $\sigma^2_{x(y)}$ is the variance of x (y). Although correlation between variables is not necessarily indicative of dependence, it is desirable that r be small for each variable combination. For clarity, the description of the

six variables used in the selection is repeated here:

$z_1 = \log_{10}[P_t(K)]$, where $P_t(K)$ is the transverse momentum of the kaon;

$z_2 = \log_{10}[P_t(\mu_{\text{soft}})]$, where $P_t(\mu_{\text{soft}})$ is the minimum transverse momentum of the two muons;

$z_3 = \log_{10}[\Gamma_B]$, where Γ_B is the B^+ decay length significance, defined in (4.13);

$z_4 = \log_{10}[S_B^2]$, where S_B is the B^+ impact parameter significance, defined in (4.12);

$z_5 = \log_{10}[S_K^2]$, where S_K is the kaon impact parameter significance;

$z_6 = \log_{10}[\chi^2(V_B)]$, where $\chi^2(V_B)$ is defined in (4.10) and (4.11);

The correlation coefficient r only measures linear dependences; more complex relations between variables are investigated by inspection of the contour plots shown in figures A.1–A.4. It is evident that there are no significant non-linear effects between the six discriminating variables. In addition, the Pearson correlations are small, as summarised in Table A.1.

In conclusion, the selection of B^+ candidates is expected to be close to optimal, with some small reductions in purity and efficiency possibly arising through slight dependences of certain variables, such as the transverse momentum and the impact parameter significance of the kaon.

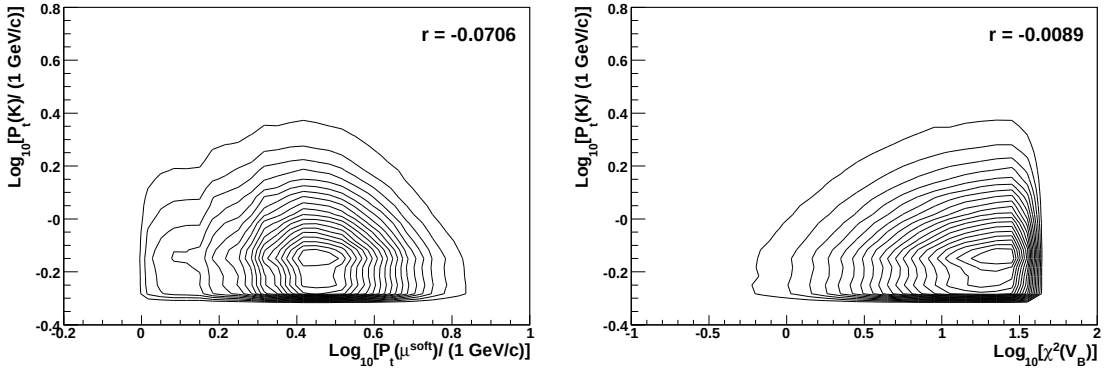

(a) $\log_{10}(P_t^K)$ vs. $\log_{10}(P_t^{\mu_{\text{soft}}})$;

(b) $\log_{10}(P_t^K)$ vs. $\log_{10}(\chi^2(V_B))$;

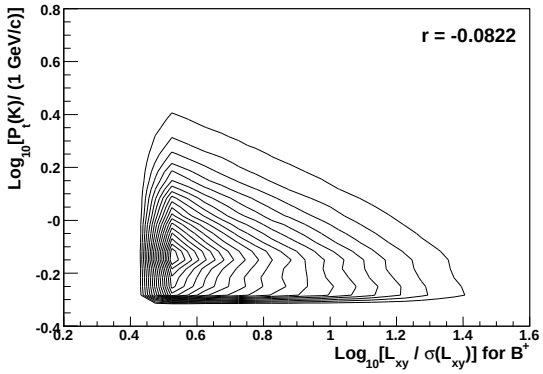

(c) $\log_{10}(P_t^K)$ vs. $\log_{10}(\Gamma_B)$

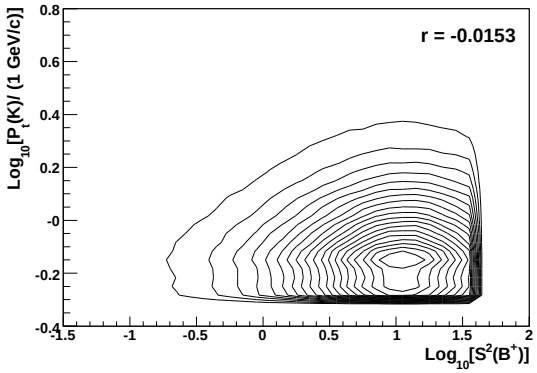

(d) $\log_{10}(P_t^K)$ vs. $\log_{10}(S^2(B^+))$

Figure A.1: Two dimensional contour plots for variables used in the optimised B^+ selection (Part 1/4). The discriminating variables are described in the text. Also shown for each plot is the value of the Pearson product-moment correlation coefficient.

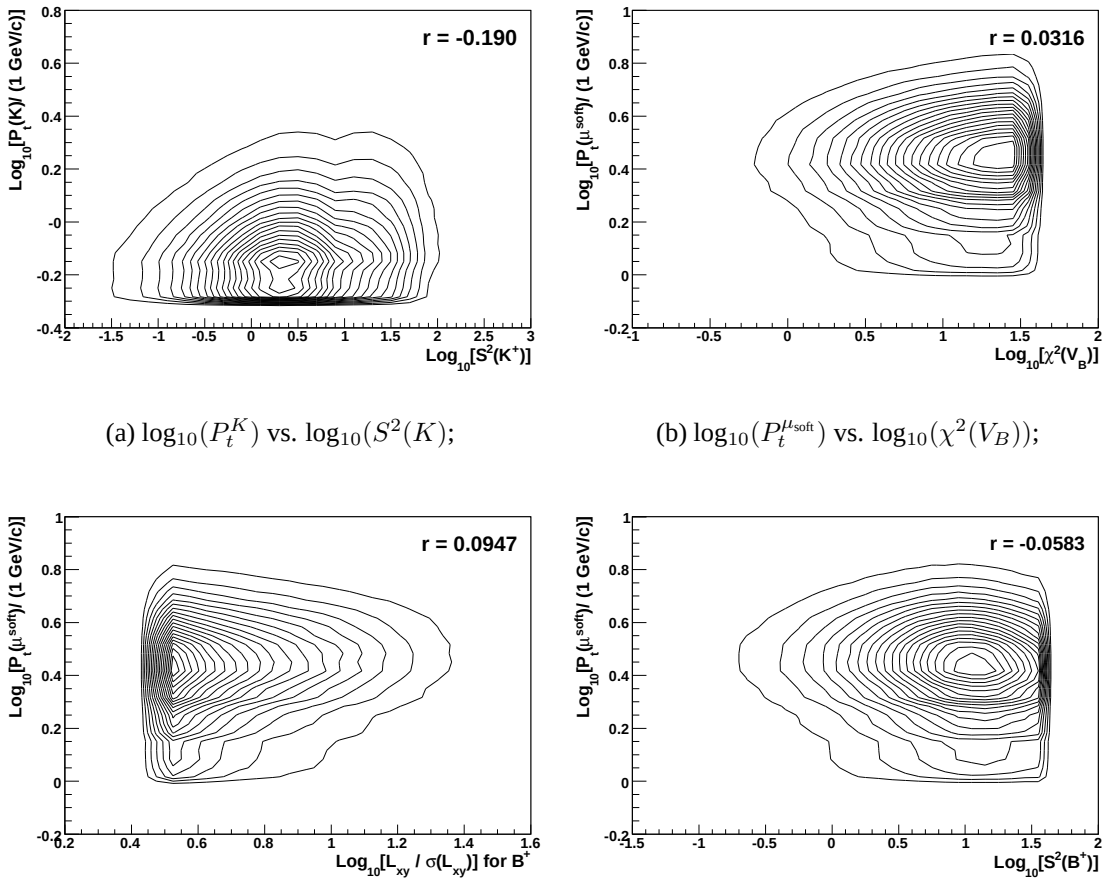

(a) $\log_{10}(P_t^K)$ vs. $\log_{10}(S^2(K)$;

(b) $\log_{10}(P_t^{\mu_{\rm soft}})$ vs. $\log_{10}(\chi^2(V_B))$;

(c) $\log_{10}(P_t^{\mu_{\rm soft}})$ vs. $\log_{10}(\Gamma_B)$;

(d) $\log_{10}(P_t^{\mu_{\rm soft}})$ vs. $\log_{10}(S^2(B^+))$;

Figure A.2: Two dimensional contour plots for variables used in the optimised B^+ selection (Part 2/4). The discriminating variables are described in the text. Also shown for each plot is the value of the Pearson product-moment correlation coefficient.

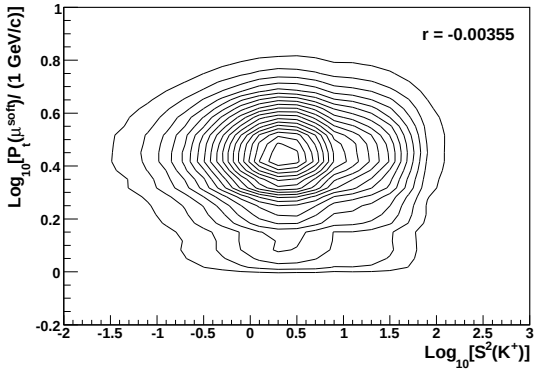

(a) $\log_{10}(P_t^{\mu_{\rm soft}})$ vs. $\log_{10}(S^2(K)$;

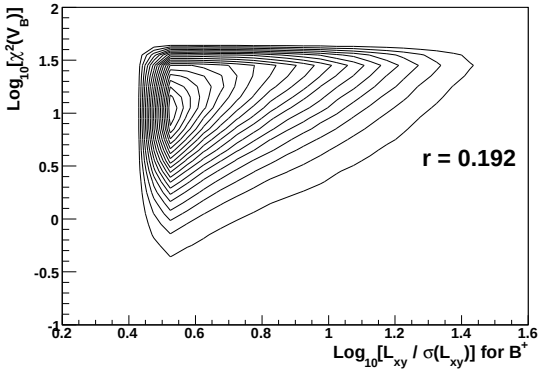

(b) $\log_{10}(\chi^2(V_B))$ vs. $\log_{10}(\Gamma_B)$;

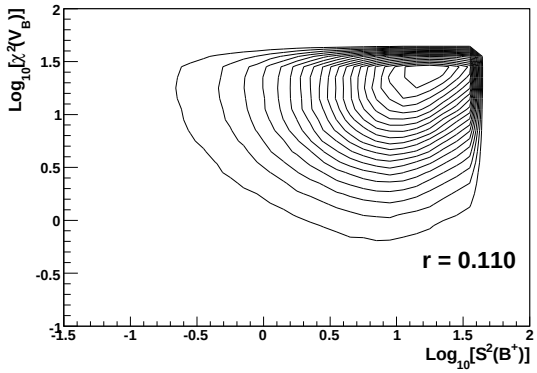

(c) $\log_{10}(\chi^2(V_B))$ vs. $\log_{10}(S^2(B^+))$;

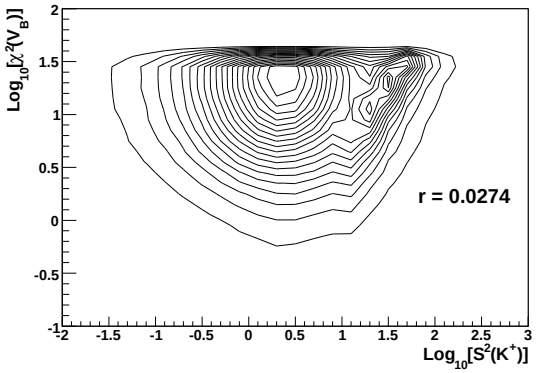

(d) $\log_{10}(\chi^2(V_B))$ vs. $\log_{10}(S^2(K)$;

Figure A.3: Two dimensional contour plots for variables used in the optimised B^+ selection (Part 3/4). The discriminating variables are described in the text. Also shown for each plot is the value of the Pearson product-moment correlation coefficient.

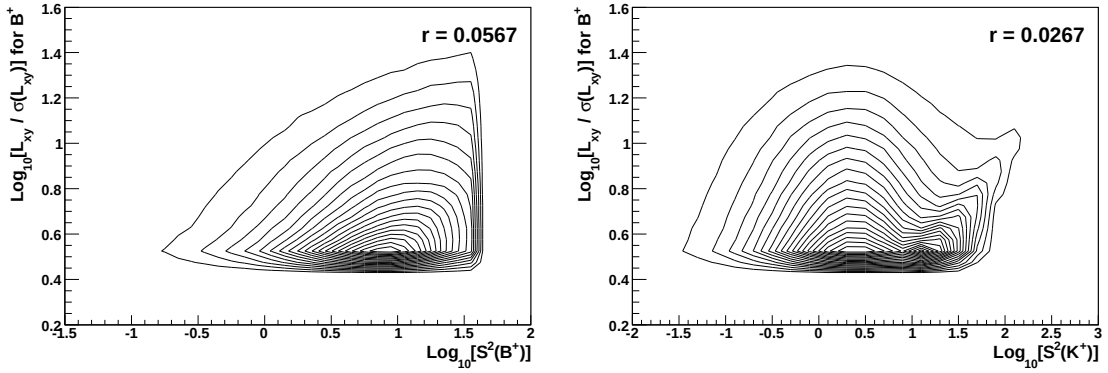

(a) $\log_{10}(\Gamma_B)$ vs. $\log_{10}(S^2(B^+))$; (b) $\log_{10}(\Gamma_B)$ vs. $\log_{10}(S^2(K)$;

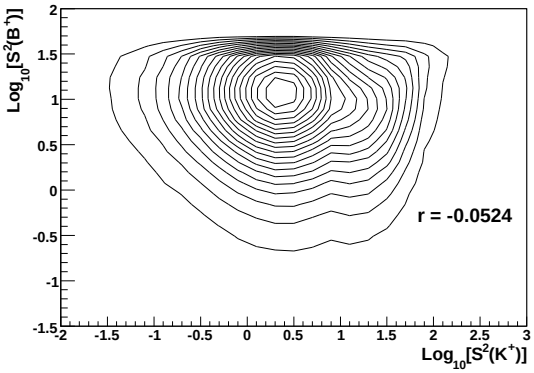

(c) $\log_{10}(S^2(B^+))$ vs. $\log_{10}(S^2(K)$;

Figure A.4: Two dimensional contour plots for variables used in the optimised B^+ selection (Part 4/4). The discriminating variables are described in the text. Also shown for each plot is the value of the Pearson product-moment correlation coefficient.

Table A.1: Pearson correlation coefficient, r, for each pair of discriminating variables used in the B^+ combined tagging selection. The variables are described in the text.

Variable	z_1	z_2	z_3	z_4	z_5	z_6
z_1	—	-0.0706	-0.0822	-0.0153	-0.190	-0.0089
z_2	-0.0706	—	0.0947	-0.0583	-0.0036	0.0316
z_3	-0.0822	0.0947	—	0.0567	0.0267	0.192
z_4	-0.0153	-0.0583	0.0567	—	-0.0524	0.110
z_5	-0.190	-0.0036	0.0267	-0.0524	—	0.0274
z_6	-0.0089	0.0316	0.192	0.110	0.0274	—

Bibliography

[1] A.F. Falk and T. Mehen, "Excited Heavy Mesons Beyond Leading Order in the Heavy Quark Expansion," *Phys. Rev.*, vol. D53, pp. 231–240, 1996.

[2] E.J. Eichten, C.J. Hill, and C. Quigg , "Orbitally Excited Heavy-Light Mesons Revisited" Prepared for Workshop on the Future of High Sensitivity Charm Experiments: CHARM2000, Batavia, Illinois. June 1994.

[3] V.M. Abazov *et al.*, D0 Collaboration, "Observation and Properties of $L = 1$ B_1 and B_2^* Mesons," *Phys. Rev. Lett.*, vol. 99, pp. 172001, 2007.

[4] V.M. Abazov *et al.*, D0 Collaboration, "Observation and Properties of the Orbitally Excited B_{s2}^* Meson," *Phys. Rev. Lett.*, vol. 100, pp. 082002, 2008.

[5] Murray Gell-Mann, "A Schematic Model of Baryons and Mesons," *Phys. Lett.*, vol. 8, pp. 214–215, 1964.

[6] F. Halzen and A.D. Martin, *Quarks and Leptons*, John Wiley & Sons, 1984.

[7] D.H. Perkins, *Introduction to High Energy Physics*, Cambridge University Press, 4 Edition, 2000.

[8] C. Amsler *et al.*, Particle Data Group, "Review of Particle Physics," *Phys. Lett.*, vol. B667, pp. 1, 2008.

[9] I.J.R. Aitchison and A.J.G. Hey, *Gauge Theories in Particle Physics*, Institute of Physics Publishing, 2003.

[10] T. Aoyama *et al.*, "Revised Value of the Eighth-Order Electron g-2," *Phys. Rev. Lett.*, vol. 99, pp. 110406, 2007.

[11] W.-M. Yao *et al.*, Particle Data Group, "Review of Particle Physics," *Journal of Physics G*, vol. 33, pp. 1, 2006.

[12] D. Buskulic *et al.*, ALEPH Collaboration, "Production of Excited Beauty States in Z Decays," *Z. Phys.*, vol. C69, pp. 393–404, 1996.

[13] P. Abreu *et al.*, DELPHI Collaboration, "Observation of Orbitally Excited B Mesons," *Phys. Lett.*, vol. B345, pp. 598–608, 1995.

[14] R. Akers *et al.*, OPAL Collaboration, "Observations of πB Charge-Flavor Correlations and Resonant $B\pi$ and BK Production," *Z. Phys.*, vol. C66, pp. 19–30, 1995.

[15] G. Abbiendi *et al.*, OPAL Collaboration, "Investigation of the Decay of Orbitally-Excited B Mesons and First Measurement of the Branching Ratio BR($B^{**} \to B^{+*}\pi(X)$)," *Eur. Phys. J.*, vol. C23, pp. 437–454, 2002.

[16] M. Acciarri *et al.*, L3 Collaboration, "Measurement of the Spectroscopy of Orbitally Excited B Mesons at LEP," *Phys. Lett.*, vol. B465, pp. 323–334, 1999.

[17] R. Barate *et al.*, ALEPH Collaboration, "Resonant Structure and Flavour Tagging in the $B\pi^{\pm}$ System using Fully Reconstructed B Decays," *Phys. Lett.*, vol. B425, pp. 215–226, 1998.

[18] A.A. Affolder *et al.*, CDF Collaboration, "Observation of Orbitally Excited B Mesons in $p\bar{p}$ Collisions at $\sqrt{s} = 1.8$ TeV," *Phys. Rev.*, vol. D64, pp. 072002, 2001.

[19] R.D. Field, "The Sources of b Quarks at the Tevatron and their Correlations," *Phys. Rev.*, vol. D65, pp. 094006, 2002.

[20] M. Paulini, "B Lifetimes, Mixing and CP Violation at CDF," *Int. J. Mod. Phys.*, vol. A14, pp. 2791–2886, 1999.

[21] D.A. Morris, "Heavy Quark Fragmentation Functions in a Simple String Model," *Nucl. Phys.*, vol. B313, pp. 634, 1989.

[22] A.F. Falk, "The CKM Matrix and the Heavy Quark Expansion," 2000.

[23] E.J. Eichten, C.J. Hill, and C. Quigg, Fermilab, "Properties of Orbitally Excited Heavy-Light Mesons," *Phys. Rev. Lett.*, vol. 71, pp. 4116–4119, 1993.

[24] N. Isgur, "Spin-Orbit Inversion of Excited Heavy Quark Mesons," *Phys. Rev.*, vol. D57, pp. 4041–4053, 1998.

[25] S. Godfrey and R. Kokoski, "The Properties of P-Wave Mesons with One Heavy Quark," *Phys. Rev.*, vol. D43, pp. 1679–1687, 1991.

[26] J. Zeng, J.W. Van Orden, and W. Roberts, "Heavy Mesons in a Relativistic Model," *Phys. Rev.*, vol. D52, pp. 5229–5241, 1995.

[27] D. Ebert, V.O. Galkin, and R.N. Faustov, "Mass Spectrum of Orbitally and Radially Excited Heavy-Light Mesons in the Relativistic Quark Model," *Phys. Rev.*, vol. D57, pp. 5663–5669, 1998, [Erratum-ibid. D **59**, 019902 (1999)].

[28] M. Di Pierro and E. Eichten, "Excited Heavy-Light Systems and Hadronic Transitions," *Phys. Rev.*, vol. D64, pp. 114004, 2001.

[29] A. Ali Khan *et al.*, "Heavy-Light Mesons and Baryons with b Quarks," *Phys. Rev.*, vol. D62, pp. 054505, 2000.

[30] History and Archives Project, Fermilab, `http://history.fnal.gov/`.

[31] S.W. Herb *et al.*, "Observation of a Dimuon Resonance at 9.5 GeV in 400-GeV Proton-Nucleus Collisions," *Phys. Rev. Lett.*, vol. 39, pp. 252–255, Aug 1977.

[32] S. Abachi *et al.*, D0 Collaboration, "Observation of the Top Quark," *Phys. Rev. Lett.*, vol. 74, pp. 2632–2637, Apr 1995.

[33] F. Abe *et al.*, CDF Collaboration, "Observation of Top Quark Production in $p\bar{p}$ Collisions with the Collider Detector at Fermilab," *Phys. Rev. Lett.*, vol. 74, pp. 2626–2631, Apr 1995.

[34] "Inquiring Minds" Web Resource, Fermilab, `http://www.fnal.gov/pub/inquiring/physics/discoveries/`.

[35] V.M. Abazov *et al.*, D0 Collaboration, "The Upgraded D0 detector," *Nucl. Instrum. Meth.*, vol. A565, issue 2, pp. 463–537, September 2006.

[36] Proton Source web pages, Fermilab, `http://www-bd.fnal.gov/proton/proton.html`.

[37] J. Thompson, "Introduction to Colliding Beams at Fermilab," *FERMILAB-TM-1909*, October 1994.

[38] C.W. Schmidt and C.D. Curtis, "Operation of the Fermilab H^- Magnetron Source," *AIP Conf. Proc.*, vol. 158, pp. 425–431, 1987.

[39] Accelerator Division Rookie Books, Fermilab, `http://www-bdnew.fnal.gov/operations/rookie_books/`.

[40] K. Junck *et al.*, "Commissioning and First Operational Experience of the 400 MeV Linac at Fermilab". Presented at the 4th European Particle Accelerator Conference (EPAC 94), London, England. June 1994.

[41] L.J. Allen *et al.*, "Operation and Improvements of the Fermilab 400 MeV Linac". Presented at the 18th International Linac Conference (Linac 96), Geneva, Switzerland. August 1996.

[42] L.J. Allen *et al.*, "Fermilab Linac 1997-1998 Operations, Studies and Improvements". Published in the proceedings of 19th International Linear Accelerator Conference (Linac 98), Chicago, IL. August 1998.

[43] C.D. Curtis *et al.*, "Linac H^- Beam Operation and Uses at Fermilab," *IEEE Trans. Nucl. Sci.*, vol. 26, pp. 3760–3762, 1979.

[44] M.D. Church and J.P. Marriner, "The Anti-proton Sources: Design and Operation," *Ann. Rev. Nucl. Part. Sci.*, vol. 43, pp. 253–295, 1993.

[45] F. Bieniosek *et al.*, "Antiproton Production and Cooling at the Tevatron". Presented at 5th European Particle Accelerator Conference (EPAC 96), Sitges, Spain. June 1996.

[46] D. Mohl, G. Petrucci, L. Thorndahl, and S. Van Der Meer, "Physics and Technique of Stochastic Cooling," *Phys. Rept.*, vol. 58, pp. 73–119, 1980.

[47] Tevatron Run II Handbook, Fermilab, `http://www-bd.fnal.gov/runII/`, August 2003.

[48] Recycler Electron Cooling web pages, Fermilab, `http://www-ecool.fnal.gov/`.

[49] D. Adams *et al.*, "CFT Technical Design Report," D0 Public Note 4164, June 2003.

[50] R.C. Ruchti, "The Use of Scintillating Fibers for Charged-Particle Tracking," *Ann. Rev. Nucl. Part. Sci.*, vol. 46, pp. 281–319, 1996.

[51] G.B. Turner *et al.*, "Visible Light Photon Counters for Scintillating Fiber Applications. I: Characteristics and Performance," Oct 1993, prepared for Workshop on Scintillating Fiber Detectors (SCIFI 93), Notre Dame, IN.

[52] M.G. Stapelbroek and M.D Petroff, "Visible Light Photon Counters for Scintillating Fiber Applications. II: Principles of Operation," Oct 1993, prepared for Workshop on Scintillating Fiber Detectors (SCIFI 93), Notre Dame, IN.

[53] L. Groer, D0 Collaboration, "D0 Calorimeter Upgrades for Tevatron Run II," *Frascati Phys. Ser.*, vol. 21, pp. 377–394, 2001.

[54] S. Abachi *et al.*, D0 Collaboration, "The D0 Detector," *Nucl. Instrum. Meth.*, vol. A338, pp. 185–253, 1994.

[55] V.M. Abazov *et al.*, D0 Collaboration, "The Muon System of the Run II D0 Detector," *Nucl. Instrum. Meth.*, vol. A552, issue 3, pp. 372–398, November 2005.

[56] V.M. Abazov *et al.*, D0 Collaboration, "Study of Direct CP Violation in $B \to J/\psi K^{\pm}(\pi^{\pm})$ Decays," *Physical Review Letters*, vol. 100, pp. 211802, 2008.

[57] B.S. Acharya *et al.*, D0 Collaboration, "Scintillation Counters for the D0 Muon Upgrade," *Nucl. Instrum. Meth.*, vol. A401, pp. 45–62, 1997.

[58] F. Borcherding *et al.*, D0 Collaboration, "The Level One Central Tracking Trigger for the D0 Upgrade," *IEEE Trans. Nucl. Sci.*, vol. 47, pp. 381–385, 2000.

[59] F. Borcherding *et al.*, D0 Collaboration, "A First Level Tracking Trigger for the Upgraded D0 Detector," *IEEE Trans. Nucl. Sci.*, vol. 46, pp. 359–364, 1999.

[60] K. Davis *et al.*, D0 Collaboration, "The Level One Muon Trigger For Run II of D0," *IEEE Trans. Nucl. Sci.*, vol. 44, pp. 348–353, 1997.

[61] R. Angstadt *et al.*, D0 Collaboration, "The D0 Level Three Data Acquisition System," *IEEE Trans. Nucl. Sci.*, vol. 51, pp. 445–450, June 2004.

[62] D. Bauer and R. Illingworth, "Level 3 Trigger: Clustering in the SMT," D0 Internal Note 3822, January 2001.

[63] Level 3 Clustering Web Page, D0 Collaboration, `http://www-d0.fnal.gov/~dbauer/physics/smtclusters/clusters.html`.

[64] Run II Software Algorithms web page, D0 Collaboration, `http://www-d0.fnal.gov/computing/algorithms/`.

[65] E. Nagy S. Baffioni and S. Protopopescu, "Thumbnail: a Compact Data Format," D0 Internal Note 3979, April 2002.

[66] Tracking Algorithm Recommendation Committee Report II, D0 Collaboration, `http://www-d0.fnal.gov/Run2Physics/WWW/documents/Reports/TARC2_vanKoote%n.pdf`, March 2003.

[67] A. Khanov, "HTF: The Algorithm Description," D0 Internal Note 3778, September 2000.

[68] R. Fr uhwirth, "Application of Kalman Filtering to Track and Vertex Fitting," *Nucl. Instrum. Meth.*, vol. A262, pp. 444–450, 1987.

[69] G.V. Borrisov , "Ordering a Chaos or... Technical Details of AA Tracking". Presented at Internal D0 Meeting. February 2003.

[70] G. Hesketh, "Central Track Extrapolation through the D0 Detector," D0 Internal Note 4079, January 2003.

[71] H. Greenlee, "The D0 Kalman Track Fit," D0 Internal Note 4303, December 2003.

[72] H. Greenlee, "Motion of a Charged Particle in a Magnetic Field," D0 Internal Note 4180, July 2003.

[73] H. Greenlee, "The D0 Interacting Propagator," D0 Internal Note 4293, November 2003.

[74] Tracking Algorithm Web Page, D0 Collaboration, `http://www-d0.fnal.gov/global_tracking`.

[75] C.M. Magass, *Search For New Heavy Charged Gauge Bosons*, Ph.D. thesis, RWTH Aachen University, November 2007, FERMILAB-THESIS-2007-33 (page 48).

[76] O. Peters, "Muon Segment Reconstruction - Linked List Algorithm," D0 Internal Note 3901, September 2001.

[77] F. Déliot, "The Fit Algorithm in muo trackreco," `http://www-d0.fnal.gov/~deliot/fitalg.ps`, November 2000.

[78] L. Chevalier *et al.*, "Track Parameter Error Propagation in Matter and Magnetic Field, Error Matrices Combination,"

`http://www-clued0.fnal.gov/~tuchming/myprop.ps`, October 2001.

[79] C. Clément *et al.*, "Muon ID Certification for p14," D0 Internal Note 4350, March 2004.

[80] P. Calfayan *et al.*, "Muon Identification Certification for p17 Data," D0 Internal Note 5157, February 2007.

[81] D. Whiteson, "Muon Tracking in the Calorimeter," D0 Internal Note 3996, September 2002.

[82] J. Abdallah *et al.*, DELPHI Collaboration, "b-tagging in DELPHI at LEP," *The European Physical Journal C*, vol. 32, issue 2, pp. 185–208, January 2004.

[83] G. Borisov, "Combined b-tagging," *Nucl. Instrum. Meth.*, vol. A417, issue 2-3, pp. 384–390, November 1998.

[84] T.W. Anderson, *An Introduction to Multivariate Statistical Analysis*, John Wiley & Sons, New York, 1958.

[85] J.L. Rodgers and W.A. Nicewander, "Thirteen Ways to Look at the Correlation Coefficient," *The American Statistician*, vol. 42, pp. 59, Feb 1988.

[86] T. Sjöstrand *et al.*, "PYTHIA 6.4 Physics and Manual," *JHEP*, vol. 05, pp. 026, 2006.

[87] D. J. Lange, "The EVTGEN Particle Decay Simulation Package," *Nucl. Instrum. Meth.*, vol. A462, pp. 152–155, 2001.

[88] R. Brun and F. Carminati, "CERN Program Library Long Writeup W5013," Tech. Rep., 1993.

[89] V.M. Abazov *et al.*, D0 Collaboration, "First Direct Two-sided Bound on the B_s^0 Oscillation Frequency," *Phys. Rev. Lett.*, vol. 97, pp. 021802, 2006.

[90] V.M. Abazov *et al.*, D0 Collaboration, "Measurement of the Ratio of B^+ and B^0 Meson Lifetimes," *Phys. Rev. Lett.*, vol. 94, pp. 182001, 2005.

[91] V.F. Blatt and J.M. Weisskopf, *Theoretical Nuclear Physics*, John Wiley & Sons, New York, 1952.

[92] F. James and M. Winkler, CERN, `http://www.cern.ch/minuit`, May 2004.

[93] E.W. Weisstein , "Chi-Squared Distribution" From Mathworld – A Wolfram Web Resource. `http://mathworld.wolfram.com/Chi-SquaredDistribution.html`.

[94] E.W. Weisstein , "The Erf Function" From Mathworld – A Wolfram Web Resource. `http://mathworld.wolfram.com/Erf.html`.

[95] E.W. Weisstein , "Poisson Distribution" From Mathworld – A Wolfram Web Resource. `http://mathworld.wolfram.com/PoissonDistribution.html`.

[96] E.W. Weisstein , "Likelihood Ratio" From Mathworld – A Wolfram Web Resource. `http://mathworld.wolfram.com/LikelihoodRatio.html`.

[97] T. Aaltonen *et al.*, CDF Collaboration, "Observation of Orbitally Excited B_s Mesons," *Phys. Rev. Lett.*, vol. 100, pp. 082001, 2008.

[98] M. Kreps, CDF Collaboration, "D and B Meson Spectroscopy, New States, Baryons at the Tevatron," October 2007, presented at the 12th International Conference on Hadron Spectroscopy (Hadron 07), Frascati, Italy. arXiv:0711.4890 [hep-ex]. CDF Public Note 8945.

[99] A.M. Badalian, Yu.A. Simonov, and M.A. Trusov, "The Chiral Transitions in Heavy-Light Mesons," *Phys. Rev.*, vol. D77, pp. 074017, 2008.

[100] X. Zhong and Q. Zhao, "Strong Decays of Heavy-Light Mesons in a Chiral Quark Model," *Phys. Rev.*, vol. D78, pp. 014029, 2008.

[101] K. Jansen *et al.*, ETM Collaboration, "Static-Light Meson Masses from Twisted Mass Lattice QCD," August 2008, arXiv:0808.2121 [hep-lat].

[102] T. Burch *et al.*, BGR Collaboration, "Excitations of Singly Beautiful Hadrons," September 2008, arXiv:0809.1103 [hep-lat].

[103] M. Bahr *et al.*, "HERWIG++ Physics and Manual," March 2008, arXiv:0803.0883 [hep-ph].

[104] R. Jesik, "Trigger Performance and Future," presented at internal meeting, D0 Summer Workshop, Prague, Czech Republic, August 2008.

[105] R. P. Feynman, R. D. Field, and G. C. Fox, "Correlations Among Particles and Jets Produced with Large Transverse Momenta," *Nucl. Phys.*, vol. B128, pp. 1, 1977.